Cu(I/II) complexes as models of the copper-(amyloid-beta) in-between state responsible for oxidative stress in Alzheimer's disease

Leonie Berthonnaud

Université Fédérale
Toulouse Midi-Pyrénées

THÈSE

En vue de l'obtention du
DOCTORAT DE L'UNIVERSITÉ DE TOULOUSE

Délivré par l'Université Toulouse 3 - Paul Sabatier

Cotutelle internationale: Collège doctoral de sciences et technologies de Nara

---

Présentée et soutenue par

Léonie BERTHONNAUD

Le 19 mai 2022

Complexes de Cu(I/II) comme modèles du cuivre-(amyloïde-beta) in-between state responsable du stress oxydant dans la maladie d'Alzheimer

---

Ecole doctorale : **SDM - SCIENCES DE LA MATIERE - Toulouse**

Spécialité : **Chimie Organométallique et de Coordination**

Unité de recherche :
LCC - Laboratoire de Chimie de Coordination

Thèse dirigée par
Christelle HUREAU-SABATER et Shun HIROTA

Jury

Mme Elodie ANXOLABEHERE-MALLART, Rapporteure
M. Marius REGLIER, Rapporteur
Mme Aurore THIBON-POURRET, Examinatrice
Mme Myriam MALET-MARTINO, Examinatrice
M. Tsuyoshi KAWAI, Examinateur
M. Gwenaël RAPENNE, Examinateur
Mme Christelle HUREAU-SABATER, Directrice de thèse
M. Shun HIROTA, Co-directeur de thèse

Acknowledgements

This PhD adventure was like a marathon to me, going through different steps more or less easy but all important. When I started, even if young doctors had shared their experiences with me, I didn't really realize what I was doing until the end. This marathon would not be possible without the "coaches" and the "organization committee", as well as the "supporters". At the end, I am very happy and grateful that I made it. With you, reading those words, and maybe the following parts of the manuscript, I am pleased to share this journey in bioinorganic chemistry.

My PhD was performed in double degree program between Université Toulouse III Paul Sabatier (UPS) in France and Nara Institute of Science and Technology (NAIST) in Japan. I am grateful to both Dr. Azzedine Bousseksou and Prof. Shun Hirota for hosting me in their respective laboratories, Laboratoire de Chimie de Coordination and Functional Supramolecular Chemistry Laboratory. I would like to thank Prof. Gwénaël Rapenne for having initiated the collaboration between Dr. Christelle Hureau and Prof. Shun Hirota, and for having followed me as a thesis sponsor and also in the administrative steps.

I thank all the jury members for the assessment of my work and the interesting and helpful discussions during the defense: Dr. Aurore Thibon-Pourret, Prof. Myriam Malet-Martino, Prof. Tsuyoshi Kawai, Prof. Gwenaël Rapenne and especially Dr. Elodie Anxolabéhère-Mallart and Dr. Marius Réglier for the deep review of my work and their great interest.

I would like to thank Prof. Shun Hirota for hosting me in his team, and for the great scientific discussions and advice during my time in Japan and also remotely during the pandemic period. I would like to thank him also for being responsive and the help he provided for the administrative part. Unfortunately, I was not able to come back to Japan to continue my research over there.

Christelle, je te remercie de m'avoir d'abord accueillie une première fois en 2015, puisque j'y ai découvert la chimie bio-inorganique qui m'a permis d'orienter mes études et de revenir dans ton équipe pour la fin. Je te remercie donc de m'avoir accueillie une deuxième fois pour une aventure plus longue et en cotutelle avec le Japon. La partie la plus stimulante de la thèse, c'est de démêler toutes les expériences pour en sortir quelque chose et c'est à travers ces

discussions scientifiques avec Charlène que ma motivation était maintenue. A chaque question tu trouves des expériences pour apporter des éléments de réponses, tes idées semblent inépuisables. Je te remercie de m'avoir partagé tes connaissances et ton expérience avec passion. Je suis reconnaissante de la confiance et la rigueur que tu m'as apportées. Tu m'as permis de développer mon esprit critique notamment dans l'interprétation des résultats (les miens et ceux publiés), en prenant toujours en compte et en essayant de comprendre mes idées un peu désordonnées parfois. Je te remercie également de m'avoir permis d'aller à plusieurs congrès et de participer à l'école d'été sur la RPE. Ton « coaching » pendant le Prison-Island restera aussi un très bon souvenir.

Je souhaite te remercier, Charlène, de m'avoir suivie au plus près pendant ces trois années et demie. Je te remercie de ta disponibilité, ton encadrement, de m'avoir soutenue notamment dans la mise en place des premières manips, et de l'écriture de mon manuscrit, d'avoir partagé tes connaissances, expériences et conseils avec moi. Je suis reconnaissante de ton implication et de ton soutien jusqu'au bout. Je garde également un bon souvenir des quelques moments en dehors du labo.

I would like to thank all the Prof. Hirota's team, for welcoming me among them and the great times together in and out of the lab. Special thanks to Cheng for his help during my stay. I would like to thank Tashiro-San for her help and availability when I was in Japan and after.

Je remercie tous les membres de l'équipe F anciens et actuels, pour les moments de partages scientifiques, professionnels et personnels, pour m'avoir soutenue dans des moments émotionnellement difficiles, pour le divertissement au travail et en dehors, pour m'avoir enseigné vos connaissances pratiques et intellectuelles, pour avoir partagé les deux bureaux dans lesquels j'ai été, pour les gâteaux, les thés, les soupes, le saucisson, les dîners au LCC, les longues soirées de travail, la convivialité, les jeux, pour m'avoir aidée à monter deux rampes, d'écouter mes longs monologues, pour l'aide apportée dans n'importe quelle situation, pour vos attentions, pour avoir partagé les labos, pour leur bonne humeur et leur sourire, pour les sorties, pour la positivité, pour les relectures, pour la rigueur de l'équipe, pour l'énergie !

Ma thèse n'aurait pas été possible sans les plateformes techniques mises à ma disposition. Je remercie tout particulièrement Sonia pour les belles analyses de cristaux, Lionel pour l'analyse de mes tubes RPE et Christian pour mes RMN sportives (ta bonne humeur était un réel encouragement pour refaire mes tubes « ratés »).

Je tiens à remercier les personnes qui ont marqué mon parcours vers la chimie et plus particulièrement qui m'ont aidée à trouver ma voie vers la chimie de coordination et la chimie bio-inorganique : Christelle Mousnier, Fabienne Alary, Diana Over. Je vous remercie pour vos encouragements, les discussions, la force et la passion que vous m'avez transmises.

Vianney, je te remercie d'avoir vécu cette aventure avec moi, je pense que c'était probablement un peu une sorte de marathon pour toi aussi. Je te remercie de t'être accroché pour comprendre ce que je faisais, pour retenir les noms des techniques de spectro que j'utilisais, pour m'avoir changé les idées, m'avoir réconforté, soutenu à fond, pour les grignotages accompagnés de petits mots ! Merci d'aimer mes posters et de vouloir tous les accrocher… Je remercie également la Pounou Prod' pour les accompagnements musicaux rythmés à la batterie pendant les journées de télétravail et les musiques démarrant des danses improvisées (on retiendra « Sway » de Rosemary Clooney et Pérez Prado comme chanson qui lançait le dancefloor) pendant les ateliers cuisine du soir, qui m'ont permis de m'échapper à une période où c'était interdit. Evidemment, je remercie Produjus pour les smoothies tout frais concoctés le matin et surtout pendant la dernière ligne droite et parfois même quand je me levais super tôt (ce qui était quand même rare).

Je souhaite évidemment remercier ma famille pour leur soutien perpétuel sans jugement, pour m'avoir donné confiance d'aller jusqu'au bout de mes projets, pour encaisser mes moments d'énervements qui ne leur sont pas (toujours) destinés, pour être toujours intéressés par ce que je fais, pour m'avoir posé des questions « naïves » qui me font réfléchir plus que des questions « pertinentes » et aussi pour me changer les idées !!!

Je remercie également ma belle-famille pour l'intérêt qu'ils ont porté à ce que je faisais et leur soutien notamment dans « la dernière ligne droite », avec tout plein de petites attentions.

Je remercie toutes mes amies et tous mes amis, pour m'avoir permis de faire le ménage de mon cerveau en oubliant tout grâce à votre bonne humeur général, votre énergie exceptionnelle, votre humour, mais aussi par votre écoute et votre soutien. Vous êtes un bol d'air frais qui m'est indispensable.

List of abbreviations

A

AA: Amino Acid

Abs: Absorbance

AD: Alzheimer's disease

APP: Amyloid Precursor Protein

Asc: Ascorbate

Asp: Aspartate

Aβ: Amyloid-β

C

CE: Counter Electrode

ClO_4^-: Perchlorate ion

CO: Carbon monoxide

Cu(I): Cuprous ion

Cu(II): Cupric ion

Cu: Copper

CV: Cyclic Voltammetry or Cyclic Voltammogram

E

EPR: Electron Paramagnetic Resonance

F

Fe: Iron

FID: Free Induction Decay

FT-IR: Fourier-Transformed Infrared

G

G: Gauss

GDP: Gross Domestic Product

H

H_2O_2: Hydrogen Peroxide

H_2SO_4: Sulfuric Acid

His: Histidine

$HO^{\bullet}$: Hydroxyl Radical

HOMO: High Occupied Molecular Orbital

I

IBS: In-Between State

J

JIB: Journal of Inorganic Biochemistry

K

KPB: Phosphate buffer

L

LMCT: Ligand To Metal Charge Transfer

LUMO: Lowest Occupied Molecular Orbital

M

MLCT: Metal To Ligand Charge Transfer

MRI: Magnetic Resonance Imaging

N

NaOH: Sodium Hydroxide

NMR: Nuclear Magnetic Resonance

NO_3^-: Nitrate ion

O

O_2: Oxygen (or dioxygen)

$O_2^{\bullet-}$: Superoxide Radical

OCP: Open Circuit Potential

P

pH: Power of Hydrogen

Phe: Phenylalanine

R

Ref: Reference Electrode

ROS: Reactive Oxygen Species

RS: Resting State

S

$S_2O_3^{2-}$: Thiosulfate ion

SO_3^{2-}: Sulfite ion

SO_4^{2-}: Sulfate ion

T

TBP: Trigonal bipyramidal geometry

TMPA = Tris(2-MethylPyridyl)Amine

TPP: Tetraphenylporphyrin

TSP: 3-(Trimethylsilyl)propionic-2,2,3,3-d4 acid sodium salt

Tyr: Tyrosine

U

USD: US Dollar

UV-Vis: Ultraviolet-Visible spectroscopy

W

WE: Working Electrode

X

XAS: X-ray Absorption Spectroscopy

Z

Zn: Zinc

Greek Letters:

ε: Molar attenuation coefficient

λ: Wavelength

Table of contents

General introduction

General introduction

The brain is an essential organ. Through the evolution, the brain has evolved and adapted giving rise to different living species. It centralizes our perceptions, feelings, memory, thoughts and controls all the body functions. It is composed by billions of inter-connected neurons. It is a fascinating organ, remaining mysterious.

Dementia is a common cause of brain's dysfunction, affecting mainly the elderly. 50 million people around the world are living with dementia and one new case occurred every 3 seconds. Alzheimer's disease (AD) is the most common cause of dementia. It is a neurodegenerative disorder characterized by memory loss, poor judgment, cognitive impairment and increased anxiety and anger. All those symptoms worsen and the main functions of brain are degraded until the death of the patient.

As the population is aging and growing, the cases of AD are increasing. Up to now there is no curative treatment. It is a burden disease for the patient, his/her relatives and caregivers as the patient becomes dependent and bed bounded. It is also a costly disease. Different researches axis focus on cure development, early detection and disease understanding.

The morphological hallmarks of AD are a brain atrophy accompanied by intracellular neurofibrillary tangles resulting from the assembly of hyperphosphorylated Tau protein and the presence of extracellular senile plaques made of fibrils from the amyloid-β (Aβ) peptide. During AD, high level of oxidative damages are observed in the brain caused by reactive oxygen species (ROS). ROS are highly reactive species and their level is well controlled by enzymatic system to the useful value in order to avoid their over-reactivity with their surrounding environment. In AD there is an overproduction of ROS causing damages.

The senile plaques are mainly composed by the Aβ peptide and biometals such as copper (Cu). Aβ can coordinate to Cu and form complexes (Cu-Aβ) able to catalyze the production of ROS through its reduction by ascorbate (a naturally present reductant) and its oxidation by dioxygen (O_2). The mechanism behind this reactivity is not well understood. The objective of my PhD was to gain more insight into the reactivity of the reduced Cu-Aβ complexes with O_2

The first chapter establishes the context of the thesis. The general features of AD are described. The etiology of the disease is given with an emphasis on Cu-Aβ complexes in link with ROS production. Then objectives of the thesis are given in relation with scientific challenges, technical bottlenecks and the planned solutions to overcome them. Among them, the use of a reference compound (Cu-TMPA (TMPA = Tris(2-MethylPyridyl)amine)) is detailed, and accordingly, short literature data are given on this well-known complex that will be used throughout the manuscript.

The second chapter gives an overview of the different spectroscopic and electrochemical characterizations techniques used in the presented studies. UV-Visible (UV-Vis), Electron Paramagnetic Resonance (EPR), Nuclear Magnetic Resonance (NMR), Fourier-Transformed Infrared (FT-IR) spectroscopies and Cyclic Voltammetry (CV) are thus briefly introduced.

The third chapter is focused on the study of Cu(II)TMPA complexes. A brief literature overview is given and then solid-state as well as solution characterizations, mainly by UV-Vis, EPR and cyclic voltammetry are described. I will show that the structure in solution is dependent on the experimental conditions (solvent, presence of various anions) in line with a labile position of the Cu(II)TMPA, which could be occupied by several kind of exogenous ligands.

The chapter four aimed at characterizing the Cu(II)Aβ complexes under study. Indeed in addition to the reference compound, I have studied three short N-terminally truncated peptide models ($A\beta_{1-16}$, $A\beta_{1-7}$ and $A\beta_{13-14}$) of the Cu(I/II) coordination site in the full-length Aβ. Furthermore, the impact on Cu(II)Aβ complexes of the use of acetonitrile as a co-solvent, conditions established to study their reactivity, is evaluated.

The chapter five is presenting the results of the reactivity study of Cu(I)Aβ toward carbon monoxide (CO) used as a surrogate of dioxygen. ^{1}H NMR, UV-Vis, FT-IR spectroscopies and cyclic voltammetry are used with a systematic comparison to the reference compound Cu(I)TMPA complex.

Chapter six, similarly to chapter five, presents the reactivity study of Cu(I)Aβ and Cu(I)TMPA complexes toward dioxygen. The ROS production is evaluated through the consumption of ascorbate followed by UV-Vis spectroscopy. It is completed by the cyclic

voltammetry study of each compound under aerobic conditions, to disentangle the dioxygen activation mechanism.

A final annex chapter presents the results obtained during the study of Cu-TPMA complex with the use of dithionite as a reductant. This study leads to the detection and quantification of thiosulfate and sulfite anions by Cu(II)TMPA species in mixed organic/aqueous solution. As a direct application, the detection of sulfite in a sugar sample was performed. All these results were published in 2021 in J. Inorg. Biochem.

Chapter I

Chapter I. Oxygen activation & Alzheimer's disease

This first chapter establishes the context of research giving insight into important aspects that will be broached throughout the manuscript. First, Alzheimer's Disease (AD) is described focusing on Reactive Oxygen Species (ROS) production, settling the background of research. The objectives and challenges of my PhD are presented in a second part. In a third section, the use of Tris(2-MethylPyridyl)Amine (TMPA) as a reference and a model ligand to establish conditions of study is explained and justified. Finally, a detailed description of this manuscript's content is given.

I.A. Reactive oxygen species in Alzheimer's disease

I.A.1. General introduction on Alzheimer's disease

Our world is always facing different challenges, according to the period of life, the discoveries, the societal issues, and our goals evolution. The increasing population on Earth, due to the rise of births and the augmentation of life expectancy, is highlighting different issues. One of them is the increasing number of people living with dementia, characterized by chronic or persistent mental disorder due to brain damages. The most common cause of dementia is AD, representing 60 to 70 % of the cases.

I.A.1.a. Prevalence

AD is a neurodegenerative disorder affecting the elderly. In 2019, 1.2 million persons in France and about 50 million persons worldwide are living with AD or related dementia.[1] These numbers are estimated to double or more in the coming 20 to 30 years. The majority of people developing AD are 65 years or older. However, an uncommon hereditary form often occurs at younger age.[2] The prevalence (number of cases) increases with aging, and the presence of other diseases such as hypertension or diabetes.[3] The percentage of women having AD is higher than for men, whereas it is more equal for other dementia type.[4-5] Beyond the longer lifetime for women than men, this gender difference of developing AD could be related to hormonal factor and differences of immune system.[6-7]

AD is a burden for the patient and his relatives, because of money cost and daily care needs, in addition to the disease itself. In 2015, the estimated global cost in France is about 32 billion euros (≈ 36 billion USD (US dollar)) for the management of AD and related diseases per year. In the world in 2015, AD global societal cost was estimated at 818 USD, per year, representing 1.1 % of worldwide GDP (Gross Domestic Product), making AD the most expensive disease of the 21st century for the society.[1]

I.A.1.b. Symptoms

AD was named after Alois Alzheimer a German psychiatrist and neuropathologist who first described it in 1906.[8] It is a progressive disease beginning with subtle short-term memory loss, and language problems. Those symptoms become stronger and are followed by cognitive impairments, behavioural disorders (depression, apathy, suspicion…), time and space disorientation and solving problem issues. Physical functions such as swallowing or walking are then affected entailing dependency. The patient needs more and more care, becoming bed-bounded as the disease progresses until death. The clinical brain changes are likely to appear over 20 years before the appearance of symptoms. The cognitive reserve enables the brain to compensate its damages. AD symptoms differ of strengths and pace from one patient to another. Patient diagnosed with AD have sometimes another dementia, called mixed dementia.[9]

I.A.1.c. Diagnosis and treatment

AD is diagnosed by crossing different techniques. The appearance of characteristic symptoms, especially memory loss, and cognitive functions tests establish the first proof. Brain MRI (Magnetic Resonance Imaging) can reveal brain atrophy involved in AD. Finally, lumbar puncture can show the presence of biological marker such as abnormal level of amyloid-β (Aβ) peptide, or the phosphorylated Tau protein.[2]

Up to date there is no curative treatment against AD or other dementia. Few drugs exist to improve the cognitive symptoms by rising the amount of neurotransmitters in the brain. However, they are not always showing great efficiency. Non-pharmacological therapies are supported to optimise physical and brain functions, through healthy stimulating life.

I.A.2. Hallmarks of Alzheimer's disease

AD is characterized by brain changes: The hyperphosphorylation of Tau protein; the formation of senile plaques and the atrophy of the brain (Figure I.A-1). The brain injuries starts in the cognitive area (hippocampus) before extending to the whole brain, with damages of neurons, other cells and finally tissues. The brain is composed by neurons interconnected by long branching extension called synapses. Information is relayed by chemical release and recognition, from one neuron to another. All this fast data flow is driving our memories, emotions and behavior. The Tau protein is localized inside neurons. During AD it undergoes transformation that induces the formation of neurofibrils tangles responsible for the lack of transportation of neurons' survival essential nutrients and molecules.[9] This aspect will not be discussed much. The origin of senile plaques and brain atrophy will be further explained.

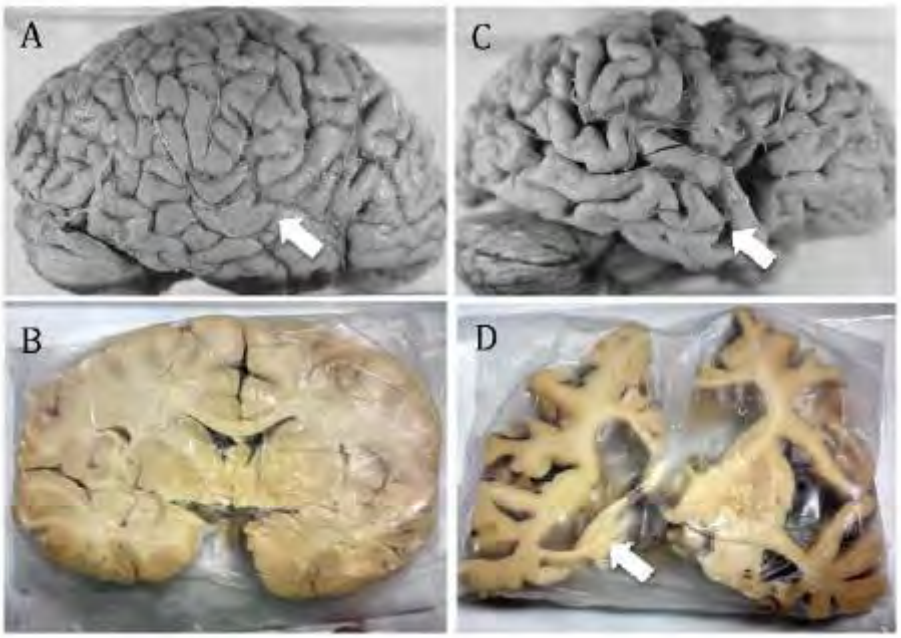

Figure I.A-1: Neuroanatomical comparison of healthy brain (A, B) and AD brain (C, D). Prominent atrophy in C compared with A (arrows). B, D: Coronal section of A and C respectively. Arrow on D shows an enlargement of the ventricles and selective hippocampal atrophy.[10]

I.A.2.a. The senile plaques

Senile plaques are produced outside neurons into synapses interfering in communication between neurons. They are mainly composed by the aggregated Aβ peptide and metal ions.

(i) The amyloid-β peptide

Healthy brain possesses the Aβ peptide in soluble form, whereas it is in aggregated form in AD patient brain. Aβ sequences are heterogeneous, spanning from 38 to 43 amino acid residues (AA); the full sequence is shown in Figure I.A-2. The N-terminal part of the Aβ peptide is soluble in water and binds to Cu, whereas the C-terminal part is highly hydrophobic, insoluble and is responsible for the aggregation process (*id est* the self-assembly of Aβ). The 16 first AA are involved in the minimal high affinity binding site for copper coordination, therefore the truncated $A\beta_{1-16}$ peptide is a valid model to represent Cu coordination to the soluble monomeric full length Aβ peptide.[11] Aβ belongs to the disordered peptides category and thus has no well-defined 3D structure in its monomeric state.[12]

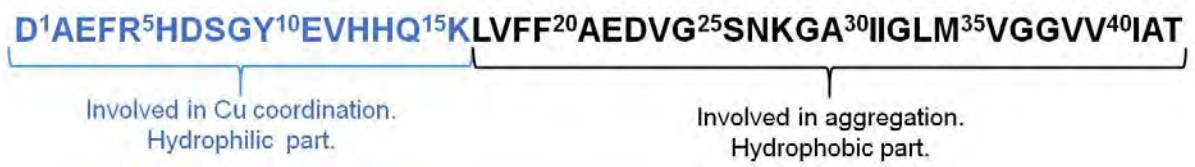

Figure I.A-2: Aβ peptide full sequence of the 43 amino acid residues.

Aβ is generated by the cleavage of the trans-membrane amyloid precursor protein (APP) by β- and γ-secretases.[11] Aβ levels in the brain are regulated by Aβ-degrading proteases. The exact biological function of Aβ remains unclear.[13]

(ii) The amyloid precursor protein

APP is a type-1 trans-membrane protein. This protein is cleaved following two different pathways: (i) the amyloidogenic path by the β-secretase (cleavage of Aβ at the first position) and γ-secretase (cleavage at the position 40 or 42) producing Aβ and (ii) the non-amyloidogenic path (predominant) starting by the α-secretase (cleavage between the 16 and 17 positions) followed by the γ-secretase giving $A\beta_{17-40}$ and $A\beta_{17-42}$ (Figure I.A-3). The C-terminal truncated peptide $A\beta_{1-16}$ can be obtained by cleavage of APP by both α- and β-secretases.[11] The most abundant Aβ peptides generated in the brain are $A\beta_{1-40}$ and and to a lesser extent $A\beta_{1-42}$.[13]

(iii) The amyloid cascade hypothesis

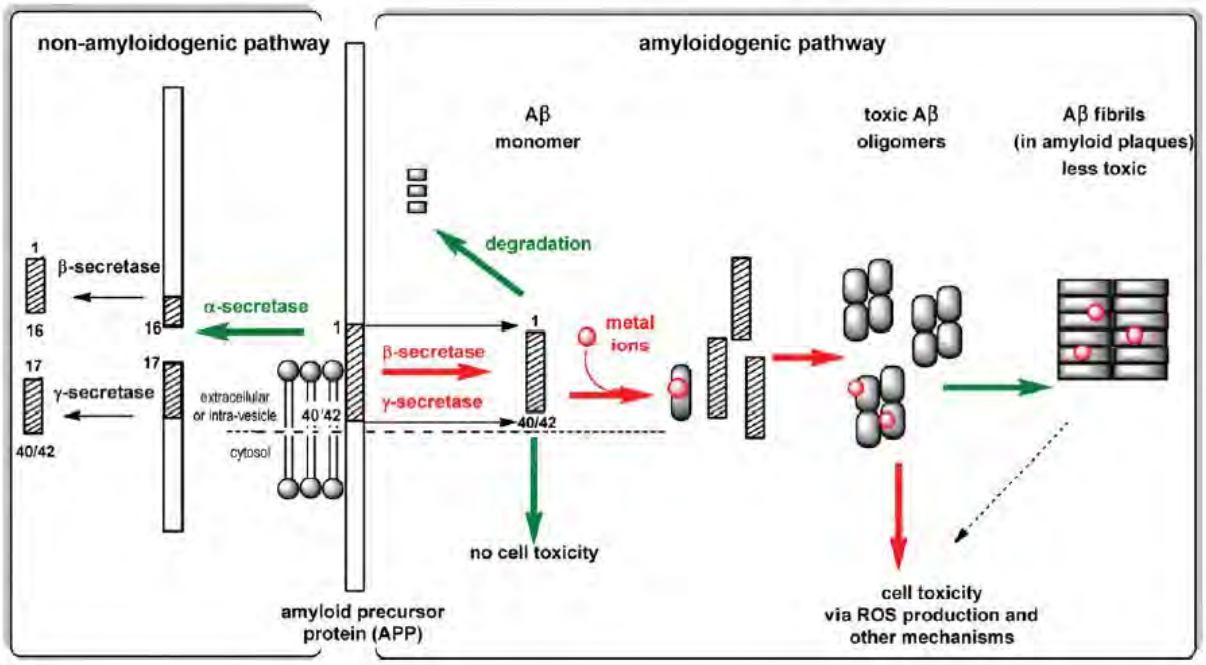

Figure I.A-3: Schematic view of APP cleavage in the pathways the non amyloidogenic (left side) and the amyloidogenic (right side) followed by the amyloid cascade.[11]

The amyloid cascade is the hypothesis formulated around 1990 to explain the formation of the senile plaques from the soluble monomeric Aβ peptide, and the following deleterious events such as the development of intracellular neurofibrillary tangles and synaptic dysfunctions, leading to neuronal cells death and dementia.[14] It is stipulated that an increase of the extracellular Aβ levels in the brain leading to its aggregation is the primary event of AD. It is followed by nerve cells toxicity leading to Tau protein hyperphosphorylation and further to neurofibrils tangles causing nerve cells death and later cognitive impairment.[15] It is the most accepted hypothesis up to now, but it remains controversial.[11, 13] This model does not fit with every case of AD.[15]

(iv) Amyloid-β aggregation

Aβ aggregation proceeds through different steps. The formation of nuclei from monomers represents the first step known as the nucleation phase. It is followed by the elongation phase corresponding to the addition of monomers at the extremities of the nuclei leading to the formation of fibrils that are further detected in the senile plaques (Figure I.A-3). The aggregation process is dynamic with exchanges between aggregation states. The oligomers

formed during the nucleation step are suggested to be the most toxic species as they can catalyze ROS production and are also implicated in other deleterious events (such as disruption of synaptic function and effects on the membrane bilayer integrity).[12] The overproduction of ROS is toxic for the surrounding molecules and cells, contributing to neurons death. Deregulation of metal homeostasis is observed in AD, likely to be due to perturbation of normal brain metal homeostasis with age.[16]

(v) Metals in plaques

The amyloid plaques are enriched with metal ions such as Cu, Zn and Fe, in high concentration (up to millimolar range).[12] They are most probably playing roles in ROS production and aggregation behavior as Cu and Zn can bind Aβ. Furthermore, aggregation process was observed to preferentially occur in Zn-releasing synaptic regions.[16] Metal ions impact the kinetics of the aggregation, especially on nucleation phase, and the morphology of the fibrils and aggregation intermediates.[12] Due to Aβ flexibility, its coordination to Zn(II) and Cu(I/II) is weaker than for well-ordered metalloproteins. Thus, different metal ions are coordinated to Aβ through different coordination sites and in a dynamic fashion. Fast ion exchange can occur intra-peptide on different coordination sites or inter-peptides. The coordination modes of those metal ions to Aβ are hard to determine in aggregated form, but are suggested to be similar to those for monomeric forms. The redox properties of Cu ion are responsible for its important role on ROS production.[16]

I.A.2.b. The oxidative stress

(i) General

ROS consist of superoxide radicals ($O_2^{\bullet -}$), hydrogen peroxide (H_2O_2), and hydroxyl radicals ($HO^{\bullet}$), the most reactive one. They are highly reactive species with their surroundings. Their generation is a normal activity during oxygen metabolism. It is involved in many physiological processes such as cell signaling. Several biological systems are responsible for their scavenging, detoxification, clearance and homeostasis. However, external or internal factors can induce an overproduction and/or dysfunction of ROS treatment. Oxidative stress occurs when there is an imbalance between the production of ROS and its detoxification, leading to cells and tissues injuries detrimental to health.[17] The oxidative stress is implicated in many diseases such as AD.

(ii) Oxidative stress mediated by Cu-Aβ complex

The oxidative stress participates to functional impairment and atrophy of the brain in AD. It is generated by different factors such as mitochondrial dysfunction and redox transition metals.[13, 18] The last is on our focus especially ROS production mediated by Cu-Aβ complex. This complex is redox active and catalyzes ROS production by successive and incomplete one-electron reduction of O_2. Cu cycles between its +1 and +2 oxidation states thanks to the presence of a reductant such as ascorbate and dioxygen (Figure I.A-4). The catalytic cycle starts from Cu(I)Aβ and O_2 binding. Cu(I) reduces O_2 by one electron transfer to give $O_2^{\bullet-}$ and Cu(II)Aβ. Cu(II)Aβ is reduced back to Cu(I)Aβ by ascorbate through electron transfer and reduces $O_2^{\bullet-}$ to form H_2O_2 with a proton source, and so on and so forth until $HO^{\bullet}$ generation. So far the mechanism of oxygen activation by Cu-Aβ is not known. However, strong hypothesis suggests the formation of a so called "in-between-state" (IBS) intermediate as the active species during the redox cycling of Cu(I)/Cu(II)Aβ complex.[19]

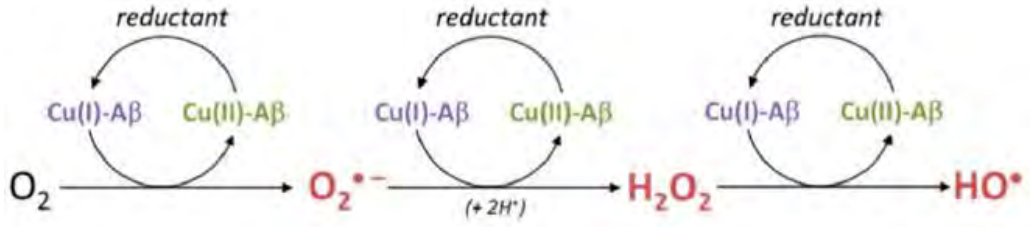

Figure I.A-4: Mechanism of ROS production from a reductant and dioxygen catalyzed by the Cu-Aβ complex. The ROS produced are the superoxide anion ($O_2^{\bullet-}$), hydrogen peroxide (H_2O_2) and the hydroxyl radical ($HO^{\bullet}$).[11]

I.A.3. Reactive oxygen species formation by Cu-Aβ complex

To understand and try to elucidate the O_2 activation mechanism it is important to have a closer look into Cu and Aβ interactions and the related spectroscopic observations made in solution.

I.A.3.a. Copper coordination to amyloid-β

As mentioned before, Aβ is a flexible peptide and this feature remains even after its coordination to Cu, inducing dynamic coordination modes in fast equilibrium. $A\beta_{1-16}$ is often used as a model to study Cu coordination to the full length Aβ as it contains the 16 first AA involved in Cu binding. The coordination sites of Cu(II) and Cu(I) to Aβ detailed after, are the major coordination sites at physiological pH.

(i) Cu(II) coordination

Cu(II) is able to bind Aβ peptide by anchoring the N-terminal amine of Asp1 and His6, His13/14 imidazole groups. Cu(II) is present in two binding modes to Aβ at physiological pH, referred to as component I and component II (Figure I.A-5) with a transition pKa at 7.8, component I being the major form at neutral pH.[20] In component I, Cu(II) is bond to Aβ by the N-terminal amine of Asp1, the carbonyl from the amide bond between Asp1 and Ala2, and the nitrogen atoms from the His6 and the His13 or His14 due to dynamic exchange. In component II, favored at higher pH, Cu(II) is coordinated by the N-terminal amine of Asp1, the deprotonated nitrogen atom from the Asp1-Ala2 amide bond, the carbonyl from the amide bond between Ala2 and Glu3, and one nitrogen atom from one of the three His residues with no preference due to dynamic exchange.[16, 19, 21] Carboxylate or aqua ligand can additionally coordinate Cu(II) in its apical position.[16] The affinity constant of $A\beta_{1-16}$ for Cu(II) is in the order of magnitude of 10^9-10^{10}.[20] The coordination mode of Cu(II) to Aβ was elucidated by complementary methods, including NMR and pulse EPR spectroscopies and ^{13}C or ^{15}N labeled peptides.[21-22]

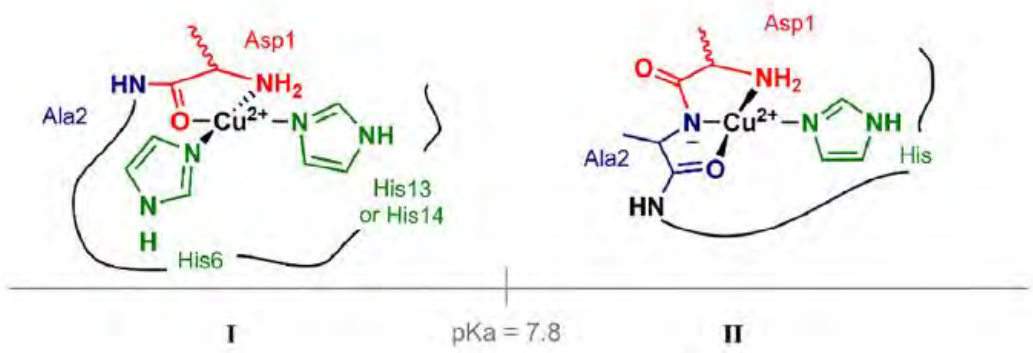

Figure I.A-5: Cu(II) coordination to Aβ in component I and II at physiological pH.[19]

(ii) Cu(I) coordination

Cu(I) coordination to $A\beta_{1-16}$ was much less investigated than Cu(II). Indeed, Cu(I)$A\beta_{1-16}$ is not easy to handle and to characterize as it is highly sensitive to oxygen. It is EPR silent, and no d-d transition are observed by circular dichroism (CD) and UV-Vis as the d-orbitals are full, thus only NMR and XAS (X-ray Absorption Spectroscopy) spectroscopies can be used. NMR showed dynamical processes for one coordination position and the involvement of the 3 His residues because of the chemical shift of each associated signals. The major coordination to Cu(I) seemed to be in linear fashion His-Cu-His with the 3 His couples involved. However the 3 His coordinated to Cu(I) could be a transient form important in the redox reaction from Cu(I) to Cu(II). The substitution of one His residue, among the three, by Ala residue decreases the binding affinities of $A\beta_{1-16}$ to Cu(I), supporting the importance of the 3 His in the coordination to Cu(I). NMR NOEs (Nuclear Overhauser Effect) correlations revealed that His6 is close in space to the dyad of His13His14, and the major coordination modes are either the 3 His or His6 and His13 in linear fashion (Figure I.A-6). The coordination of the His13His14 dyad only is less probable but still possible.[23-24] The association constant of $A\beta_{1-16}$ toward Cu(I) is in the order of magnitude between 10^7 to 10^{10} depending on the affinity for the dyes used for the UV-Vis experiment.[19]

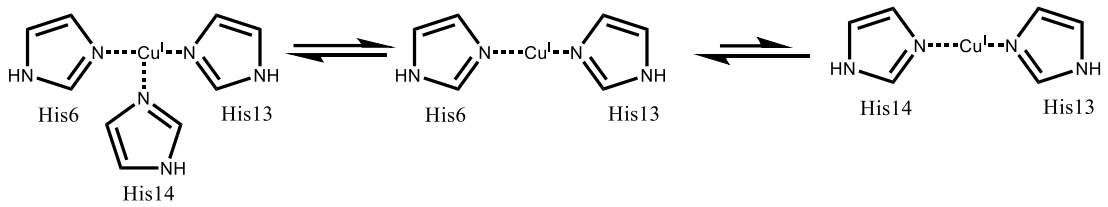

Figure I.A-6: Schematic view of Cu(I) coordination to Aβ peptide. Adapted from reference 23.

I.A.3.b. In-between state theory

ROS generation catalysed by Cu-Aβ complex requires a redox cycling between Cu(I) and Cu(II) with the help of a reductant such as ascorbate and a source of oxygen like O_2 or H_2O_2. The most populated form of Cu(I)Aβ and Cu(II)Aβ also called resting states (RS) have very different coordination spheres. Consequently, they would require huge reorganization energy during the redox cycling between the two forms. Indeed, Cu(II)Aβ has a 4-coordination distorted square planar geometry whereas Cu(I)Aβ has a 2-coordination linear geometry.[20] Cyclic Voltammetry (CV) studies on Cu-$Aβ_{1-16}$ complex showed a slow electron transfer with a separation of anodic and cathodic peaks of 600 mV at 50 mV/s. The large reduction wave is interpreted as an unusual small transfer coefficient meaning a slow rate of variation of the activation energy with driving force. The electron transfer accompanied by the geometric rearrangement is determined to follow a preorganization electron transfer mechanism (Chemical-Electrochemical-Chemical mechanism). This mechanism stipulates that the redox cycling goes through intermediates with coordination in the mid-way between Cu(II)Aβ and Cu(I)Aβ RS to allow minimal electron transfer reorganization energy.[25] The so-called IBS is in equilibrium with the two RS, (Figure I.A-7) reachable because of the flexibility of Aβ and would represent only 0.1 % of the species in solution.[25-26] The IBS was never spectroscopically characterized as it is elusive. The postulated IBS intermediate was not only proposed from electrochemical studies but also from chemical reactions with involvement of substrates such as ascorbate for Cu(II) and O_2 or H_2O_2 for Cu(I). A coordination sphere is proposed for the IBS based on first oxidative damages observed by mass spectrometry on the peptide itself and impacts of Aβ mutations on ROS production level. For the IBS, it is proposed that Aβ is bound to Cu via the N-terminal amine, the Asp1 carboxylate group, and a nitrogen atom from the imidazole ring of one of the 3 His residues.[26] Studies using $Aβ_{1-16}$ mutants and following ascorbate consumption by the corresponding Cu complexes, as a mirror of ROS production,

showed that when the His6 is the only His residue, the intrinsic rate of ascorbate oxidation is the highest suggesting that among the three His residue, His6 would lead to the most active IBS.[20]

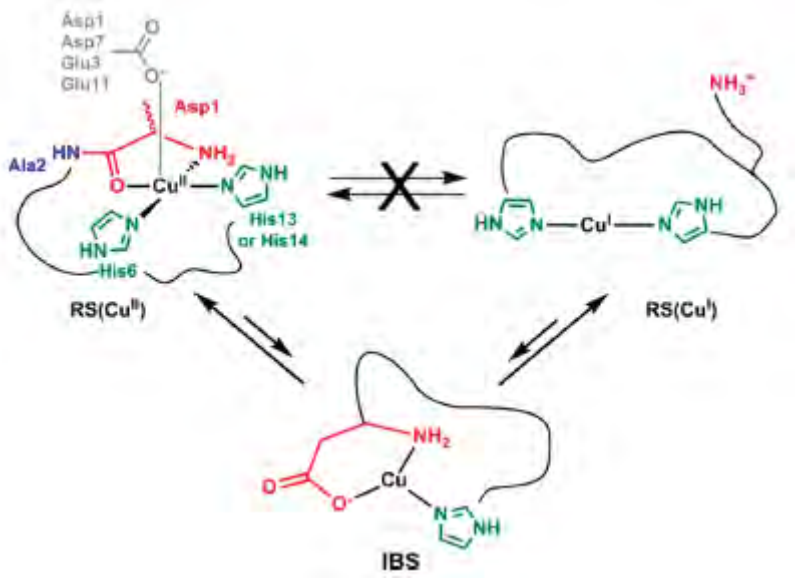

Figure I.A-7: Equilibrium between the most populated resting states of Cu(II) and Cu(I) and the IBS of the Cu-Aβ complex during ROS production at physiological pH.[20]

The involvement of IBS on the ROS production is now a strong hypothesis, according to that a mechanism of oxygen activation by the Cu-Aβ and especially the active species IBS has been proposed (Figure I.A-8). The binding of O_2 in a η^1 end-on to Cu(I)IBS would lead to the electron transfer from Cu(I) to O_2, which will become Cu(II) and superoxo η^1 end-on ligand respectively, the superoxide would then be released and the resulting Cu(II)IBS can be reduced by ascorbate to start a new catalytic cycle. Similar mechanism could be considered for the following one electron reductions of $O_2^{\bullet-}$, and H_2O_2.[26]

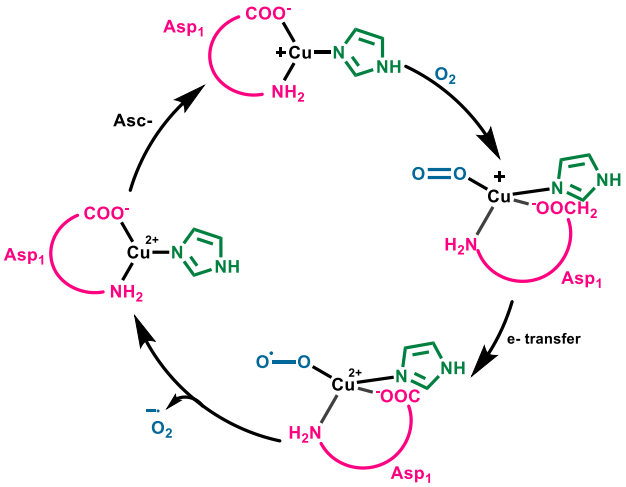

Figure I.A-8: Proposed mechanism for O_2 activation by Cu-Aβ through the IBS. Adapted from reference 26.

I.B. Objectives of the thesis and bottlenecks to overcome

I.B.1. Objectives: identification of the O_2 intermediates in the in-between state mechanism

ROS are implicated in AD causing oxidative stress damages and brain atrophy. Understanding ROS production process could give crucial information on this key deleterious event in AD. ROS are proposed to be generated mainly from the oligomeric species. A closer look to the amyloid plaques revealed the presence of high amount of metal ions with redox properties, such as Fe and Cu. Cu is able to coordinate Aβ impacting the formation of the amyloid plaques. Cu-Aβ can also catalyze the production of ROS. In other words, Cu-Aβ is able to activate and reduced O_2 naturally present in the brain. This reaction is fueled by a physiological reductant such as ascorbate also naturally present in the brain (in high level 300 μM).

Two main populated states called resting states (RS) were identified and characterized: Cu(II)Aβ RS and Cu(I)Aβ RS. Cu(II)Aβ RS having a square planar geometry and Cu(I)Aβ RS a linear geometry, the electron transfer would go along with a huge reorganization energy. However, CV studies on Cu-A$\beta_{1\text{-}16}$ complex showed that the electron transfer goes through an intermediate species having a geometry in the mid-way between Cu(II) or Cu(I) RS starting from both of them and able to redox cycle very rapidly. This intermediate called IBS is proposed to be the active species for O_2 activation. It cannot be spectroscopically observed or characterized because of its elusive and low-populated features. However, a coordination sphere has been proposed based on oxidative damages induced on the peptide itself and rate of ROS production using different Aβ mutants (Figure I.A-7).[20, 26]

Confirming the exact active species of the catalytic ROS production is of special interest to better understand Cu-Aβ-based oxidative damages in AD. O_2-bound intermediate in the IBS would also give insight into the O_2 activation mechanism by Cu-Aβ, that could be extended to other flexible peptide coordinated to Cu involved in ROS production. The detection of any intermediate during O_2 catalytic activation and determining its coordination sphere were the main objectives of my PhD work.

Different challenges concerning the study of O_2 intermediates and particularly with IBS are foreseen. First of all this IBS is a transient and low populated species. Second, for the IBS elucidation to be pertinent, it has to be performed in a biologically relevant medium. The dynamic encountered in Cu-Aβ system due to the flexibility of Aβ has also to be taken into account, and would require the use of model complexes.

I.B.1.a. Chemical properties of dioxygen – General features

The chemical properties of O_2 are fundamental to understand its interaction and activation by a particular species.

Although O_2 (oxygen or dioxygen) is an essential element to life, it is also toxic through its reduction into ROS. The brain consumes 20 % of the body oxygen and energy supplies.[9] O_2 represents 21 % of the volume of air composition. Oxygen is an odorless, colorless and tasteless gas under normal conditions of pressure and temperature. It is a diatomic O-O non-polar molecule, with a covalent bond of 1.21 Å length and 494 $kJ.mol^{-1}$ strength. O_2 is hazardous under its liquid state at temperatures below its boiling point (-183 °C) becoming pale blue. As a pure gas it has a density of 1.429 $g.L^{-1}$ at 273 K and 1.0 atm being a little heavier than air (1.204 $g.L^{-1}$ at 273 K and 1.0 atm).[27]

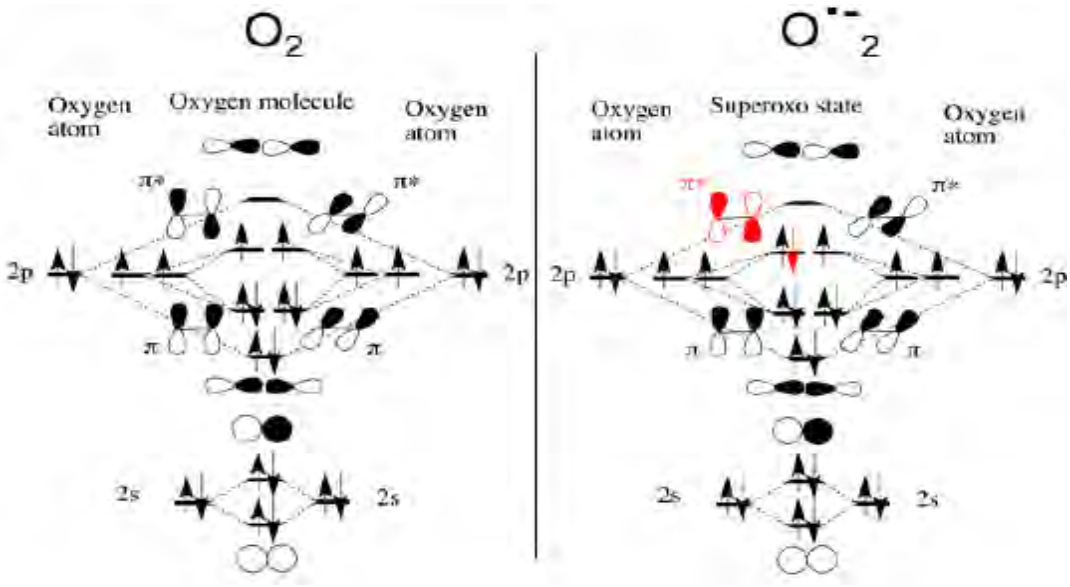

Figure I.B-1: Molecular diagrams of O_2 and $O_2^{\bullet-}$. In red on the left diagram is the electron given by the Cu(I) center to form $O_2^{\bullet-}$ (energy scale is arbitrary).[28]

O_2 is paramagnetic in its triplet ground state with two unpaired electrons in π* molecular orbitals (Figure I.B-1). It is the only natural element with this property. The triplet state represents the most abundant and stable form of O_2. The singlet state is less common but much more reactive.[27] It binds metal ions through its HOMO π* orbitals. Cu(I) can easily reduce O_2 by one electron transfer from the d orbitals to the π* of oxygen to form $O_2^{\bullet-}$ (Figure I.B-1).

Table I.B-1: Standard reduction potential for one and two-electron reduction of dioxygen species in water.[29]

Reaction	E° (V) vs NHE, pH 7.25
$O_2 + e^- \rightarrow O_2^{\bullet-}$	-0.33
$O_2^{\bullet-} + e^- + 2\ H^+ \rightarrow H_2O_2$	+0.89
$H_2O_2 + e^- + H^+ \rightarrow H_2O + HO^{\bullet}$	+0.38
$HO^{\bullet} + e^- + H^+ \rightarrow H_2O$	+2.31
$O2 + 2\ e^- + 2\ H^+ \rightarrow H_2O_2$	+0.281
$H2O2 + 2\ e^- + 2\ H^+ \rightarrow 2\ H_2O$	+1.349

The four electrons reduction of O_2 to H_2O in water at pH 7 with a standard potential of 0.815 V vs NHE is thermodynamically favorable. However, under chemical conditions a fully concerted four-electron reduction is unexpected and will preferably proceed through one or two-electron steps. Table I.B-1 presents the standard potentials for one or two-electron reduction of dioxygen species in water. All reduction steps are thermodynamically favored except the one-electron reduction of O_2 into superoxide radical with a potential of -0.33 V vs NHE. Metal-catalyzed oxygen reduction could avoid the kinetics restriction due to the spin-conversion rule because of the triplet state of O_2 and thermodynamic restriction encountered during the one-electron reduction pathways by stabilization of $O_2^{\bullet-}$ or by giving two-electron reduction from O_2.[29]

I.B.1.b. Solubility and diffusion coefficient

Oxygen has the property to dissolve and diffuse into aqueous and organic liquid. However, the amount of O_2 and its rate of diffusion varies with the type of solvent, the pressure, the temperature, and the other compounds present in solution. The amount of a compound per unit of solvent defines the solubility. The diffusion coefficient represents the rate of flow of a soluble substance in a solution from high concentration region to a lower concentration area. It is mathematically defined by Fick's law (Equation I.B-1).[27]

$$J = -D\left(\frac{dC}{dx}\right)$$

Equation I.B-1

(J: amount of substance that flows through a unit area per unit time (mol.cm^{-3}.s^{-1}); D: diffusion coefficient (cm^2.s^{-1}); C: concentration of the substance (mol.cm^{-3}); x: distance from the higher concentration area to the lower (cm)).

The solubility and diffusion coefficient values found in the literature, the type of solvent, the origin of O_2 (air or pure O_2 gas) and their conversion in common unit are given below. Only values measured at 25 °C and 1.0 atm pressure of gas (air or O_2) are presented in Table I.B-2.

Table I.B-2: Solubility and diffusion coefficient of O_2 in different solvents.

Solvent	Air or O_2 gas (1 atm)	Solubility (mM)	Diffusion Coefficient (10^{-5} cm^2.s^{-1})	Ref
H_2O	O_2	1.22 to 1.28	2.2 to 2.55	27, 30-33
	Air	0.26 to 0.34	-	27, 34
D_2O	O_2	1.25 to 1.40	-	33
CH_3CN	O_2	8.10	-	33, 35
	Air	2.42 to 2.60	-	34, 36
CH_3CN/TBAP* or TEAP (0.1 M)**	O_2	8.10	-	37
	Air	1.26	9.2	38
THF	O_2	10.1	-	31, 33

*TBAP: Tetrabutylammonium perchlorate. **TEAP: Tetraethylammonium perchlorate.

O_2 solubility is inversely proportional to the ionic strength defined by Equation I.B-2.[39]

$$I = \frac{1}{2}\sum c_i z_i^2$$

Equation I.B-2

(I: ionic strength (mol.L^{-1}); c_i: ionic concentration (mol.L^{-1}); z_i: number of charge of the ion considered).

An increase in temperature will decrease O_2 solubility, whereas it is the opposite with a rising pressure.[27] The non-polar feature of O_2 makes it more soluble in organic (8.1 mM in CH_3CN) than in aqueous solvents (around 1.25 mM in H_2O) (Table I.B-2).[29] The differences for the solubility values given for a same solvent depend on the determination technique used.

O_2 diffusion coefficient increases with the rising temperature. The higher the viscosity of a solution the lower the O_2 diffusion coefficient. Thus the composition of the solution (salts) will affect its viscosity so the diffusion coefficient too. The pressure does not affect much the viscosity and thus the diffusion coefficient of O_2. As the solubility, the diffusion coefficient for O_2 is higher in CH_3CN than in H_2O, 9.2 $x10^{-5}$ and around 2.4 x 10^{-5} $cm^2.s^{-1}$ respectively (Table I.B-2).

I.B.2. Bottleneck 1: elusive character of the in-between state

I.B.2.a. Intermediate stabilization by carbon monoxide

The unstable and elusive features of IBS makes it hard to detect and characterize, the same holds true for O_2-bound intermediates in the IBS. Lowering the temperature to slow down reactivity of transient species was often used to increase their lifetime and thus allow their characterizations. However, this approach cannot be applied in our case, because if we want to keep a biological relevance we need to work as much as possible in aqueous buffered media (limiting the possibility to decrease the temperature). An alternative to overcome this issue is to use carbon monoxide (CO) gas as a surrogate of O_2. CO is redox-inactive and should bind to Cu(I) without any further reactivity. In this manner, it should stabilize key intermediates Cu(I)Aβ(CO) during the Cu(I)/(II)Aβ catalytic cycle (Figure I.B-2).

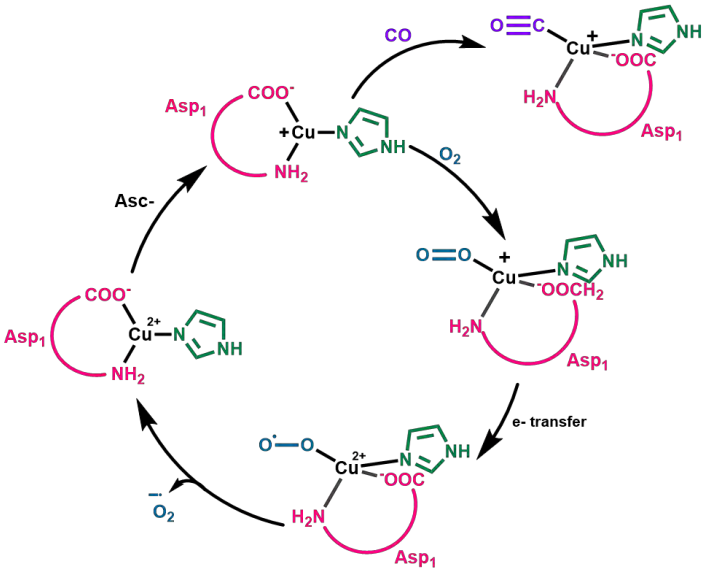

Figure I.B-2: Proposed Cu-Aβ(CO) adduct during the catalytic cycle of O_2 reduction by Cu-Aβ IBS.

The lifetime of the CO-adduct should be longer than O_2 intermediate allowing its accumulation in solution and consequently its characterization. The use of CO as O_2 analogue is classical and, in our field, found in the literature with calixarene-based[40] or linear two-coordinate His-based dyad cuprous complexes for exemple.[41-42] Information on Cu(I) state using Fourier-transformed infrared (FT-IR) spectroscopy were extracted.

The general features of CO are important to understand its behavior and specificity as Cu(I) ligand.

I.B.2.b. General features of carbon monoxide

Carbon monoxide is a odorless, colorless, tasteless and highly toxic gas. Indeed, it strongly binds to the iron center of hemoglobin responsible for O_2 transportation in body and replaces it, thus causing headache, tiredness, nausea that can quickly evolve to coma and death.

Figure I.B-3 presents the molecular diagram of carbon monoxide. It has ten valence electrons distributed in the triple C-O bond and in the lone pairs on each atom. CO has a singlet ground state. It is a diamagnetic ligand suitable for Cu(I) ions as its orbital arrangement is favorable to bind metal ions in low formal oxidation state and high d electrons energy.

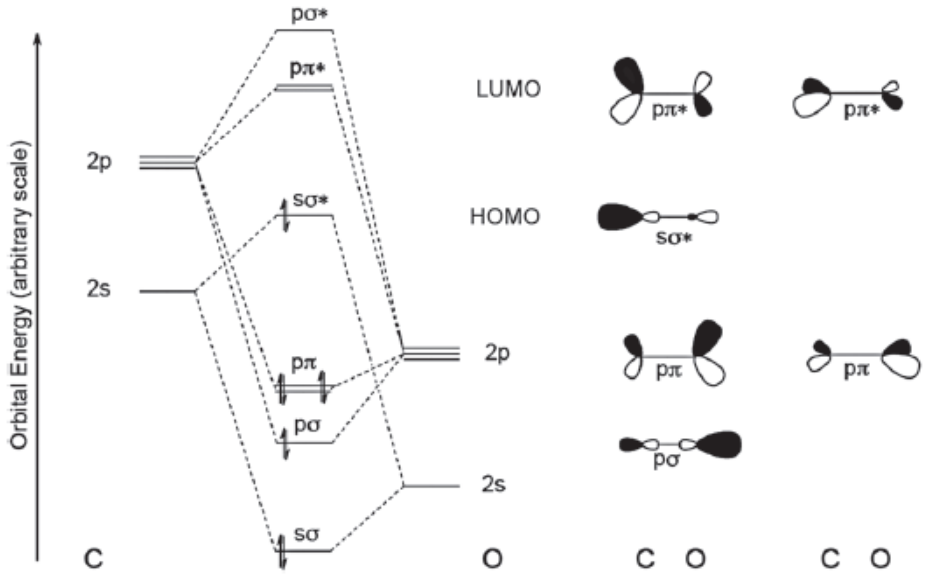

Figure I.B-3: Molecular diagram of CO (energy scale is arbitrary).[43]

CO is a L-type ligand, meaning that it does not affect metal oxidation state upon binding. It is coordinated to Cu(I) through a strong σ-bond from the non-bonding HOMO σ* of CO to d

orbital of Cu(I) (Figure I.B-3 and Figure I.B-4). Furthermore, the LUMO π* of CO is in good symmetry and energy level for the filled d orbitals of the metal ion to give back electron density as π-back donation (Figure I.B-4).[43] π-back donation strengths the M-CO bond and weakens the C-O bond. This is observed by IR with a decrease in vibrational frequency. The more the Cu(I) center will be electron rich, the more the π-back donation will be significant.

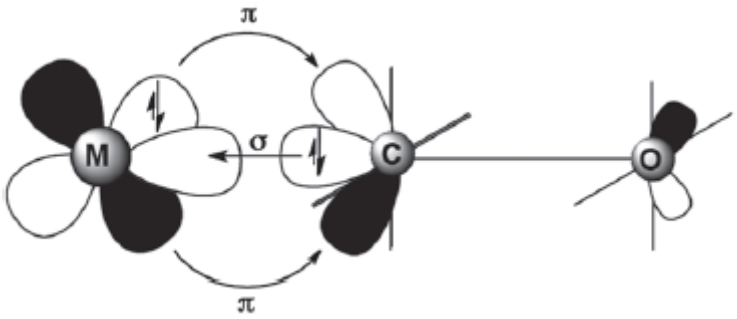

Figure I.B-4: Metal-CO binding mode scheme representing σ-donation from CO to metal ion and π-back donation from metal ion to CO molecular orbitals.[43]

CO short triple bond (1.13 Å) is composed by two covalent bonds and one dative covalent bond with a resulting strong dissociation energy of 1072 kJ/mol.[44] The CO bond is weakly polarized and a small negative charge could be considered on C and a small positive charge on O atoms with a dipolar moment of 0.11 D pointing from C to O atoms.[44] The IR stretching vibration of free CO gas is at 2143 cm^{-1}.[45] However, when CO is dissolved in water, its stretching band is too broad to be detected by IR at room temperature.[46] There is much less data and studies for CO solubility in various solvents than for O_2. The concentrations of CO in CO saturated H_2O, CH_3CN, and THF are 1 mM, 100 mM and 10 mM respectively.[47-49]

The inherent CO features, namely, being able to form strong M-CO bond and redox inactivity, make it a great candidate to overcome the elusive character of the IBS. Indeed, CO could strongly bind to Cu(I)IBS similarly to O_2. The stability of the resulting CO adduct could allow its accumulation and thus its detection and characterization.

I.B.3. Bottleneck 2: having enough concentration of the intermediate species to allow study

The study of the IBS requires to be in biologically relevant media as Cu-Aβ complex is sensitive to pH, i.e. in aqueous buffered solution at physiological pH. It was mentioned previously that the IBS represents only 0.1 % of the species in solution during the catalytic cycle of O_2 activation by Cu-Aβ complex. The use of CO as a surrogate of O_2 explained before will allow the accumulation of the Cu(I)Aβ(CO) adduct in the bulk as it should not further evolve. To be detectable by NMR and IR spectroscopies, the concentration of the Cu(I)Aβ(CO) adduct should be high enough (around 2 mM). However, it was mentioned previously that CO solubility in H_2O is around 1 mM. In general the solubility of a gas has a tendency to decrease with the presence of salt in solution,[50] consequently, CO solubility in buffered aqueous solution is expected to be lower than 1 mM becoming the limiting reagent. The solubility of CO in CH_3CN (100 mM) is 100 times higher than in H_2O, thus 10 % of CH_3CN in the media should drastically increase the CO amount in solution and drive the reaction of Cu(I)Aβ + CO ⇄ Cu(I)Aβ(CO) toward the adduct formation. If we consider the solubility of CO being linear in mixture of solvent of CH_3CN and H_2O (which is an approximation as it is not usually the case for other mixtures of H_2O and organic solvent[47]), the CO concentration in CH_3CN/H_2O 10/90 v/v would be near 10 mM. 10 % of CH_3CN in buffered media should not affect much the behavior of Cu-Aβ, however, this has to be experimentally confirmed.

I.B.4. Bottleneck 3: flexibility of the peptide: need for benchmark studies with well-described system

The flexibility of Aβ peptide enables it to take various dynamic coordination modes with Cu(II) or Cu(I). This features make the IBS more prone to different dynamic coordination modes that would be in equilibrium and thus more difficult to identify depending on the spectroscopic techniques used. Decreasing the length of the peptide and the number of coordination site available will reduce its flexibility. In order to favor or stabilized main coordination modes separately, specific truncated peptides of $A\beta_{1-16}$ were chosen as detailed below.

$A\beta_{1-16}$-$CONH_2$: *DAEFRHDSGYEVHHQK-$CONH_2$*

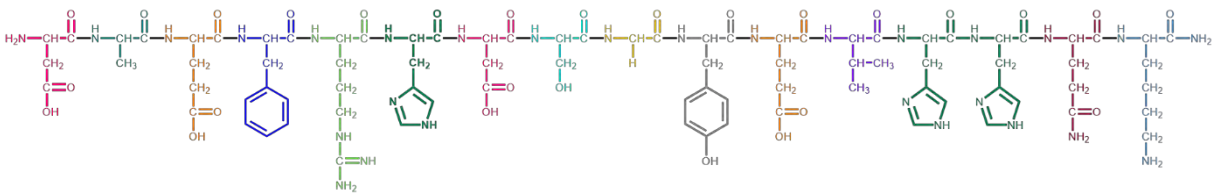

$A\beta_{1-16}$ is considered as the most appropriate model for the study of Cu-Aβ complexes in general as it contains all the amino acids implicated in the coordination to copper, without the C-terminal hydrophobic sequence responsible for the aggregation process.[11] The coordination of $A\beta_{1-16}$ peptide to copper was extensively studied. $A\beta_{1-16}$ allowed the identification of the amino acids involved in Cu(II) and Cu(I) coordinations as well as the evidence for the existence of an IBS by cyclic voltammetry.[19-20, 23, 51]

$A\beta_{13-14}$-$CONH_2$: *HH-$CONH_2$* 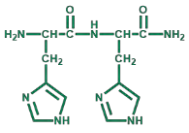

$A\beta_{13-14}$ is composed by only two histidine residues. $A\beta_{13-14}$ was selected with the hope of increasing the stability and constraining the coordination to Cu(I) by the two histidine residues, and thus model the Cu(I)Aβ RS.

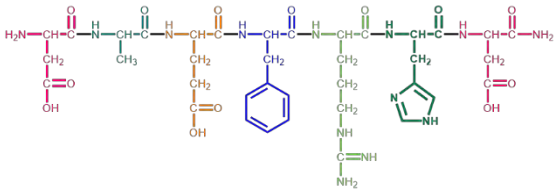

Aβ$_{1-7}$-CONH$_2$: *DAEFRHD-CONH$_2$*

Aβ$_{1-7}$ is composed by 7 amino acids containing only one histidine residue. It binds Cu(II) in the same manner as the component II in Cu(II)Aβ$_{1-16}$ with the His6.[26] Aβ$_{1-7}$ coordination to Cu(I) will be different than the one for Cu-Aβ$_{1-16}$, as it contains only one histidine. This peptide might favor the IBS form.

Protection in the C-term position:

Every peptide selected for this study is protected in the C-terminal position with an amidation to avoid any participation of –COO$^-$ in the coordination to Cu, which would not be relevant.

The study of CO coordination to the Cu-Aβ model complexes requires to rely on well-described references. The well-known and vastly studied TMPA (Tris(2-MethylPyridine)Amine, also known as TPA and TPMA) ligand is used to set up conditions of studies for Aβ model peptides, and as a reference with the different characterization techniques.

TMPA (Tris(2-MethylPyridyl)Amine): 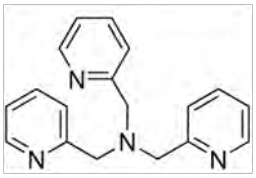

TMPA is a N-donor ligand with pyridine groups anchored to a central tertiary amine. It can model small peptide ligands with histidine residues. Cu(I)(TMPA) complexes were extensively studied in organic solvents by the groups of K.D. Karlin and G.J. Meyer especially for CO an O_2 binding (affinity, binding rates, photodissociation, solvent effect...). TMPA derivatives and other tripodal tetradentate ligands were studied as well.[48, 52-53] TMPA has the advantage to be highly soluble in many organic and aqueous solvents. The knowledge acquired on Cu-TMPA reactivity toward CO and O_2 in organic solvents will serve as a reference to study it in aqueous medium and then with Cu-Aβ model complexes.

I.C. Cu-TMPA as a reference

Cu-TMPA complexes are used as reference for the study of Cu-Aβ model complexes under CO atmosphere. Cu-TMPA complexes are soluble in aqueous and organic solvents. They were widely studied. A general overview of those studies is presented. More details from literature are given in the following chapters according to the themes broached.

I.C.1. TMPA a bio-inspired ligand

TMPA is a tripodal tetradentate ligand with three 2-pyridylmethyl arms attached to a central tertiary amine. It can mimic the binding site of small peptides containing N-donor atoms, like histidine residues. TMPA is a non-planar tetradendate ligand which cannot adopt tetrahedral coordination with transition metal ions due to small bite angles. Thus it coordinates Cu(II) in a trigonal bipyramidal geometry leaving an open coordination site allowing the binding of a exogenous ligand.[54]

I.C.1.a. Cu(II)TMPA

Cu(II)TMPA complexes were thoroughly characterized in solution, mainly in organic solvents, by UV-Vis and EPR spectroscopies and in solid-state by X-ray crystallography. Solution and solid-state characterizations of Cu(II)TMPA complexes, regardless of the 5th ligand, are in agreement with a penta-coordinated trigonal bipyramidal (TBP) geometry (Figure I.C-1). It is characterized in UV-Vis spectroscopy by typical d-d absorption bands with a low energy transition and a higher energy one less intense, appearing as a shoulder. These two transitions originate from an electronic transfer upon excitation from the orbitals d_{xz}/d_{yz} to the d_{z^2} (high energy) and from the $d_{x^2-y^2}/d_{xy}$ to the d_{z^2} (lower energy) (Figure I.C-1 (B)). A representative example of such UV-Vis spectrum is given in Figure I.C-1 (B) for [CuTMPA(Br)]Br in acetonitrile with one d-d transition at 981 nm (ε=178 $M^{-1}cm^{-1}$) and the second one at 759 nm (ε=75 $M^{-1}cm^{-1}$).[55-56] Depending on the 5th ligand and the solvent, a LMCT band can be observed between 300 and 450 nm. In EPR, the classic spectra obtained are representative of a non-classical reversed axial system with typical g-values of $g_{\perp} \approx 2.20$ and $g_{//} \approx 2.0$ (Figure I.C-1 (C)). More detailed solution and solid-state characterizations of Cu(II)TMPA complexes are given in Chapter III.

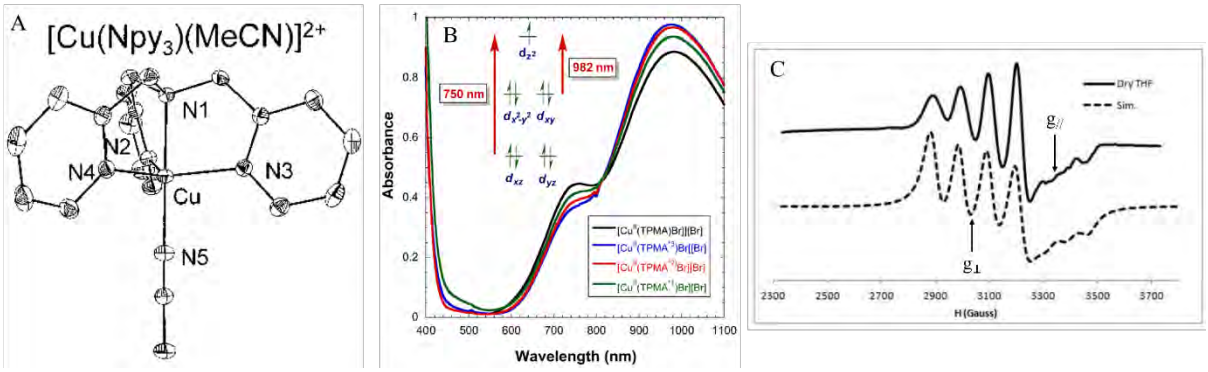

Figure I.C-1: Structure of [CuTMPA(CH$_3$CN)]$^{2+}$ drawn with 50 % probability ellipsoids (A).[57] UV-Vis spectra focused on d-d region of [CuTMPA(Br)]Br (black) and other Cu(II)TMPA derivatives complexes in CH$_3$CN (B).[56] Experimental (solid line) and simulated (dashed line) EPR spectra of [CuTMPA(H$_2$O)](OTf)$_2$ in dry THF (C).[58]

I.C.1.b. Cu(I)TMPA

Cu(I)TMPA complexes are EPR silent and no transition is observed by UV-Vis spectroscopy in the d-d region as Cu(I) is a d^{10} cation. However, they often display a metal to ligand charge transfer (MLCT) band around 350 nm in UV-Vis.[48, 59-60] They can be characterized by NMR in solution or by X-ray crystallography in solid-state. Structures of Cu(I)TMPA complexes show that it can be pseudo-pentacoordinated with 4 N atoms from TMPA and a 5th ligand or tetra-coordinated with two different cases, (i) the tertiary amine and two of the three pyridyl-arms from TMPA and an external ligand are coordinated, or (ii) the 4 N atoms from TMPA are binding and the 5th position is unoccupied. All Cu(I)TMPA structures have an elongated Cu-$N_{alkyl\text{-}amine}$ bond length around 2.4-2.5 Å being weak compare to typical Cu-N bonds length which lies around 2.0 to 2.1 Å.[61] This feature is not linked to the nature of fifth ligand because the Cu-N bond remains weak independently of the ligand and even without any. It is rather due to the preference of Cu(I) for tetrahedral geometry. The pseudo coordination of the $N_{alkyl\text{-}amine}$ arises from the TMPA rigidity that cannot bend enough to adopt a tetrahedral geometry. The geometries are thus qualified of pseudo-pentacoordinate distorted TBP or pseudo-tetracoordinate distorted tetrahedral.[48, 55, 57, 61-63] Cu(I)TMPA having a structure with a pyridyl-arm uncoordinated, are distorted tetrahedral without ambiguity.[61, 64]

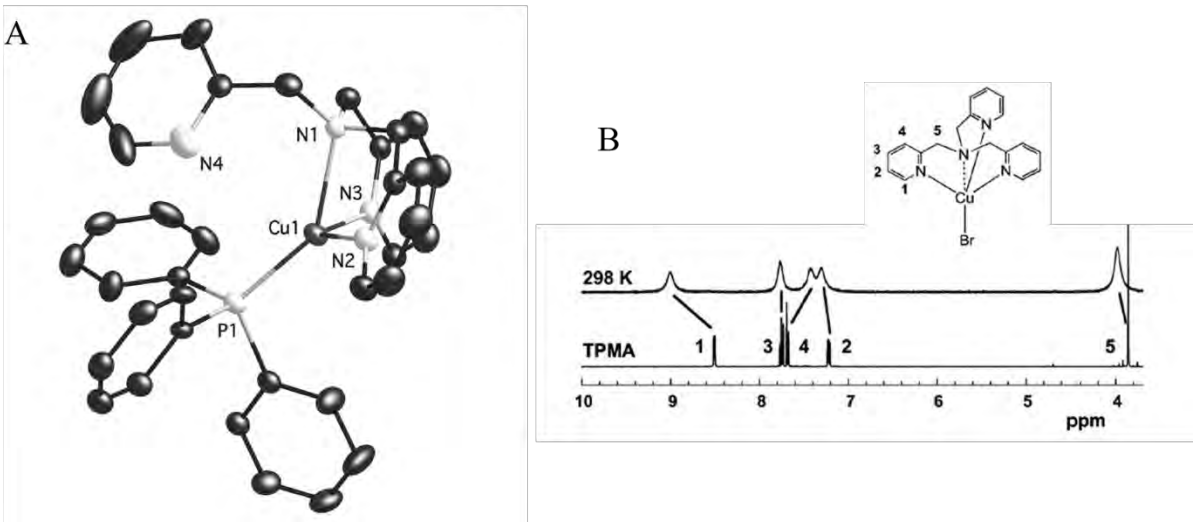

Figure I.C-2: Structure of [CuTMPA(PPh$_3$)](BPh$_4$) drawn with 50 % probability ellipsoids (A).[61] ^{1}H NMR spectra of TMPA and [CuTMPA(Br)] 400 MHz, in (CD$_3$)$_2$CO (B).[55]

Figure I.C-2 B displays the ^{1}H NMR spectra of TMPA and [CuTMPA(Br)] in $(CD_3)_2CO$ at 298 K. Compare to the ligand alone, all proton signals are shifted for the Cu(I) complex, indicative of the involvement of the 4 N atoms to the Cu(I) coordination. The proton closest to the $N_{pyridine}$ (H1) is the most deshielded indicative for the $N_{pyridine}$ coordination. The coordination of $N_{akyl\text{-}amine}$ is proven by the downfield shift of the methylene proton (H5). However the shift of H5 is much smaller than the shift of H1 consistent with the weaker coordination of the $N_{akyl\text{-}amine}$ in solid-state compare to $N_{pyridine}$. H2 and H3 protons from the pyridine ring are also slightly downfield shifted. However, H4 proton is shielded when TMPA is coordinated to Cu(I). Similar ^{1}H NMR features are observed for other monomeric Cu(I)TMPA complexes at 298 K.[61] The broadening of each signal of TMPA upon coordination to Cu(I) resulted from the dynamic ligand dissociation of Br^-.[55] However the dynamic coordination is also proposed to come from the dissociation of one pyridyl arm from TMPA upon coordination to Cu(I).[63]

I.C.1.c. Cu(I)/Cu(II) cyclic voltammetry

Cyclic Voltammetry (CV) is often used to characterize the redox properties of compounds, especially with their $E_{1/2}$ potential and peak-to-peak separation values. In CH_3CN under inert atmosphere, the redox behavior of Cu(I)/Cu(II)TMPA complex is qualified as quasi-reversible as the anodic and cathodic current are almost equal and the peak-to-peak separation is 79 mV greater than 58 mV (theoretical value for reversible redox couple). The $E_{1/2}$ potential is around -20 mV vs SCE (value converted from vs Fc+/Fc in CH_3CN) and represents a single electron transfer process.[48, 65-67] Figure I.C-3 (A) shows an example of CVs of $[CuTMPA(CH_3CN)]^{2+}$ in CH_3CN under inert atmosphere. The coordination of a halogen ions such as Br^- or Cl^- induces a potential shift of $E_{1/2}$ toward more negative values, indicative of a more stable Cu(II) oxidation state.[55, 68]

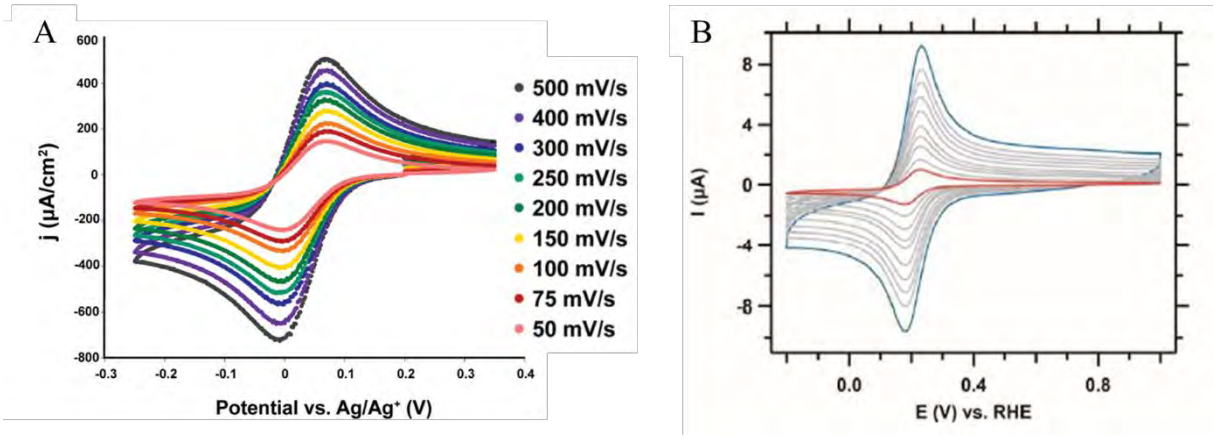

Figure I.C-3: Cyclic voltammograms under inert atmosphere of $[CuTMPA(CH_3CN)]^{2+}$ (1 M in CH_3CN) (A)[69] and CuTMPA (0.3 mM in phosphate buffer pH 7) (B).[70]

In aqueous solvent the redox behavior of Cu(II)/Cu(I)TMPA complex is also reversible with a peak-to-peak separation of 59 mV almost equal to the theoretical value for redox reversible one-electron process (58 mV) (Figure I.C-3). The $E_{1/2}$ in aqueous solution at pH 7 is around -0.4 V vs SCE.[70-72]

I.C.2. Reactivity of Cu(I)TMPA toward carbon monoxide and dioxygen

Cu-TMPA reactivity was extensively studied toward O_2 with the identification and characterizations of intermediates at low temperature in organic solvents and toward CO used as a redox-inactive surrogate of O_2.

I.C.2.a. Reactivity and characterization with carbon monoxide

The lowest unoccupied molecular (LUMO) of CO is an antibonding π*-orbital and is low enough in energy to function as an acceptor orbital when interacting with filled d-orbitals of Cu(I). $[CuTMPA]^+$ was shown to form a $[CuTMPA(CO)]^+$ adduct under CO atmosphere and in organic solvents. Typically in CH_3CN, the formation of $[CuTMPA(CO)]^+$ has been followed by UV-Vis and is accompanied by a decrease and a blue-shift of the MLCT transition around 340 nm upon CO coordination (Figure I.C-4). The binding of CO is reversible as the starting $[CuTMPA]^+$ can be regenerated by applying a reduced pressure to the Cu-CO adduct solution, or by photolysis in nitrile solvents and THF.[48, 59, 64] The equilibrium binding constant of CO (K_{CO}) to $[CuTMPA]^+$ is dependent on the coordinating ability of the solvent used. In THF, K_{CO} is 1.25 x 10^{-5}, much greater than in CH_3CN with K_{CO} = 220, which is a better coordinating solvent.[48] In coordinating solvent, CO binding is in competition with solvent binding, which disfavor the CO-adduct formation compare to non-coordinating solution.

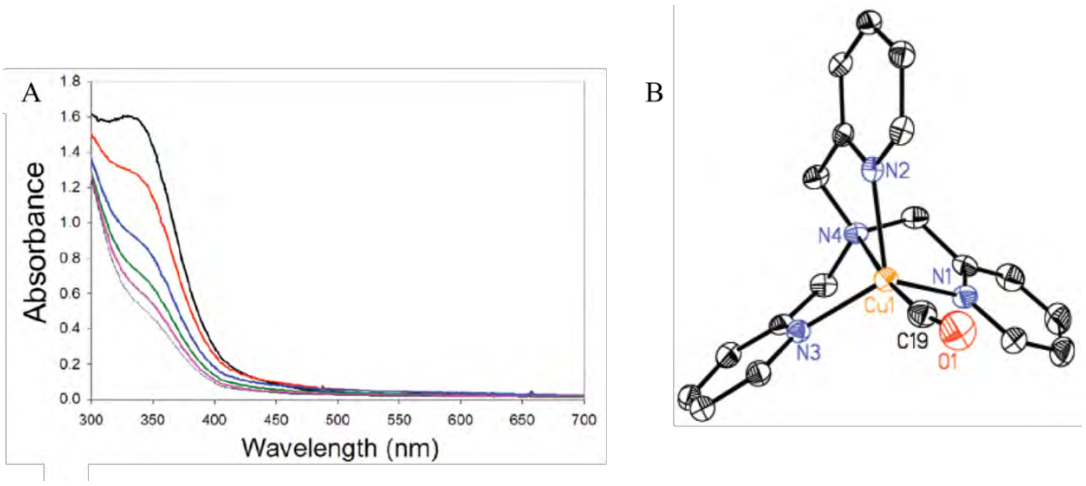

Figure I.C-4: Spectrophotometric titration of CO to $[CuTMPA(solv.)]^+$ in CH_3CN (Black, [CO] = 0.0 mM; red, [CO]) 1.0 mM; blue, [CO]) 3.0 mM; green, [CO]) 5.0 mM; magenta, [CO]) 7.0 mM; thin black, [CO]) 10 mM (A). Structure of $[CuTMPA(CO)]^+$.[48]

In solid-state, the structure of [CuTMPA(CO)]+ displayed in Figure I.C-4, is qualified as pseudo-tetrahedral geometry, because the Cu-$N_{alkyl\text{-}amine}$ bond length of ~ 2.5 Å reflects the weak coordination of the $N_{alkyl\text{-}amine}$.[48]

The formation of the Cu-CO adduct has also been evidences by FTIR in solid-state and in solution. The positions of the infrared absorption bands of CO are very sensitive to the Cu coordination sphere. For $[CuTMPA(CO)]^+$, CO vibration frequencies band gives information on the dissociation of one pyridyl-ring. Indeed, as shown in Figure I.C-5, the $[CuTMPA(CO)]^+$ adduct is in equilibrium between two different coordination modes: (i) a tetracoordinate species with the decoordination of a pyridyl ring characterized by a υ_{CO} = 2092 cm^{-1} in solution and (ii) a pseudo pentacoordinate species with a υ_{CO} = 2077 cm^{-1} in solid-state.[48, 67] The two υ_{CO} frequencies were attributed to each coordination modes thanks to (i) a TMPA analog lacking a pyridyl arm ($[CuPY1(CO)]^+$ (PY1 = tridentate ligand bis-(2-picolyl)amine)) having a CO band matching the frequency of $[CuTMPA(CO)]^+$ (υ_{CO} = 2092 cm^{-1}) and (ii) the solid-state FTIR of the crystallized $[CuTMPA(CO)]^+$ (Figure I.C-4) which displays a CO band at υ_{CO} = 2077 cm^{-1}. In CH_3CN and THF, only the frequency around 2092 cm^{-1} is observed for CO stretching band, confirming decoordination of a pyridyl-arm in solution.[48] The 4-coordinate compound as a higher υ_{CO} frequency than the 5-coordinate one, mirroring a stronger CO bond and thus a weaker Cu-CO binding. Indeed, with the decoordination of a pyridyl-arm, Cu(I) is less electron rich and gives less electron density through π-back donation to CO weakening the metal-carbonyl bonding compared to the 5-coordinate one.

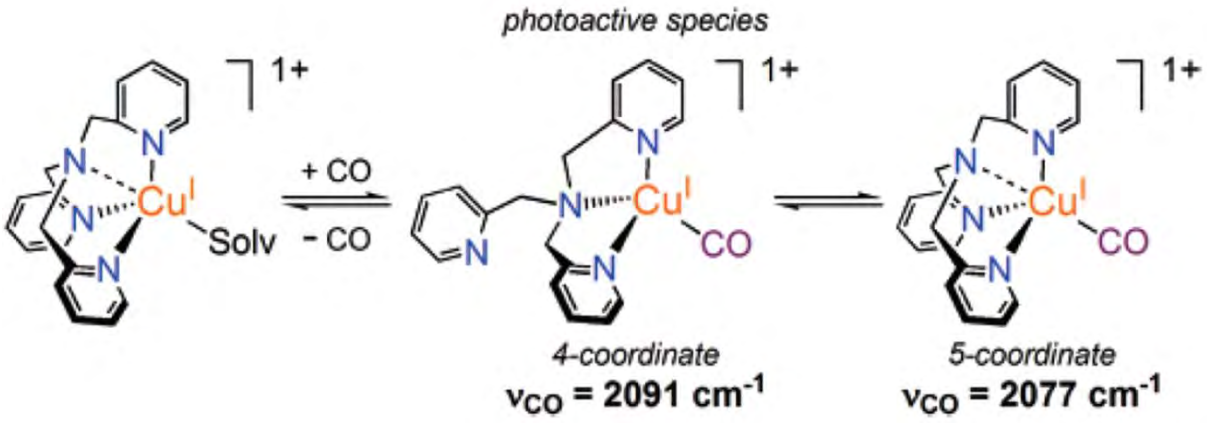

Figure I.C-5: Scheme of the reversible reaction of CO with $[CuTMPA(solv.)]^+$ and the equilibrium of the two coordination modes of $[CuTMPA(CO)]^+$ with their respective υ_{CO} frequencies.(Figure from ref 48)

I.C.2.b. Reactivity and characterization with dioxygen

Many enzyme mimics were designed to elucidate the reactivity of Cu active site with dioxygen (O_2). Those mimics are usually build on small ligands offering a coordination sphere close to the main coordinating amino acid residues (histidine, methionine).[73] TMPA ligand has served this purpose. From a general point of view, O_2 can first bind to Cu(I) and then be one-electron reduced to form the superoxo. The superoxo can be either bound to Cu with one oxygen atom (*end-on* η^1) or with both (*side-on* η^2) as illustrated Figure I.C-6. This adduct can further react with a second Cu(I) center to form a dinuclear peroxo species with different coordination modes possible: *trans*-μ-1,2 and μ- η^2:η^2.[74]

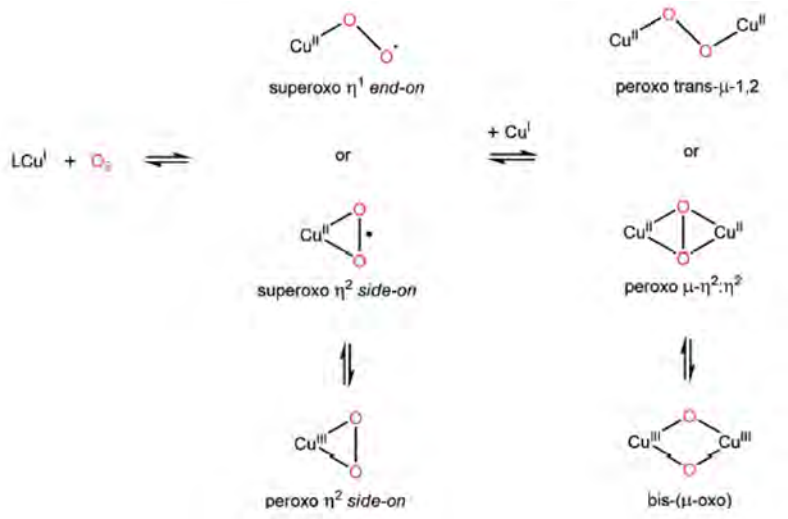

Figure I.C-6: Different binding modes of O_2 to one or two Cu centers.[74]

Cu(I)TMPA complex has been shown to react with O_2 and to form a trans-μ-1,2 dinuclear peroxo $[\{CuTMPA\}c_2(O_2)]^{2+}$ through a Cu-superoxo intermediate suggested to have an *end-on* $O_2^{\bullet-}$ coordination. Those observations were made in organic solvents at low temperature (- 78 °C or lower).[59, 75] The dinuclear complex is characterized by UV-Vis by two LMCT absorption bands from the peroxo to the Cu(II) at 525 nm (ε = 11500 $M^{-1}cm^{-1}$) and 590 (ε = 7600$M^{-1}cm^{-1}$) and a d-d transition band at 1035 nm (ε = 160 $M^{-1}cm^{-1}$) in EtCN (Figure I.C-7).[59] The $[\{CuTMPA\}_2(O_2)]^{2+}$ has been further characterized by raman resonance with a υ_{O-O} = 831 cm^{-1} and υ_{Cu-O} = 561 cm^{-1} in MeOH.[75] Finally, $[\{CuTMPA\}_2(O_2)]^{2+}$ was successfully crystallized, its structure is presented Figure I.C-7. Each Cu center is pentacoordinated with a distorted TBP geometry having the 3 pyridyl N atoms in equatorial positions and the $N_{akyl\text{-}amine}$

and the O_{peroxo} atoms in axial positions.[59] A strong antiferromagnetic coupling is observed between the two Cu(II) centers of the dinuclear species being separated by 4.36 Å. This is demonstrated by magnetic susceptibility measurements in solution and solid-state, as well as the species being EPR silent but displaying ^{1}H and ^{13}C NMR signal.[64] The O_2 binding to Cu(I)TMPA and the formation of the $[\{CuTMPA\}_2(O_2)]^{2+}$ is reversible. Indeed, when an EtCN solution of peroxo dicopper species is subjected to vacuum and brief heating, $[CuTMPA(EtCN)]^+$ is formed, and the dinuclear species is regenerated by cooling down the solution back to -80 °C with addition of O_2.[59, 75] The intermediate species was observed at -135 °C in MeTHF by UV-Vis displaying an intense band at 423 nm (ε = 5600 $M^{-1}cm^{-1}$) and at 752 nm (Figure I.C-7) and by raman resonance of υ_{O-O} around 1120 cm^{-1}.[76-78] The mechanism of O_2 binding to Cu(I)TMPA is influenced by the nature of the solvent of study. In EtCN it follows a dissociative mechanism (decoordination of EtCN followed by coordination of O_2), whereas in THF it follows an associative mechanism (O_2 binding before THF decoordination, if coordinated).[79] Those two proposed mechanisms are directly linked to the strong coordinating ability of EtCN inducing a competition with O_2 binding compared to the non-competitive weak coordinating ability of THF.

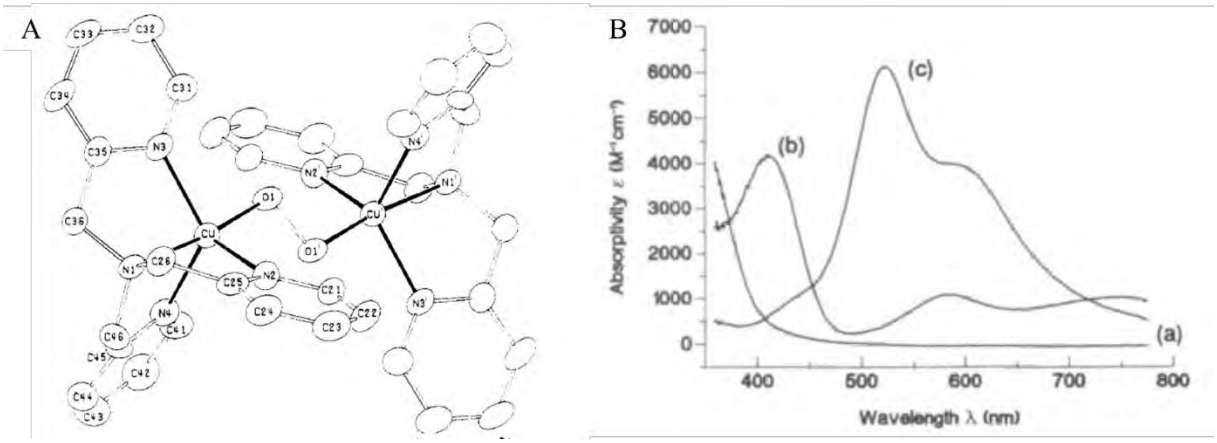

Figure I.C-7: Structure of $[\{CuTMPA\}_2(O_2)]^{2+}$ (A).[59] Calculated absorption spectra from kinetic data analysis of $[CuTMPA(EtCN)]^+$ (a), $[CuTMPA(O_2)]^+$ (b) and $[\{CuTMPA\}_2(O_2)]^{2+}$ (c).[77]

Cu(I)TMPA was also shown to react with H_2O_2. $[CuTMPA(OOH)]^+$ was obtained by addition of an excess of H_2O_2 to a CH_3CN solution of $[CuTMPA(H_2O)]^{2+}$ containing Et_3N at -40 °C.[80] It is characterized in CH_3CN by a LMCT band at 379 nm (ε = 1700 $M^{-1}cm^{-1}$) in UV-Vis and by an EPR spectrum with a reverse axial spectrum with $g_\perp$ ($g_x = g_y$) > $g_{//}$ (g_z) indicative of a TBP geometry.[80-81] The υ_{O-O} = 847 cm^{-1} and υ_{Cu-O} = 512 cm^{-1} bond frequencies were

obtained by raman spectroscopy in MeOH at – 80 °C.[80-81] $[CuTMPA(OOH)]^+$ is unstable and decomposed with a $t_{1/2}$ of 7.5 min at -40 °C.[80]

From the dinuclear $[\{CuTMPA\}_2(O_2)]^{2+}$, the addition of CO produces $[CuTMPA(CO)]^+$. This species subjected to reduced pressure loses its CO and becomes $[CuTMPA(solv.)]^+$, from which the peroxo dicopper compound can be regenerated by addition of O_2 at low temperature. This behavior indicates that CO is a better ligand than O_2 for Cu(I).[64, 75]

I.C.2.c. Dioxygen reduction in aqueous solvent by Cu-TMPA

Cyclic voltammetry studies revealed a reversible fast one-electron redox for Cu-TMPA in aqueous solvent under anaerobic conditions.[70-72] In presence of oxygen, Cu-TMPA complex was shown to electro-catalyze the O_2 reduction in aqueous buffered solution. The O_2 reduction occurred at a potential shifted toward positive values compare to the reduction potential of Cu(II) to Cu(I)TMPA under inert conditions.[70-71] The four-electron four-proton reduction of O_2 occurred stepwise at a single Cu center, going through an H_2O_2 intermediate before being reduced to H_2O in two separate catalytic reactions as presented Figure I.C-8. O_2 binding to Cu(I)TMPA is the rate determining step for the formation of H_2O_2. The two catalytic reactions are first order in Cu(I)TMPA.[70]

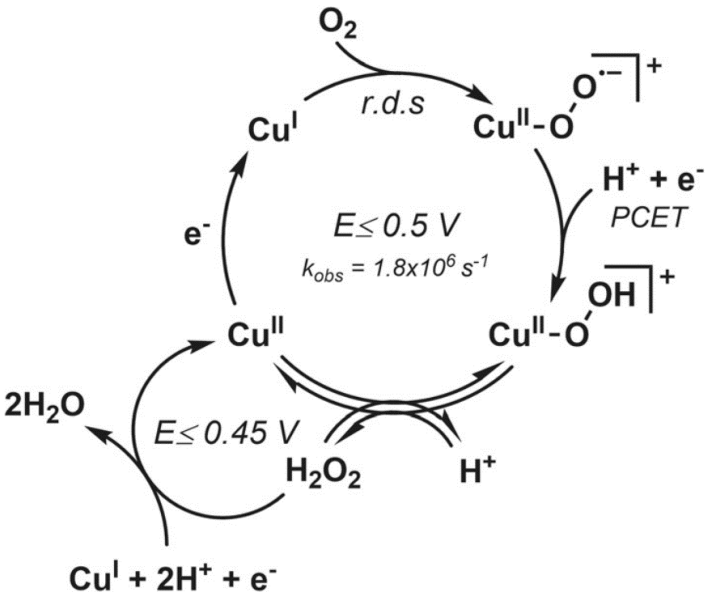

Figure I.C-8: Proposed stepwise mechanism for the electrocatalytic O_2 reduction by Cu-TMPA in aqueous solution pH 7. For clarity, the TMPA ligand is not depicted. PCET (proton-coupled electron transfer).[70]

I.D. Process of the manuscript

The following part of the manuscript is organized in 5 chapters and an additional annex one.

Chapter II presents the methods used during all this PhD work. It gives a brief description of spectroscopies and electrochemical technique employed for the study of Cu(I), Cu(II) complexes and CO ligand (UV-Vis, EPR, NMR, FT-IR, CV).

Chapter III is devoted to the study of Cu(II)TMPA in solid-state by X-ray crystallography and in solution by UV-Vis, and EPR. During the process of the adaptation of the conditions of study of Cu-TMPA complex from organic solvent (CH_3CN) to biologically relevant media, different unexpected observations were made. Indeed, different UV-Vis spectra were obtained for Cu(II)TMPA species in the same conditions but generated from different Cu(II) salts. Those observations and the X-ray characterizations of solid-state of several Cu(II)TMPA compounds led us to look more carefully to the coordinated 5th ligand. Different Cu(II) salts or inorganic salts were used and their impact on Cu(II)TMPA was followed by UV-Vis and EPR spectroscopy in solution and by X-ray crystallography when crystals suitable for analysis were obtained. This study allow us to better deduced the coordinated 5th ligand (anion *vs* solvent molecule) in the stepwise solvent study from CH_3CN to HEPES buffer pH 7.4 with two Cu(II) salts. Cyclic voltammetry studies were performed in different solvents (CH_3CN and buffered aqueous solution) to evaluate the impact of the solvent on the redox properties of Cu-TMPA and its reactivity toward O_2.

Chapter IV is dedicated to the characterization of Cu(II)Aβ model complexes of interest and the study of the impact of 10 % of CH_3CN by UV-Vis and EPR and on Cu(I)/Cu(II)Aβ by cyclic voltammetry.

Chapter V, presents the characterization of Cu(I)L (L = TMPA and Aβ models) reactivity to CO in biologically relevant media by ^{1}H NMR, UV-Vis, CV and FT-IR. Cu(I)TMPA was used as reference for the study of Cu-Aβ model complexes. Cu(I)TMPA experiments were important to acquire reference data but also manipulations skills of reactive Cu(I) species and handling CO gas. The coordination sphere for each Cu(I)Aβ(CO) complexes were proposed based on ^{1}H NMR and CV studies, and previous data from literature.

Chapter VI presents the reactivity of Cu(I)L toward O_2 in the same conditions established for the study of the reactivity toward CO. The reactivity is monitored through UV-Vis ascorbate consumption experiments and CV studies under aerobic conditions.

The annex chapter presents the sulfite and thiosulfate detection through the solid-state and solution characterization of [CuTMPA(SO_3)] and [CuTMPA(S_2O_3)] complexes. During the course of the study of Cu(I)TMPA reactivity in mixtures of CH_3CN/HEPES, dithionite was used to reduce Cu(II)TMPA. The following oxidation of the obtained Cu(I)TMPA displayed new feature in UV-Vis and EPR spectroscopies reminiscent of Cu(II)-OOH species with tripodal tetradentate ligand. However, after a closer look to the degradation products from dithionite in water this "new" species was identified as [CuTMPA(SO_3)] and characterized. To the best of our knowledge, [CuTMPA(SO_3)] was the first structure reported of Cu(II)-SO_3 complex. During the identification process, another complex [CuTMPA(S_2O_3)] was isolated and characterized. Sulfite ion is often found in the food preservatives and can cause allergy. Its amount should be monitored. Cu(II)TMPA turned out to be efficient to detect and quantified the sulfite and thiosulfate anions. An example of sulfite detection and quantification is given in a sugar sample. This study has been published.[82]

References

1. Alzheimer, F. M. Les chiffre clés. https://www.fondation-mederic-alzheimer.org/les-chiffres-cles.

2. Inserm Maladie d'Alzheimer, Une maladie neurodégérative complexe mais de mieux en mieux comprise. https://www.inserm.fr/dossier/alzheimer-maladie (accessed 28/02/2022).

3. Barbiellini Amidei, C.; Fayosse, A.; Dumurgier, J.; Machado-Fragua, M. D.; Tabak, A. G.; van Sloten, T.; Kivimäki, M.; Dugravot, A.; Sabia, S.; Singh-Manoux, A., Association Between Age at Diabetes Onset and Subsequent Risk of Dementia. *Journal of the American Medical Association* **2021,** *325* (16), 1640-1649.

4. France, S. P. Maladie d'Alzheimer et autres démences. https://www.santepubliquefrance.fr/maladies-et-traumatismes/maladies-neurodegeneratives/maladie-d-alzheimer-et-autres-demences (accessed 28/02/2022).

5. Beam, C. R.; Kaneshiro, C.; Jang, J. Y.; Reynolds, C. A.; Pedersen, N. L.; Gatz, M., Differences Between Women and Men in Incidence Rates of Dementia and Alzheimer's Disease. *Journal of Alzheimer's disease : JAD* **2018,** *64* (4), 1077-1083.

6. Viña, J.; Lloret, A., Why women have more Alzheimer's disease than men: gender and mitochondrial toxicity of amyloid-beta peptide. *Journal of Alzheimer's disease : JAD* **2010,** *20 Suppl 2*, S527-33.

7. Budson, A. E. Why are women more likely to develop Alzheimer's disease? 2022. https://www.health.harvard.edu/blog/why-are-women-more-likely-to-develop-alzheimers-disease-202201202672 (accessed 06/04/2022).

8. Stelzmann, R. A.; Norman Schnitzlein, H.; Reed Murtagh, F., An english translation of alzheimer's 1907 paper, "über eine eigenartige erkankung der hirnrinde". *Clinical Anatomy* **1995,** *8* (6), 429-431.

9. Wiley, J., Alzheimer's disease facts and figures. *Alzheimers Dement* **2021,** *17*, 327-406.

10. Soto-Rojas, L. O.; de la Cruz-López, F.; Torres, M. A. O.; Viramontes-Pintos, A.; del Carmen Cárdenas-Aguayo, M.; Meraz-Ríos, M. A.; Salinas-Lara, C.; Florán-Garduño, B.; Luna-Muñoz, J., *Neuroinflammation and alteration of the blood-brain barrier in Alzheimers disease*. InTech Open London, UK: 2015.

11. Hureau, C., Coordination of redox active metal ions to the amyloid precursor protein and to amyloid-β peptides involved in Alzheimer disease. Part 1: An overview. *Coordination Chemistry Reviews* **2012,** *256* (19), 2164-2174.

12. Faller, P.; Hureau, C.; Berthoumieu, O., Role of Metal Ions in the Self-assembly of the Alzheimer's Amyloid-β Peptide. *Inorganic Chemistry* **2013,** *52* (21), 12193-12206.

13. Cheignon, C.; Tomas, M.; Bonnefont-Rousselot, D.; Faller, P.; Hureau, C.; Collin, F., Oxidative stress and the amyloid beta peptide in Alzheimer's disease. *Redox Biology* **2018,** *14*, 450-464.

14. Selkoe, D. J.; Hardy, J., The amyloid hypothesis of Alzheimer's disease at 25 years. *EMBO Mol Med* **2016,** *8* (6), 595-608.

15. Frisoni, G. B.; Altomare, D.; Thal, D. R.; Ribaldi, F.; van der Kant, R.; Ossenkoppele, R.; Blennow, K.; Cummings, J.; van Duijn, C.; Nilsson, P. M.; Dietrich, P.-Y.; Scheltens, P.; Dubois, B., The probabilistic model of Alzheimer disease: the amyloid hypothesis revised. *Nature Reviews Neuroscience* **2022,** *23* (1), 53-66.

16. Faller, P.; Hureau, C.; La Penna, G., Metal Ions and Intrinsically Disordered Proteins and Peptides: From Cu/Zn Amyloid-β to General Principles. *Accounts of Chemical Research* **2014,** *47* (8), 2252-2259.

17. Pizzino, G.; Irrera, N.; Cucinotta, M.; Pallio, G.; Mannino, F.; Arcoraci, V.; Squadrito, F.; Altavilla, D.; Bitto, A., Oxidative Stress: Harms and Benefits for Human Health. *Oxidative Medicine and Cellular Longevity* **2017,** *2017*, 8416763.

18. Zhu, X.; Su, B.; Wang, X.; Smith, M. A.; Perry, G., Causes of oxidative stress in Alzheimer disease. *Cellular and Molecular Life Sciences* **2007,** *64* (17), 2202-2210.

19. Atrián-Blasco, E.; Gonzalez, P.; Santoro, A.; Alies, B.; Faller, P.; Hureau, C., Cu and Zn coordination to amyloid peptides: From fascinating chemistry to debated pathological relevance. *Coordination Chemistry Reviews* **2018,** *371*, 38-55.

20. Atrián-Blasco, E.; del Barrio, M.; Faller, P.; Hureau, C., Ascorbate Oxidation by Cu(Amyloid-β) Complexes: Determination of the Intrinsic Rate as a Function of Alterations in the Peptide Sequence Revealing Key Residues for Reactive Oxygen Species Production. *Analytical Chemistry* **2018,** *90* (9), 5909-5915.

21. Dorlet, P.; Gambarelli, S.; Faller, P.; Hureau, C., Pulse EPR Spectroscopy Reveals the Coordination Sphere of Copper(II) Ions in the 1–16 Amyloid-β Peptide: A Key Role of the First Two N-Terminus Residues. *Angewandte Chemie International Edition* **2009,** *48* (49), 9273-9276.

22. Hureau, C.; Coppel, Y.; Dorlet, P.; Solari, P. L.; Sayen, S.; Guillon, E.; Sabater, L.; Faller, P., Deprotonation of the Asp1 □ Ala2 Peptide Bond Induces Modification of the Dynamic Copper(II) Environment in the Amyloid-β Peptide near Physiological pH. *Angewandte Chemie International Edition* **2009,** *48* (50), 9522-9525.

23. De Gregorio, G.; Biasotto, F.; Hecel, A.; Luczkowski, M.; Kozlowski, H.; Valensin, D., Structural analysis of copper(I) interaction with amyloid β peptide. *Journal of Inorganic Biochemistry* **2019,** *195*, 31-38.

24. Hureau, C.; Balland, V.; Coppel, Y.; Solari, P. L.; Fonda, E.; Faller, P., Importance of dynamical processes in the coordination chemistry and redox conversion of copper amyloid-β complexes. *Journal of Biological Inorganic Chemistry* **2009,** *14* (7), 995-1000.

25. Balland, V.; Hureau, C.; Savéant, J.-M., Electrochemical and homogeneous electron transfers to the Alzheimer amyloid-β copper complex follow a preorganization mechanism. *Proceedings of the National Academy of Sciences* **2010,** *107* (40), 17113-17118.

26. Cheignon, C.; Jones, M.; Atrián-Blasco, E.; Kieffer, I.; Faller, P.; Collin, F.; Hureau, C., Identification of key structural features of the elusive Cu–Aβ complex that generates ROS in Alzheimer's disease. *Chemical Science* **2017,** *8* (7), 5107-5118.

27. Xing, W.; Yin, M.; Lv, Q.; Hu, Y.; Liu, C.; Zhang, J., 1 - Oxygen Solubility, Diffusion Coefficient, and Solution Viscosity. In *Rotating Electrode Methods and Oxygen Reduction Electrocatalysts*, Xing, W.; Yin, G.; Zhang, J., Eds. Elsevier: Amsterdam, 2014; pp 1-31.

28. Hess, F.; Staykov, A. T.; Yildiz, B.; Kilner, J., Solid Oxide Fuel Cell Materials and Interfaces. In *Handbook of Materials Modeling: Applications: Current and Emerging Materials*, Andreoni, W.; Yip, S., Eds. Springer International Publishing: Cham, 2018; pp 1-31.

29. Ho, R. Y.; Liebman, J. F.; Valentine, J. S., Overview of the Energetics and Reactivity of Oxygen. In *Active Oxygen in Chemistry*, Springer: 1995; pp 1-23.

30. Baird, M. H. I.; Davidson, J. F., Annular jets—II: Gas absorption. *Chemical Engineering Science* **1962,** *17* (6), 473-480.

31. Battino, R.; Rettich, T. R.; Tominaga, T., The Solubility of Oxygen and Ozone in Liquids. *Journal of Physical and Chemical Reference Data* **1983,** *12* (2), 163-178.

32. Series, I. S. D., Volume 7: Oxygen and Ozone, ed. R. Battino. Pergamon Press, Oxford: 1981.

33. Miyamoto, H.; Yampolski, Y.; Young, C. L., IUPAC-NIST Solubility Data Series. 103. Oxygen and Ozone in Water, Aqueous Solutions, and Organic Liquids (Supplement to Solubility Data Series Volume 7). *Journal of Physical and Chemical Reference Data* **2014,** *43* (3), 033102.

34. Quaranta, M.; Murkovic, M.; Klimant, I., A new method to measure oxygen solubility in organic solvents through optical oxygen sensing. *Analyst* **2013,** *138* (21), 6243-6245.

35. Achord, J. M.; Hussey, C. L., Determination of dissolved oxygen in nonaqueous electrochemical solvents. *Analytical Chemistry* **1980,** *52* (3), 601-602.

36. Franco, C.; Olmsted, J., Photochemical determination of the solubility of oxygen in various media. *Talanta* **1990,** *37* (9), 905-909.

37. Sawyer, D. T.; Chiericato, G.; Angelis, C. T.; Nanni, E. J.; Tsuchiya, T., Effects of media and electrode materials on the electrochemical reduction of dioxygen. *Analytical Chemistry* **1982,** *54* (11), 1720-1724.

38. Li, Q.; Batchelor-McAuley, C.; Lawrence, N. S.; Hartshorne, R. S.; Compton, R. G., Anomalous solubility of oxygen in acetonitrile/water mixture containing tetra-n-butylammonium perchlorate supporting electrolyte; the solubility and diffusion coefficient of oxygen in anhydrous acetonitrile and aqueous mixtures. *Journal of Electroanalytical Chemistry* **2013,** *688*, 328-335.

39. Solomon, T., The definition and unit of ionic strength. *Journal of Chemical Education* **2001,** *78* (12), 1691.

40. Rondelez, Y.; Sénèque, O.; Rager, M.-N.; Duprat, A. F.; Reinaud, O., Biomimetic Copper(I)–CO Complexes: A Structural and Dynamic Study of a Calix[6]arene-Based Supramolecular System. *Chemistry – A European Journal* **2000,** *6* (22), 4218-4226.

41. Himes, R. A.; Park, G. Y.; Barry, A. N.; Blackburn, N. J.; Karlin, K. D., Synthesis and X-ray Absorption Spectroscopy Structural Studies of Cu(I) Complexes of HistidylHistidine Peptides: The Predominance of Linear 2-Coordinate Geometry. *Journal of the American Chemical Society* **2007,** *129* (17), 5352-5353.

42. Park, G. Y.; Lee, J. Y.; Himes, R. A.; Thomas, G. S.; Blackburn, N. J.; Karlin, K. D., Copper–Peptide Complex Structure and Reactivity When Found in Conserved His-Xaa-His Sequences. *Journal of the American Chemical Society* **2014,** *136* (36), 12532-12535.

43. Romão, C. C.; Blättler, W. A.; Seixas, J. D.; Bernardes, G. J. L., Developing drug molecules for therapy with carbon monoxide. *Chemical Society Reviews* **2012,** *41* (9), 3571-3583.

44. Kim, H.; Doan, V. D.; Cho, W. J.; Valero, R.; Aliakbar Tehrani, Z.; Madridejos, J. M. L.; Kim, K. S., Intriguing Electrostatic Potential of CO: Negative Bond-ends and Positive Bond-cylindrical-surface. *Scientific Reports* **2015,** *5* (1), 16307.

45. Alben, J. O.; Beece, D.; Bowne, S. F.; Doster, W.; Eisenstein, L.; Frauenfelder, H.; Good, D.; McDonald, J. D.; Marden, M. C.; Moh, P. P.; Reinisch, L.; Reynolds, A. H.; Shyamsunder, E.; Yue, K. T., Infrared spectroscopy of photodissociated carboxymyoglobin at low temperatures. *Proceedings of the National Academy of Sciences* **1982,** *79* (12), 3744-3748.

46. Dixon, A. J.; Glyn, P.; Healy, M. A.; Hodges, P. M.; Jenkins, T.; Poliakoff, M.; Turner, J. J., Fast time-resolved i.r. spectroscopy of biological molecules in aqueous solution: The reaction kinetics of myoglobin with carbon monoxide. *Spectrochimica Acta Part A: Molecular Spectroscopy* **1988,** *44* (12), 1309-1314.

47. Cargill, R. W. B. R., *Carbon monoxide*. Pergamon: Oxford; New York, 1990.

48. Fry, H. C.; Lucas, H. R.; Narducci Sarjeant, A. A.; Karlin, K. D.; Meyer, G. J., Carbon Monoxide Coordination and Reversible Photodissociation in Copper(I) Pyridylalkylamine Compounds. *Inorganic Chemistry* **2008,** *47* (1), 241-256.

49. Lopez-Castillo, Z. K.; Aki, S. N. V. K.; Stadtherr, M. A.; Brennecke, J. F., Enhanced Solubility of Oxygen and Carbon Monoxide in CO2-Expanded Liquids. *Industrial & Engineering Chemistry Research* **2006,** *45* (15), 5351-5360.

50. Weisenberger, S.; Schumpe, A., Estimation of gas solubilities in salt solutions at temperatures from 273 K to 363 K. *AIChE Journal* **1996,** *42* (1), 298-300.

51. Balland, V.; Hureau, C.; Savéant, J.-M., Electrochemical and homogeneous electron transfers to the Alzheimer amyloid-β copper complex follow a preorganization mechanism. *Proceedings of the National Academy of Sciences* **2010,** *107* (40), 17113-17118.

52. Bravin, C.; Badetti, E.; Licini, G.; Zonta, C., Tris(2-pyridylmethyl)amines as emerging scaffold in supramolecular chemistry. *Coordination Chemistry Reviews* **2021,** *427*, 213558.

53. Diaz, D. E.; Quist, D. A.; Herzog, A. E.; Schaefer, A. W.; Kipouros, I.; Bhadra, M.; Solomon, E. I.; Karlin, K. D., Impact of Intramolecular Hydrogen Bonding on the Reactivity of Cupric Superoxide Complexes with O−H and C−H Substrates. *Angewandte Chemie International Edition* **2019,** *58* (49), 17572-17576.

54. Blackman, A. G., Tripodal Tetraamine Ligands Containing Three Pyridine Units: The other Polypyridyl Ligands. *European Journal of Inorganic Chemistry* **2008,** *2008* (17), 2633-2647.

55. Eckenhoff, W. T.; Garrity, S. T.; Pintauer, T., Highly Efficient Copper-Mediated Atom-Transfer Radical Addition (ATRA) in the Presence of Reducing Agent. *European Journal of Inorganic Chemistry* **2008,** *2008* (4), 563-571.

56. Kaur, A.; Ribelli, T. G.; Schröder, K.; Matyjaszewski, K.; Pintauer, T., Properties and ATRP Activity of Copper Complexes with Substituted Tris(2-pyridylmethyl)amine-Based Ligands. *Inorganic Chemistry* **2015,** *54* (4), 1474-1486.

57. Lim, B. S.; Holm, R. H., Molecular Heme−Cyanide−Copper Bridged Assemblies: Linkage Isomerism, Trends in νCN Values, and Relation to the Heme-a3/CuB Site in Cyanide-Inhibited Heme−Copper Oxidases. *Inorganic Chemistry* **1998,** *37* (19), 4898-4908.

58. Porras Gutiérrez, A. G.; Zeitouny, J.; Gomila, A.; Douziech, B.; Cosquer, N.; Conan, F.; Reinaud, O.; Hapiot, P.; Le Mest, Y.; Lagrost, C.; Le Poul, N., Insights into water coordination associated with the CuII/CuI electron transfer at a biomimetic Cu centre. *Dalton Transactions* **2014,** *43* (17), 6436-6445.

59. Jacobson, R. R.; Tyeklar, Z.; Farooq, A.; Karlin, K. D.; Liu, S.; Zubieta, J., A copper-oxygen (Cu2-O2) complex. Crystal structure and characterization of a reversible dioxygen binding system. *Journal of the American Chemical Society* **1988,** *110* (11), 3690-3692.

60. Wei, N.; Murthy, N. N.; Tyeklar, Z.; Karlin, K. D., Copper(I) Complexes with Pyridyl- and Imidazoyl-Containing Tripodal Tetradentate Ligands and Their Reactions with Dioxygen. *Inorganic Chemistry* **1994,** *33* (6), 1177-1183.

61. Eckenhoff, W. T.; Pintauer, T., Structural Comparison of Copper(I) and Copper(II) Complexes with Tris(2-pyridylmethyl)amine Ligand. *Inorganic Chemistry* **2010,** *49* (22), 10617-10626.

62. Eckenhoff, W. T.; Pintauer, T., Atom Transfer Radical Addition in the Presence of Catalytic Amounts of Copper(I/II) Complexes with Tris(2-pyridylmethyl)amine. *Inorganic Chemistry* **2007,** *46* (15), 5844-5846.

63. Hsu, S. C. N.; Chien, S. S. C.; Chen, H. H. Z.; Chiang, M. Y., Synthesis and Characterization of Copper(I) Complexes Containing Tri(2-Pyridylmethyl)Amine Ligand. *Journal of the Chinese Chemical Society* **2007,** *54* (3), 685-692.

64. Tyeklar, Z.; Jacobson, R. R.; Wei, N.; Murthy, N. N.; Zubieta, J.; Karlin, K. D., Reversible reaction of dioxygen (and carbon monoxide) with a copper(I) complex. X-ray

structures of relevant mononuclear Cu(I) precursor adducts and the trans-(.mu.-1,2-peroxo)dicopper(II) product. *Journal of the American Chemical Society* **1993,** *115* (7), 2677-2689.

65. Pavlishchuk, V. V.; Addison, A. W., Conversion constants for redox potentials measured versus different reference electrodes in acetonitrile solutions at 25°C. *Inorganica Chimica Acta* **2000,** *298* (1), 97-102.

66. Chuang, C.-L.; dos Santos, O.; Xu, X.; Canary, J. W., Synthesis and Cyclic Voltammetry Studies of Copper Complexes of Bromo- and Alkoxyphenyl-Substituted Derivatives of Tris(2-pyridylmethyl)amine: Influence of Cation−Alkoxy Interactions on Copper Redox Potentials. *Inorganic Chemistry* **1997,** *36* (9), 1967-1972.

67. Zhang, C. X.; Kaderli, S.; Costas, M.; Kim, E.-i.; Neuhold, Y.-M.; Karlin, K. D.; Zuberbühler, A. D., Copper(I)−Dioxygen Reactivity of [(L)CuI]+ (L = Tris(2-pyridylmethyl)amine): Kinetic/Thermodynamic and Spectroscopic Studies Concerning the Formation of Cu−O2 and Cu2−O2 Adducts as a Function of Solvent Medium and 4-Pyridyl Ligand Substituent Variations. *Inorganic Chemistry* **2003,** *42* (6), 1807-1824.

68. Qiu, J.; Matyjaszewski, K.; Thouin, L.; Amatore, C., Cyclic voltammetric studies of copper complexes catalyzing atom transfer radical polymerization. *Macromolecular Chemistry and Physics* **2000,** *201* (14), 1625-1631.

69. Ward, A. L.; Elbaz, L.; Kerr, J. B.; Arnold, J., Nonprecious Metal Catalysts for Fuel Cell Applications: Electrochemical Dioxygen Activation by a Series of First Row Transition Metal Tris(2-pyridylmethyl)amine Complexes. *Inorganic Chemistry* **2012,** *51* (8), 4694-4706.

70. Langerman, M.; Hetterscheid, D. G. H., Fast Oxygen Reduction Catalyzed by a Copper(II) Tris(2-pyridylmethyl)amine Complex through a Stepwise Mechanism. *Angewandte Chemie International Edition* **2019,** *58* (37), 12974-12978.

71. Asahi, M.; Yamazaki, S.-i.; Itoh, S.; Ioroi, T., Electrochemical reduction of dioxygen by copper complexes with pyridylalkylamine ligands dissolved in aqueous buffer solution: the relationship between activity and redox potential. *Dalton Transactions* **2014,** *43* (28), 10705-10709.

72. Nagao, H.; Komeda, N.; Mukaida, M.; Suzuki, M.; Tanaka, K., Structural and Electrochemical Comparison of Copper(II) Complexes with Tripodal Ligands. *Inorganic Chemistry* **1996,** *35* (23), 6809-6815.

73. Elwell, C. E.; Gagnon, N. L.; Neisen, B. D.; Dhar, D.; Spaeth, A. D.; Yee, G. M.; Tolman, W. B., Copper–Oxygen Complexes Revisited: Structures, Spectroscopy, and Reactivity. *Chemical Reviews* **2017,** *117* (3), 2059-2107.

74. Gomila, A.; Le Poul, N.; Kerbaol, J.-M.; Cosquer, N.; Triki, S.; Douziech, B.; Conan, F.; Le Mest, Y., Electrochemical behavior and dioxygen reactivity of tripodal dinuclear copper complexes linked by unsaturated rigid spacers. *Dalton Transactions* **2013,** *42* (6), 2238-2253.

75. Paul, P. P.; Tyeklar, Z.; Jacobson, R. R.; Karlin, K. D., Reactivity patterns and comparisons in three classes of synthetic copper-dioxygen {Cu2-O2} complexes: Implication

for structure and biological relevance. *Journal of the American Chemical Society* **1991,** *113* (14), 5322-5332.

76. Bhadra, M.; Lee, J. Y. C.; Cowley, R. E.; Kim, S.; Siegler, M. A.; Solomon, E. I.; Karlin, K. D., Intramolecular Hydrogen Bonding Enhances Stability and Reactivity of Mononuclear Cupric Superoxide Complexes. *Journal of the American Chemical Society* **2018,** *140* (29), 9042-9045.

77. Karlin, K. D.; Wei, N.; Jung, B.; Kaderli, S.; Zuberbuehler, A. D., Kinetic, thermodynamic, and spectral characterization of the primary copper-oxygen (Cu-O2) adduct in a reversibly formed and structurally characterized peroxo-dicopper(II) complex. *Journal of the American Chemical Society* **1991,** *113* (15), 5868-5870.

78. Itoh, S., Mononuclear copper active-oxygen complexes. *Current Opinion in Chemical Biology* **2006,** *10* (2), 115-122.

79. Lucas, H. R.; Meyer, G. J.; Karlin, K. D., CO and O2 Binding to Pseudo-tetradentate Ligand−Copper(I) Complexes with a Variable N-Donor Moiety: Kinetic/Thermodynamic Investigation Reveals Ligand-Induced Changes in Reaction Mechanism. *Journal of the American Chemical Society* **2010,** *132* (37), 12927-12940.

80. Syuhei, Y.; Akira, W.; Shigenori, N.; Teizo, K.; Koichiro, J.; Hideki, M., Thermal Stability of Mononuclear Hydroperoxocopper(II) Species. Effects of Hydrogen Bonding and Hydrophobic Field. *Chemistry Letters* **2004,** *33* (12), 1556-1557.

81. Yamaguchi, S.; Masuda, H., Basic approach to development of environment-friendly oxidation catalyst materials. Mononuclear hydroperoxo copper(II) complexes. *Science and Technology of Advanced Materials* **2005,** *6* (1), 34-47.

82. Berthonnaud, L.; Esmieu, C.; Mallet-Ladeira, S.; Hureau, C., Solid-state and solution characterizations of [(TMPA)Cu(II)(SO3)] and [(TMPA)Cu(II)(S2O3)] complexes: Application to sulfite and thiosulfate fast detection. *Journal of Inorganic Biochemistry* **2021,** *225*, 111601.

Chapter II

Chapter II. Methods

We have selected five out the most relevant techniques to study Cu(I) and Cu(II) complexes (UV-Vis, EPR, NMR and electrochemistry) and CO ligand (FT-IR). Description of general principles of each spectroscopy or electrochemical technique used in this PhD work is given, with a special emphasis on applications for Cu species.

II.A. UV-Vis spectroscopy

UV-Vis spectroscopy is an analytical electronic technique that measures the light absorption by a compound in the range of UV and visible light from 185 nm to 1100 nm. UV-Vis spectroscopy gives information on charge transfer (ligand to metal and metal to ligand) and electron transitions, from different transitions between electronic states, which are related to the structure, oxidation state, and geometry of the molecular system studied.

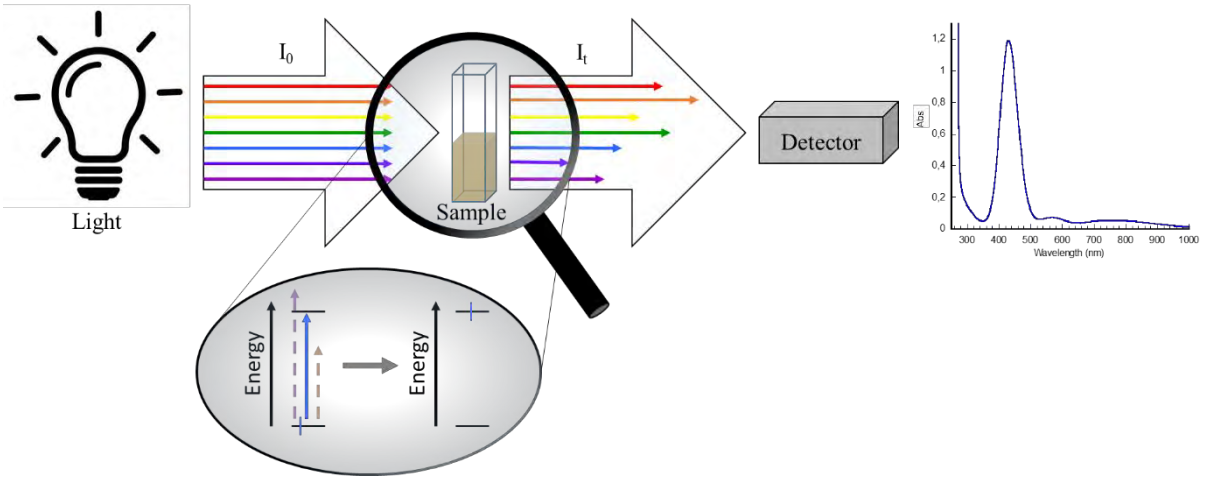

Figure II.A-1: Schematic view of general principle of UV-Vis spectroscopy.

Our UV-Vis spectrometer is composed by a light source (deuterium lamp for the UV range (< 350 nm) and a tungsten lamp for the visible range (> 350 nm)) a sample holder and a detector. Spectrometers can either measure one wavelength at a time as single or double beam instruments with a monochromator or a wavelength filter, or measure the absorbance at all wavelengths simultaneously when equipped with a diode array detector (our case). Usually the sample is in quartz cuvette as it does not absorb light in the UV region. A ground state electron of the sample will be promoted to its excited state by the absorption of a photon from the light

at the required energy. The excited light with transmitted intensity from the sample is collected by the detector, transformed as an electrical signal and the result spectrum is obtained as absorbance as a function of wavelength (Figure II.A-1). The transmitted light is called transmittance (T) and is the ratio between the intensity of transmitted light (I_t) over the intensity of induced light (I_0) (Equation II.A-1).

$$T = \left(\frac{I_t}{I_0}\right)$$

Equation II.A-1

(T: transmittance (no dimension); I_t: Intensity of transmitted light (cd); I_0: Intensity of induced light (cd)).

The absorbance can be calculated from T using Equation II.A-2, and is dependent on the concentration of the species in the sample according to the Beer-Lambert Law (Equation II.A-3)

$$Abs = \log\left(\frac{1}{T}\right)$$

Equation II.A-2

(Abs: absorbance (no dimension); T: transmittance (no dimension)).

$$Abs_\lambda = \varepsilon_\lambda * l * C$$

Equation II.A-3

(Abs_λ: absorbance at a particular wavelength (no dimension); *ε_λ:* molar extinction coefficient singular for each transition (particular wavelength) of each species ($L.mol^{-1}.cm^{-1}$); *l*: optical path length through the sample (cm); C: concentration of the species ($mol.L^{-1}$)).

To apply the Beer-Lambert Law, the solvent should be inert toward the species studied, a monochromatic light has to be used (application of the Law for a specific wavelength), the concentration of the sample should be low enough to have an absorbance value lower than 1, solution should be homogeneous and not fluorescent, and no photochemical transformation should occur. If different species absorb at close or same wavelength, the total absorbance is the sum of the absorbances of each compound (Equation II.A-4).

$$\mathrm{Abs}_{\lambda\ \mathrm{Total}} = \mathrm{Abs}_{\lambda A} + \mathrm{Abs}_{\lambda B}$$

Equation II.A-4

($Abs_{\lambda Total}$: total absorbance at a particular wavelength (no dimension); $Abs_{\lambda A}$: absorbance of compound A at a particular wavelength (no dimension); $Abs_{\lambda B}$: absorbance of compound B at a particular wavelength (no dimension)).

The electron can be excited from σ-bonding to σ-antibonding (σ → σ*), or non-bonding to σ-antibonding (n → σ*), or non-bonding to π-antibonding (n → π*), or π-bonding to π-antibonding (π → π*). σ → σ* transitions require a high energy so they are usually not observed in the range of near UV-Vis spectrometer. The wavelength of the absorbed photons and the absorption extinction coefficient are dependent on the molecular structure.

In the context of Cu(II) complexes, this technique enables the observation of characteristic absorption bands from the ligand and the interactions between the ligand and the metal over a wide wavelength range (200-1000 nm).

Typically, three types of transitions are likely to be observed in the standard range of study (200-1000nm):

(i) Internal transitions of the ligand (λ < 300 nm).

(ii) d-d transitions of the metal. They are orbital forbidden but allowed by the spin rules. They are mainly influenced by the nature of the ligand and the geometry around the metal cation. For example, for a complex with a trigonal bipyramid geometry, the bands are expected to be around 800 nm, and for a square pyramid geometry around 700 nm. As they are forbidden molar extinction coefficient values are low (ε < 1000).

(iii) Ligand to metal charge transfer (LMCT) and Metal to Ligand charge transfer (MLCT) transitions. These are allowed and therefore have higher molar extinction coefficients than the d-d transitions (λ 300-600 nm; ε > 1000).

II.B. Electron Paramagnetic Resonance (EPR)

II.B.1. General

Electron paramagnetic resonance is an absorption spectroscopy technique based on the interaction between magnetic moments of electrons and an external electromagnetic field that will induce changes in energy state. The range of frequency of the absorbed electromagnetic wave is from 1 to 500 GHz, corresponding to microwave. EPR spectroscopy is used to characterized structure and dynamics of paramagnetic centers, like radicals and paramagnetic metal ions. In our case, EPR is used to characterize structures in frozen state.

Only the molecules having a permanent magnetic moment without the application of a magnetic field are considered as dipole, they correspond to paramagnetic or ferromagnetic systems. An external magnetic field B_0 is applied to the molecule studied to reveal its paramagnetic feature. B_0 induces the alignment of the magnetic moment in a sample. The spin quantum number S = ½, the magnetic moment μ and two spin states m_s = + ½ and m_s = - ½ characterize the unpaired electron. In diamagnetic molecules, the electron spins are coupled, resulting in a magnetic moment equal to zero. Paramagnetic molecules are those with an unpaired electron.

An electromagnetic wave is considered as an electric field E_1 perpendicular to a magnetic field B_0 and both perpendicular to the propagation axis. E_1 and B_0 oscillate at a frequency υ. For the electromagnetic wave to be absorbed by the analyte, two requirements need to be satisfied: (i) the applied magnetic field (B_0) should interact with a magnetic dipole leading to the splitting of the degenerate electronic levels, (ii) the energy of the electromagnetic wave should fit with the energy gap between two energy levels of the analyte.

II.B.2. Principle

An electron is a particle with a negative charge q and a mass m. It is rotating around the nucleus, which creates the orbital magnetic moment and it is also spinning around its own axis giving the spin magnetic moment. The spin magnetic moment of unpaired electron is the main contributor to the magnetic moment of the whole molecule.[1]

The interaction between an unpaired electron and an applied magnetic field, B_0 is called Zeeman effect as shown in Figure II.B-1. The magnetic moment μ of the unpaired electron can become aligned to the magnetic field giving its lowest energy state, or aligned against B_0, giving its highest energy. The two states have the values of m_s = - ½ for the parallel direction to B_0, and m_s = + ½ for the antiparallel direction. The energy of each state, called Zeeman levels, are given by Equation II.B-1. The energy difference (ΔE) of the two states linked to the magnetic field strength is given by the Equation II.B-2. The absorption of photons occurs when the energy difference matches with the microwave radiation. The spin states of an electron are degenerated and equal to zero in the absence of a magnetic field (Figure II.B-1).

$$E_{\pm 1/2} = \pm \frac{1}{2} g_e \beta B_0$$

Equation II.B-1

($E_{\pm 1/2}$: energy of the electron (J); g_e: Landé factor (g_e = 2.00232 for free electron)(no dimension); β: Bohr magneton (9.2740 x 10^{-28} $J.G^{-1}$); B_0: magnetic field (in G)).

$$\Delta E = h\upsilon = g_e \beta B_0$$

Equation II.B-2

(ΔE: energy difference (J); h: Planck's constant (6.626 x 10^{-34} J.s); υ: radiation frequency (s^{-1}); g_e: Landé factor (g_e = 2.00232 for free electron) (no dimension); β: Bohr magneton (9.2740 x 10^{-28} $J.G^{-1}$); B_0: magnetic field (G)).

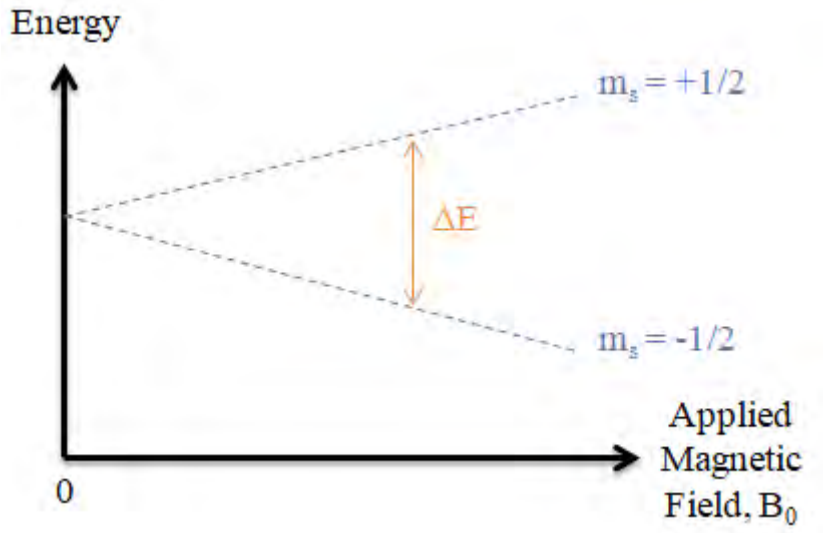

Figure II.B-1: Zeeman levels for an electron spin (ms = ±1/2) in an applied magnetic field, B_0.[1]

II.B.3. EPR spectrometer

The EPR spectrometer varies the magnetic field and keeps the microwave frequency constant. The absorption occurs when the difference of energy between the two spin states matches with the frequency of the applied magnetic field. Different microwave frequency ranges that are called bands L (1 GHz), X (9 GHz) the most used, Q (34 GHz) and W (90 GHz) will give different spectra and thus various information can be extracted.

EPR spectrometer emits microwaves going through an attenuator before passing through a circulator and finally through the sample located in a microwave cavity between magnets (Figure II.B-2). The magnets generate a magnetic field that is swept up to about 1T (for bands X and Q). Transition between the two Zeeman levels occurs in the paramagnetic sample as the microwaves are absorbed. The non-absorbed microwaves are reflected back and caught by the detector diode, and transformed into a current signal that reveals the microwaves absorbed by the sample.[2]

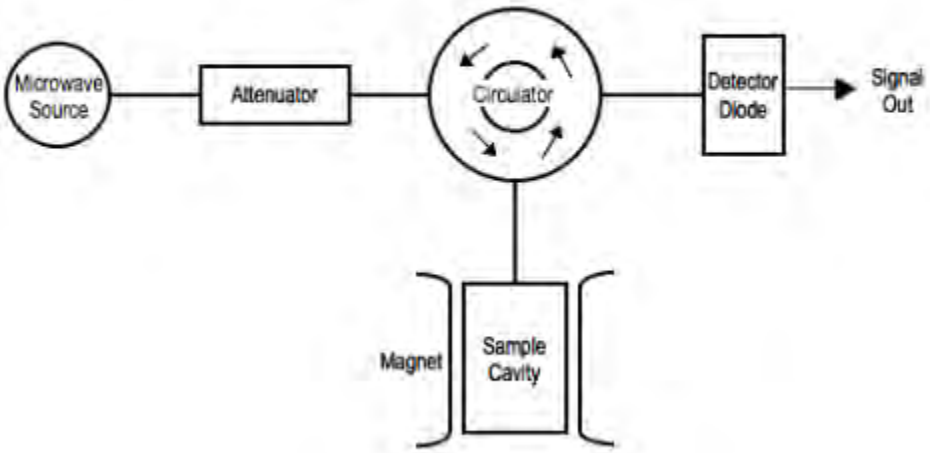

Figure II.B-2: Schematic representation of a EPR spectrometer.[2]

The signal obtained displays the absorption of the microwave as a function of the magnetic field. The spectrum is usually the first derivative of the absorption, to increase the signal over noise ratio (Figure II.B-3). The magnetic field strength is reported in Gauss or in mTesla. The analysis of the spectra can be supported with predicting computer programs.

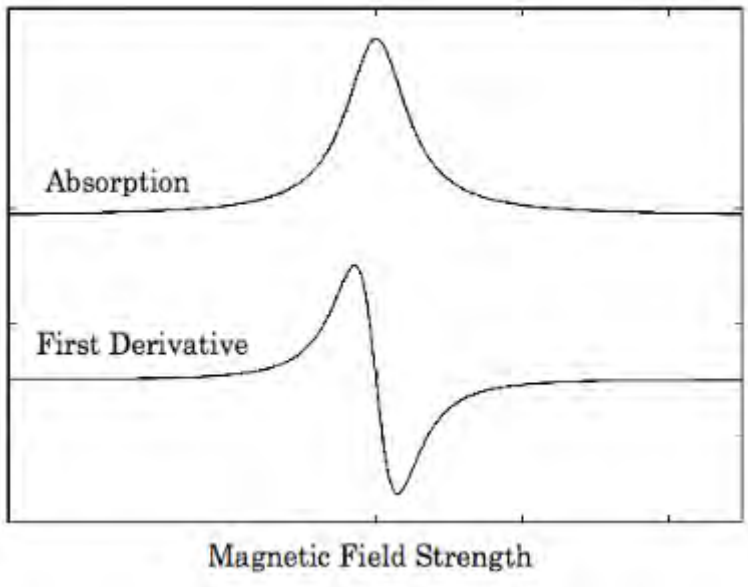

Figure II.B-3: Example of absorption and first derivative EPR spectrum.[2]

II.B.4. Interpretation of EPR spectrum

II.B.4.a. The g factor for paramagnetic species

The fundamental interaction between the unpaired electron(s) at the applied magnetic field is described by Landé factor g. The g values can be extracted and calculated from the spectrum and are specific to each analyte (the free-electron g_e value is 2.00232). The magnitude of the shift depends mainly on the molecular environment and is sensitive to electronic structure changes. In a frozen sample, the g-factor is dependent on the orientation of the molecule with respect to the magnetic field as orbitals containing unpaired electrons are oriented in the molecule. It is called anisotropy. Thus, the g-factor is divided in 3 values following Cartesian coordinates, g_x, g_y and g_z. The anisotropy gives information about the symmetry of the electronic distribution within the paramagnetic species. When $g_x = g_y = g_z$, the spectrum is considered isotropic and thus does not depend on its orientation in the magnetic field. The g value measured in solution is the average of the three components and is also referred as the g_{iso}. The Landé factor g is axial and distorted along the z-axis if $g_x = g_y \neq g_z$. The notation of $g_\perp$ (g_{perp}) is often used for the value of $g_x = g_y$ and $g_{//}$ (g_{para}) for g_z. When $g_x = g_y < g_z$, the spectrum displays a small peak at low field and a large peak at high field and when $g_x = g_y > g_z$ the spectrum is shortened in the xy plane displaying a large peak at low field and a small peak at high field. The spectrum is called rhombic when $g_x \neq g_y \neq g_z$ and is characterized by three peaks corresponding to each g component.[2]

II.B.4.b. Hyperfine couplings

The spectrum will display a maximum of 2nI + 1 (I = nuclear spin and n = number of equivalent nuclei) lines, due to the electron-nuclear magnetic moment coupling. The hyperfine coupling is the interaction of the magnetic moment of the electron, with the magnetic moment of its own nucleus, thus in the formula "2nI +1" (n=1 for complex monomeric species and I=3/2 for Cu(II)). The intensity is the same for each lines for the hyperfine couplings of an isotropic system (non-oriented) (Figure II.B-4). The distance between two successive lines, **a**, gives the hyperfine coupling constant *A*, following the Equation II.B-3.

$$A = \frac{ag\beta}{hc}$$

Equation II.B-3

(A: hyperfine coupling constant (10^{-4} cm^{-1}), a: distance between two hyperfine lines (G), g: Landé factor (no dimension), β: Bohr magneton (9.2740 x 10^{-28} $J.G^{-1}$), h: Planck's constant (6.626 x 10^{-34} J.s), c: light speed (2.9979 x 10^{10} $cm.s^{-1}$)).

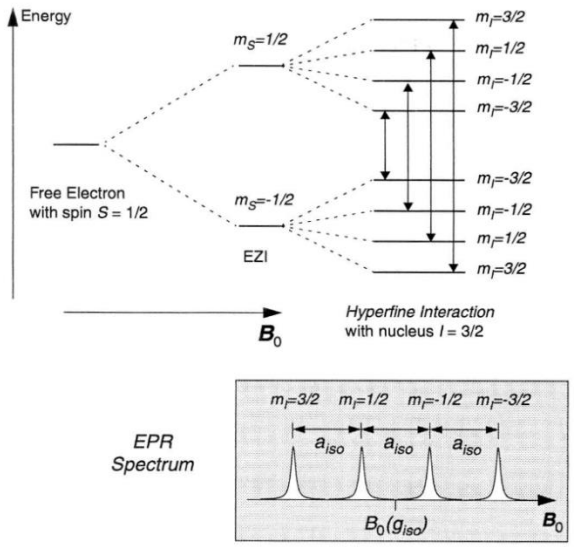

Figure II.B-4: Zeeman energy level diagram (top) and EPR spectrum (bottom) for a hyperfine coupling and isotrope system with one electron and a nuclear spin I = 3/2.

The magnetic moment of the electron can also couple with nuclei from ligands of the metal center (in general nitrogen atoms); this is called super hyperfine splitting. On the spectrum, super-hyperfine couplings are seen by the splitting of lines with a multiplicity given

by (2nI+1) where n is the number of equivalent nuclei from the ligand(s) and I the corresponding nuclear spin. The intensity is given according to the Pascal triangle. When unequivalent nuclei are at play then the multiplity of the line is given by $(2n_1I_1 +1)(2n_2I_2+1)$...

A textbook example that perfectly illustrate g-anisotropy, hyperfine and superhyperfine couplings is shown in Figure II.B-5, in case of a Cu(II) tetraphenylporphyrin (Cu-TPP).

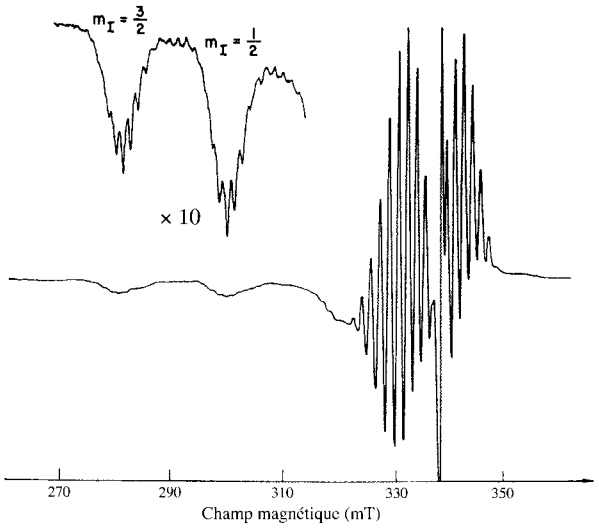

Figure II.B-5: Powder EPR spectrum at X-band and 77 K of [CuTPP] diluted in H_2TPP.

In Figure II.B-5, the two low field lines (280 and 300 mT) are due to the hyperfine interaction of the S = 1/2 electron spin of the complex with the I = 3/2 core of the copper. If these lines are further amplified, a finer structure becomes apparent. There are in fact nine equidistant lines that reflect the interaction of the electron spin with the nuclei of the four nitrogen atoms of the porphyrin ring. For four equivalent nuclear spins I = 1, one expects 2*4*1 + 1 = 9 lines in ratios 1:4:10:16:19:16:10:4:1, which is the case here. The effect of this superhyperfine interaction is also seen at higher fields, on the perpendicular and parallel lines.

The separation between the lines is of the order of 1.5 mT, which corresponds to a superhyperfine interaction of about 15.10^{-4} cm^{-1}. It is important to note that the spin density on the coordinating atoms remains very low. Consequently, the coupling constant will be much lower than the one related to the coupling with the nuclear spin of the metal ion.

II.C. Nuclear Magnetic Resonance (NMR)

The nuclear magnetic resonance (NMR) spectroscopy is an analytical technique based on the interaction between a nuclear spin and a magnetic field. The principle is similar to EPR spectroscopy with the application of a magnetic field by magnets and absorption of radiowaves frequency. In contrast to EPR, the magnetic field is fixed while the incident radiowave varies. It is used for structural dynamics and chemical environment analysis.

II.C.1. General principle

Every atomic nucleus is composed by elementary particles (protons and neutrons) and has a spin characterized by a quantum number I (I=0; integer or ½ integer). The magnetic moment of an atom nucleus depends on its atomic number Z, and mass number A: (i) for A odd, I= ½ integer whatever Z; (ii) for Z and A even, I=0; A even and Z odd, I=integer. Only nuclei having a quantum number different than 0, i.e. a magnetic moment, can be studied by NMR. The application of a magnetic field B_0 will interact and disturb the spin moments and a Larmor procession occurs, thus the quantum number I becomes m. The magnetization of the nucleus is when the sum of magnetic moment vector is different than zero because the level of lower energy (parallel to B_0) is more populated than the higher energy level (anti-parallel to B_0). For any quantum number $I \neq 0$, there is $2I + 1$ energy levels, E, expressed by Equation II.C-1. Those energy levels are degenerated when there is no magnetic field, however when the magnetic field is applied the Zeeman Effect splits them. For example ^1H nucleus (I= ½) can occupy two energy levels (2I + 1): either parallel to B_0 (magnetic quantum number m = ½) or anti-parallel to B_0 (m = - ½).

$$E = -m * h * \gamma * B_0$$

Equation II.C-1

(E: energy (J); h: Planck's constant (6.626×10^{-34} J.s); γ: gyromagnetic ratio ($rad.s^{-1}.T^{-1}$) specific for each nucleus; B_0: magnetic field (T)).

The intensity of the magnetic moment is related to the strength of the applied magnetic field, B_0. Indeed, the energy difference between two spin states (ΔE) is given by Equation II.C-2.

$$\Delta E = h * \gamma * B_0$$

Equation II.C-2

(ΔE: difference of energy (J); h: Planck's constant (6.626 x 10^{-34} J.s); γ: gyromagnetic ratio (rad.s^{-1}.T^{-1}) specific for each nucleus; B_0: magnetic field (T)).

The higher difference between two spin states, the higher difference of population between those two states, and the higher is the intensity of magnetic moment. Each type of nucleus will have a specific range of frequencies, thus only one isotope can be detected at a time giving rise to different NMR sorts such as ^{1}H NMR or ^{13}C NMR.

NMR signal is recorded during the application of a radiofrequency (B_1) to a sample perpendicular to the magnetic field B_0. B_1 is absorbed by the nucleus studied leading to a change of the magnetization until the angle between the radiofrequency applied and the magnetization is 90°. The relaxation creates an electric signal oscillation at the NMR frequency named free induction decay (FID). In order to have an energy transition between the nuclei energy levels, B_1 should be at the radio frequency corresponding to the energy difference of the two levels (the resonance frequency) to be absorbed. After the absorption of a photon, the magnetization is relaxing for the nuclei of the sample to return to their ground state creating a FID signal as intensity in function of time. The NMR spectrum is obtained after a Fourier transformation of the FID signal. The two most common types of relaxation are spin lattice relaxation (T_1) and spin-spin relaxation (T_2). The spin lattice relaxation is the time for 63 % of sample nuclei to come back to their initial position along the z-axis. Spin-spin relaxation is the time for the spins of the sample to be in different magnetization, when they lose coherence.[3]

II.C.2. Spectrum interpretation

An NMR spectrum is analyzed by looking at the position of the peaks, their multiplicity and their relative integration. Each atom nucleus is surrounded by electrons negatively charged that will create their own magnetic field and thus slightly affect the energy levels of the nucleus. This phenomenon is known as shielding. Same atoms, but having different electronic environments will see different magnetic field and thus absorb at different resonance frequencies. The spectrum will display different absorption peaks, at different chemical shift (δ) expressed in parts per million (ppm). The chemical shift is given according to a frequency (υ) of a reference as stated in Equation II.C-3.

$$\delta = \frac{\upsilon_{observed} - \upsilon_{reference}}{\upsilon_{spectrometer}}$$

Equation II.C-3

(δ: chemical shift (ppm); υ: frequency (Hz)).

The relative areas of the peaks correspond to the number of equivalent nuclei. The multiplicity of each peak is due to spin-spin coupling, characterized by coupling constant. This phenomenon is explained by the splitting of the signal thanks to the coupling, through chemical bonds, of spins of same type nuclei in the neighbourhood that are not chemically equivalent. The area distribution of a peak set follows the Pascal triangle (Figure II.C-1) according to the number of neighbours (n) giving the multiplicity (n+1, for protons). The coupling constant gives information on the magnitude of the splitting. It is calculated between two peaks in the same multiplet and is expressed in Hz.

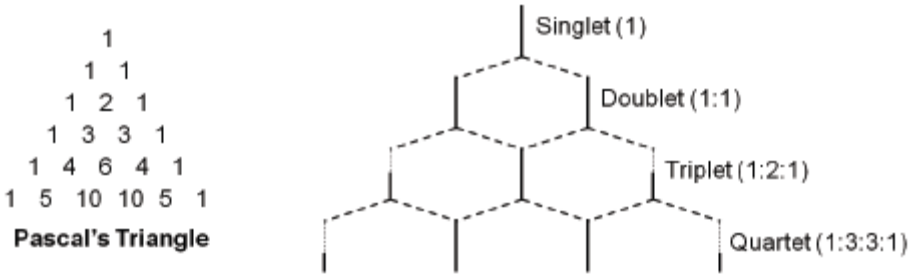

Figure II.C-1: Pascal's triangle and the intensities prediction according to the multiplicity of the peak.[4]

II.D. FT-IR spectroscopy

Fourier Transformed Infrared spectroscopy (FT-IR) is a vibrational technique of analysis, giving information on bond strength. It works with light in the infrared region with longer wavelength and lower frequency than visible light (> 800 nm), usually in the mid-infrared region between 4000 cm^{-1} and 400 cm^{-1}.

The apparatus is composed by a continuous infrared radiation source, a Michelson interferometer, a sample holder and a detector (Figure II.D-1). The continuous light source emits an infrared beam that goes through the interferometer composed by a splitter and two mirrors (a fixed one and a moving one). The splitter divides the incoming light into two optical beams; one of them is reflected by the fixed mirror and the other by the moving mirror. The two beams recombine at the splitter with optical path difference and generate an interference pattern due to changes in the relative position of the two mirrors to the splitter. The light continues its path through the sample and is absorbed by the molecule studied at the frequency of vibration of its polar bond, before being collected by a detector. Finally, the Fourier transformation is performed by a computer which received the interference signal as a function of optical path difference from the detector.

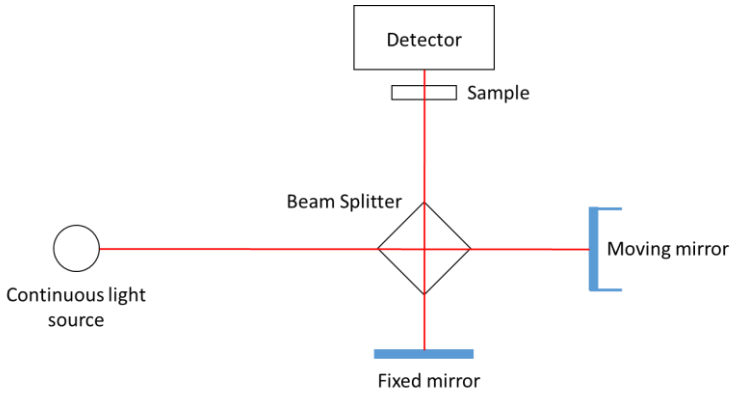

Figure II.D-1: Schematic representation of FT-IR spectrometer (adapted from ref 4).

The result is given as a spectrum of absorption intensity (A or Abs) or percent transmittance (%T) as a function of the wavenumber (cm^{-1}). As for UV-Vis spectroscopy, the transmittance (T) is the ratio between the transmitted light (I_t) after the sample and the incident light (I_0) emitted (Equation II.A-1), and absorbance is the logarithm to the base 10 of the reciprocal of T (Equation II.A-2). The Beer-Lambert law (Equation II.A-3) can be applied as

well. The bands on the spectrum give information on functional groups in the molecule, from 4000 cm^{-1} to 1300 cm^{-1}, but also a fingerprint of the molecule from 1300 cm^{-1} to 400 cm^{-1}. The fingerprint region is harder to interpret because of the superposition of many bending vibrations, but can be used to compare two molecules. IR spectroscopy can be realised on solid, liquid and gas samples.

The absorption of infrared radiation by a molecule makes its chemical bonds vibrating at a particular frequency, inducing a change in dipole moment. Two main types of vibration exist for a molecule: (i) stretching, which is a vibration along the bond and (ii) bending, happening between at least 3 atoms either in or out of the plane along the different bonds (Figure II.D-2).

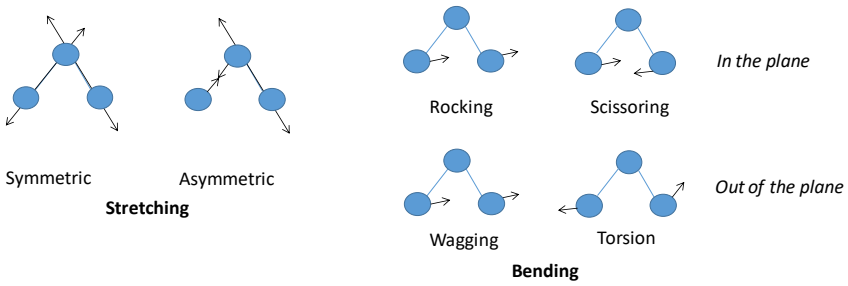

Figure II.D-2: Vibration modes for a molecule.

The bond between two atoms can be considered as a spring with a force constant k in $N.cm^{-1}$. The Equation II.D-1 expresses its vibrational frequency in cm^{-1}.[5]

$$\upsilon = \frac{1}{2\pi c} * \sqrt{\frac{k}{\mu}}$$

Equation II.D-1

(υ: frequency (cm^{-1}); c: speed of light (2.9979 x 10^{10} $cm.s^{-1}$); k: force constant ($N.cm^{-1}$); μ: reduced mass (Kg) defined by Equation II.D-2, where m_1 and m_2 are the masses (Kg) of two atoms involved in the chemical bond).[5]

$$\mu = \frac{m_1 * m_2}{m_1 + m_2}$$

Equation II.D-2

(μ: reduced mass (Kg); m: masse of atom (Kg)).

II.E. Cyclic voltammetry

Cyclic Voltammetry (CV) is an electrochemical technique to probe the redox processes of molecular compounds, and electron transfer occurring in chemical reactions such as catalysis. It relates the flow of electrons to chemical changes. A potential E is applied between electrodes in a solution containing an electrolyte and the compound to probe. The current response i is recorded to obtain a voltammogram showing the intensity (in Ampere) as a function of the potential (in Volt).

II.E.1. Experimental setup

The measurement is carried out in electrochemical cell equipped with three electrodes. The electrolyte is a salt used to keep electrical neutrality and to ensure migration of ions in solution. It is selected to be completely soluble in the solvent and should not degrade. It should have a large potential redox window, at least larger than the compound studied. A potentiostat and three electrodes are used in the cell containing the analyte (Figure II.E-1):

(i) The reference electrode (Ref) maintains a constant potential. It is selected according to the used solvent and electrolyte. It should have a well-defined and stable equilibrium potential. Different cyclic voltammograms can be compared according to this Ref. Molecular internal standard such as ferrocene can also be used.

(ii) The working electrode (WE): The electron transfer of interest is occurring at its surface. A potential is applied to the WE as function of the reference electrode potential. Window potential of WE should be in the range of studies.

(iii) The counter (or auxiliary) electrode (CE): The current is recorded as electron flow between the WE and CE. CE should be as inert as possible; usually it is platinum disk or wire.

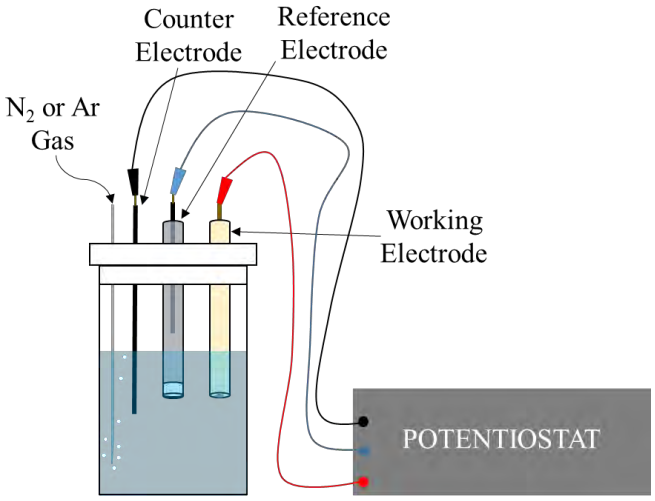

Figure II.E-1: Schematic representation of electrochemical cell setup for voltammetry.

CV is often performed under inert conditions to avoid the detection of oxygen reduction and oxidation as well as processes resulting from O_2 interaction with the compound studied. In the electrolyte solution containing the compound to analyse and the electrodes, without any applied voltage, a potential is naturally developing, this is the open circuit potential (OCP).[6] Many parameters can be adjusted for the experiment such as:

(iv) The number of scan.

(v) The starting potential from OCP or a desired potential.

(vi) The equilibration time which is the time the starting potential applied will stay constant before scanning. This parameter allows the species to be at the same redox state at the electrode surface.

(vii) The potential window and the direction sweep towards negative or positive potentials.

(viii) The potential step which defines the number of point per scan.

(ix) The scan rate which can give information on other chemical reaction happening at the surface electrode. Indeed, if a reduced or oxidized analyte is involved in a side chemical reaction, playing on the scan rate can give time for this reaction to occur or not. Futhermore, the faster the scan rate the smaller the diffusion layer and thus higher current is recorded.

The residual current is corrected by the subtraction of the corresponding blank voltammogram recorded under the same conditions and parameters.

II.E.2. Cyclic voltammogram interpretation

In Figure II.E-2, from the initial potential at 0 V toward negative potentials, the reduction occurs first at E_{pc} = -0.484 V, and then scanning backward, the oxidation happens at E_{pa} = -0.425 V. The i_{pc} is the cathodic current recorded during the reduction process, while the i_{pa} is the anodic current for the oxidation process. Those currents are measured at the cathodic and anodic peak potentials reached when all the substrate at the surface of the WE has been reduced (E_{pc}) or oxidized (E_{pa}) respectively.

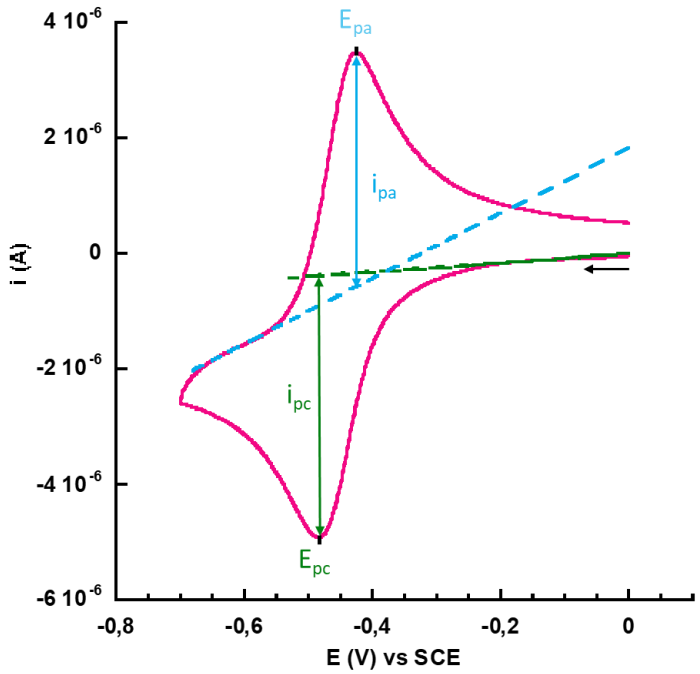

Figure II.E-2: Typical cyclic voltammogram for reversible redox compound (here Cu-TMPA complex).

Each redox couple has a standard reduction potential (E°') given by the Equation II.E-1. Below this potential, the oxidized form is predominant whereas above it, the reduced form is.[7]

$$E^{\circ\prime} = \frac{E_{pa} + E_{pc}}{2}$$

Equation II.E-1

(E°': standard potential (V); E_{pa}: oxidation peak potential (V); E_{pc}: reduction peak potential (V)).

When the system is well-behaved, the standard potential corresponds to the half wave potential $E_{1/2}$, and the anodic and cathodic peaks current are equals.

Nernst equation gives the relation between the potential and the amount of reduced or oxidized form at the electrode for the reversible reaction: $aOx + ne^- \rightleftharpoons bRed$ (Equation II.E-2).[8]

$$E = E°' - \frac{RT}{nF}\ln\left(\frac{[Red]^b}{[Ox]^a}\right)$$

Equation II.E-2

(E: potential at the electrode (V); E°': standard potential of the redox couple studied (V); R: noble gas constant (8.3145 $J.mol^{-1}.K^{-1}$); T: temperature (K); n: number of electron involved in the reaction; F: Faraday constant (96485 $C.mol^{-1}$)).

In a quiescent solution, when the oxidation or the reduction of a compound occurs at the electrode, the concentration of the reduced or oxidized form is not the same at the surface of the electrode where the reaction is taking place and in the bulk solution. Indeed if we start with a bulk solution containing only the oxidized form of a redox couple, when a potential is applied to reduce the analyte, the concentration of the oxidized form decreases while amount of reduced form increases. A gradient of concentration is generated from the electrode surface to the bulk solution, called the diffusion layer. A driving force is taking away from the electrode the reduced compound and brings more oxidized analyte. This phenomenon is governed by mass transfer diffusion and expressed with the Fick's law (Equation II.E-3).[7]

$$\frac{\partial C_A}{\partial t} = D_A\left(\frac{\partial^2 C_A}{\partial x^2}\right)$$

Equation II.E-3

(C_A: analyte concentration ($mol.cm^{-3}$); t: time (s); D_A: diffusion coefficient of the analyte ($cm^2.s^{-1}$); x: distance from the electrode (cm)).

In our case there is no other mass transport than diffusion, as the solution is not stirred there is no convection and the presence of high concentration of inert electrolyte prevent from migration.

Randles-Sevcik equation gives the peak current for reversible electron transfer (Equation II.E-4). The peak current should increases linearly with the square root of the scan rate.[6]

$$i_p = 0.446nFAC_A\left(\frac{nF\upsilon D_A}{RT}\right)^{1/2}$$

Equation II.E-4

(i_p: peak current (A); n: number of electrons; F: Faraday constant (96485 C.mol^{-1}); A: electrode surface area (cm^2); C_A: analyte concentration (mol.cm^{-3}); υ: scan rate (V.s^{-1}); D_A: diffusion coefficient of analyte (cm^2.s^{-1}); R: noble gas constant (8.3145 J.mol^{-1}.K^{-1}); T: temperature (K)).

To assess the reversibility of redox system, the separation between the two peaks potential (ΔE_p) should be close to Equation II.E-5. If ΔE_p remains constant while varying the scan rate, the system is reversible, and vice-versa.[9]

$$\Delta E_p = E_{pa} - E_{pc} = \frac{0.058}{n}$$

Equation II.E-5

(ΔE_p: peak-to-peak potential separation (V); E_{pa}: oxidation peak potential (V); E_{pc}: reduction peak potential (V); n: number of electron).

References

1. Kaur, P.; Oyala, P.; Guo, Y., EPR: Theory. In *Physical & Theoretical Chemistry*, LibreTexts, 2020.

2. Bovet, C.; Barron, A. R., EPR Spectroscopy: An Overview. CNX, O., Ed. OpenStax CNX: 2009. http://cnx.org/contents/7cc9e808-c99b-4cd6-9284-949303c856a1@3 (accessed 23/01/2022).

3. Kaseman, D.; Iyer, R. S. G. 5.2: Introduction. https://chem.libretexts.org/@go/page/167052 (accessed 01/02/2022).

4. Raja, P. M. V.; Barron, A. R., Physical Methods in Chemistry and Nano Science. Raja, P. M. V.; Barron, A. R., Eds. 2019; p. 1375. http://cnx.org/content/col10699/1.25/ (accessed 21/03/2021).

5. Helton, M. E.; Chen, P.; Paul, P. P.; Tyeklár, Z.; Sommer, R. D.; Zakharov, L. N.; Rheingold, A. L.; Solomon, E. I.; Karlin, K. D., Reaction of Elemental Sulfur with a Copper(I) Complex Forming a trans-μ-1,2 End-On Disulfide Complex: New Directions in Copper−Sulfur Chemistry. *Journal of the American Chemical Society* **2003,** *125* (5), 1160-1161.

6. Elgrishi, N.; Rountree, K. J.; McCarthy, B. D.; Rountree, E. S.; Eisenhart, T. T.; Dempsey, J. L., A Practical Beginner's Guide to Cyclic Voltammetry. *Journal of Chemical Education* **2018,** *95* (2), 197-206.

7. Quiroga, A. Cyclic Voltammetry. https://chem.libretexts.org/@go/page/311 (accessed 02/02/2022).

8. Harvey, D., 11: Electrochemical Methods. In *Analytical Chemistry 3.0*, DePauw University: 2021.

9. Kelly, R. S. ii) Important parameters in CV. https://chem.libretexts.org/@go/page/61490 (accessed 02/02/2022).

Chapter III

Chapter III. Solid-state and solution characterizations of $[Cu(II)TMPA(L)]^{n+}$ with L = H_2O, CH_3CN, SO_4^{2-}, NO_3^- HO^-, CO_3^{2-}…

Because the formation of Cu(I)-CO adduct with TMPA and model peptides will require the use of acetonitrile as co-solvent to increase the concentration of dissolved CO to displace the equilibrium toward the formation of the adduct, we have first characterized the effect of adding 10% of acetonitrile (CH_3CN) to a buffered aqueous solution (HEPES 0.1 M pH 7.4) on the Cu(II)(TMPA) complex. During this study, several unexpected Cu(II)TMPA complexes have been formed with different exogenous ligands occupying the labile position. Their formation depends on the starting Cu(II) salt and the solvent mixture used. Quite surprisingly, given the huge literature on Cu(II)TMPA complex, this is barely documented. We sought to characterize all of them as much as possible, including by solid-state X-ray diffraction studies.

Hence, this third chapter is devoted to the study of Cu(II)TMPA complexes formed from different Cu(II) salts in various solvent mixtures or in presence of external inorganic salts. During the course of our study various Cu(II)TMPA complex crystals suitable for X-Ray analyses were obtained in different conditions and from several Cu(II) salts. A first part is presenting the solid-state characterizations of those species with diverse anions or solvent molecules as a fifth ligand. A second part is devoted to their solution characterizations, mainly by EPR and UV-Vis spectroscopies.

III.A. Solid-state characterizations of Cu(II)TMPA

III.A.1. Overview

Solid-state characterizations of a numerous Cu(II)TMPA complexes was performed by X-ray crystallography. Most of the Cu(II)TMPA complexes are penta-coordinated. Therefore, they take square pyramidal (SPy) to trigonal bipyramid (TBP) geometries (Scheme III.A-1). The well accepted Addison τ parameter is a useful tool to distinguish those two geometries.[1] It is defined as Equation III.A-1 where α and β are the two largest L-M-L angles. τ = 1 corresponds to a TBP geometry while τ = 0 to SPy geometry. The values in-between allow the evaluation of the distortion toward one or the other geometry.

$$\tau = \frac{|\alpha_{L-M-L} - \beta_{L-M-L}|}{60}$$

Equation III.A-1

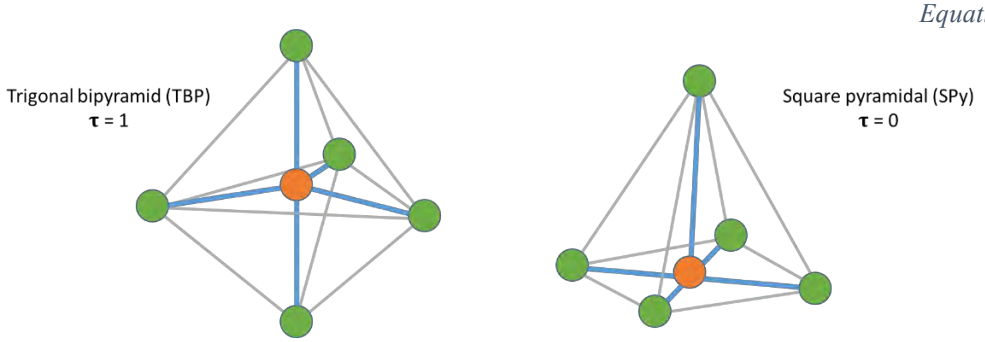

Scheme III.A-1: Trigonal bipyramid and square pyramidal geometries, the green circles represent the ligands and the orange circles the metal center.

The Table III.A-1 gives an overview of τ parameter obtained from crystallographic data of different Cu(II)TMPA complexes. All of them have τ parameters close to 1 indicative of a TBP geometry. The counter ion or other non-binding molecules in the crystals structures are not presented but their size can induce distortion from the ideal geometry. For example $[CuTMPA(H_2O)]^{2+}$ crystallize with an almost perfect TBP geometry with τ = 0.97 or 0.95 with small perchlorate or triflate counter-anion respectively[2-3], whereas it has τ = 0.90 when it crystallizes with the bulky [β-Mo_8O_{26}] polyanion.[4] $[CuTMPA(ONO)]^+$ and $[CuTMPA(BNPP)]^+$ complex display a τ = 0.85 and τ = 0.70 implying a greater distortion toward SPy geometry than most of the Cu(II)TMPA complexes. In the latter case this may be linked to the bulkiness of the exogenous ligand. It is interesting to see the variety of fifth ligand especially looking at the coordinated atom, such as oxygen, nitrogen, carbon or halogen (Table

III.A-1). To the best of our knowledge, no mononuclear Cu(II)TMPA structure was reported with a fifth ligand coordinated through a sulfur atom (except in our JIB (Journal of Inorganic Biochemistry) article, see annex chapter and ref. 5). However, a dinuclear $[\{CuTMPA\}_2S_2]^+$ with a bridging sulfide ligand was published.[6]

Table III.A-1: Overview of τ parameter calculated from X-ray crystallographic data of various Cu(II)TMPA complexes.

Complex	5th Ligand coordination mode	τ	Ref
$[CuTMPA(H_2O)]^{2+}$	$-OH_2$	0,97	2
		0,95	3
		0,90	4
$[CuTMPA(CH_3CN)]^{2+}$	$-NCCH_3$	1,00	7
		0,96	8
$[CuTMPA(Cl)]^+$	-Cl	1,04	9
		1,01	10
		0,98	11
		0,95	12
		0,94	11
		0,88	13
		0,87	13
		0,86	14
$[CuTMPA(Br)]^+$	-Br	1,04	15
		0,99	16
		0,90	13
		0,89	16
		0,86	13
$[CuTMPA(F)]^+$	-F	0,91	17
$[CuTMPA(CN)]^+$	-CN	0,96	18
		0,95	18
		0,94	19
$[CuTMPA(N_3)]^+$	$-N_3$	0,91	20
$[CuTMPA(NCS)]^+$	-NCS	0,96	21
$[CuTMPA(NCNCN)]^+$	-NCNCN	0,95	22
$[CuTMPA(ONO)]^+$	-ONO	0,85	12
		0,84	20
$[CuTMPA(BNPP)]^+$	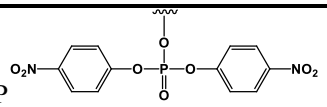 BNPP	0,70	23

It is obvious that Cu(II)TMPA complexes in solid state have a preference for TBP geometry. However, they are flexible enough to accept big fifth ligands inducing a higher distortion of TBP toward SPy geometry ($[CuTMPA(BNPP)]^+$). Cu(II)TMPA are even able to form hexa-coordinated[24] and polynuclear complexes through bridging ligand.[6, 25-26]

According to the conditions of studies, different anions or solvent molecules can compete for the coordination to Cu(II) center. R. Dìaz-Torres and S. Avarez published coordinating ability tables for various anions and solvents toward transition metals. They defined a coordinating ability index a^{TM} given by the Equation III.A-2, where c, s and u correspond to the number of structures with the studied anion or solvent coordinated, semi-coordinated (weak interaction to metal center) and uncoordinated (but coexisting) respectively.[27]

$$a^{TM} = \log\left(\frac{c + s}{u}\right)$$

Equation III.A-2

This index can be useful to understand the trend of coordination competition toward a metal center. However, it should be considered carefully as it is based on solid-state data, thus the tendency can be different in solution. All transition metals are considered in the calculation but looking at Cu(II) only could show a different classification list.

III.A.2. Solid-state X-ray structures obtained

Looking at the literature on Cu(II)TMPA complexes in solid-state, it is clear that mostly neutral and mono-anionic ligands were reported to be coordinated in the fifth position. During the course of my PhD different new compounds were identified, especially with di-anionic ligands and sulfur-containing ligands. For example, $[CuTMPA(SO_3)]$ was generated firstly from the degradation product of dithionite used as a reductant during the study of Cu(I)TMPA reactivity under air atmosphere. $[CuTMPA(S_2O_3)]$ was then generated when trying to identify the previous species. Those results and their full characterizations have been published and are presented in an annex chapter of this manuscript.[5] $[CuTMPA(SO_4)]$ was first identified in solution by UV-Vis spectroscopy and then crystals suitable for X-ray analyses were obtained. The unusual presence of sulfate ion in the first coordination sphere of Cu(II)TMPA complex is

in line with the low solubility of SO_4^{2-} ion in organic solvents. Seeing that the Cu(II) or inorganic salts used to generate the complex had an influence on the fifth ligand coordination, different Cu(II) sources such as $Cu(II)(OTf)_2$, $Cu(SO_4)$ were used. Throughout all this chapter, $[CuTMPA(H_2O)]^{2+}$ and $[CuTMPA(CH_3CN)]^{2+}$ are of particular interest. Those two complexes were already characterized by X-ray crystallography, EPR and UV-Vis spectroscopies (Table III.A-1; Table III.B-1 and Table III.B-2) in the literature.[7-8, 28-29] The aim of this first part is to give solid-state characterizations of five new Cu(II)TMPA complexes and compare them with the parent complexes $[CuTMPA(H_2O)]^{2+}$ and $[CuTMPA(CH_3CN)]^{2+}$.

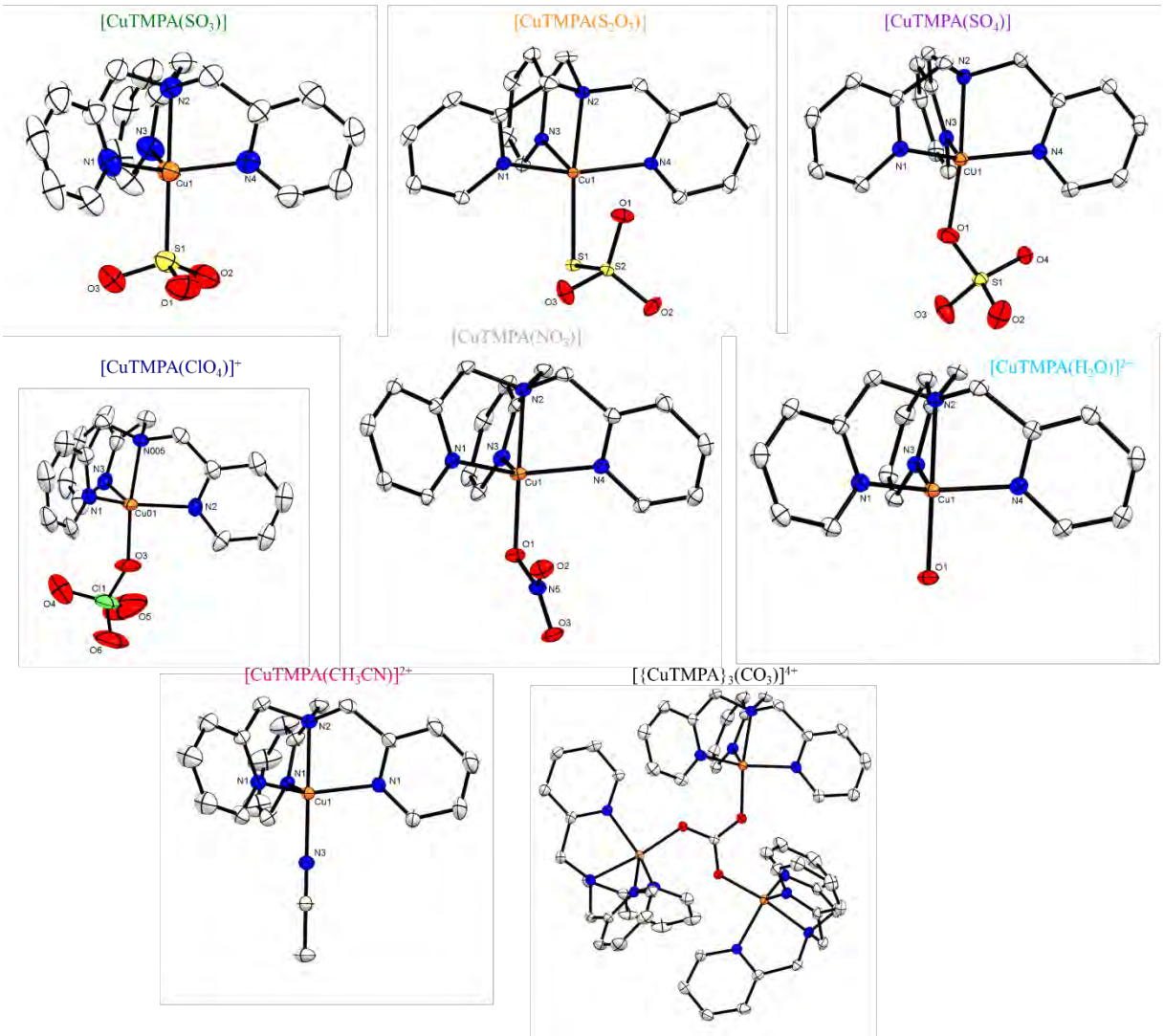

Figure III.A-1: X-ray structures of $[CuTMPA(SO_3)]$; $[CuTMPA(S_2O_3)]$; $[CuTMPA(SO_4)]$; $[CuTMPA(ClO_4)]^+$; $[CuTMPA(NO_3)]^+$; $[CuTMPA(H_2O)]^{2+}$; $[CuTMPA(CH_3CN)]^{2+}$ and $[\{CuTMPA\}_3(CO_3)]^{4+}$ drawn with 50 % of ellipsoid.

Seven mononuclear and one trinuclear solid-state pentacoordinated Cu(II)TMPA complexes were compared by X-ray crystallography characterization: $[CuTMPA(SO_3)]$; $[CuTMPA(S_2O_3)]$; $[CuTMPA(SO_4)]$; $[CuTMPA(ClO_4)]^+$; $[CuTMPA(NO_3)]^+$; $[CuTMPA(H_2O)]^{2+}$; $[CuTMPA(CH_3CN)]^{2+}$ and the trinuclear complex $[\{CuTMPA\}_3(CO_3)]^{4+}$. An ORTEP representation of their structures is given in Figure III.A-1. Selected bond distances and angles are listed in Table III.A-2 where X represents the fifth coordinated atom. As defined previously, the Addison τ parameter is used to compare geometries and distortion toward SPy (τ = 0) or TBP (τ = 1).

$[CuTMPA(SO_3)]$, $[CuTMPA(H_2O)]^{2+}$, and $[CuTMPA(CH_3CN)]^{2+}$ have nearly perfect TBP geometry with τ = 1.02, 0.94, and 1.01 respectively. The two latter results are consistent with the τ-values previously reported for $[CuTMPA(H_2O)]^{2+}$, and $[CuTMPA(CH_3CN)]^{2+}$ (Table III.A-1).[3, 7] Those three complexes have similar equatorial angle close to 120 °. Their N_{ax}-Cu-X is close to linearity, especially for $[CuTMPA(CH_3CN)]^{2+}$ and $[CuTMPA(SO_3)]$. The Cu-N_{eq} bond lengths are comparable for $[CuTMPA(H_2O)]^{2+}$ and $[CuTMPA(SO_3)]$, and a bit shorter for $[CuTMPA(CH_3CN)]^{2+}$. The Cu-N_{ax} distances are shorter than Cu-N_{eq} for $[CuTMPA(CH_3CN)]^{2+}$ and $[CuTMPA(H_2O)]^{2+}$ but longer for $[CuTMPA(SO_3)]$. The Cu-X bond lengths are similar for the coordination of CH_3CN through nitrogen and H_2O through oxygen (1.96 Å (which is shorter than typical Cu-N bond of 2.0 to 2.1 Å)[13] and 1.95 Å respectively). However, it is longer for the coordination of SO_3^{2-} by sulfur atom due to the bulkiness of the sulfur coordinating atom (2.25 Å).

$[CuTMPA(SO_4)]$, $[CuTMPA(NO_3)]^+$ and $[CuTMPA(ClO_4)]^+$ have distorted TBP geometry with τ = 0.89, 0.85, 0.83 respectively. The higher distortion witnesses the higher difference between the equatorial angles. $[CuTMPA(NO_3)]^+$ has two close equatorial angles (115 ° and 116 °) and a larger one (123 °), whereas for $[CuTMPA(ClO_4)]^+$ two of them are equal to 120 ° and 121 ° and the last one is shorter with 113 °. $[CuTMPA(SO_4)]$ on the contrary has close equatorial angles (two of 117 ° and one of 119 °). $[CuTMPA(SO_4)]$, $[CuTMPA(NO_3)]^+$ and $[CuTMPA(ClO_4)]^+$ are also characterized by an X-Cu-N_{ax} angle farther from linearity (172 °, 174 ° and 171 ° respectively). Their crystallographic resemblance is due to the coordination of an anion ligand through an oxygen atom. The O-Cu bond length for $[CuTMPA(NO_3)]^+$ is comparable to Cu-O_{H2O} of 1.95 Å. This Cu-O axial bond is shorter for the coordination of SO_4^{2-} (1.92 Å) and even more for ClO_4^- (1.90 Å).

[CuTMPA(S_2O_3)] is much different than the other structures reported earlier and in the literature for Cu(II)TMPA complexes. With a τ = 0.11, it has a geometry highly distorted toward SPy, because of the weak interaction of an oxygen atom from $S_2O_3^{2-}$ with the Cu center (Cu-$O_{(S2O3)}$ = 2.7 Å). The presence of this oxygen atom has for consequence to send away N(1) and N(4). The structure is characterized by a longer Cu-N(3) bond (2.2 Å) becoming the axial bond in trans to the oxygen atom (O(1)). The equatorial plane, now defined by the N(1), N(2), N(4) and S(1) atoms, presents N(1)-Cu-N(4) and S(1)-Cu-N(2) angles approaching linearity (162 ° and 168 ° respectively). Such unusual SPy geometry for a Cu complex with tripodal tetradentate ligand was reported for a [(Me_3tren)Cu(S_2O_3)] structure.[30]

Table III.A-2: Selected bond lengths (Å) and angles (°) and τ parameter for $[CuTMPA(X)]^{n+}$ (where X= coordinating atom from CH_3CN; H_2O; SO_3^{2-}; $S_2O_3^{2-}$; SO_4^{2-}; NO_3^-; ClO_4^-; CO_3^{2-} and n= 0; 1; 2).

	CH_3CN	H_2O	SO_3^{2-}	$S_2O_3^{2-}$	SO_4^{2-}	NO_3^-	ClO_4^-	(CO_3) 1	(CO_3) 2	(CO_3) 3
Cu-N(1)eq	2.05	2.073(1)	2.072(7)	2.029(1)	2.055(3)	2.055(2)	2.0389	2.066(2)	2.179(2)	2.054(2)
Cu-N(2)ax	2.018	2.008(1)	2.087(7)	2.0618(9)	2.044(4)	2.012(2)	2.0294	2.032(2)	2.036(2)	2.031(2)
Cu-N(3)eq	2.05	2.060(1)	2.077(7)	2.2025(9)	2.078(2)	2.086(2)	2.0894	2.072(2)	2.074(2)	2.099(2)
Cu-N(4)eq	2.047	2.061(1)	2.085(7)	2.0417(9)	2.078(3)	2.053(2)	2.0363	2.081(2)	2.030(2)	2.089(2)
Cu-X	1.955	1.952(1)	2.253(2)	2.2878(4)	1.924(3)	1.949(2)	1.8973	1.929(2)	1.935(2)	1.915(1)
Cu-O(S_2O_3)	-	-	-	2.695(1)	-	-	-	-	-	-
N(1)-Cu-N(3)	118.6	117.71(5)	118.5(3)	93.95(4)	119.0(1)	114.90(7)	113.34	114.97(7)	107.90(7)	124.96(8)
N(1)-Cu-N(4)	118.6	117.01(5)	116.1(3)	161.62(4)	117.1(1)	122.99(7)	120.97	118.14(7)	111.78(7)	115.51(7)
N(3)-Cu-N(4)	118.6	119.90(5)	117.2(3)	92.80(4)	116.8(1)	116.07(7)	120.14	120.20(7)	131.93(8)	114.10(7)
X-Cu-N(2)	180	176.48(6)	178.9(2)	168.09(3)	172.2(1)	173.88(7)	170.56	171.27(7)	172.88(7)	171.70(7)
O(S_2O_3)-Cu-N3				173.72(3)				-	-	-
τ	1.02	0.94	1.01	0.11	0.89	0.85	0.83	0.85	0.68	0.78

For the trinuclear complex [{CuTMPA}$_3$(CO_3)]$^{4+}$ structure, each {Cu(II)TMPA} unit is linked through a CO_3^{2-} bridging ligand. This crystal structures was obtained twice under the conditions tested to grow crystals of $[CuTMPA(OH)]^+$, *i.e.* in presence of hydroxyl anions. This structure was already published and obtained in aqueous solution in presence of triethylamine.[31] The CO_3^{2-} bridging ligand is obtained from the reaction of CO_2 from the atmosphere in basic conditions. All three {Cu(II)TMPA} units have distorted TBP geometry with τ = 0.68, 0.78 and 0.85. The O-Cu-N_{ax} angles are deviated from linearity (171 ° to 173 °) due to steric hindrance

of the whole structure. The Cu-O bond length are among the shortest one for the complexes presented here around 1.93 Å, comparable to the one for SO_4^{2-}.

III.B. Solution characterizations of Cu(II)TMPA complexes as a function of the fifth ligand

III.B.1. Cu(II) UV-Vis and EPR general features

Cu(II) is a (d^9) paramagnetic metal ion with a nuclear spin of I = 3/2 displaying EPR signal split into 4 lines (2nI + 1) resulting from the hyperfine coupling. Cu(II) complexes take diverse geometries with different numbers of coordination sites (tetra-, penta-, and hexa-coordinated). This diversity affects the electronic properties of the Cu(II) center and the orbital splitting order of the d electrons in the complex (Figure III.B-1) and thus the spectroscopic signatures associated such as UV-Vis and EPR. EPR is convenient to characterize Cu(II) species as $g_{//}$ and $A_{//}$ values are very sensitive to the nature of the equatorial ligands.

Cu(II) complexes adopt usually octahedral elongated, square planar or square pyramidal geometry with typical axial EPR spectra having $g_{//} > g_{\perp}$ corresponding to a $d_{x^2-y^2}$ ground state (Figure III.B-1).[32-33] Penta-coordinated Cu(II) complexes take two distinct geometries: square pyramid or trigonal bipyramid. Coordinated with tripodal tetradentate ligands, Cu(II) prefers primarily TBP geometry.[34-35] This geometry is characterized by inverse axial EPR spectrum (with $g_{\perp} > g_{//} \approx 2.0$ and A values between 60 and 100 × 10^{-4} cm^{-1}) featuring a d_{z^2} ground state.[33, 36] In UV-Vis this geometry is identified in the d-d region of the spectrum by a d-d band around 800 to 950 nm and a higher energy less intense shoulder attributed to $d_{x^2-y^2, xy} \rightarrow d_{z^2}$ and $d_{xz,yz} \rightarrow d_{z^2}$ transitions, respectively.

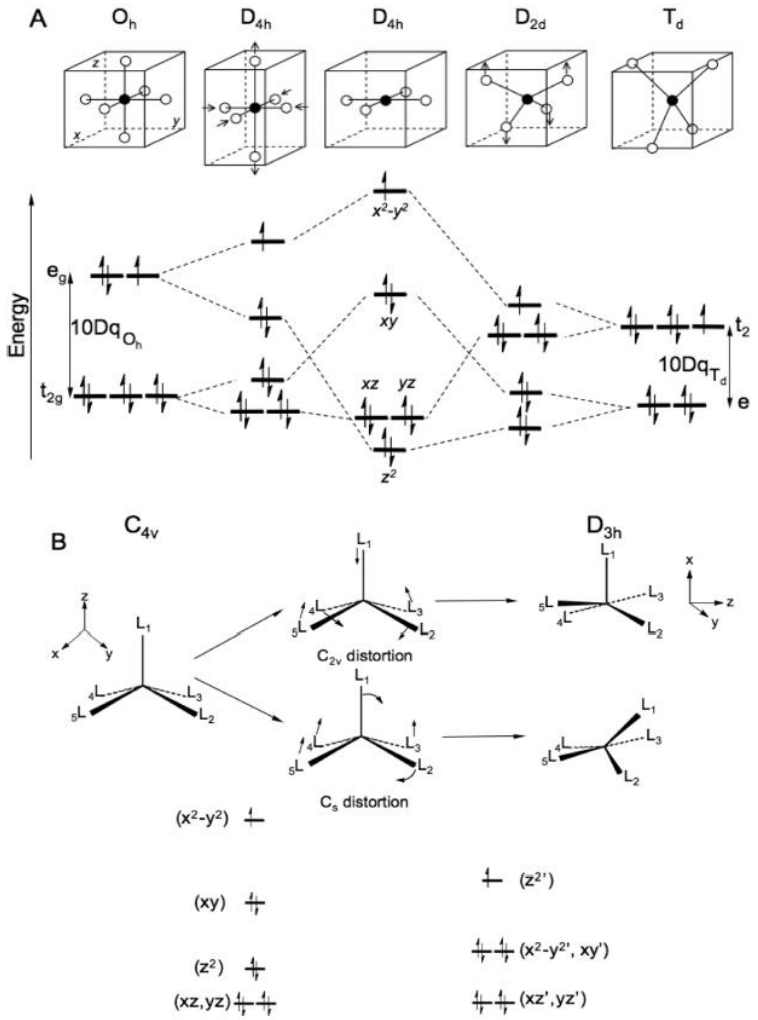

Figure III.B-1: Ligand field splitting of d orbitals in complexes according to the geometry and distortion. (A) From octahedral to square planar to tetrahedral geometries. (B) From square pyramidal to trigonal bipyramidal geometries.[32]

To illustrate the different geometries encounter for Cu(II) complexes and their effects on UV-Vis and EPR spectroscopies typical examples will be briefly described hereafter.

III.B.1.a. Axial Cu(II) EPR spectra

The most common geometry of Cu(II) complexes in a non-constrained environment is distorted octahedral due to Jahn-Teller effect. In this geometry, the unpaired electron is in the $d_{x^2-y^2}$ orbital leading to EPR spectrum with equivalent x and y axes and two values of g, $g_{//}$ (g_z) and $g_\perp$ ($g_x = g_y$). The EPR spectrum of Cu(II) will thus display an axial EPR spectrum with a large splitting of the $g_{//}$-line and a minor splitting of $g_\perp$-lines. As an example, Figure III.B-2 displays the axial EPR spectrum of frozen Cu(II) in aqueous solution.[37]

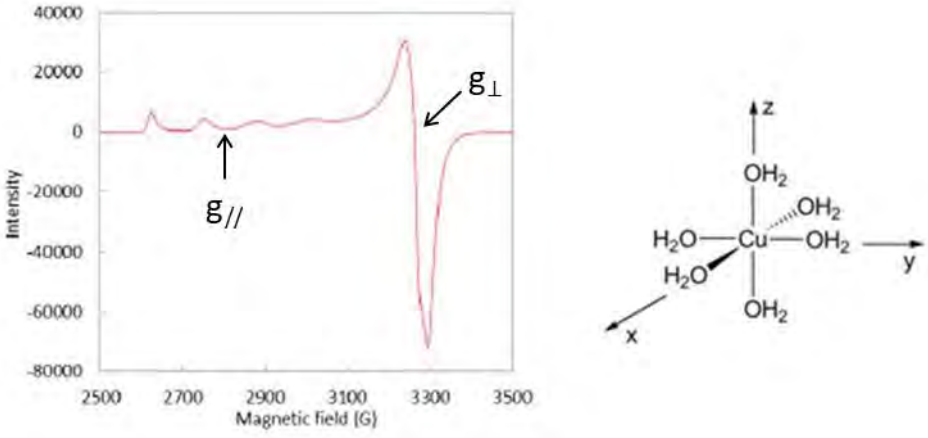

Figure III.B-2: Left: EPR spectrum of Cu(II) aqueous solution. Right: Geometry of Cu(II) in aqueous solution.[37]

Square planar and square pyramidal geometries found for example for Cu(II)Aβ complexes will also display similar axial EPR spectra as the single electron is in the $d_{x^2-y^2}$ orbital (Figure III.B-1).

III.B.1.b. Inverse axial EPR spectra

Copper complexes in compressed octahedron or trigonal bipyramid geometries have their single electron in the d_{z^2} orbital (Figure III.B-1), and thus display an axial inverse EPR spectrum with $g_\perp$ ($g_x = g_y$) > $g_{//}$ (g_z). This is the case of Cu(II)TMPA complexes, such as the one shown in Figure III.B-3.[33]

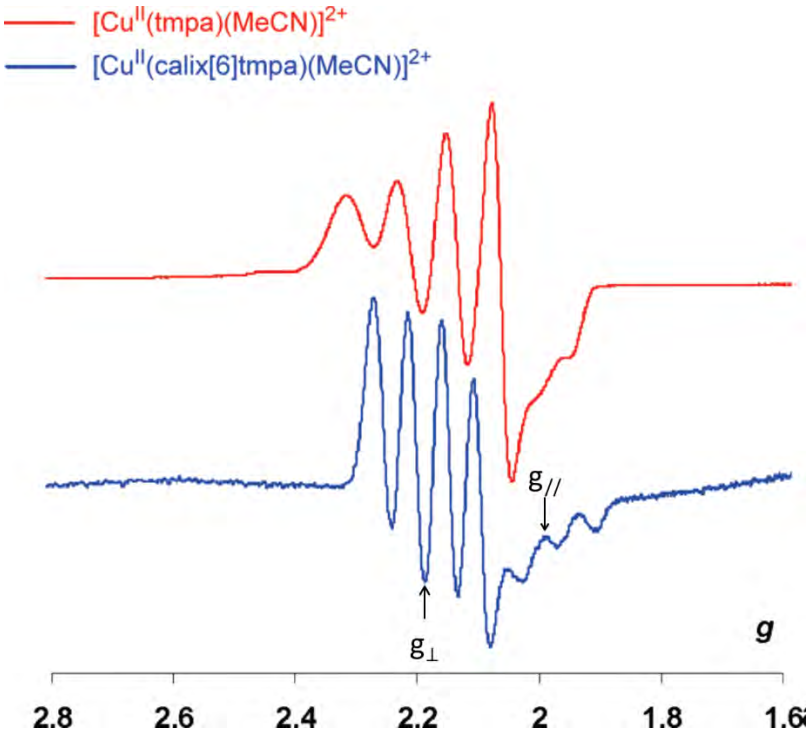

Figure III.B-3: EPR spectrum of $[Cu(II)(calix[6]TMPA)(CH_3CN)]^{2+}$ and $[Cu(II)TMPA(CH_3CN)]^{2+}$ in CH_3CN at 150 K. Calix[6]TMPA is a TMPA based cavity ligand separating the Cu center and the available labile coordination site by a funnel-like pocket from the medium.[29]

III.B.1.c. Intermediate or rhombic spectra

Pentacoordinated complex with intermediate geometry between square pyramidal and trigonal bipyramid have contribution of both d_{z^2} and $d_{x^2-y^2}$ orbitals for the single electron occupancy. However, one orbital can predominate on the other, defined by R parameter according to g_x, g_y, g_z values (Equation III.B-1). If R < 1 there is a greater contribution of the dx^2-y^2 orbital and thus a geometry closer to square pyramidal. If R > 1 the dz^2 orbital is predominant for the single electron occupancy and the geometry is closer to trigonal bypiramid.[33] Figure III.B-4 displays an EPR rhombic spectrum of $[Cu(II)(phen)_2(H_2O)](NO_3)_2$ which have a geometry between square pyramid and trigonal bipyramidal but closer to the last one.

$$R = \frac{g_y - g_z}{g_x - g_y}$$

Equation III.B-1

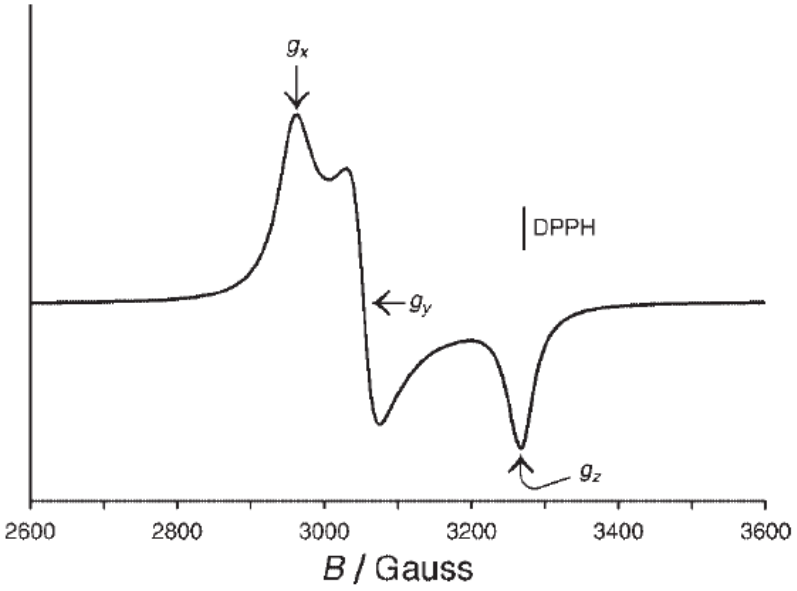

Figure III.B-4: EPR spectrum of $[Cu(II)(phen)_2(H_2O)](NO_3)_2$.[33]

III.B.1.d. EPR overview of Cu(II)TMPA

EPR spectra and EPR parameters of various Cu(II)TMPA complexes are shown and summarized in Figure III.B-5 and Table III.B-1. All of them are characterized by a TBP geometry, with $g_{//} = 2.0$ and the $g_\perp$ near to 2.20. The variation of solvent or fifth ligand impacts the EPR signature of Cu(II)TMPA complexes, especially on A values (Table III.B-1). On spectra, the variations are observed in the positions of the hyperfine lines and their relative intensities. The parallel region of the spectra is more or less defined according to the fifth ligand.

EPR simulation of Cu(II)TMPA species are quite difficult. Indeed, the position of the peaks is often achieved, but the relative intensities and width of peaks are harder to fit.[3, 38-39] The intricate EPR simulation of such system might be due to dynamical processes resulting in distortion from the ideal TBP geometry, with vibrational effects probably involving a small participation of the orbital $d_{x^2-y^2}$ in the ground state (keeping in mind that it corresponds to the Cu(II) preferred geometry).[40] Finally, intra- and intermolecular effects can also participate to the strain, particularly with solvent.

Table III.B-1: Overview of EPR data for Cu(II)TMPA complexes with different fifth ligands in various conditions.

Complex	Solvent	$g_\perp$ ($A_\perp$, 10^{-4} cm^{-1})	$g_{//}$ ($A_{//}$, 10^{-4} cm^{-1})	Ref
$[CuTMPA(H_2O)]^{2+}$	CH_2Cl_2dry	2.21 (103)	1.99 (66)	3
	CH_2Cl_2wet	2.21 (105)	2.00 (66)	3
	THFdry	2.20 (106)	2.00 (64)	3
	THFwet	2.20 (106)	2.00 (64)	3
	H_2O/Ethylene Glycol	2.199 (106)	2.0 (64)	41
	H_2O/MeOH/EtOH	2.198 (100)	2.004 (59)	17
$[CuTMPA(CH_3CN)]^{2+}$	CH_3CN	2.19 (115)	2.01 (61)	28
	CH_2Cl_2	2.200 (113)	2.0147 (65)	29
$[CuTMPA(Cl)]^+$	DMF/$CHCl_3$	2.19(96)	2.00	10
	DMF/Toluene 1/1 v/v	2.18 (100)	2.01 (78)	38
	MeTHF	2.190 (98)	2.004 (65)	12
$[CuTMPA(F)]^+$	CH_2Cl_2/Toluene	2.224 (94)	1.954 (80)	17
$[CuTMPA(NO_2)]^+$	MeTHF	2.200 (105)	1.992 (78)	12
$[CuTMPA(OOH)]^+$	Acetone	2.20 (89)	2.01 (78)	42
	CH_3CN	2.19 (97)	2.01 (78)	43

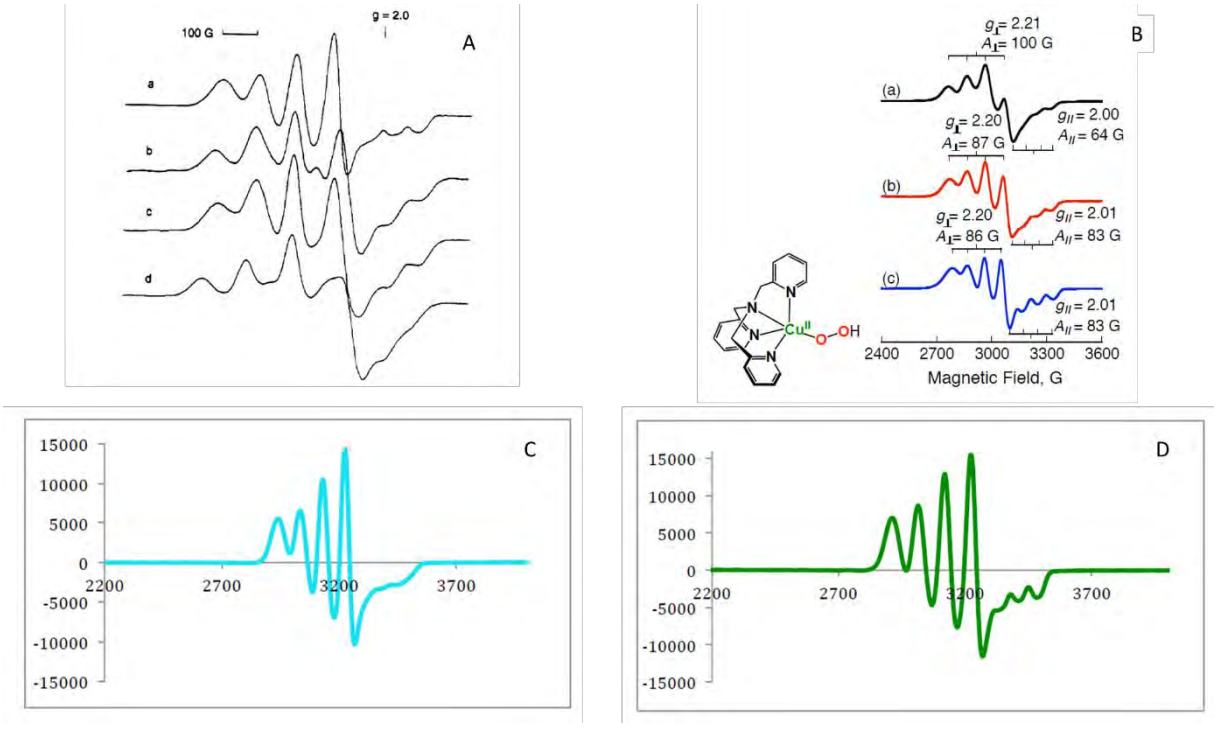

Figure III.B-5: EPR spectra of different Cu(II)TMPA complexes in various conditions. (A) Continuous wave EPR (X-band) spectrum of $[CuTMPA(L)](ClO_4)_2$ with L= H_2O (a), imidazole (b), 4-methylimidazole (c) and 2-methylimidazole (d) in H_2O/Ethylene Glycol at 77 K.[41] (B) EPR spectra of $[CuTMPA]^{2+}$ (black line), and of $[CuTMPA(OOH)]^+$ (red and blue line) generated in two different ways in acetone, at 77 K.[42] (C) EPR spectrum $[CuTMPA(Cl)]B(C_6F_5)_4$ in MeTHF at 20 K.[12] (D) EPR spectrum of $[CuTMPA(NO_2)]B(C_6F_5)_4$ in MeTHF at 20 K.[12]

III.B.1.e. UV-Vis overview of Cu(II)TMPA

Table III.B-2: Overview of UV-Vis spectral data for Cu(II)TMPA complexes with different fifth ligands in various conditions.

Complex	Solvent (T °C)	λ_{max1} (nm)	ε ($M^{-1}cm^{-1}$)	λ_{max2} (nm)	ε ($M^{-1}cm^{-1}$)	λ_{max3} (nm)	ε ($M^{-1}cm^{-1}$)	Ref
$[CuTMPA(CH_3CN)]^{2+}$	CH_3CN	-	-	630	-	889	238	[28]
$[CuTMPA(H_2O)]^{2+}$	H_2O-MeOH-EtOH	-	-	-	-	870	213	[17]
	CH_2Cl_2 dry	-	-	695	54	940	249	[3]
	CH_2Cl_2 wet	-	-	694	53	898	317	[3]
	THF dry	-	-	677	67	892	185	[3]
	THF wet	-	-	667	120	846	215	[3]
$[CuTMPA(Cl)]^+$	CH_3CN	- -	- -	632 730	88 sh	962 ~950	210 209	[10-11]
	H_2O	-	-	-	-	~875	237	[11]
$[CuTMPA(F)]^+$	CH_3CN	254	10600	715	99	881	192	[17]
$[CuTMPA(CN)]^+$	H_2O	-	-	-	-	817	271	[18]
$[CuTMPA(N_3)]^+$	MeOH	413	3470	672	350	879	310	[44]
$[CuTMPA(NO_2)]^+$	Acetone	413	1156	-	-	843	216	[12]
	MeTHF	427	-	-	-	843	216	[12]
$[CuTMPA(OOH)]^+$	CH_3CN (-40)	379	17000	668	170	828	200	[45]
$[CuTMPA(O_2)]^+$	EtCN (-90 to -75)	410	4000	580	1100	747	1000	[46-47]
	MeTHF (-135)	423	5600	585	-	752	-	[48]
$[\{CuTMPA\}_2(O_2)]^{2+}$	EtCN (-80)	440	4000	525	11500	590	7600	[47]

The UV-Vis parameters of the Cu(II)TMPA(L) complexes are presented in Table III.B-2. The complexes display similar features especially in the d-d transitions region, with a band between 800 and 1000 nm and a higher energy less intense shoulder typical for TBP geometry. Depending on the fifth ligand and the solvent a Ligand to Metal Charge Transfer (LMCT) band or shoulder can be observed between 300 and 450 nm (Table III.B-2). The increasing polarity of solvent induces a blue shift of the LMCT band as observed for $[CuTMPA(O_2)]^+$ in MeTHF (0.207: relative polarity of THF) and EtCN (0.460: relative polarity of CH_3CN) (Table III.B-2) and $[CuTMPA(NO_2)]B(C_6F_5)_4$ in acetone(relative polarity: 0.355) and in MeTHF.

III.B.2. UV-Vis and EPR characterizations in THF/H_2O mixtures

All the complexes characterized in solid-state in part III.A.2, except the trinuclear species, were then characterized in solution by UV-Vis and EPR. The chemical nature of the complexes in solution can be different from those obtained in solid-state. With the aim to compare the different complexes together and reduce competition with solvent as ligand, they were first characterized in THF (considered as a weak to non-coordinating solvent) with 20 % H_2O, and 2 % H_2O. 20 % of H_2O was necessary to avoid precipitation of the [Cu(TMPA)(SO_4)], [Cu(TMPA)(SO_3)] and [Cu(TMPA)(S_2O_3)] complexes.

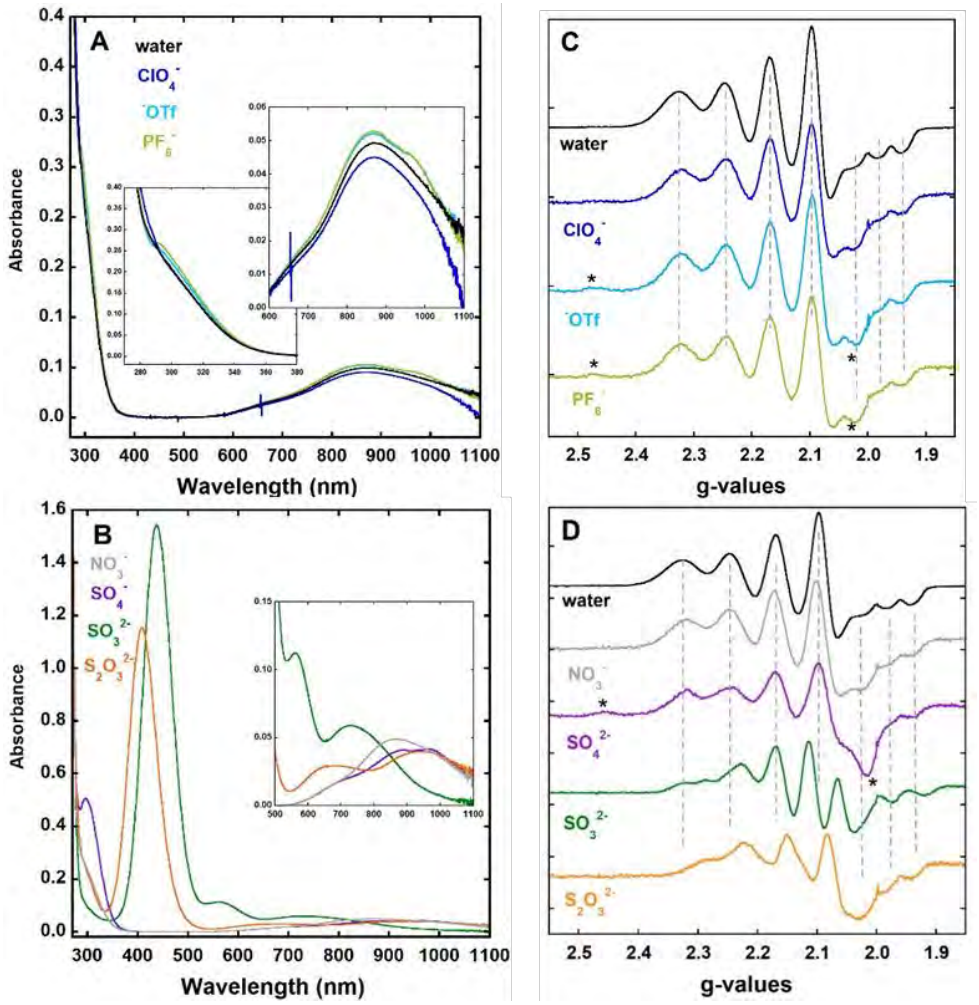

Figure III.B-6: UV-Vis (left, panels A and B) and EPR (right, panels C and D) spectra of Cu(II)TMPA complexes obtained from $Cu(OTf)_2$ (A & C, light blue); $Cu(ClO_4)_2$ (A & C, dark blue); $Cu(OTf)_2$ + Na_2SO_3 (B & D, green); $Cu(OTf)_2$ + $Na_2S_2O_3$ (B & D, orange); $Cu(SO_4)$•$5H_2O$ (B & D, purple), $Cu(NO_3)_2$ (A & C, grey) in THF/H_2O 80/20 v/v and $Cu(OTf)_2$ (A & C, black) or $Cu(SO_4)$ (D, black) in pure water as a control. Conditions

*for UV-Vis: [TMPA] = 0.22 mM; [Cu(II)] = 0.2 mM; ℓ = 1 cm; T = 25 °C. Conditions for EPR: [TMPA] = 0.22 mM; [Cu(II)] = 0.2 mM; T = 120 K; microwave power: 5 mW. * corresponds to a minor contaminating species.*

The UV-Vis and EPR spectra of the Cu(II)TMPA complexes in THF/H_2O 80/20 v/v formed from four Cu(II) salts and the addition of two inorganic salts are given Figure III.B-6 and the corresponding UV-Vis and EPR parameters are listed in Table III.B-3.

In presence of SO_3^{2-}, $S_2O_3^{2-}$ and SO_4^{2-} a LMCT band is clearly observed at 438 nm (ε = 7700 $M^{-1}cm^{-1}$), 408 nm (ε = 5800 $M^{-1}cm^{-1}$) and 296 nm (ε = 2500 $M^{-1}cm^{-1}$), respectively mirroring their coordination to the Cu(II) center (Figure III.B-6, panel B and Table III.B-3). Small LMCT shoulders are also seen for the other complexes (Figure III.B-6, zoom in panel A). In the d-d transition region, the profile is similar for all the complexes expect for [CuTMPA(SO_3)], [CuTMPA(S_2O_3)] and [CuTMPA(SO_4)]. The complex [CuTMPA(SO_3)], shows two d-d transitions at low wavelengths: 561 nm ((ε = 560 $M^{-1}cm^{-1}$) and 726 nm (ε = 295 $M^{-1}cm^{-1}$). [CuTMPA(S_2O_3)] displays one d-d transition at low wavelength (668 nm (ε = 145 $M^{-1}cm^{-1}$)) and the other one at high wavelength (947 nm (ε = 200 $M^{-1}cm^{-1}$)). The high separation between the two bands allow to better see the former that usually appears as a shoulder. [CuTMPA(SO_4)] shows three weaker d-d transitions at 704 nm (ε = 94 $M^{-1}cm^{-1}$), 890 nm (ε = 205 $M^{-1}cm^{-1}$) and 970 nm (ε = 210 $M^{-1}cm^{-1}$). For the other species (Figure III.B-6, Panel A) several d-d are coalesced with a maximum at 870 nm (ε from 225 to 265 $M^{-1}cm^{-1}$). The signatures are very close to the one recorded in water only (thus with a water as a fifth ligand). This indicates that in a 80/20 (THF/H_2O) mixture, the SO_3^{2-}, $S_2O_3^{2-}$ and SO_4^{2-} stay bound to the Cu(II) center while the fifth coordination position is mainly occupied by a water molecule for the other cases. In EPR, the signatures observed are all characteristic of a TBP geometry (as described in the previous paragraph) and no significant changes are observed in presence of ClO_4^-, TfO^- and PF_6^- compared to the spectrum in pure water (Figure III.B-6, Panel C – $g_\perp$ = 2.20; $A_\perp = 109.10^4$ cm^{-1}: $g_{//} = 2.00$; $A// = 60.10^4$ cm^{-1}). A weak change is detected in presence of NO_3^- ($g_\perp = 2.21$; $A_\perp = 108.10^4$ cm^{-1}: $g_{//} = 2.00$; $A// = 63.10^4$ cm^{-1}) while in presence of SO_3^{2-} or $S_2O_3^{2-}$ a fully different signature is observed. Hence the EPR data are in full agreement with the conclusions drawn from the UV-Vis signatures.

In order to displace the equilibrium toward the coordination of ClO_4^-, TfO^- and NO_3^- ions as seen in the solid-state, Cu(II)TMPA complexes from $Cu(OTf)_2$, $Cu(ClO_4)_2$•$6H_2O$, and $Cu(NO_3)_2$•$2.5H_2O$ were also characterized in THF/H_2O 98/2 as presented in Figure III.B-7. It

was not possible to compare with SO_4^{2-}, SO_3^{2-} and $S_2O_3^{2-}$ in the same conditions for solubility issue.

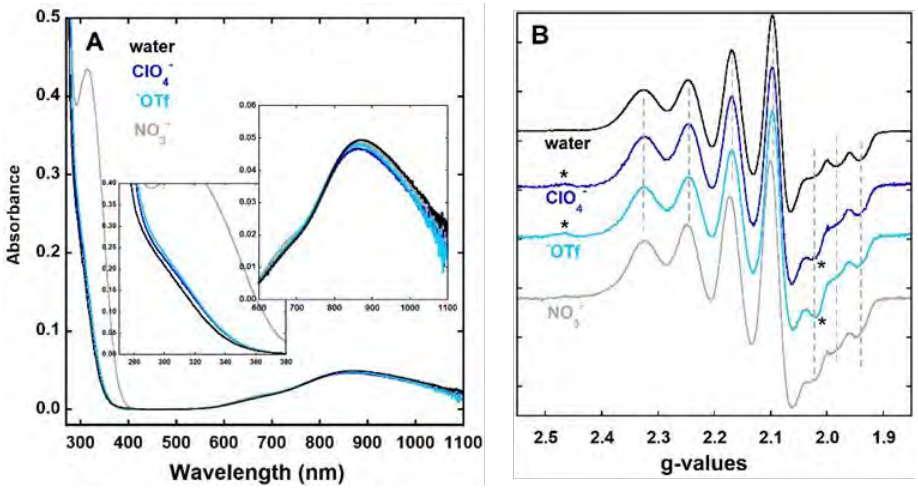

*Figure III.B-7: UV-Vis (panel A) and EPR (panel B) spectra of Cu(II)TMPA from different Cu(II) salts: $Cu(OTf)_2$ (light blue); $Cu(ClO_4)_2$ (dark blue) and $Cu(NO_3)_2$ (grey) in THF/H_2O 98/2 v/v. Conditions for UV-Vis: [TMPA] = 0.22 mM; [Cu(II)] = 0.2 mM; ℓ = 1 cm; T = 25 °C. Conditions for EPR: [TMPA] = 0.22 mM; [Cu(II)] = 0.2 mM; T = 120 K; microwave power: 5 mW. * corresponds to a minor contaminating species.*

The use of the THF/H_2O 98/2 ratio of solvent makes possible to observe the coordination of NO_3^- with a LMCT band detected at 314 nm (ε = 2170 $M^{-1}cm^{-1}$). The UV-Vis signatures for Cu(II)TMPA complexes formed from $Cu(OTf)_2$ or $Cu(ClO_4)_2$•$6H_2O$ are virtually the same than the one recorded in pure water indicating that neither ClO_4^- nor TfO^- are able to replace the aqua ligand in such a solvent mixture. In EPR, a similar trend is observed with the spectra recorded in presence of ClO_4^-, or TfO^- similar to the one in water while as anticipated from data in 80 /20 (THF/H_2O), the EPR spectrum in presence of NO_3^- is slightly different in line with the binding of NO_3^- detected by UV-Vis.

Table III.B-3: Physico-chemical parameters of Cu(II)TMPA(H_2O) and Cu(II)TMPA(NO_3) in THF/H_2O 98/2 v/v and Cu(II)TMPA(SO_4), Cu(II)TMPA(SO_3) and Cu(II)TMPA(S_2O_3) in THF/H2O 80/20 v/v.(The atom coordinated is indicated in brackets).

5th ligand	λ_{LMCT} (nm) (ε ($M^{-1}cm^{-1}$))	λ_{dd1} (nm) (ε ($M^{-1}cm^{-1}$))	λ_{dd2} (nm) (ε ($M^{-1}cm^{-1}$))	λ_{dd3} (nm) (ε ($M^{-1}cm^{-1}$))	$g_\perp$	$A_\perp$ (10^{-4} cm^{-1})	$g_{//}$	$A_{//}$ (10^{-4} cm^{-1})
H_2O (O)	300 (1200 ± 60)	660 (73 ± 4)	860 (240 ± 12)	-	2.20	109	2.00	60
NO_3^- (O)	314 (2170 ± 110)	680 (94 ± 5)	870 (240 ± 12)	-	2.21	108	2.00	63
SO_4^{2-} (O)	296 (2500 ± 130)	704 (94 ± 5)	890 (205 ±10)	970 (210 ± 10)	2.21	108	-	-
SO_3^{2-} (S)	438 (7700 ± 390)	561 (560 ± 30)	726 (295 ± 15)	-	2.14	80	2.00	90
$S_2O_3^{2-}$ (S)	408 (5800 ± 300)	668 (145 ± 7)	947 (200 ± 10)	-	2.18	103	2.00	69

Concluding remark

The solid-state characterization gives strong proof of the coordination mode, and geometry. However, it is not always the same case in solution. Indeed all the complexes were attributed to TBP or distorted TBP geometry in solution and solid-sate, except [CuTMPA(S_2O_3)] that has a geometry SPy distorted toward TBP in solid-state and TBP geometry in solution. This is due to weak interaction of oxygen from S_2O_3 taking the place of a hexa-ligand and thus inducing a strong distortion and a participation of $d_{x^2-y^2}$ to the ground state. Furthermore a crystal suitable for X-ray diffraction analysis was obtained with ClO_4^- as fifth ligand but it was not characterized in solution. The coordination in solution of an anion is usually characterized by a strong LMCT band as long as the polarity of the solvent allow to see it out of the TMPA ligand internal transition band (< 300 nm).

Although the crystal structure of all the Cu(II)TMPA complexes characterized earlier were attributed to a geometry TBP except the with $S_2O_3^{2-}$ as additional ligand, the geometry seems to be more or less distorted in solution. Cu(II)TMPA(SO_3) and Cu(II)(TMPA)(S_2O_3) have particularly much different d-d transition bands. The particularity of those two compounds compared to the others is to be coordinated through an S atom instead of N or O atoms, which is bigger. In the case, of Cu(II)TMPA(SO_3) there is probably a destabilization of the d_{z^2} orbital as the d-d transitions are at lower wavelengths. Whereas for Cu(II)TMPA(S_2O_3) the interaction of the O-atom with the Cu center as seen in the structure would distorted the TBP geometry toward SPy and destabilized the $d_{x^2-y^2}$ thus slightly participating to the ground state, as seen by the shift of the d-d transition band toward higher wavelength and the increased intensity of the d-d shoulder. The other anion NO_3^- and SO_4^{2-} are coordinated through their O atom, thus the geometry is closer to the one of Cu(II)TMPA(H_2O) with low distortion of the TBP geometry in solution.

III.B.3. UV-Vis and EPR characterizations in CH_3CN/H_2O mixtures

In the following studies, CH_3CN will be the organic co-solvent of choice because it allows the solubilization of CO up to 100 mM (CO solubility is 10 mM in THF and 1 mM in H_2O)[49-51] which is needed if one aims at detecting Cu(I)-CO adduct in concentrations high enough for spectroscopy (here, in the mM range). The starting Cu(II) salts used are $Cu(OTf)_2$ (TfO^- being considered as non-coordinating based on previous studies) or $Cu(SO_4)$ (coordinating but the "most" classical Cu(II) salt, with which I had started my experiments).

III.B.3.a. $Cu(SO_4)$ as starting salt

The impact of adding CH_3CN as a co-solvent to H_2O was studied by UV-Vis and EPR spectroscopies on Cu(II)TMPA with the EPR and UV-Vis parameters listed in Table III.B-4. Figure III.B-8 displays the UV-Vis and EPR spectra of Cu(II)TMPA complexes generated *in situ* in several ratios of CH_3CN/H_2O from $Cu(SO_4)$. For amounts of CH_3CN higher than 90% in the mixture, a LMCT band is observed at 330 nm (ε = 2500 $M^{-1}.cm^{-1}$) at a ratio of 99.8/0.2 v/v and 303 nm (ε = 2520 $M^{-1}.cm^{-1}$) at 90/10 v/v. These bands are attributed to the binding of SO_4^{2-} anion to the Cu(II) center and are strongly reminiscent of the LMCT band previously observed in THF/H_2O mixture. It is worth noting that the band position is shifted with the increasing polarity of the solvent mixture. For amounts of CH_3CN lesser than 90%, the band decreases mirroring the replacement of the SO_4^{2-} ion by water for the fifth Cu(II) coordination position. In the d-d transition region, the signatures are different with two main features: (i) a shoulder present at 730 nm (ε = 110 $M^{-1}.cm^{-1}$) for ratio $CH_3CN/H_2O \geq 90/10$ and (ii) a constant shift toward higher wavelengths when increasing the proportions of CH_3CN (from 870 to 920 nm) accompanied by a decrease in the epsilon values (245 to 200 $M^{-1}cm^{-1}$). In EPR, similar modifications are observed: in a 2/98 CH_3CN/H_2O mixture it is possible to isolate the signature of Cu(II)TMPA(SO_4), at 90/10 the signal is different in line with the UV-Vis indicating that the EPR is also sensitive to change in the polarity of the solvent, and at higher ratio, the signature is similar to the one in pure water.

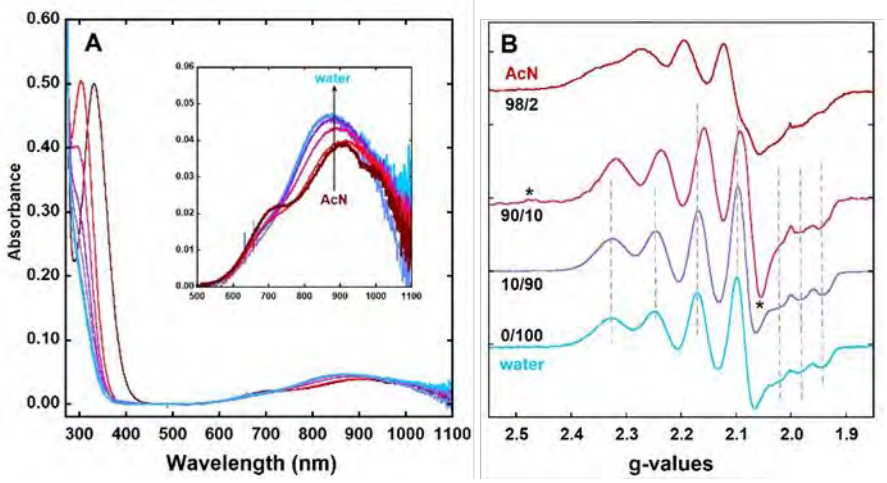

*Figure III.B-8: UV-Vis spectra of $[CuTMPA(SO_4)]$ to $[CuTMPA(H_2O)]^{2+}$ in CH_3CN/H_2O 99.8/0.2 to 0/100 v/v under ambient atmosphere. Conditions: [TMPA] = 0.22 mM; $[Cu(SO_4)•5H_2O]$ = 0.2 mM; ℓ = 1 cm; T = 25 °C. Conditions for EPR: [TMPA] = 0.55 mM; [Cu(II)] = 0.5 mM; T = 120 K; microwave power: 5 mW. * corresponds to a minor contaminating species.*

III.B.3.b. $Cu(OTf)_2$ as starting salt

The UV-Vis and EPR data of Cu(II)TMPA complexes obtained from $Cu(OTf)_2$ in various CH_3CN/H_2O mixtures are shown in Figure III.B-9 and corresponding parameters listed in Table III.B-4. From 10% of H_2O in the mixture, the UV-Vis signature is the same as Cu(II)TMPA(H_2O) with a small LMCT shoulder around 297 nm (ε = 1100 $M^{-1}cm^{-1}$), a d-d shoulder around 690 nm (85 $M^{-1}cm^{-1}$) and d-d band at 870 nm (ε = 240 $M^{-1}cm^{-1}$) (Table III.B-4). This result is in agreement with the literature in H_2O/MeOH/EtOH with a d-d transition band at 870 nm (ε = 213 $M^{-1}cm^{-1}$) (Table III.B-2).[17]

In CH_3CN > 90%, the signature is different and could mirror either the binding of CH_3CN or of TfO^- as the fifth ligand, but TfO^- is a weak coordinating anion compared to CH_3CN molecule, thus the latter is more prone to be coordinated. In the literature, the UV-Vis signature of Cu(II)TMPA(CH_3CN) is defined by d-d transitions at 630 nm (shoulder) and 889 nm (ε = 238 $M^{-1}cm^{-1}$) (Table III.B-2) which is not in agreement with ours, defined with a LMCT shoulder around 314 nm (ε = 1480 $M^{-1}cm^{-1}$), a d-d shoulder around 650 nm (ε = 50 $M^{-1}cm^{-1}$) and a d-d band at 858 nm (ε = 225 $M^{-1}cm^{-1}$) (Table III.B-4). The d-d are usually large so the exact maximum absorption wavelength is not always precise. The differences observed for the UV-Vis signatures in CH_3CN with data from literature could be due to the amount of water present in the CH_3CN solvent. However, the EPR parameters are close to the ones in literature

(literature: $g_\perp$ = 2.19, $A_\perp$ = 115.10^{-4} cm^{-1} , g// = 2.01 and A// = 61.10^{-4} cm^{-1}; this study : $g_\perp$ = 2.19, $A_\perp$ = 112.10^{-4} cm^{-1} , g// = 2.00 and A// = 53.10^{-4} cm^{-1}) (Table III.B-1 and Table III.B-4).[28]

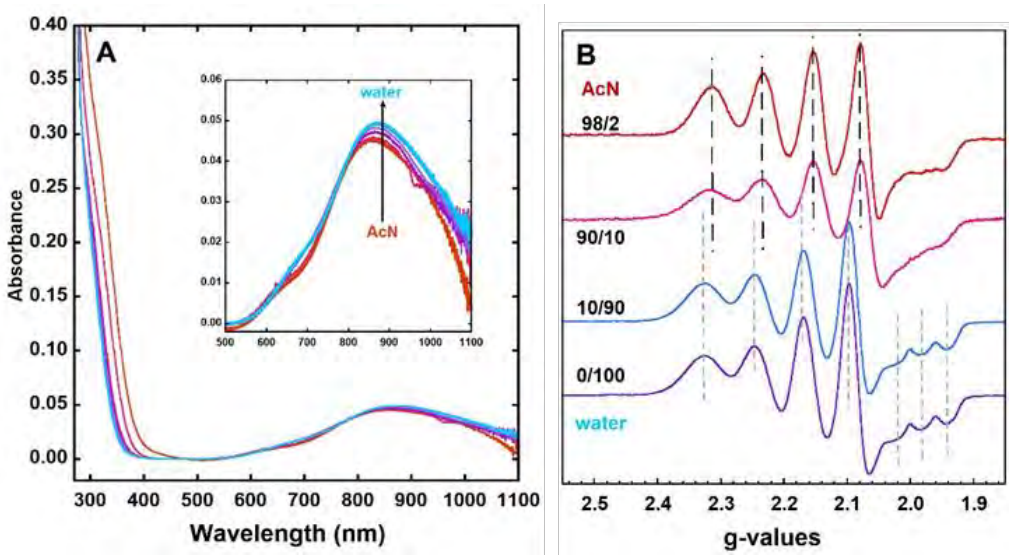

Figure III.B-9: UV-Vis spectra of $[CuTMPA(CH_3CN)]^{2+}$ to $[CuTMPA(H_2O)]^{2+}$ in CH_3CN/H_2O 100dry/0 to 0/100 v/v under ambient atmosphere. Conditions: [TMPA] = 0.22 mM; $[Cu(OTf)_2]$ = 0.2 mM; ℓ = 1 cm; T = 25°C - Conditions for EPR: [TMPA] = 0.55 mM; [Cu(II)] = 0.5 mM; T = 120 K;10 % (in volume) glycerol was added at 10/90 and 0/100; microwave power: 5 mW. corresponds to a minor contaminating species*

In EPR, the signature in CH_3CN/H_2O (98/2) is significantly different than the one obtained in water and the one obtained with $Cu(SO_4)$ salt (see also Table III.B-4). Increasing the amount of water to 10% leads to a broadening of the first hyperfine features but their position remains the same. In 10/90 CH_3CN/H_2O, the spectrum equals that of Cu(II)TMPA(H_2O).

Table III.B-4: Physico-chemical parameters of Cu(II)TMPA complexes from $Cu(SO_4)$ or $Cu(OTf)_2$ salts in different ratios of CH_3CN/H_2O v/v.

CH_3CN/H_2O ratio v/v	Cu(II) salt	λ_{LMCT} (nm) (ε ($M^{-1}cm^{-1}$))	λ_{dd1} (nm) (ε ($M^{-1}cm^{-1}$))	λ_{dd2} (nm) (ε ($M^{-1}cm^{-1}$))	$g_\perp$	$A_\perp$ (10^{-4} cm^{-1})	$g_{//}$	$A_{//}$ (10^{-4} cm^{-1})
98/2	$Cu(SO_4)$	330 (2500 ± 130)	730 (110 ± 6)	920 (200 ± 10)	2.23	107	-	-
	$Cu(OTf)_2$	309 (1210 ± 60)	650 (56 ± 3)	860 (230 ± 12)	2.19	112	2.00	53
90/10	$Cu(SO_4)$	303 (2520 ±130)	690 (84 ± 4)	910 (200 ± 10)	2.20	109	-	-
	$Cu(OTf)_2$	300 (1180 ± 60)	690 (88 ± 4)	865 (235 ± 12)	2.19	115	-	-
10/90	$Cu(SO_4)$	297 (1140 ± 60)	690 (89 ± 4)	870 (235 ± 12)	2.20	108	2.00	66
	$Cu(OTf)_2$	297 (1140 ± 60)	690 (87 ± 4)	870 (245 ±12)	2.20	112	2.00	65
0/100	$Cu(SO_4)$	296 (1080 ± 50)	690 (83 ± 5)	870 (235 ± 12)	2.20	110	2.00	64
	$Cu(OTf)_2$	297 (1110 ± 60)	690 (89 ± 4)	870 (245 ±12)	2.20	110	2.00	66

Concluding remarks.

In general, the coordination of an anion to Cu(II)TMPA is due to its low solubility in the solvent system of study, otherwise it is usually a solvent molecule coordinated in the fifth labile position. The increasing polarity of the solvent induces blue shift of the LMCT band.

Altogether these data show, once again, how versatile is the ligand binding to the fifth position of Cu(II)TMPA as a function of the working conditions (counter-ion, solvent). This will be even more obvious in the next paragraph where the impact of HEPES buffer on Cu(II)TMPA coordination environment is investigated.

III.B.4. UV-Vis, EPR and electrochemical characterizations in CH_3CN/Buffer mixtures

III.B.4.a. UV-Vis and EPR

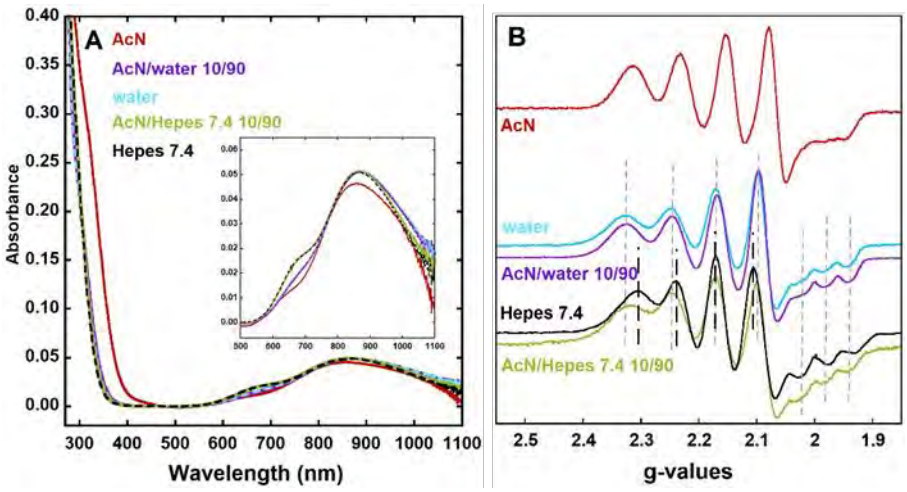

Figure III.B-10: UV-Vis and EPR spectra of Cu(II)TMPA in CH_3CN/H_2O and CH_3CN/HEPES pH 7.4 100 mM 100/0, 10/90 and 0/100 v/v under ambient atmosphere. Conditions: [TMPA] = 0.22 mM; $[Cu(OTf)_2]$ = 0.2 mM; ℓ = 1 cm; T = 25°C - Conditions for EPR: [TMPA] = 0.55 mM; $[Cu(OTf)_2]$ = 0.5 mM; T = 120 K;10 % (in volume) glycerol was added at 10/90 and 0/100; microwave power: 5 mW. corresponds to a minor contaminating species*

In this part, we will only show data obtained with $Cu(OTf)_2$ as a starting salt, as we are interested in the difference between water and HEPES buffer (4-(2-hydroxyethyl)-1-piperazineethanesulfonic acid) (Scheme III.B-1), and for $CH_3CN \leq 10\%$, the data are the very same regardless on the starting salt ($Cu(OTf)_2$ or $Cu(SO_4)$).

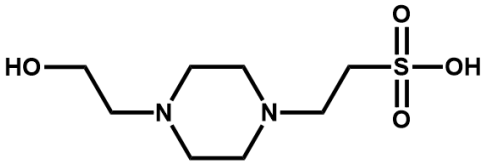

Scheme III.B-1: HEPES (4-(2-hydroxyethyl)-1-piperazineethanesulfonic acid).

The characterizations performed in CH_3CN/HEPES mixture make it possible to get an "apparent" pH values. In Figure III.B-10, the UV-Vis and EPR signatures of the Cu(II)TMPA complexes in CH_3CN, CH_3CN/H_2O or CH_3CN/HEPES are compared to check for the impact of HEPES on Cu(II) coordination inside the TMPA cavity. While the addition of 10% of CH_3CN has no impact in UV-Vis (the spectra in pure aqueous media or in presence of 10%

CH_3CN are virtually identical, compare plain versus dotted line in Figure III.B-10) and only a broadening effect on the hyperfine lines in EPR (compare blue versus purple and black versus green lines). The UV-Vis and EPR fingerprints, more specifically the d-d region and the low field hyperfine lines are modified when water is replaced by HEPES. This effect was unexpected and may mirror the binding of HEPES buffer at the fifth position of the Cu(II)TMPA complex. This will be further studied by varying the nature of the buffer (although HEPES is already considered as "a low-binding buffer") and by a pH-dependent study.

Table III.B-5: Physico-chemical parameters of Cu(II)TMPA complexes in CH_3CN, H_2O, CH_3CN/H_2O 10/90 v/v, HEPES pH 7.4 and CH_3CN/HEPES pH 7.4 10/90 v/v.

Solvent	λ_{LMCT} (nm) (ε ($M^{-1}cm^{-1}$))	λ_{dd1} (nm) (ε ($M^{-1}cm^{-1}$))	λ_{dd2} (nm) (ε ($M^{-1}cm^{-1}$))	$g_\perp$	$A_\perp$ (10^{-4} cm^{-1})	$g_{//}$	$A_{//}$ (10^{-4} cm^{-1})
CH_3CN (AcN)	314 (1480 ± 80)	650 (50 ± 3)	858 (225 ± 11)	2.19	112	2.00	63
H_2O (water)	297 (1110 ± 60)	690 (89 ± 4)	870 (245 ±12)	2.20	110	2.00	66
CH_3CN/H_2O 10/90	297 (1140 ± 60)	690 (87 ± 4)	870 (245 ±12)	2.20	112	2.00	65
HEPES pH 7.4	290 (1550 ± 80)	678 (104 ± 5)	870 (245 ± 12)	2.20	98	2.00	79
CH_3CN/HEPES pH7.4 10/90	290 (1550 ± 80)	678 (103 ± 5)	870 (245 ± 12)	2.20	101	2.00	62

III.B.4.b. Cyclic voltammetry

In addition to UV-Vis and EPR characterizations, the Cu(II)TMPA(H_2O) complex was characterized by cyclic voltammetry. Its cyclic voltammograms (CV) in HEPES, CH_3CN/ HEPES 10/90 and CH_3CN are shown in Figure III.B-11. The three CVs are very similar except for their $E_{1/2}$ values, showing quasi-reversible process (H_2O: $E_{1/2}$ = -0.46 V vs SCE and ΔE = 0.06 V; CH_3CN/H_2O 10/90: $E_{1/2}$ = -0.36 V vs SCE and ΔE = 0.06 V; CH_3CN: $E_{1/2}$ = 0.01 V vs SCE and ΔE = 0.07 V) (Table III.B-6). The change in the $E_{1/2}$ values indicate a stronger stabilization of Cu(I)TMPA in CH_3CN and of Cu(II)TMPA in aqueous solvent.

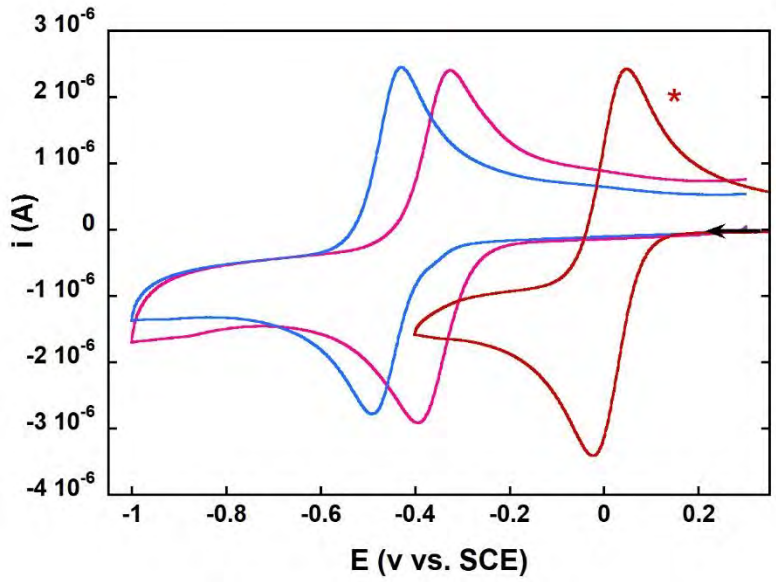

*Figure III.B-11: Cyclic voltammograms of Cu(II)TMPA in HEPES pH 7.4 (blue), with 10 % CH_3CN (pink) and in CH_3CN (red). Conditions: [HEPES pH 7.4] = 100 mM; [TMPA] = 0.75 mM; [$Cu(OTf)_2$] = 0.5 mM; WE = Glassy carbon; Ref = SCE; CE = Pt wire, scan rate: 100 mV/s. First scans are shown starting from 0.3 V indicated by the arrow. *: different concentration (0.3 mM in Cu(II)TMPA)*

As shown in Figure III.B-12 and Figure III.B-13, the cathodic and anodic intensities are linear with the square-root of the scan rate in aqueous and CH_3CN solutions respectively, indicating diffusion controlled processes. In mixture of solvents, the process remains reversible with $E_{1/2}$ being in-between $E_{1/2}$ values in pure organic and aqueous solvent. Since we have previously shown that water stays bound to Cu(II)TMPA in presence of 10% CH_3CN, this mirrors either that (i) water stays bound to the Cu(I) state, the potential being sensitive to the polarity of the solvent or (ii) CH_3CN replaces water in the Cu(I) state and the $E_{1/2}$ is shifted by a ECEC mechanism as shown Scheme III.B-2.

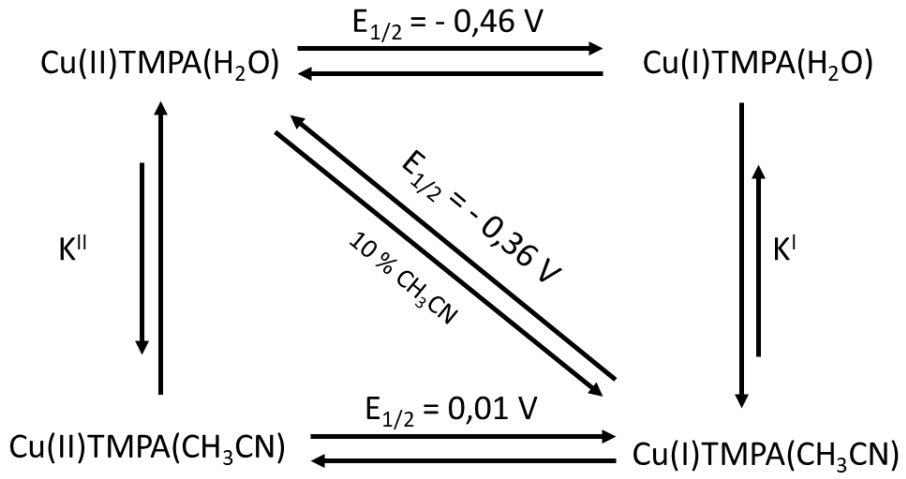

Scheme III.B-2: Electrochemical-Chemical-Electrochemical-Chemical mechanism for the electron transfer process of Cu(II)TMPA in H_2O and CH_3CN.

The symmetry of the redox wave is higher in pure CH_3CN, in line with Cu(I) and Cu(II) state in the very same geometry requiring a weak reorganization energy. In water, it is less symmetrical with increasing the scan rate, which may indicate that the Cu(I) complex electro-generated lies in a different environment (decoordination of one pyridyl-arm or removal of the fifth water solvent in fast equilibrium).

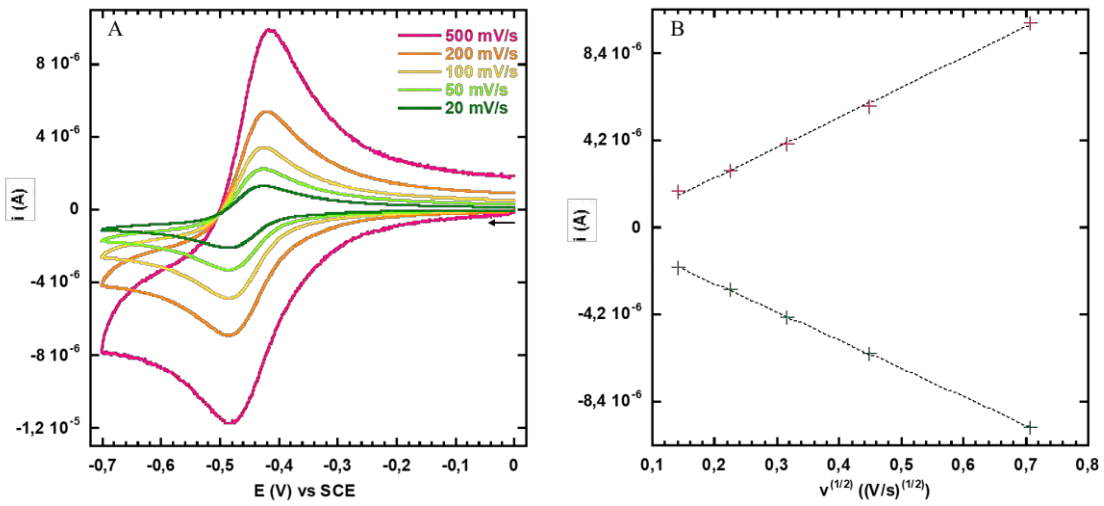

Figure III.B-12: (A) Cyclic voltammograms of aqueous solution of Cu(II)TMPA under Ar atmosphere at different scan rates between 500 and 20 mV/s. (B) Plot of the peak oxidative and reductive currents as a function of $v^{1/2}$. Conditions: [KPB pH 7] = 100 mM; [TMPA] = 0.45 mM; [$Cu(SO_4)•5H_2O$] = 0.3 mM; WE = Glassy carbon; Ref = SCE; CE = Pt wire. First scans are shown starting from 0 V indicated by the arrow.

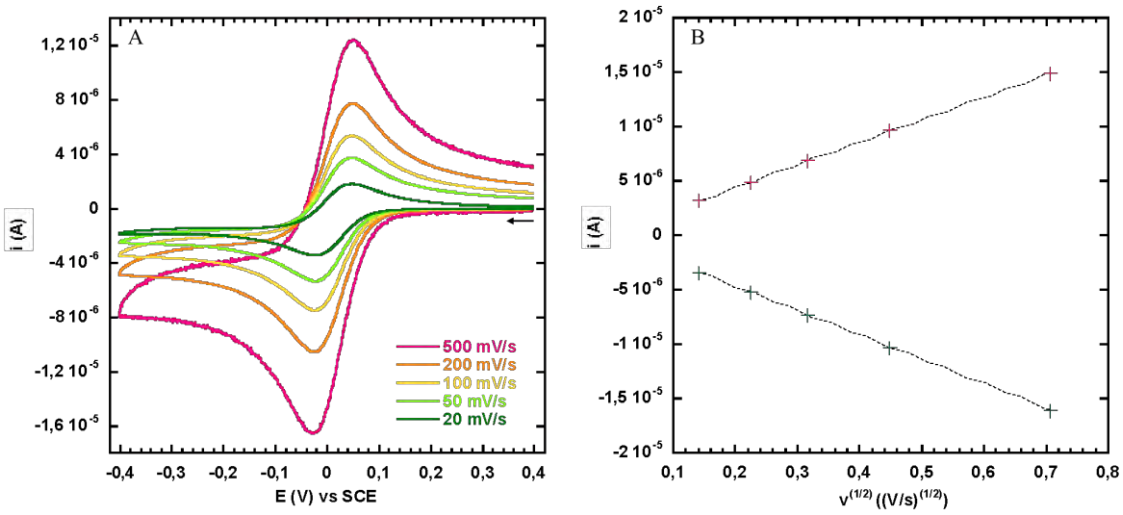

Figure III.B-13: (A) Cyclic voltammograms of Cu(II)TMPA in CH_3CN dry under Ar atmosphere at different scan rates between 500 and 20 mV/s. (B) Plot of the peak oxidative and reductive currents as a function of $v^{1/2}$.Conditions: [$TBAPF_6$] = 100 mM; [TMPA] = 0.45 mM; [$Cu(OTf)_2$] = 0.3 mM; WE = Glassy carbon; Ref = $Ag/AgNO_3$; CE = Pt wire. First scans are shown starting from 0.4 V vs SCE indicated by the arrow. Converted vs SCE.

Table III.B-6: Cyclic voltammetry parameters for Cu-TMPA in CH_3CN/HEPES pH 7.4 100/0, 10/90 and 0/100 and 10/90 under Ar. Values given in V vs SCE.

CH_3CN/HEPES pH 7.4 ratio v/v	E_{pc} (V)	E_{pa} (V)	ΔE (V)	$E_{1/2}$ (V)
100/0	-0.02	0.04	0.07	0.01
10/90	-0.39	-0.33	0.06	-0.36
0/100	-0.49	-0.43	0.06	-0.46

These first studies show that, due to the high versatility of the fifth Cu(II) site in Cu-TMPA complex, the speciation of Cu-TMPA is strongly dependent and sensitive to the medium in which the complex is solubilized and that while the signatures are similar they show weak but meaningful differences, mainly on LMCT and on the first d-d shoulder in UV-Vis and on the low-field hyperfine transition in EPR. In CV, the presence of equilibria is also observed that will be confirmed by scan rate (at higher than 500 mV/s) and temperature studies. In addition, a side-effect, *id est* the anisotropic line broadening of the low-field hyperfine lines, was detected in EPR. The effect is so strong that it distorts the EPR signature. Further studies at higher frequencies, in solid-state (in Zn-diamagnetic matrix) and spectra simulation are planned to get rid out as much as possible of this strain effect.

III.B.5. pH-dependent speciation of Cu(II)TMPA

The speciation of Cu(II)TMPA complex in a mixture of solvent CH_3CN/HEPES 100 mM 50/50 v/v (or 10/90) was followed by UV-Vis, EPR and electrochemistry.

III.B.5.a. UV-Vis

To deeper characterize the Cu(II)TMPA complex, a pH-dependent study was performed from pH 6.4 to pH 1.0 and from pH 6.4 to pH 13.0. The results are presented in Figure III.B-14. In the CH_3CN/HEPES 100 mM 50/50 v/v (chosen in agreement with the study reported in JIB – Annex chapter)[5], the UV-Vis signature of Cu-TMPA in such mixture is in-between that of in HEPES and CH_3CN (Figure III.B-14). When decreasing the pH, the d-d band is progressively shifted towards higher wavelengths (from 870 nm (pH 6.4) to 910 nm (pH 1.0)) while a shoulder appears at 950 nm along with the LMCT band increases. It is worth noting that even at pH 1.0 the signal corresponds to a TMPA-bound Cu(II) but in a different form that at neutral pH. The pH transition between the Cu(II)TMPA and this new complex is at about pH 4 (estimated from the appearance of the shoulder at 950 nm), while the new complex may be a Cu(II) bound to tridentate TMPA where one of the pyridine arm or the central tripodal amine is decoordinated, due to protonation (Scheme III.B-3 up). In the basic titration, from pH 8.1, a shoulder clearly appears and grows in the d-d region around 680 nm and the intensity of the d-d band also increases. On the LMCT region, an isosbestic point is observed at 301 nm, while the band decreases at 320 nm. All those observations are in line with the deprotonation of the H_2O fifth ligand leading to a hydroxo exogenous ligand (Scheme III.B-3 down). From calculations on the d-d shoulder at 680 nm, the pKa of the water deprotonation is about 9.5.

This preliminar pH dependent study shows (i) the robustness of the Cu(II)TMPA scaffold that is retained down to pH 1.0 and (ii) the formation of an hydroxo-Cu(II)TMPA species. The speciation in pure water and in buffer are planned to avoid interference with CH_3CN binding and to determine the “real” pKa of Cu(TMPA)-bound water deprotonation, to confirm the possible intervention of HEPES as a fifth ligand on Cu(II)TMPA deduced from previous study (Figure III.B-10). This could be for instance deduced for a change in the pKa values of the water deprotonation process (that would appear at higher pH values if HEPES is bound).

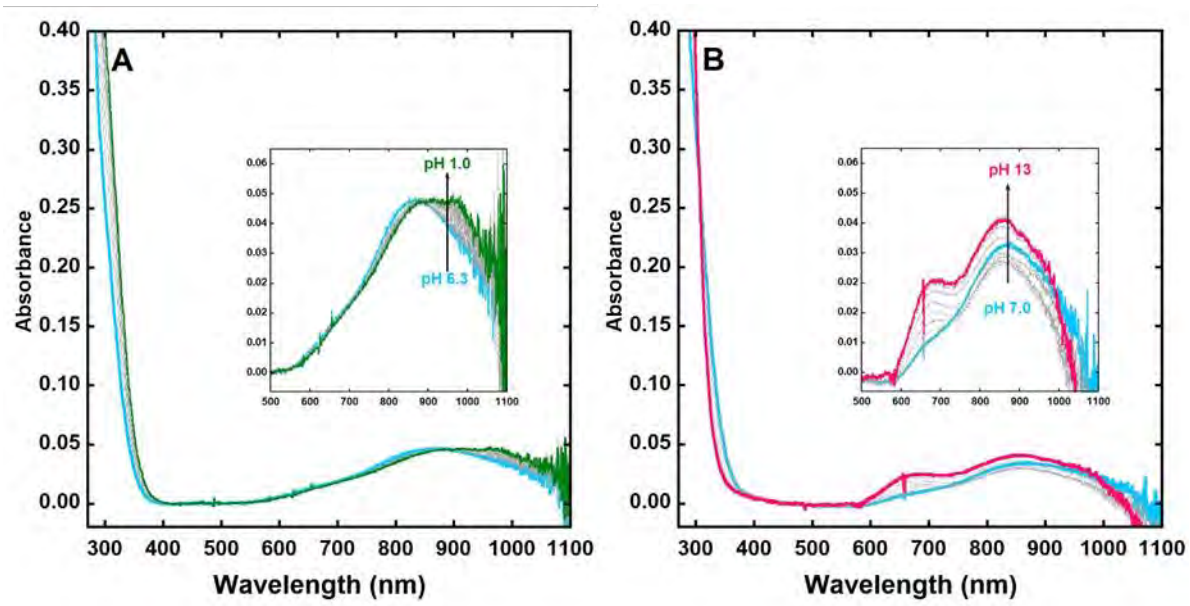

Figure III.B-14: UV-Vis spectra of $[CuTMPA(H_2O)]^{2+}$ in CH_3CN/HEPES 100 mM 50/50 v/v from pH 6.3 to pH 1.0 (panel A) and from pH 6.3 to pH 13 (panel B) under ambient atmosphere. Conditions: [TMPA] = 0.22 mM; $[Cu(II)SO_4•5H_2O]$ = 0.2 mM; addition of H_2SO_4 or NaOH solutions; ℓ = 1 cm; T = 25 °C.

III.B.5.b. EPR

For some selected pH values, the EPR spectra were also recorded (Figure III.B-15) CH_3CN/HEPES 50/50 (dotted line) and 10/90 mixture (plain line). At neutral pH, both EPR are close. Only broadening effects differ (higher in the 10 (CH_3CN) / 90 (HEPES) mixture). At basic pH, the EPR signature is new, independent of the solvent mixture used. It is still characteristic of TBP geometry. Hence the deprotonation of the water molecule to lead to Cu(II)TMPA(OH) doesn't change the overall geometry of the complex. The EPR parameters are different from those of the aqua likely counterpart mirroring the shortening of the HO—Cu(II) bond compared to Cu(II)-aqua bond. In addition, the hyperfine line-width are smaller indicating a weaker broadening in line with a better-defined structure of the hydroxo complex versus the aqua one, also in line with the independency on the solvent mixture. Last, it is also of note that the spectrum is highly reminiscent of the EPR spectra attributed to Cu(II)TMPA(OOH) as seen in Figure III.B-5 (panel B, blue line),[42] in line with the binding of an anionic O-based ligand (or to a wrong assignment of the spectra in ref. 42). The species was obtained by the reaction of Cu(II)TMPA with HO_2^- in acetone at 213 K.[42] When going to acidic pH values, in 10 (CH_3CN) / 90 (HEPES), the spectra evolves progressively to a new species (predominant at pH 3.0) that exhibits a more isotropic signature (spectrum width is smaller

compared to those of other pH values). At pH 1.5, the signature is reminiscent of the superimposition of unbound Cu(II) (marked by #) and of a Cu(II) in a "classical" axial geometry (marked by §). In 50 (CH_3CN) / 50 (HEPES), a signature also characteristic of a square planar geometry (SP) is observed, the position of its hyperfine lines (marked by *) being shifted to down-field compare to the species noted §. We tentatively proposed that the two SP species correspond to the decoordination of one pyridine arm due to its protonation. (Scheme III.B-3).

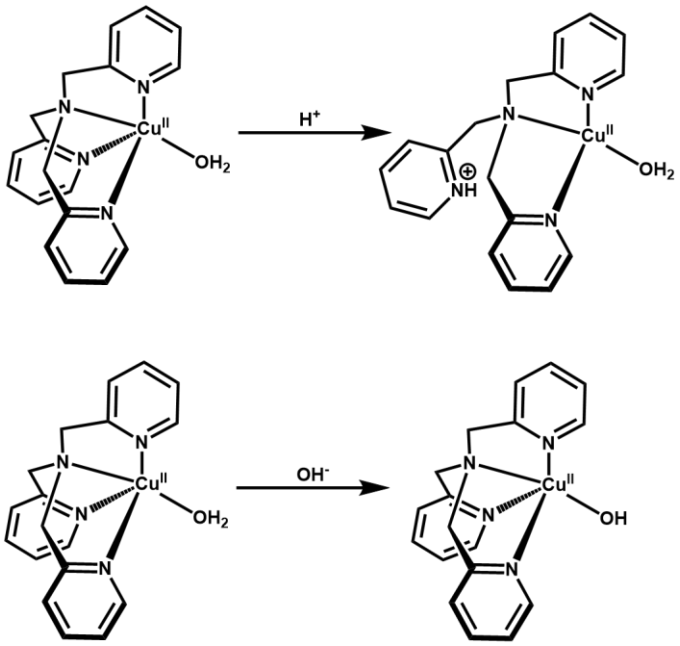

Scheme III.B-3: Up: Protonation of a pyridine ring at low pH inducing the decoordination of one-pyridyl-arm. Down: Deprotonation of the H_2O fifth ligand leading to hydroxo ligand.

It is worth noting that the first hyperfine line and the one at g ~ 2.0 (marked either by * or #) are reminiscent of the contaminant observed in several of the previous EPR spectra described above. Currently, we don't know why specific conditions induces its formation. Our working hypothesis is that the Cu-TMPA(H_2O) species could also exist in solution in a "classical" SP in equilibrium with the TBP geometry and that depending on the way of freezing the EPR tube, it is possible to grasp the SP species.

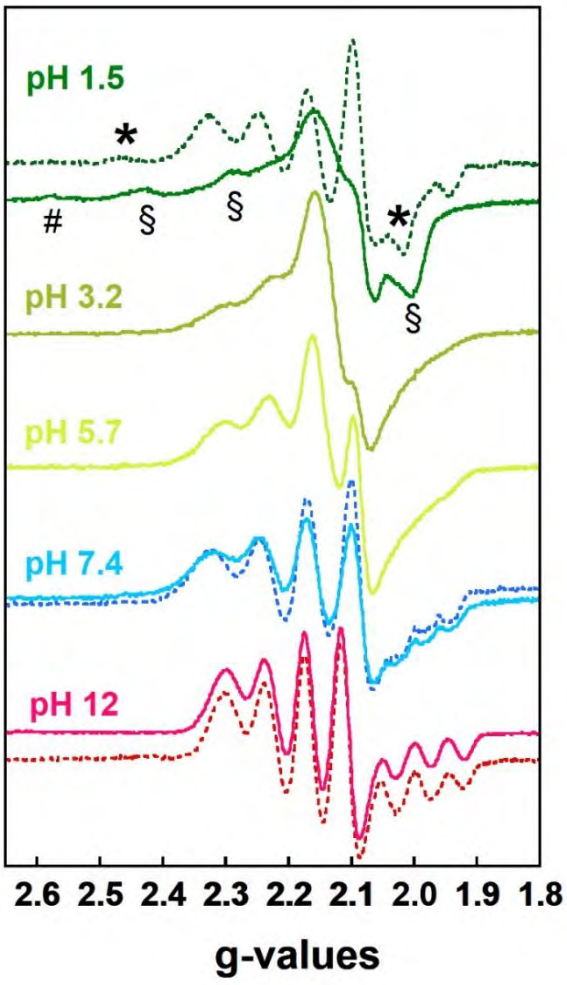

Figure III.B-15 :EPR spectra of Cu(II)TMPA at different pH in CH_3CN/HEPES 50/50 (dotted lines) and CH_3CN/HEPES 10/90 (solid lines). EPR: [TMPA] = 0.22 mM; [$Cu(OTf)_2$] = 0.2 mM; T = 120 K; glycerol = 10 % (in volume); microwave power: 5 mW.

Table III.B-7: Physico-chemical parameters of Cu(II)TMPA complexes in CH_3CN/HEPES pH 7.4 50/50 and 10/90 v/v, at different pH.

pH	CH_3CN/HEPES ratio	λ_{LMCT} (nm) (ε ($M^{-1}cm^{-1}$))	λ_{dd1} (nm) (ε ($M^{-1}cm^{-1}$))	λ_{dd2} (nm) (ε ($M^{-1}cm^{-1}$))	λ_{dd2} (nm) (ε ($M^{-1}cm^{-1}$))	$g_\perp$	$A_\perp$ (10^{-4} cm^{-1})	$g_{//}$	$A_{//}$ (10^{-4} cm^{-1})
1.5	**50/50**	300 (2000 ± 100)	680 (75 ± 4)	910 (250 ± 13)	950 (250 ± 13)	2.13	105	1.97	-2.20
	10/90	-	-	-	-	2.10	-	2.35	175
3.2	**50/50**	300 (1900 ± 100)	680 (75 ± 4)	910 (250 ± 13)	950 (250 ± 13)	-	-	-	-
	10/90	-	-	-	-	-	-	-	-
5.7	**50/50**	299 (1650 ± 80)	680 (75 ± 4)	885 (230 ± 12)	-	-	-	-	-
	10/90	-	-	-	-	2.20	102	-	-
7.4	**50/50**	297 (1900 ± 100)	680 (50 ± 3)	870 (155 ± 8)	-	2.20	106	2.00	69
	10/90	-	-	-	-	2.21	106	2.00	64
12	**50/50**	285 (3000 ± 150)	680 (125 ± 6)	855 (200 ± 10)	-	2.20	91	2.00	83
	10/90	-	-	-	-	2.20	91	2.00	89

III.B.5.c. Cyclic voltammetry

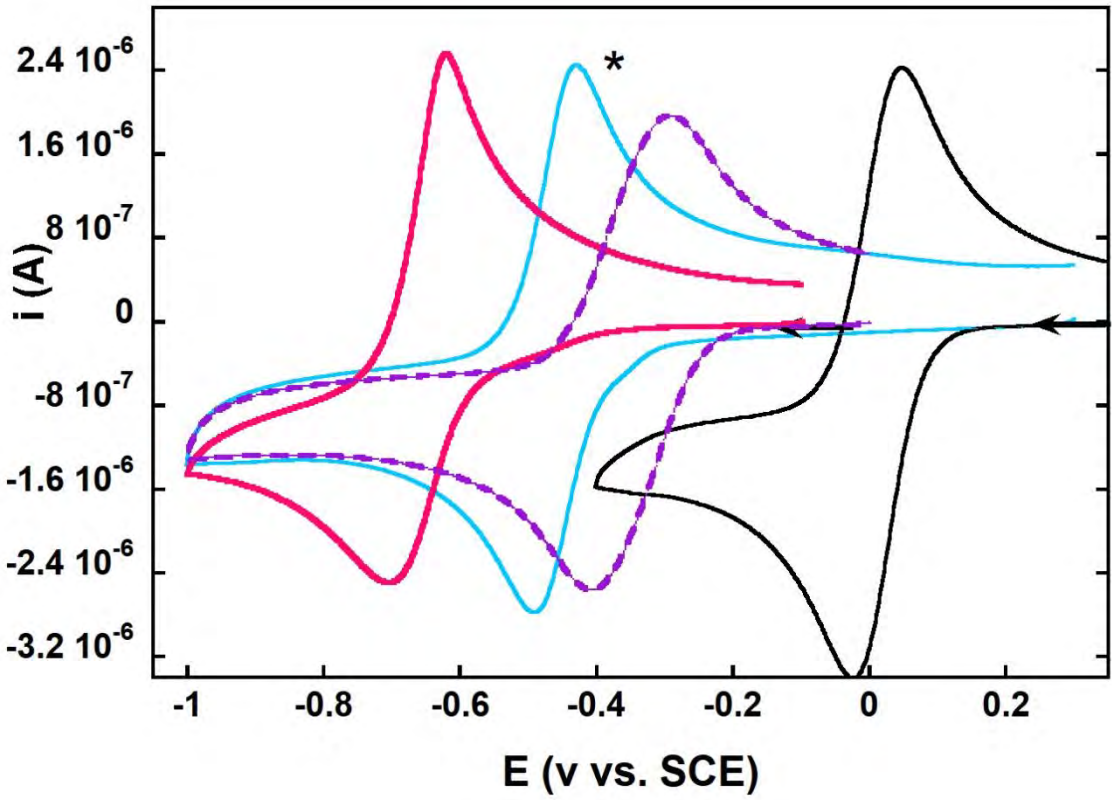

*Figure III.B-16: Cyclic voltammograms of $[Cu(II)TMPA(solvent)]^{2+}$ (dashed purple) and $[Cu(II)TMPA(OH)]^{+}$ (pink) in CH_3CN/HEPES 10/90 v/v, $[Cu(II)TMPA(H_2O)]^{2+}$ (blue) and $[Cu(II)TMPA(CH_3CN)]^{2+}$ (black). Conditions: [HEPES pH 7.4] = 100 mM; [TMPA] = 0.45 mM; $[Cu(OTf)_2]$ = 0.3 mM; WE = Glassy carbon; Ref = SCE; CE = Pt wire; scan rate: 100 mV/s. First scans are shown with the start indicated by the arrow. *: different concentration (0.2 mM in Cu(II)TMPA)*

The CV recorded at high pH to characterize the $[Cu(II)TMPA(OH)]^{+}$ species is shown in Figure III.B-16 and compared to $[Cu(II)TMPA(H_2O)]^{2+}$ in the same solvent mixture (pink and dashed purple line, respectively). The CV shows a reversible process centered at $E_{1/2}$ = -0.66 V vs SCE (ΔE = 0.08 V). As expected based on the decreasing of the overall charge on the complex the $E_{1/2}$ value is shifted towards cathodic potentials. The process is less reversible with an anodic peak on the reverse scan more intense than the cathodic peak. Once again, this may mirrored a ECEC mechanism where the hydroxo ligand is fastly replaced by CH_3CN or water after reduction to Cu(I) and, where HO^- replaces rapidly the CH_3CN or water-bound to Cu(I) after reoxidation to Cu(II) (Scheme III.B-4). A full study as a function of the scan rate and in pure aqueous media (to avoid interference of CH_3CN) is planned to better reveal this

mechanism. In addition, a pH-dependent study will be further performed to determine whether a proton-coupled electron transfer is at play.

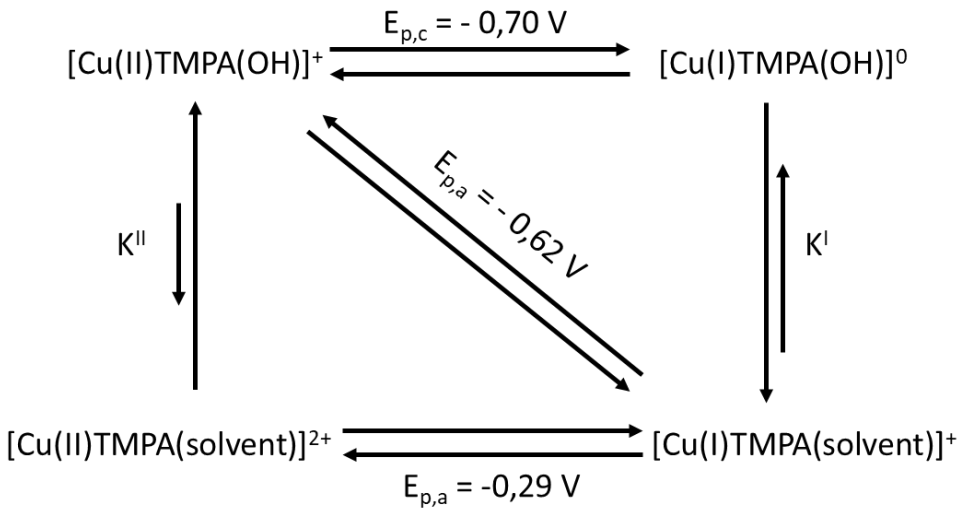

Scheme III.B-4: Electrochemical-Chemical-Electrochemical-Chemical mechanism for the electron transfer process of Cu(II)TMPA(OH) in CH_3CN/H_2O 10/90 v/v.

Concluding remark: In this part, two important points have been demonstrated: (i) the TMPA is a strong binding scaffold that keeps coordinated to Cu(II) even at very low pH (below pH 1), while protonation-induced decoordination of one pyridine arm may occur below pH 1. (ii) at slightly basic pH (about 9) the deprotonation of the bound water leading to the hydroxo complex which is poorly described in literature.[52] The crystallization of the hydroxo-complex was always thwarted likely because it was performed under ambient atmosphere. Hence we plan to try again in a glove bag. The pH-dependent study will also be reproduced in pure aqueous buffer ou in water (the use of organic/water mixtures was consistent with the study reported in JIB, in which we had initially foreseen to include the results described in this last paragraph, and with the studies detailed after in the manuscript).

III.C. Conclusion

General features are highlighted throughout this chapter both from literature and the results obtained: (i) the versatile nature of the the fifth ligand coordinated to the Cu(II)TMPA, (ii) the remaining distorted TBP geometry of Cu(II)TMPA complexes in solution and in solid-state whatever the solvent, the source of Cu(II) or the fifth ligand. However Cu(II)TMPA complexes are flexible enough to adjust their geometry and coordinate bigger ligand in fifth position or even a sixth ligand or weak interaction seen with Cu(II)TMPA(S_2O_3) for which a O atom is interacting with the Cu center. A Cu-TMPA(Bipy) (Bipy = 2,2-bipyridine) hexa-coordinated complex was also isolated. This flexibility is especially noticed in solid-state with the τ parameter and in solution by EPR that seem more sensitive to the slight geometry modification than UV-Vis spectroscopy. A special care should be given to the compounds and solvent used for the study of Cu(II)TMPA as the fifth ligands are various and sometimes unexpected. Indeed, the use of dithionite salt as a reductant was shown to generate a new species from its degradation product, that was attributed to Cu(II)TMPA(SO_3).[5] This species was observed but not mentioned in the literature also formed through the reduction Cu(II)TMPA by dithionite followed by its reoxidation.[53]

References

1. Addison, A. W.; Rao, T. N.; Reedijk, J.; van Rijn, J.; Verschoor, G. C., Synthesis, structure, and spectroscopic properties of copper(II) compounds containing nitrogen–sulphur donor ligands; the crystal and molecular structure of aqua[1,7-bis(N-methylbenzimidazol-2′-yl)-2,6-dithiaheptane]copper(II) perchlorate. *Journal of the Chemical Society, Dalton Transactions* **1984,** (7), 1349-1356.

2. Nagao, H.; Komeda, N.; Mukaida, M.; Suzuki, M.; Tanaka, K., Structural and Electrochemical Comparison of Copper(II) Complexes with Tripodal Ligands. *Inorganic Chemistry* **1996,** *35* (23), 6809-6815.

3. Porras Gutiérrez, A. G.; Zeitouny, J.; Gomila, A.; Douziech, B.; Cosquer, N.; Conan, F.; Reinaud, O.; Hapiot, P.; Le Mest, Y.; Lagrost, C.; Le Poul, N., Insights into water coordination associated with the CuII/CuI electron transfer at a biomimetic Cu centre. *Dalton Transactions* **2014,** *43* (17), 6436-6445.

4. Guo, H.; Gong, C.; Zeng, X.; Xu, H.; Zeng, Q.; Zhang, J.; Zhong, Z.; Xie, J., Isopolymolybdate-based inorganic–organic hybrid compounds constructed by multidentate N-donor ligands: syntheses, structures and properties. *Dalton Transactions* **2019,** *48* (17), 5541-5550.

5. Berthonnaud, L.; Esmieu, C.; Mallet-Ladeira, S.; Hureau, C., Solid-state and solution characterizations of [(TMPA)Cu(II)(SO3)] and [(TMPA)Cu(II)(S2O3)] complexes: Application to sulfite and thiosulfate fast detection. *Journal of Inorganic Biochemistry* **2021,** *225*, 111601.

6. Helton, M. E.; Chen, P.; Paul, P. P.; Tyeklár, Z.; Sommer, R. D.; Zakharov, L. N.; Rheingold, A. L.; Solomon, E. I.; Karlin, K. D., Reaction of Elemental Sulfur with a Copper(I) Complex Forming a trans-μ-1,2 End-On Disulfide Complex: New Directions in Copper−Sulfur Chemistry. *Journal of the American Chemical Society* **2003,** *125* (5), 1160-1161.

7. Ward, A. L.; Elbaz, L.; Kerr, J. B.; Arnold, J., Nonprecious Metal Catalysts for Fuel Cell Applications: Electrochemical Dioxygen Activation by a Series of First Row Transition Metal Tris(2-pyridylmethyl)amine Complexes. *Inorganic Chemistry* **2012,** *51* (8), 4694-4706.

8. Lim, B. S.; Holm, R. H., Molecular Heme−Cyanide−Copper Bridged Assemblies: Linkage Isomerism, Trends in νCN Values, and Relation to the Heme-a3/CuB Site in Cyanide-Inhibited Heme−Copper Oxidases. *Inorganic Chemistry* **1998,** *37* (19), 4898-4908.

9. Eckenhoff, W. T.; Pintauer, T., Atom Transfer Radical Addition in the Presence of Catalytic Amounts of Copper(I/II) Complexes with Tris(2-pyridylmethyl)amine. *Inorganic Chemistry* **2007,** *46* (15), 5844-5846.

10. Karlin, K. D.; Hayes, J. C.; Juen, S.; Hutchinson, J. P.; Zubieta, J., Tetragonal vs. trigonal coordination in copper (II) complexes with tripod ligands: structures and properties of [Cu (C21H24N4) Cl] PF6 and [Cu (C18H18N4) Cl] PF6. *Inorganic Chemistry* **1982,** *21* (11), 4106-4108.

11. Xu, W.; Craft, J. A.; Fontenot, P. R.; Barens, M.; Knierim, K. D.; Albering, J. H.; Mautner, F. A.; Massoud, S. S., Effect of the central metal ion on the cleavage of DNA by [M(TPA)Cl]ClO4 complexes (M=CoII, CuII and ZnII, TPA=tris(2-pyridylmethyl)amine): An efficient artificial nuclease for DNA cleavage. *Inorganica Chimica Acta* **2011,** *373* (1), 159-166.

12. Hematian, S.; Siegler, M. A.; Karlin, K. D., Heme/Copper Assembly Mediated Nitrite and Nitric Oxide Interconversion. *Journal of the American Chemical Society* **2012,** *134* (46), 18912-18915.

13. Eckenhoff, W. T.; Pintauer, T., Structural Comparison of Copper(I) and Copper(II) Complexes with Tris(2-pyridylmethyl)amine Ligand. *Inorganic Chemistry* **2010,** *49* (22), 10617-10626.

14. Yan, S.; Li, C.; Cheng, P.; Liao, D.; Jiang, Z.; Wang, G.; Yao, X.; Wang, H., Copper, a chemical Janus: two copper(II) complexes with different ligand in one single crystal. *Journal of Chemical Crystallography* **1999,** *29* (10), 1085-1088.

15. Eckenhoff, W. T.; Garrity, S. T.; Pintauer, T., Highly Efficient Copper-Mediated Atom-Transfer Radical Addition (ATRA) in the Presence of Reducing Agent. *European Journal of Inorganic Chemistry* **2008,** *2008* (4), 563-571.

16. Bridgman, E. C.; Doherty, M. M.; Ellis, K. A.; Homer, E. A.; Lashbrook, T. N.; Mraz, M. E.; Pernesky, G. C.; Vreeke, E. M.; Oshin, K. D.; Oliver, A. G., Crystal structure of [tris(pyridin-2-ylmethyl)amine-[kappa]4N]copper(II) bromide. *Acta Crystallographica Section E* **2016,** *72* (6), 801-804.

17. Jacobson, R. R.; Tyeklar, Z.; Karlin, K. D.; Zubieta, J., Fluoride as a terminal and bridging ligand for copper: isolation and x-ray crystallographic characterization of copper monomeric and dimeric complexes [CuII (TMPA) F] nn+ (n= 1 or 2; TMPA= tris [(2-pyridyl) methyl] amine). *Inorganic chemistry* **1991,** *30* (9), 2035-2040.

18. Parker, R. J.; Spiccia, L.; Moubaraki, B.; Murray, K. S.; Skelton, B. W.; White, A. H., Cyano bridged dinuclear Cu(II) complexes. *Inorganica Chimica Acta* **2000,** *300-302*, 922-931.

19. Corsi, D. M.; Murthy, N. N.; Young, V. G.; Karlin, K. D., Synthesis, Structure, and Solution NMR Studies of Cyanide−Copper(II) and Cyanide-Bridged Iron(III)−Copper(II) Complexes. *Inorganic Chemistry* **1999,** *38* (5), 848-858.

20. Mukhopadhyay, U.; Bernal, I.; Massoud, S. S.; Mautner, F. A., Syntheses, structures and some electrochemistry of Cu(II) complexes with tris[(2-pyridyl)methyl]amine: [Cu{N(CH2-py)3}(N3)]ClO4 (I), [Cu{N(CH2-py)3}(O–NO)]ClO4 (II) and [Cu{N(CH2-py)3}(NCS)]ClO4 (III). *Inorganica Chimica Acta* **2004,** *357* (12), 3673-3682.

21. Eckenhoff, W. T.; Biernesser, A. B.; Pintauer, T., Kinetic and Mechanistic Aspects of Atom Transfer Radical Addition (ATRA) Catalyzed by Copper Complexes with Tris(2-pyridylmethyl)amine. *Inorganic Chemistry* **2012,** *51* (21), 11917-11929.

22. Mautner, F. A.; Soileau, J. B.; Bankole, P. K.; Gallo, A. A.; Massoud, S. S., Synthesis and spectroscopic characterization of dicyanamido–Cu(II) complexes. Part 21For Part 1 see Ref. [1].1: Crystal structure of the complexes of tris[2-(2-pyridylethyl)]amine, tris(2-

pyridylmethyl)amine and 1,4-bis[2-(2-pyridylethyl)]piperazine. *Journal of Molecular Structure* **2008,** *889* (1), 271-278.

23. Zhu, L.; dos Santos, O.; Koo, C. W.; Rybstein, M.; Pape, L.; Canary, J. W., Geometry-Dependent Phosphodiester Hydrolysis Catalyzed by Binuclear Copper Complexes. *Inorganic Chemistry* **2003,** *42* (24), 7912-7920.

24. Zuin Fantoni, N.; Molphy, Z.; Slator, C.; Menounou, G.; Toniolo, G.; Mitrikas, G.; McKee, V.; Chatgilialoglu, C.; Kellett, A., Polypyridyl-Based Copper Phenanthrene Complexes: A New Type of Stabilized Artificial Chemical Nuclease. *Chemistry – A European Journal* **2019,** *25* (1), 221-237.

25. Massoud, S. S.; Mautner, F. A.; Vicente, R.; Louka, F. R., μ-1,3- (trans) and μ-1,2- (cis) Bonding in Squarato-Bridged Dinuclear Copper(II) and Nickel(II) Complexes Derived from Polypyridyl Amines. *European Journal of Inorganic Chemistry* **2008,** *2008* (23), 3709-3717.

26. Flay, M.-L.; Vahrenkamp, H., Cyanide-Bridged Oligonuclear Complexes Containing Ni-CN-Cu and Pt-CN-Cu Linkages. *European Journal of Inorganic Chemistry* **2003,** *2003* (9), 1719-1726.

27. Díaz-Torres, R.; Alvarez, S., Coordinating ability of anions and solvents towards transition metals and lanthanides. *Dalton Transactions* **2011,** *40* (40), 10742-10750.

28. Gomila, A.; Le Poul, N.; Kerbaol, J.-M.; Cosquer, N.; Triki, S.; Douziech, B.; Conan, F.; Le Mest, Y., Electrochemical behavior and dioxygen reactivity of tripodal dinuclear copper complexes linked by unsaturated rigid spacers. *Dalton Transactions* **2013,** *42* (6), 2238-2253.

29. Le Poul, N.; Douziech, B.; Zeitouny, J.; Thiabaud, G.; Colas, H.; Conan, F.; Cosquer, N.; Jabin, I.; Lagrost, C.; Hapiot, P.; Reinaud, O.; Le Mest, Y., Mimicking the Protein Access Channel to a Metal Center: Effect of a Funnel Complex on Dissociative versus Associative Copper Redox Chemistry. *Journal of the American Chemical Society* **2009,** *131* (49), 17800-17807.

30. Fischmann, A. J.; Warden, A. C.; Black, J.; Spiccia, L., Synthesis, Characterization, and Structures of Copper(II)−Thiosulfate Complexes Incorporating Tripodal Tetraamine Ligands. *Inorganic Chemistry* **2004,** *43* (21), 6568-6578.

31. Yan, S.; Cui, J.; Liu, X.; Cheng, P.; Liao, D.; Jiang, Z.; Wang, G.; Wang, H.; Yao, X., Trinuclear Cu(II) and Zn(II) complexes bridged by μ3-carbonato anion. *Science in China Series B: Chemistry* **1999,** *42* (5), 535-542.

32. Solomon, E. I.; Heppner, D. E.; Johnston, E. M.; Ginsbach, J. W.; Cirera, J.; Qayyum, M.; Kieber-Emmons, M. T.; Kjaergaard, C. H.; Hadt, R. G.; Tian, L., Copper Active Sites in Biology. *Chemical Reviews* **2014,** *114* (7), 3659-3853.

33. Garribba, E.; Micera, G., The Determination of the Geometry of Cu(II) Complexes: An EPR Spectroscopy Experiment. *Journal of Chemical Education* **2006,** *83* (8), 1229.

34. Blackman, A. G., The coordination chemistry of tripodal tetraamine ligands. *Polyhedron* **2005,** *24* (1), 1-39.

35. Blackman, A. G., Tripodal Tetraamine Ligands Containing Three Pyridine Units: The other Polypyridyl Ligands. *European Journal of Inorganic Chemistry* **2008,** *2008* (17), 2633-2647.

36. Schatz, M.; Becker, M.; Thaler, F.; Hampel, F.; Schindler, S.; Jacobson, R. R.; Tyeklár, Z.; Murthy, N. N.; Ghosh, P.; Chen, Q.; Zubieta, J.; Karlin, K. D., Copper(I) Complexes, Copper(I)/O2 Reactivity, and Copper(II) Complex Adducts, with a Series of Tetradentate Tripyridylalkylamine Tripodal Ligands. *Inorganic Chemistry* **2001,** *40* (10), 2312-2322.

37. Dorlet, P.; Hureau, C., Chapitre 4 - Complexation du cuivre par les peptides impliqués dans les maladies neurodégénératives. In *La spectroscopie de résonance paramagnétique électronique: Applications*, EDP Sciences: 2021; pp 79-104.

38. Lucchese, B.; Humphreys, K. J.; Lee, D.-H.; Incarvito, C. D.; Sommer, R. D.; Rheingold, A. L.; Karlin, K. D., Mono-, Bi-, and Trinuclear CuII-Cl Containing Products Based on the Tris(2-pyridylmethyl)amine Chelate Derived from Copper(I) Complex Dechlorination Reactions of Chloroform. *Inorganic Chemistry* **2004,** *43* (19), 5987-5998.

39. Wijeratne, G. B.; Hematian, S.; Siegler, M. A.; Karlin, K. D., Copper(I)/NO(g) Reductive Coupling Producing a trans-Hyponitrite Bridged Dicopper(II) Complex: Redox Reversal Giving Copper(I)/NO(g) Disproportionation. *Journal of the American Chemical Society* **2017,** *139* (38), 13276-13279.

40. Kokoszka, G.; Karlin, K.; Padula, F.; Baranowski, J.; Goldstein, C., EPR of copper (II) complexes with tripodal ligands: dynamical properties. *Inorganic Chemistry* **1984,** *23* (25), 4378-4380.

41. Jiang, F.; Karlin, K. D.; Peisach, J., An electron spin echo envelope modulation (ESEEM) study of electron-nuclear hyperfine and nuclear quadrupole interactions of dz2 ground state copper (II) complexes with substituted imidazoles. *Inorganic Chemistry* **1993,** *32* (11), 2576-2582.

42. Kakuda, S.; Peterson, R. L.; Ohkubo, K.; Karlin, K. D.; Fukuzumi, S., Enhanced Catalytic Four-Electron Dioxygen (O2) and Two-Electron Hydrogen Peroxide (H2O2) Reduction with a Copper(II) Complex Possessing a Pendant Ligand Pivalamido Group. *Journal of the American Chemical Society* **2013,** *135* (17), 6513-6522.

43. Yamaguchi, S.; Masuda, H., Basic approach to development of environment-friendly oxidation catalyst materials. Mononuclear hydroperoxo copper(II) complexes. *Science and Technology of Advanced Materials* **2005,** *6* (1), 34-47.

44. Wada, A.; Honda, Y.; Yamaguchi, S.; Nagatomo, S.; Kitagawa, T.; Jitsukawa, K.; Masuda, H., Steric and Hydrogen-Bonding Effects on the Stability of Copper Complexes with Small Molecules. *Inorganic Chemistry* **2004,** *43* (18), 5725-5735.

45. Fujii, T.; Naito, A.; Yamaguchi, S.; Wada, A.; Funahashi, Y.; Jitsukawa, K.; Nagatomo, S.; Kitagawa, T.; Masuda, H., Construction of a square-planar hydroperoxo-copper(ii) complex inducing a higher catalytic reactivity. *Chemical Communications* **2003,** (21), 2700-2701.

46. Karlin, K. D.; Wei, N.; Jung, B.; Kaderli, S.; Zuberbuehler, A. D., Kinetic, thermodynamic, and spectral characterization of the primary copper-oxygen (Cu-O2) adduct in

a reversibly formed and structurally characterized peroxo-dicopper(II) complex. *Journal of the American Chemical Society* **1991,** *113* (15), 5868-5870.

47. Lee, D.-H.; Wei, N.; Murthy, N. N.; Tyeklar, Z.; Karlin, K. D.; Kaderli, S.; Jung, B.; Zuberbuehler, A. D., Reversible O2 Binding to a Dinuclear Copper(I) Complex with Linked Tris(2-pyridylmethyl)amine Units: Kinetic-Thermodynamic Comparisons with Mononuclear Analogs. *Journal of the American Chemical Society* **1995,** *117* (50), 12498-12513.

48. Bhadra, M.; Lee, J. Y. C.; Cowley, R. E.; Kim, S.; Siegler, M. A.; Solomon, E. I.; Karlin, K. D., Intramolecular Hydrogen Bonding Enhances Stability and Reactivity of Mononuclear Cupric Superoxide Complexes. *Journal of the American Chemical Society* **2018,** *140* (29), 9042-9045.

49. Cargill, R. W. B. R., *Carbon monoxide*. Pergamon: Oxford; New York, 1990.

50. Fry, H. C.; Lucas, H. R.; Narducci Sarjeant, A. A.; Karlin, K. D.; Meyer, G. J., Carbon Monoxide Coordination and Reversible Photodissociation in Copper(I) Pyridylalkylamine Compounds. *Inorganic Chemistry* **2008,** *47* (1), 241-256.

51. Lopez-Castillo, Z. K.; Aki, S. N. V. K.; Stadtherr, M. A.; Brennecke, J. F., Enhanced Solubility of Oxygen and Carbon Monoxide in CO2-Expanded Liquids. *Industrial & Engineering Chemistry Research* **2006,** *45* (15), 5351-5360.

52. Asahi, M.; Yamazaki, S.-i.; Itoh, S.; Ioroi, T., Acid-base and redox equilibria of a tris(2-pyridylmethyl)amine copper complex; their effects on electrocatalytic oxygen reduction by the complex. *Electrochimica Acta* **2016,** *211*, 193-198.

53. Abreu, C. M. R.; Fu, L.; Carmali, S.; Serra, A. C.; Matyjaszewski, K.; Coelho, J. F. J., Aqueous SARA ATRP using inorganic sulfites. *Polymer Chemistry* **2017,** *8* (2), 375-387.

Chapter IV

Chapter IV. Cu(II)Aβ model complexes in aqueous buffer containing 10 % CH_3CN

Three Aβ peptides were selected to model the in-between-state (IBS) intermediate (for details see § I.B.4.). This chapter presents the coordination sphere of each of the resulting Cu(II)Aβ model complexes, deduced from their EPR and UV-vis signatures. As studies to characterize the IBS will require 10% CH_3CN (to increase the level of carbon monoxide (CO) in the medium), its impact on Cu(II)Aβ complexes is evaluated as well. Finally, the Cu(I)/Cu(II)Aβ redox properties are assessed by cyclic voltammetry under anaerobic conditions.

IV.A. Cu(II)Aβ models coordination sphere

Cu(II)Aβ model complexes and their coordination sphere were studied by EPR and UV-vis spectroscopies. At physiological pH, the coordination spheres of Cu(II)Aβ_{1-16} and Cu(II)Aβ_{1-7} were already determined.[1-3] Compare to the present study the peptides were not protected by an amidation on C-terminal. Here, to avoid possible irrelevant coordination of the C-terminal COOH group, we protect the C-term. This may be particularly important for the short peptides, for which a few metal binding spots are present.

Figure IV.A-1 presents the EPR and UV-vis spectra of Cu(II)Aβ_{1-16}; Cu(II)Aβ_{1-7} and Cu(II)Aβ_{13-14} in HEPES pH 7.4 and with 10 % of CH_3CN. The UV-Vis and EPR spectra display classical square-planar type geometry signal.[4] For each species, the EPR and UV-vis spectra are very similar without (dark line) and with 10 % CH_3CN (light line, Figure IV.A-1 and Table IV.A-1). This observation is strongly indicative that CH_3CN does not participate to the coordination to any Cu(II)Aβ models studied.

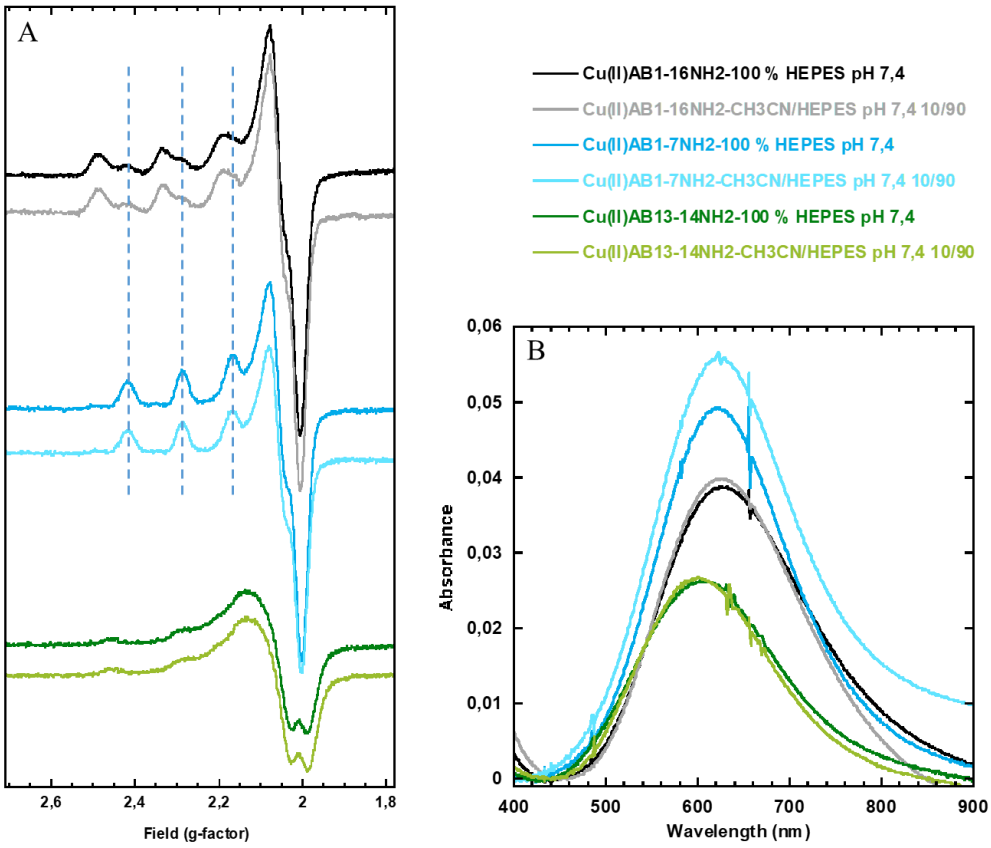

Figure IV.A-1: EPR (A) and UV-Vis (B) spectra of Cu(II)Aβ$_{1-16}$ (black); Cu(II)Aβ$_{1-7}$ (blue) and Cu(II)Aβ$_{13-14}$ (green) in HEPES pH 7.4 100 mM (dark lines) and CH_3CN/HEPES pH 7.4 100 mM 10/90 v/v (light lines). The dotted lines in the EPR panel show the position of the hyperfine transitions corresponding to component II (see Chapter I.A.3. and below) EPR conditions: [Aβ] = 0.55 mM; [^{65}Cu] = 0.5 mM; 10 % glycerol; T = 120 K; microwave power: 5 mW. UV-Vis conditions: [Aβ] = 0.55 mM; [$Cu(SO_4)•5H_2O$] = 0.5 mM; ℓ = 1 cm; T = 25 °C.

Table IV.A-1: UV-Vis and EPR parameters of Cu(II)Aβ$_{1-16}$; Cu(II)Aβ$_{1-7}$ and Cu(II)Aβ$_{13-14}$ complexes in HEPES pH 7.4 and in CH_3CN/HEPES pH 7.4 10/90 v/v.

Complex	**CH_3CN/HEPES pH 7.4 100 mM ratio v/v**		**λ_{max} (nm)**	**ε ($M^{-1}cm^{-1}$)**	**$g_{//}$**	**$A_{//}$ (10^{-4} cm^{-1})[a]**
Cu(II)Aβ$_{1-16}$	0/100	Component I	625	78 ± 4	2.26	189
		Component II			2.23	160
	10/90	Component I	625	80 ± 4	2.26	189
		Component II			2.23	156
Cu(II)Aβ$_{1-7}$	0/100		620	98 ± 5	2.23	160
	10/90		620	92 ± 5	2.23	156
Cu(II)Aβ$_{13-14}$	0/100		600	52 ± 3	2.22	192
	10/90		600	53 ± 3	2.22	192
Cu(II)Aβ$_{13-14}$ + Im*	0/100		-	-	2.21	205

* Im: Imidazole (2 equivalents)

[a]: $A_{//}$ parameters are calculated for ^{63}Cu isotope for comparison with the literature, by using the ratio g(^{65}Cu)/g(^{63}Cu)

The coordination sphere of Cu(II)$A\beta_{1-16}$ was already elucidated at physiological pH.[1-2] Two components are in equilibrium with a distorted square-planar geometry. Component I, predominant at lower pH has a coordination sphere composed by the -NH_2 terminal amine, the O atom from the CO of Asp1-Ala2 peptide bond, and the N atoms from the imidazole rings of His6 and His13 or His14. Component II binding mode includes the -NH_2 terminal amine, the N^- from the amidyl function of the peptide bond between Asp1-Ala2, the O atom from CO of the peptide bond between Ala2-Glu3 and the N atom from the imidazole ring of one His residue among the three (Figure IV.A-4, left and middle).[1] Those two components have a pKa of 7.8.[2] The comparison of the UV-vis and EPR parameters of the complexes obtained with the C-terminally amidated (this work) or free COO^- peptide (literature data) indicates that the protection of the C-terminal does not induce a change in the Cu(II) coordination. Indeed both Cu(II) complexes have close d-d transition band in UV-vis (literature: 625 nm (ε = 65 $M^{-1}cm^{-1}$); this study: 625 nm (ε = 78 $M^{-1}cm^{-1}$)) and EPR parameters (Component I: [literature: $g_{//}$ = 2.27 and $A_{//}$ = 181.10^{-4} cm^{-1}; this study: $g_{//}$ = 2.26 and $A_{//}$ = 189.10^{-4} cm^{-1}] and Component II: [literature: $g_{//}$ = 2.23 and $A_{//}$ = 158.10^{-4} cm^{-1}; this study: $g_{//}$ = 2.23 and $A_{//}$ = 160.10^{-4} cm^{-1}]) (Table IV.A-1).[1, 3, 5] The Cu(II)$A\beta_{1-16}$ has the same coordination sphere than previously deduced with the two components in equilibrium, component I being the major form at pH 7.4 (Figure IV.A-4, left and middle).

Based on EPR spectroscopy, Cu(II)$A\beta_{1-7}$ was already shown to have the same coordination sphere as the Component II of Cu(II)$A\beta_{1-16}$, which is consistent in our case by comparison of blue and black spectra in Figure IV.A-1.[3] EPR parameters obtained for Cu(II)$A\beta_{1-7}$ with C-terminally amidated (this work) and free COO^- peptide (literature data) show that the Cu(II) coordination remains the same independently of the C-terminal protection. Indeed, for both $A\beta_{1-7}$ peptides, the EPR parameters of the complexes are very close (literature: $g_{//}$ = 2.22 and $A_{//}$ = 158.10^{-4} cm^{-1}; this study: $g_{//}$ = 2.23 and $A_{//}$ = 160.10^{-4} cm^{-1}) (Table IV.A-1).[3] Cu(II)$A\beta_{1-7}$ coordination includes the -NH_2 terminal amine, the N^- from the amidyl function of Asp1-Ala2 peptide bond, the O atom from CO of Ala2-Glu3 peptide bond and the N atom from the imidazole ring of one His6 residue (Figure IV.A-4, middle).[3]

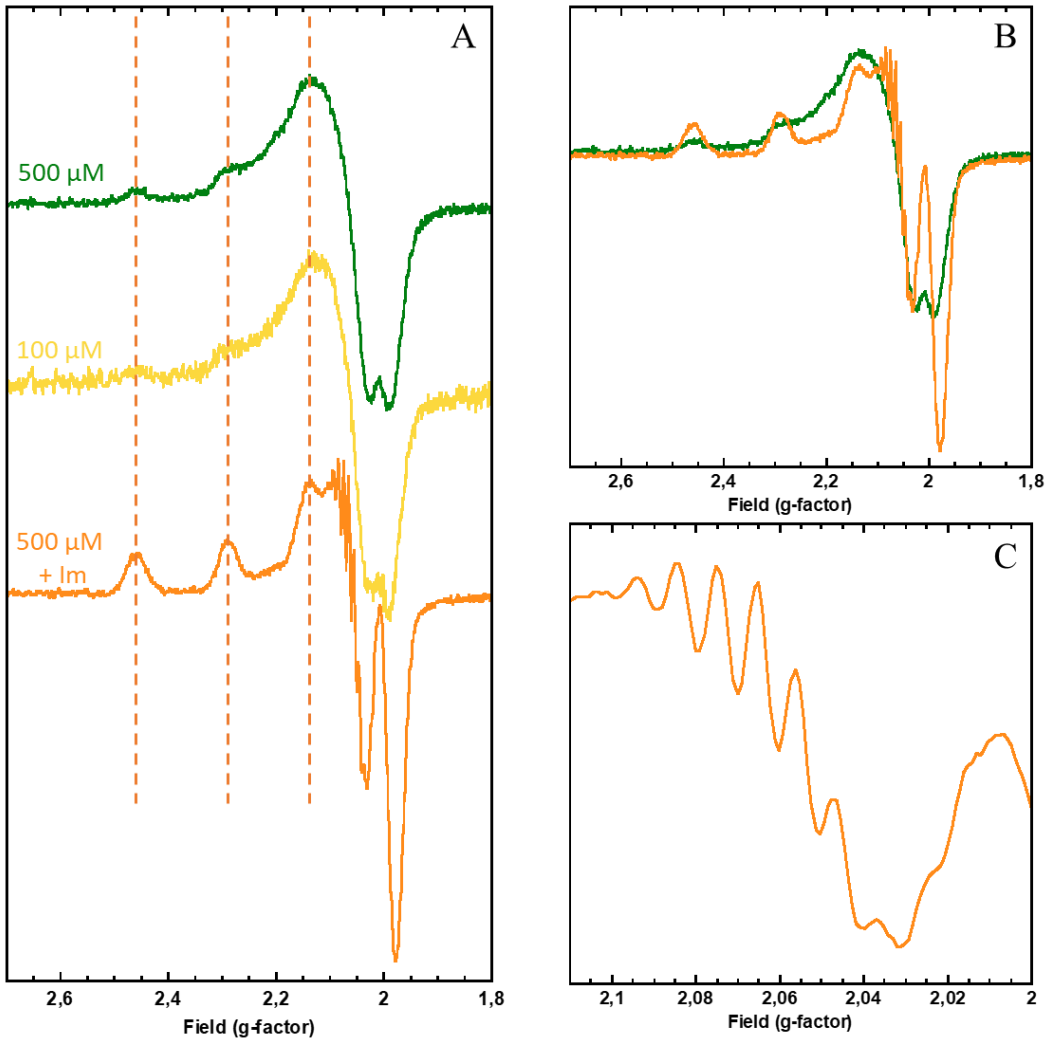

Figure IV.A-2: EPR spectra of Cu(II)Aβ_{13-14} (green and yellow) with two equivalents of imidazole (orange) in HEPES pH 7.4 100 mM stacked (A) overlaid (B)and enlargement of the $g_\perp$ region to better see the superhyperfine pattern (C). EPR conditions: [Aβ] = 0.55 mM or 0.11 mM (yellow); [^{65}Cu] = 0.5 mM or 0.1 mM (yellow); 10 % glycerol; T = 120 K; microwave power: 5 mW.

Cu(II)Aβ_{13-14} shows different EPR spectrum than those of Cu(II)Aβ_{1-16} or Cu(II)Aβ_{1-7} with less intense and broader hyperfine lines while the d-d transition band is at lower wavelength and has a lower absorption intensity (600 nm; ε = 52 $M^{-1}cm^{-1}$) (Figure IV.A-1 and Table IV.A-1). It was first hypothesized that the broadening observed was due to precipitation of the complexes. However, upon dilution the EPR signal remains the same (100 µM (yellow spectrum) versus 500 µM (green spectrum) Figure IV.A-2). Another event that could influence that way the EPR spectrum would be the coordination of two Cu(II) ions in close vicinity, for instance bridged by Aβ_{13-14}, leading to dipole-dipole interactions responsible for the observed broadening (Figure IV.A-3). To check this hypothesis by preventing such dimer formation, we

added 2 equivalents of imidazole (orange spectrum in Figure IV.A-2). This addition induces the appearance of a new signature, where the hyperfine lines are well-resolved and where superhyperfine lines are detected in the $g_\perp$ region mirroring a 4N coordination. Such signature was reminiscent of the Cu(II)(AH) + Im signature.[6] Indeed, both complexes with the addition of imidazole display similar EPR parameters (Cu(II)(AH) + Im: $g_{//} = 2.21$ and $A_{//} = 200.10^{-4}$ cm^{-1}; Cu(II)Aβ$_{13-14}$ + Im: $g_{//} = 2.21$ and $A_{//} = 205.10^{-4}$ cm^{-1}).[7] Without or with imidazole, UV-Vis are close: without Im: with $\lambda_{max} = 600$ nm ($\varepsilon = 59$ $M^{-1}cm^{-1}$) for Cu(II)(AH) and $\lambda_{max} = 600$ nm ($\varepsilon = 52$ $M^{-1}cm^{-1}$) for Cu(II)Aβ$_{13-14}$, with Im: $\lambda_{max} = 560$ nm ($\varepsilon = 68$ $M^{-1}cm^{-1}$) for Cu(II)(AH)(Im).[7] The proposed binding mode of Cu(II)(AH) was the terminal $–NH_2$ function, the amidyl from the peptide chain and N atom from the imidazole ring of the Histidine residue.[7-8]

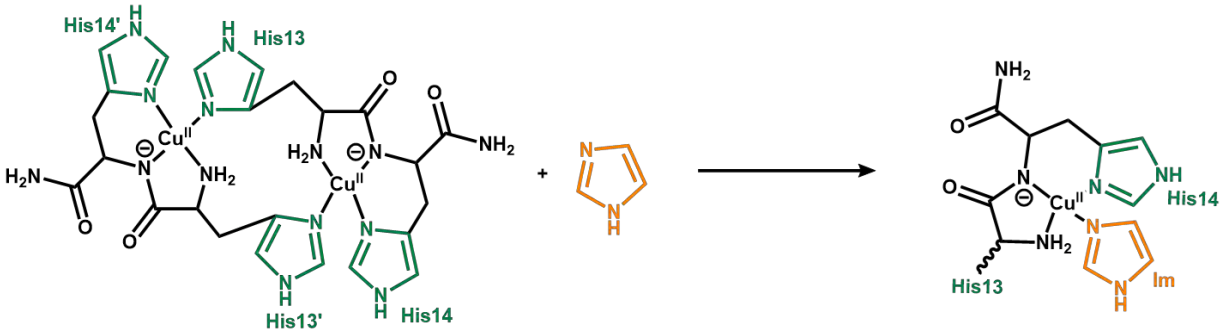

Figure IV.A-3: Hypothesis for dimeric coordination of Aβ$_{13-14}$ to Cu(II) becoming monomeric through the addition of imidazole (Im).

Based on these similarities upon imidazole addition, we proposed the formation of the Cu(II) complex shown Figure IV.A-4 (right) where the metal ion lies in a square-planar environment made of the N-terminal amine, the N atom from the imidazole ring of His, the deprotonated amide bond in between the two histidine residues and a exogenous N atom from the imidazole. Addition of imidazole makes the formation of a mononuclear species possible, whose EPR signature is perfectly resolved. In absence of imidazole the EPR parameters are close indicating that in the dimeric species Cu(II)$_2$(Aβ$_{13-14}$)$_2$, the Cu(II) environment is the same, but with the imidazole ring from an His of the second peptide occupying the fourth equatorial position of the first Cu(II)Aβ$_{13-14}$ moiety as represented in Figure IV.A-3.

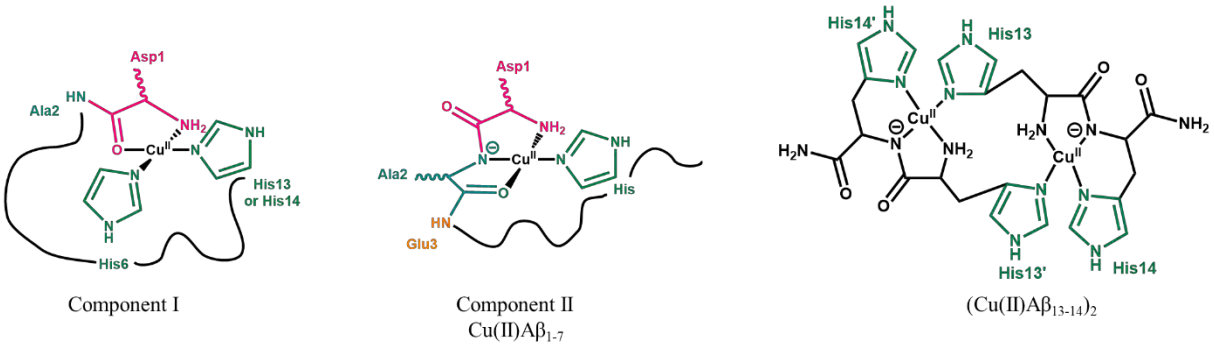

Figure IV.A-4: Cu(II) coordination to $A\beta_{1-16}$ in Component I and II (left and middle), to $A\beta_{1-7}$ (middle) and to $A\beta_{13-14}$ as dimer (right).

The coordination spheres of the three Cu(II)Aβ complexes have been elucidated, all displaying square planar geometries. The coordination spheres of $A\beta_{1-16}$ and $A\beta_{1-7}$ coordinated to Cu(II) remain the same than the ones already described in the literature being not impacted by the C-terminal protection of the peptide with 3N1O type of coordination. Cu(II)$A\beta_{13-14}$ have a 4N coordination probably forming dimers between two peptides. The coordination sphere of Cu(II)$A\beta_{13-14}$ could be confirmed by X-ray absorption spectroscopy (XAS) that make possible the detection of Cu-Cu interactions.

IV.B. Cu(II)/Cu(I)Aβ cyclic voltammetry

After a spectroscopic characterization, the Cu(II)-peptide complexes were studied by cyclic voltammetry (CV). Because unbound Cu could participate to the redox process via equilibria with peptide-bound Cu, it has first been studied in the very same conditions.

IV.B.1. Free copper

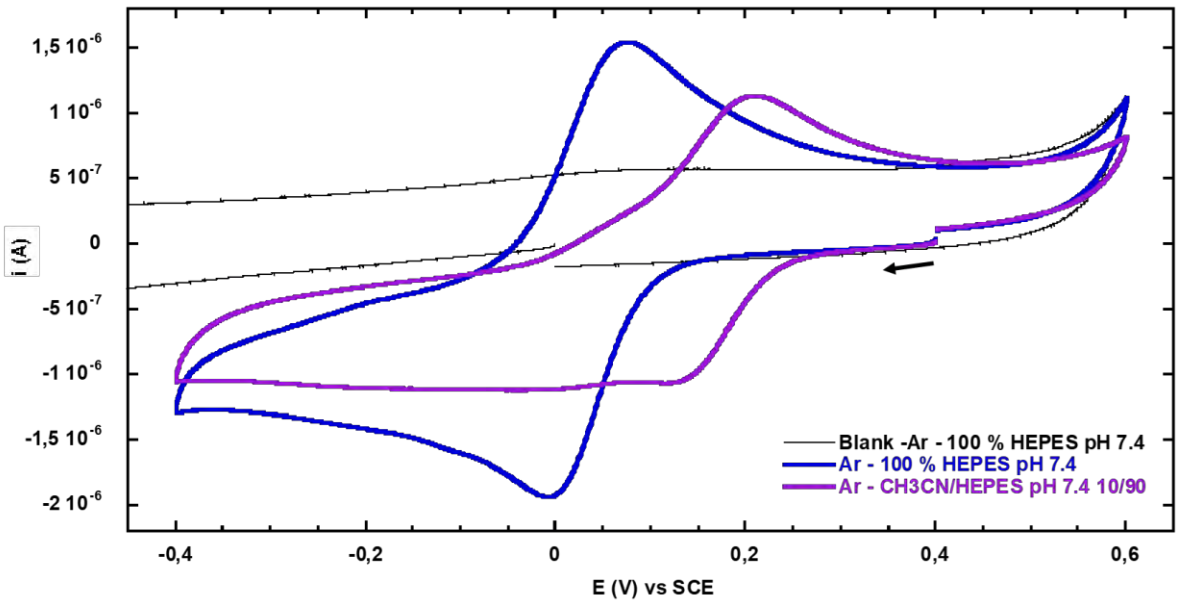

Figure IV.B-1: Cyclic voltammograms (CV) of free Cu under Ar in CH_3CN/HEPES pH 7.4 100 mM 0/100 (blue line) and 10/90 (purple line) v/v. Conditions: [$Cu(SO_4)•5H_2O$] = 0.5 mM; scan rate = 100 mV/s; WE = Glassy carbon; Ref = SCE; CE = Pt wire. First scans are shown starting from 0.4 V indicated by the arrow.

Figure IV.B-1 shows the cyclic voltammograms of free Cu(II) in HEPES pH 7.4 and with 10 % CH_3CN. In HEPES pH 7.4, Cu(II)/Cu(I) electron transfer process is quasi-reversible with a peak-to-peak separation of 0.08 V and a $E_{1/2}$ = 0.03 V (Table IV.B-1). In presence of 10 % of CH_3CN, the quasi-reversibility is kept with a peak-to-peak separation of 0.09 V but the signal is less intense and is shifted toward higher potential at $E_{1/2}$ = 0.17 V indicating the stabilization of Cu(I) by CH_3CN (Table IV.B-1). A second less intense process is observed at the same position than in HEPES only. Hence we can hypothesize that two redox couples exist in solution differing by the number of bound CH_3CN.[9]

IV.B.2. $A\beta_{1-16}$

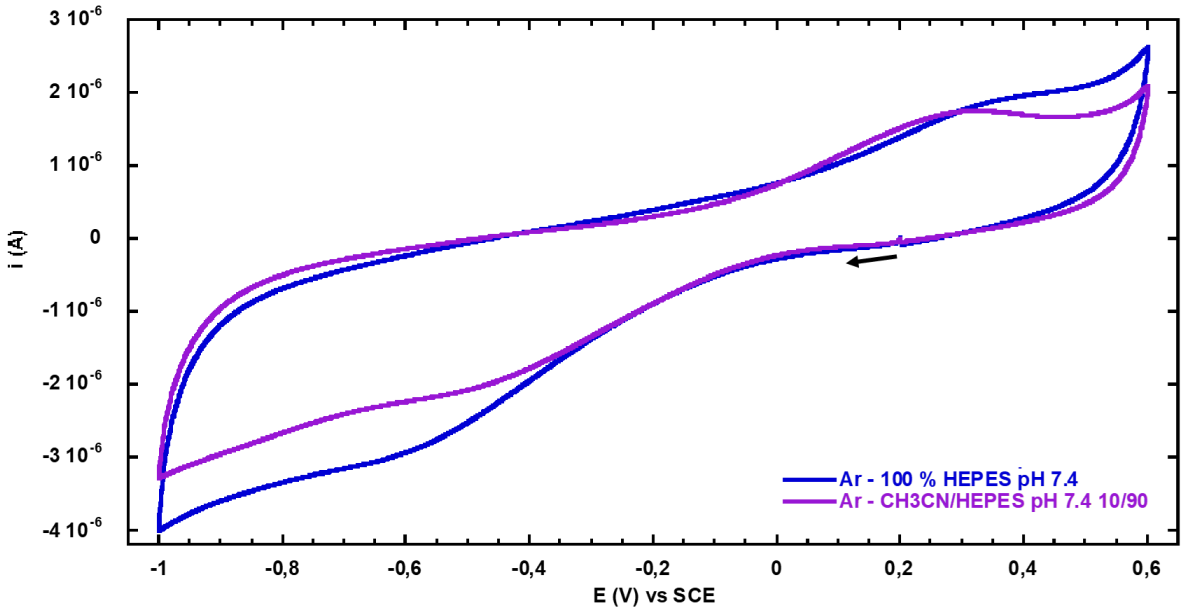

Figure IV.B-2: Cyclic voltammograms (CV) of Cu(II)$A\beta_{1-16}$ under Ar in CH_3CN/HEPES pH 7.4 100 mM 0/100 (blue lines) and 10/90 (purple lines) v/v. Conditions: [$A\beta_{1-16}$] = 0.55 mM; [$Cu(SO_4)•5H_2O$] = 0.5 mM; scan rate = 100 mV/s; WE = Glassy carbon; Ref = SCE; CE = Pt wire. First scans are shown starting from 0.2 V indicated by the arrow.

Figure IV.B-2 displays the CVs of Cu(II)$A\beta_{1-16}$ in CH_3CN/HEPES pH 7.4 0/100 and 10/90 under Ar. In both solvent systems, Cu(II)$A\beta_{1-16}$ shows irreversible electron transfer with a peak-to-peak separation of 0.94 V in HEPES pH 7.4 and 0.83 V with 10 % of CH_3CN (Table IV.B-1). The irreversibility and broad oxidation and reduction waves are already known for Cu(II)$A\beta_{1-16}$ in aqueous solution. Indeed, a huge reorganization energy would be required for a direct electron transfer to occur as the two resting states (RS) of Cu-Aβ have very different coordination spheres: Cu(II)Aβ RS has a square planar geometry whereas Cu(I)Aβ RS has a linear coordination mode (Scheme IV.B-1). The broad waves convey the diversity of coordination modes taken by Cu-$A\beta_{1-16}$ in solution due to the flexibility of $A\beta_{1-16}$ peptide.

An advanced electrochemical study revealed that the electron transfer follows a preorganization electron transfer mechanism typical of Chemical-Electrochemical-Chemical mechanism (Scheme IV.B-1).[10] In other words a small fraction of the complex is pre-organized with a geometry in-between the two RS to minimize the reorganization energy. The species active for the electron transfer is called “in-between state” (IBS). Starting the mechanism from

Cu(II)Aβ_{1-16} RS, a small fraction will follow chemical reaction to be coordinated as the IBS to allow the electrochemical electron transfer. The reduced IBS will then be chemically transformed to Cu(I) RS (Scheme IV.B-1, left). In presence of CH_3CN, the mechanism would be mainly the same, but CH_3CN might participate to the IBS coordination sphere, since it might be coordinated to Cu(I)Aβ_{1-16} RS reducing its stability through the loss of linearity (Scheme IV.B-1, right).

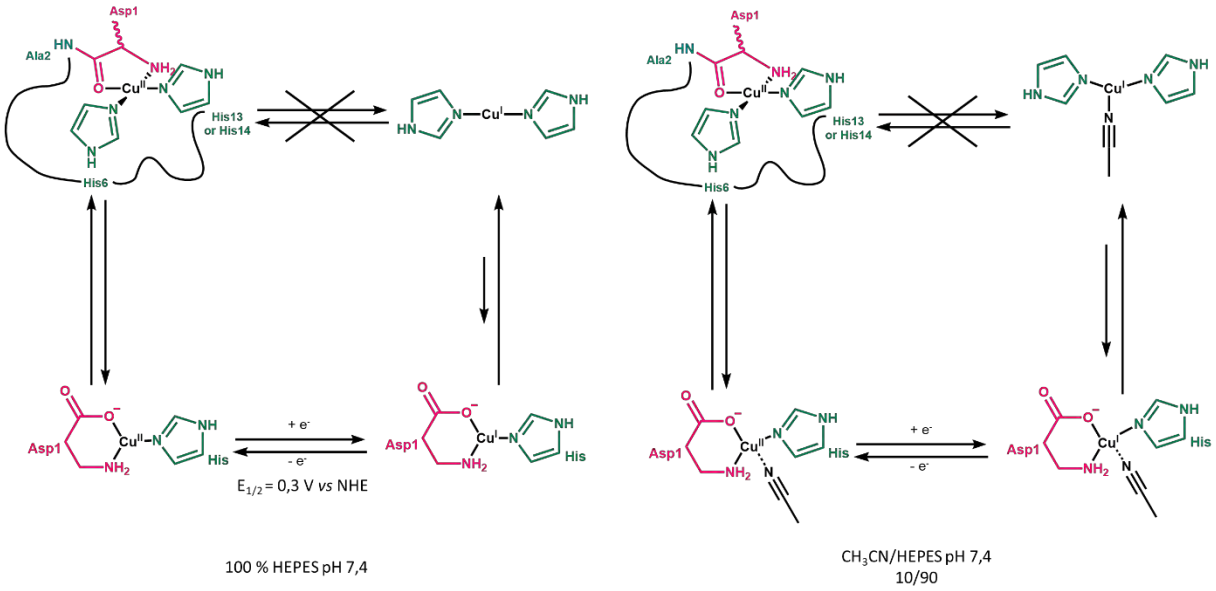

Scheme IV.B-1: Chemical-Electrochemical-Chemical mechanisms proposed for the electron transfer process of Cu(II)Aβ_{1-16} in HEPES pH 7.4 (left) and in CH_3CN/HEPES pH 7.4 10/90 (right).

IV.B.3. $A\beta_{1-7}$

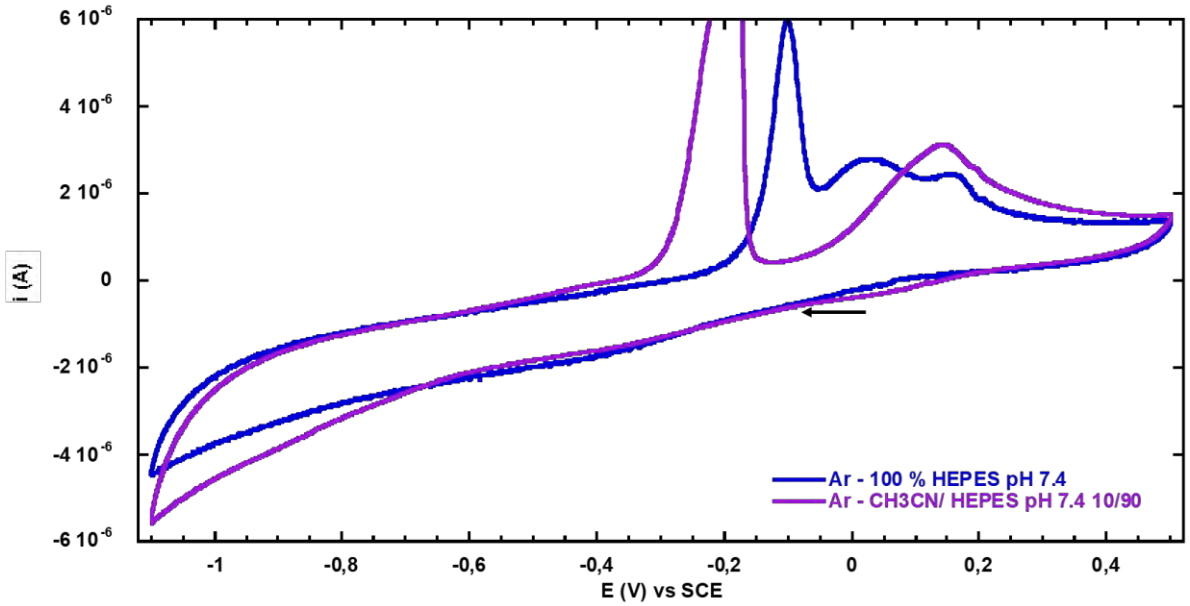

Figure IV.B-3: Cyclic voltammograms (CV) of Cu(II)$A\beta_{1-7}$ under Ar in CH_3CN/HEPES pH 7.4 100 mM 0/100 (blue lines) and 10/90 (purple lines) v/v. Conditions: [$A\beta_{1-7}$] = 0.55 mM; [$Cu(SO_4)•5H_2O$] = 0.5 mM; scan rate = 100 mV/s; WE = Glassy carbon; Ref = SCE; CE = Pt wire. First scans are shown starting from the open circuit potential indicated by the arrow.

Figure IV.B-3 shows the CVs of Cu(II)$A\beta_{1-7}$ in CH_3CN/HEPES pH 7.4 0/100 and 10/90 under Ar. Cu(II)$A\beta_{1-7}$ is characterized by irreversible cyclic voltammograms in both systems of solvent, with a particularly very broad reduction wave hard to see around -0.4 V (Table IV.B-1). The broad reduction wave revealed that many different processes are ongoing during the reduction of Cu(II)$A\beta_{1-7}$ to Cu(I)$A\beta_{1-7}$. In HEPES, the anodic peak at 0.03 V is attributed to the re-oxidation of Cu(I)$A\beta_{1-7}$ to Cu(II)$A\beta_{1-7}$. With 10 % of CH_3CN the oxidation wave is sharper than in HEPES and shifted toward more positive potentials from 0.03 V (HEPES only) to 0.14 V (10 % CH_3CN) mirroring the stabilization of Cu(I)$A\beta_{1-7}$ by CH_3CN. At -0.10 V in HEPES pH 7.4 only and -0.18 V in presence of CH_3CN an intense and sharp oxidation peak is observed and is attributed to the oxidation and solubilization of Cu(0) to Cu(I) from unbounded Cu deposited at the electrode during reduction.

We hypothesize that the electron transfer is suggested to follow a similar mechanism than for Cu-$A\beta_{1-16}$, with Cu(II)$A\beta_{1-7}$ being chemically transformed to Cu(II)IBS allowing its electrochemical reduction to Cu(I)IBS that would become Cu(I)$A\beta_{1-7}$ through chemical

rearrangement (Scheme IV.B-2, left). However, Cu-Aβ_{1-7} has a smaller peak-to-peak separation and a sharper anodic peak than Cu-Aβ_{1-16}, which could mirror changes in the chemical equilibria between the RS and IBS. The mechanism remains the same with the addition of CH_3CN, but impacting Cu(I)Aβ_{1-7}. Similarly than for Cu-Aβ_{1-16}, CH_3CN might participate to the IBS coordination sphere but there is no proof. However, CH_3CN is coordinated to Cu(I)Aβ_{1-7} and stabilizing it, probably through a more stable tetrahedral geometry (Scheme IV.B-2, right).

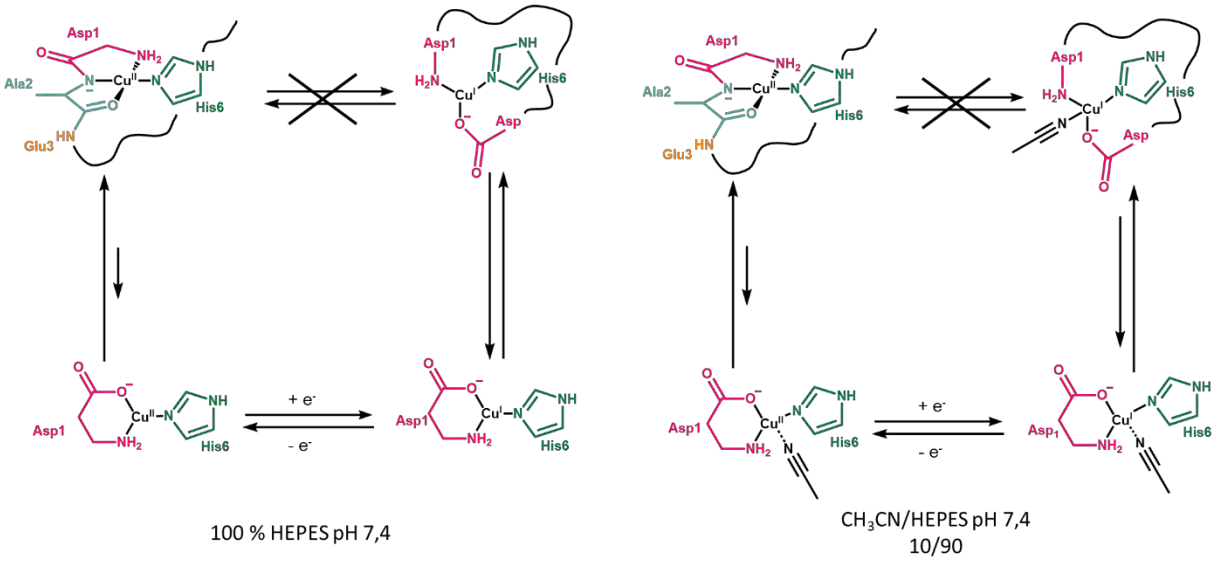

Scheme IV.B-2: Chemical-Electrochemical-Chemical mechanisms proposed for the electron transfer process of Cu(II)Aβ_{1-7} in HEPES pH 7.4 (left) and in CH_3CN/HEPES pH 7.4 10/90 (right).

IV.B.4. $A\beta_{13-14}$

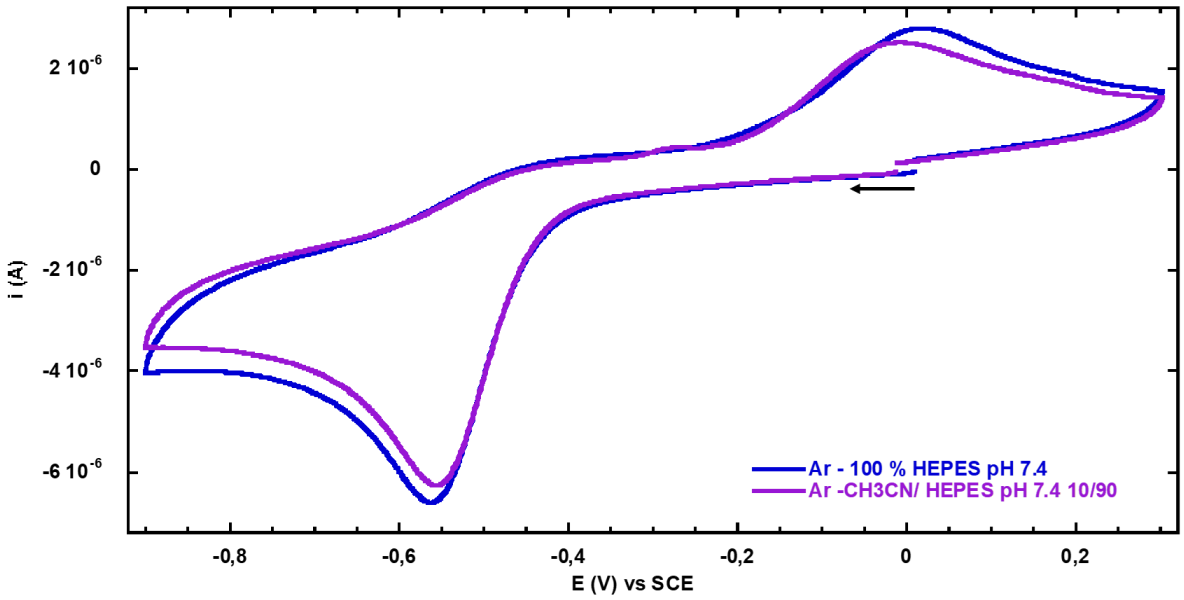

Figure IV.B-4: Cyclic voltammograms (CV) of Cu(II)$A\beta_{13-14}$ under Ar in CH_3CN/HEPES pH 7.4 100 mM 0/100 (blue lines) and 10/90 (purple lines) v/v. Conditions: [$A\beta_{13-14}$] = 0.55 mM; [$Cu(SO_4)•5H_2O$] = 0.5 mM; scan rate = 100 mV/s; WE = Glassy carbon; Ref = SCE; CE = Pt wire. First scans are shown starting from the open circuit potential indicated by the arrow.

Figure IV.B-4 shows the CVs of Cu(II)$A\beta_{13-14}$ in CH_3CN/HEPES pH 7.4 0/100 and 10/90 under Ar. In both solvent systems, Cu(II)$A\beta_{13-14}$ shows irreversible electron transfer process with a peak-to-peak separation of 0.58 V in HEPES pH 7.4 and 0.55 V with 10 % CH_3CN (Table IV.B-1). The irreversibility was expected as the Cu(II)$A\beta_{13-14}$ was defined as a dimeric species with 4N coordination environment shared by two bridging $A\beta_{13-14}$, whereas Cu(I) is postulated to have a 2N linear coordination between two imidazole rings (see further chapter V). The reduction wave is at high negative potential -0.56 V and remains the same in CH_3CN/HEPES pH 7.4 10/90 (Table IV.B-1). This value mirrors the high stability of Cu(II)$A\beta_{13-14}$. Furthermore, as expected by the UV-Vis and EPR studies of Cu(II)$A\beta_{13-14}$, CH_3CN does not participate to the Cu(II) state coordination sphere. In HEPES, an anodic peak attributed to the oxidation of Cu(I)$A\beta_{13-14}$ to Cu(II)$A\beta_{13-14}$ is seen at 0.02 V and is shifted toward negative potential values with 10 % of CH_3CN at -0.01 V. This observation is attributed to the destabilization of Cu(I)$A\beta_{13-14}$ by CH_3CN as seen for Cu(I)$A\beta_{1-16}$ RS postulated to have the same linear coordination sphere. The cyclic voltammogram of Cu(II)$A\beta_{13-14}$ is reminiscent of the one of Cu(II)GHK (GHK: GlyHisLys) by the shape of the CV and also the peak-to-peak

separations (ΔE = 0.51 V for Cu(II)GHK and 0.58 V for Cu(II)$A\beta_{13-14}$) and the low reduction potential values (-0.54 V vs SCE (converted value) for Cu(II)GHK and -0.56 V for Cu(II)$A\beta_{13-14}$) (Table IV.B-1).[8] The addition of CH_3CN had a similar effect on Cu(II)$A\beta_{13-14}$ than the addition of histidine on Cu(II)GHK, by lowering the oxidation potential.[8]

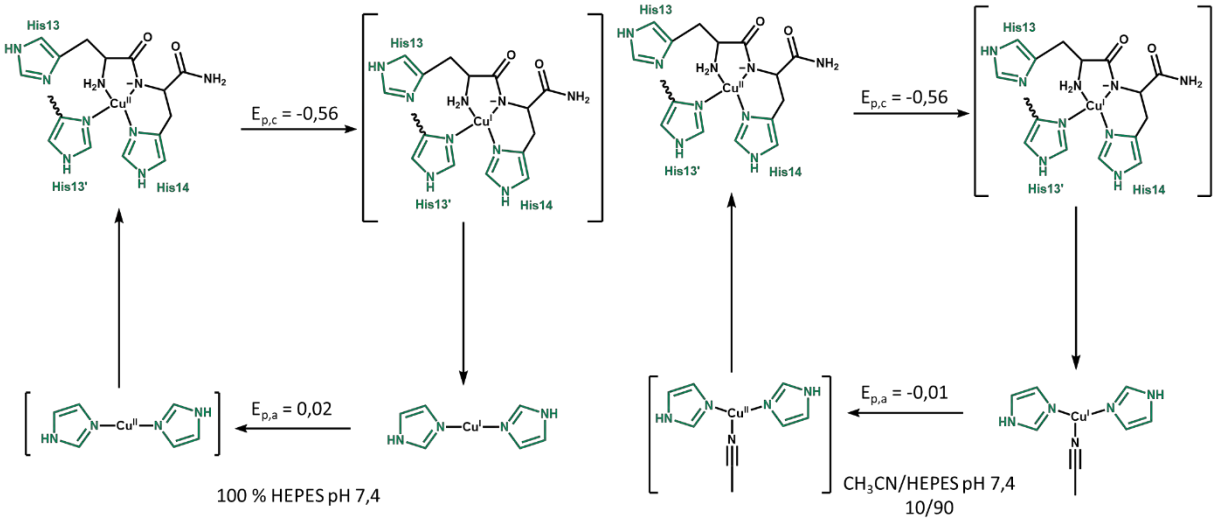

Scheme IV.B-3: Electrochemical-Chemical-Electrochemical-Chemical mechanisms proposed for the electron transfer process of Cu(II)$A\beta_{13-14}$ in HEPES pH 7.4 (left) and in CH_3CN/HEPES pH 7.4 10/90 (right). His13' corresponds to His from the second peptide in the dimeric complex. The species in square brackets are not observed.

The irreversible electron transfer for Cu(II)$A\beta_{13-14}$ is proposed to follow a electrochemical-chemical-electrochemical-chemical mechanism (Scheme IV.B-3, left). It starts with Cu(II)$A\beta_{13-14}$ with a 4N square planar (SP) geometry electrochemically reduced to Cu(I)$A\beta_{13-14}$ keeping a 4N coordinate (not observed). This species evolves to form the linear Cu(I)$A\beta_{13-14}$ that would be re-oxidized electrochemically to Cu(II)$A\beta_{13-14}$ linear species, which is not observed since it forms the SP 4N-coordinated Cu(II). In presence of CH_3CN, the mechanism remains similar, but the chemical reactions at play may be accompanied by the coordination/decoordination of CH_3CN. Compared to in absence of CH_3CN, the re-oxidation peak is at lower potential in line with the loss of the stabilizing linear geometry (Scheme IV.B-3, right).

Table IV.B-1: Cyclic voltammetry parameters for free Cu, Cu-Aβ$_{1-16}$; Cu-Aβ$_{1-7}$ and Cu-Aβ$_{13-14}$ in CH_3CN/HEPES pH 7.4 0/100 and 10/90 under Ar. Values given in V vs SCE.

	CH_3CN/HEPES pH 7.4	**E_{pc} (V)**	**E_{pa} (V)**	**ΔE (V)**	**$(E_{p,a} + E_{p,c})/2$ (V)**
Free Cu	0/100	-0.01	0.07	0.08	0.03
	10/90	0.12	0.21	0.09	0.17
Cu-Aβ$_{1-16}$	0/100	~-0.60	0.34	0.94	-0.13
	10/90	~-0.51	0.32	0.83	-0.10
Cu-Aβ$_{1-7}$	0/100	~-0.40	0.03	0.43	-0.19
	10/90	~-0.40	0.14	0.54	-0.13
Cu-Aβ$_{13-14}$	0/100	-0.56	0.02	0.58	-0.27
	10/90	-0.56	-0.01	0.55	-0.29

IV.C. Conclusion

The coordination spheres of Cu(II)Aβ$_{1-16}$, Cu(II)Aβ$_{1-7}$ and Cu(II)Aβ$_{13-14}$ were proposed based on the literature, UV-vis and EPR studies. All the Cu(II)Aβ model complexes have square planar geometry either 3N1O for Cu(II)Aβ$_{1-16}$ and Cu(II)Aβ$_{1-7}$ or 4N for Cu(II)Aβ$_{13-14}$.

The cyclic voltammetry of the Cu-Aβ models are characterized by irreversible electron transfer behavior that requires high reorganization energy due to the difference of coordination modes of Cu(II) and Cu(I) states. Cu(II)Aβ$_{1-16}$ and Cu(II)Aβ$_{1-7}$ cyclic voltammograms display particularly broad reduction peaks in agreement with the presence of different redox competent species postulated by molecular modelling study and with the variety of coordination modes differently populated due to peptide flexibility.[11]

CH_3CN is not participating in the first coordination sphere of Cu(II)Aβ models as their spectroscopic signatures were not impacted by its presence. However, it has an impact on the Cu(I)Aβ states. For the complexes postulated to have a linear coordination which is known to be quite stable for Cu(I) oxidation state, CH_3CN is causing their destabilization through the loss of the linearity, as observed for Cu(I)Aβ$_{1-16}$ and Cu(I)Aβ$_{13-14}$. However, Cu(I)Aβ$_{1-7}$ is stabilized by the coordination of CH_3CN by entailing a tetrahedral geometry.

References

1. Hureau, C., Coordination of redox active metal ions to the amyloid precursor protein and to amyloid-β peptides involved in Alzheimer disease. Part 1: An overview. *Coordination Chemistry Reviews* **2012,** *256* (19), 2164-2174.

2. Hureau, C.; Dorlet, P., Coordination of redox active metal ions to the amyloid precursor protein and to amyloid-β peptides involved in Alzheimer disease. Part 2: Dependence of Cu(II) binding sites with Aβ sequences. *Coordination Chemistry Reviews* **2012,** *256* (19), 2175-2187.

3. Cheignon, C.; Jones, M.; Atrián-Blasco, E.; Kieffer, I.; Faller, P.; Collin, F.; Hureau, C., Identification of key structural features of the elusive Cu–Aβ complex that generates ROS in Alzheimer's disease. *Chemical Science* **2017,** *8* (7), 5107-5118.

4. Garribba, E.; Micera, G., The Determination of the Geometry of Cu(II) Complexes: An EPR Spectroscopy Experiment. *Journal of Chemical Education* **2006,** *83* (8), 1229.

5. Esmieu, C.; Ferrand, G.; Borghesani, V.; Hureau, C., Impact of N-Truncated Aβ Peptides on Cu- and Cu(Aβ)-Generated ROS: CuI Matters! *Chemistry – A European Journal* **2021,** *27* (5), 1777-1786.

6. Gonzalez, P.; Vileno, B.; Bossak, K.; El Khoury, Y.; Hellwig, P.; Bal, W.; Hureau, C.; Faller, P., Cu(II) Binding to the Peptide Ala-His-His, a Chimera of the Canonical Cu(II)-Binding Motifs Xxx-His and Xxx-Zzz-His. *Inorganic Chemistry* **2017,** *56* (24), 14870-14879.

7. Gonzalez, P.; Bossak-Ahmad, K.; Vileno, B.; Wezynfeld, N. E.; El Khoury, Y.; Hellwig, P.; Hureau, C.; Bal, W.; Faller, P., Triggering Cu-coordination change in Cu(ii)-Ala-His-His by external ligands. *Chemical Communications* **2019,** *55* (56), 8110-8113.

8. Hureau, C.; Eury, H.; Guillot, R.; Bijani, C.; Sayen, S.; Solari, P.-L.; Guillon, E.; Faller, P.; Dorlet, P., X-ray and Solution Structures of CuIIGHK and CuIIDAHK Complexes: Influence on Their Redox Properties. *Chemistry – A European Journal* **2011,** *17* (36), 10151-10160.

9. Kamau, P.; Jordan, R. B., Complex Formation Constants for the Aqueous Copper(I)−Acetonitrile System by a Simple General Method. *Inorganic Chemistry* **2001,** *40* (16), 3879-3883.

10. Balland, V.; Hureau, C.; Savéant, J.-M., Electrochemical and homogeneous electron transfers to the Alzheimer amyloid-β copper complex follow a preorganization mechanism. *Proceedings of the National Academy of Sciences* **2010,** *107* (40), 17113-17118.

11. Arrigoni, F.; Prosdocimi, T.; Mollica, L.; De Gioia, L.; Zampella, G.; Bertini, L., Copper reduction and dioxygen activation in Cu–amyloid beta peptide complexes: insight from molecular modelling†. *Metallomics* **2018,** *10* (11), 1618-1630.

Chapter V

Chapter V. CO-adducts of Cu(I) complexes (with TMPA and Aβ peptides as ancillary ligands)

This chapter presents the formation of Cu(I)(CO) adduct with TMPA and Aβ peptides. Different techniques are used to characterize those species, such as ^{1}H NMR, UV-Vis, cyclic voltammetry and FT-IR. Throughout this chapter the studies were performed in aqueous buffered solution at pH 7.4 with 10 % of CH_3CN to increase the concentration of CO and drive the formation of the CO-adducts.

Carbon monoxide (CO), used as a redox inactive surrogate of dioxygen, could stabilize Cu(I) intermediate and give information on its coordination sphere. This strategy is used here on Aβ peptides, with the aim of gaining new insights on the Cu(I) complexes reactivity.

V.A. ^{1}H NMR

^{1}H NMR is a powerful although barely reported and indirect method to monitor the binding of (i) Cu(I) to a ligand and of (ii) CO to the resulting complex and help to elucidate the coordination mode. Firstly, Cu(I) will affect the electronic density of the protons close to the coordination sites and induce chemical shifts. Secondly, CO will modify the electronic density on Cu(I) as a σ-donor and π-acceptor ligand, and thus will also have an influence on the protons surrounding the coordination site.

V.A.1. TMPA

TMPA, Cu(I)TMPA(CH_3CN) and Cu(I)TMPA(CO) were already characterized by ^1H NMR in organic solvents, but to the best of our knowledge, never in aqueous solvent.[1-3]

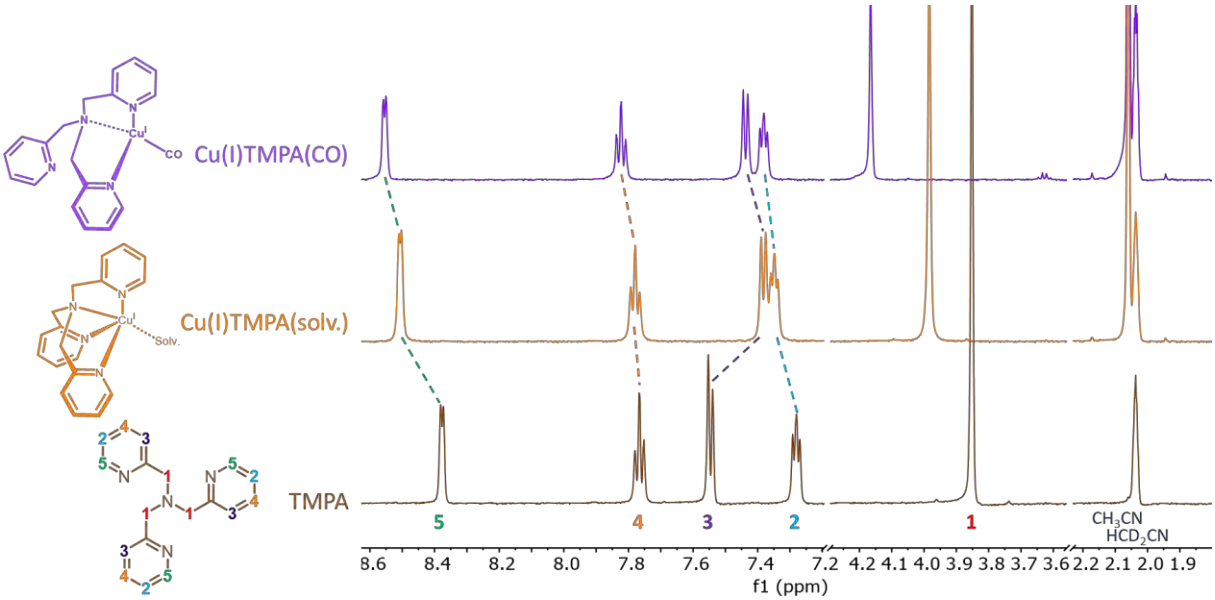

Figure V.A-1: ^1H NMR spectra of TMPA (brown), Cu(I)TMPA(solvent) (orange) and Cu(I)TMPA(CO) (purple) in CD_3CN/KPB pD 7.4 100 mM (13/87 v/v) under air, Ar and CO atmosphere respectively. The chemical shifts are indicated with dotted lines. Conditions: [TMPA] = 2.2 mM; [$[Cu(CH_3CN)_4]BF_4$] = 2 mM; internal reference HCD_2CN = 2.037 ppm, (600 MHz).

Figure V.A-1 displays the ^1H NMR spectra of TMPA (brown), Cu(I)TMPA under Ar atmosphere (orange) and under CO atmosphere (purple) in CD_3CN/phosphate buffer (KPB) pD 7.4 (13/87 v/v). For NMR studies phosphate buffer is used instead of HEPES, as it does not have signal in ^1H NMR. Here, the solvent ratio is 13/87 instead of 10/90 (CD_3CN/KPB) due to the "low" concentration of the Cu(I) stock solution in CD_3CN. To reach the desired 2 mM final concentration it was then needed to add 13 % in volume of Cu dissolved in CD_3CN. The chemical shifts in ppm for each proton of each species are reported in Table V.A-1.

^1H NMR spectra of TMPA, Cu(I)TMPA and Cu(I)TMPA(CO) showed only one set of five resonances for the three methyl-pyridine moieties indicating their equivalence. This observation is in line with the formation of a monomeric species in solution and against the formation of a dimeric species for which 2 sets of methylene proton signals were observed.[1, 4] Indeed, in non-coordinating organic solvent (such as acetone-d_6) at low temperature, two sets of signals were observed for the methylene protons in a 2:1 ratio indicating the unequal

chemical environment for one methylene group compare to the two others. This observation was suggested to arise from the formation of a dimeric structure in which each Cu(I) center is coordinated by the tertiary amine and two pyridyl nitrogens from one TMPA ligand and the $N_{pyridyl}$ from a second TMPA ligand.[4] In our case, for Cu(I)TMPA this suggests that solvent (CH_3CN or H_2O) could be coordinated to prevent dimer formation.[1] Note that it is not possible to observe the peak corresponding to CH_3CN bound to Cu(I) because the vast majority of acetonitrile in solution is CD_3CN (about 1000 times more concentrated than CH_3CN or HCD_2CN). The coordination of Cu(I) to TMPA induces a downfield shift (+ 0.130 ppm) for the H5 protons and (+ 0.132 ppm) for the methylene protons H1. H4 and H2 protons are also deshielded but less than H5-1 protons (+0.013 ppm for H4 and +0.067 ppm for H2 versus ~ + 0.13 ppm for H5 and H1). Conversely, H3 is shielded (~ - 0.16 ppm). Globally, the chemical shifts induced by Cu(I) in aqueous solution are in agreement with the literature for monomeric Cu(I)TMPA complexes in organic solvent.[1, 5] Nevertheless, for Cu(I)TMPA(Br) in $(CD_3)_2CO$, the H1 protons were less shifted than the H5 protons mirroring a weaker N_{amine}-Cu(I) interaction compared to the N_{py}-Cu(I) interaction due to the presence of the bromide.[5] In our case, chemical shifts undergone by H1 and H5 are closed in line with an aqua or CH_3CN ligand as exogenous ligand, weaker coordinating molecules than bromide anion (Figure V.A-1).[4-5] In the literature spectra obtained in organic solvent for Cu(I)TMPA(Br) or Cu(I)TMPA(CH_3CN) complexes with respectively Br^- or CH_3CN as fifth ligand show a broadening attributed to dynamical exchange between the pyridine (two coordinating and one being decoordinated).[1-2, 5] Here, the thin proton signals is indicative of either a fast exchange regime or no exchange at all. Hence, the possible Cu(I) coordination could be: tetrahedral with fast exchange between the pyridine and with a fourth solvent ligand, 4-coordinated with no exogenous solvent ligand or 5-coordinated with solvent exogenous ligand. The later proposition is favored based on the prevention of dimer formation and from the comparison with spectrum in presence of CO (see next paragraph) (Figure V.A-1, middle orange).

Through the coordination of CO to Cu(I)TMPA, all protons are deshielded, H1 being the most affected one (+ 0.18 ppm). All the other protons are similarly affected with small downfield shifts, +0.048 for H5, +0.044 for H4, +0.054 ppm for H3 and +0.034 for H2. In CH_3CN, Cu(I)TMPA(CO) is proposed to be tetra-coordinated with one pyridyl arm uncoordinated as elucidated by FT-IR (Figure V.A-1).[3] Here, the resonance signals for

Cu(I)TMPA(CO) are sharp and equivalent for each pyridyl arm moiety, thus the three pyridyl arms are suggested to be in fast equilibrium (Figure V.A-1, top purple). While the effect of addition of Cu(I) on TMPA resonances was different for the 5 protons, CO binding leads to a downfield shift for all protons, with a more important extent for H1. This strengthen the suggestion that in Cu(I)TMPA, the three pyridine arms were bound at the same time.

Table V.A-1: Chemical shifts (δ) (in ppm) of ^{1}H NMR of TMPA, Cu(I)TMPA(solv.) and Cu(I)TMPA(CO) in CD_3CN/KPB pD 7.4 100 mM 13/87 v/v and Δδ from free TMPA to Cu(I)TMPA(solv.) and to Cu(I)TMPA(CO) (internal reference HCD_2CN = 2.037 ppm).

	5	**4**	**3**	**2**	**1**	**CH_3CN**	**HCD_2CN**
Cu(I)TMPA(CO)	8.555	7.823	7.437	7.382	4.166	2.060	2.037
Cu(I)TMPA(solv.)	8.507	7.779	7.383	7.348	3.984	2.060	2.037
$\Delta_{Cu(I)-Cu(I)CO}$	*+0.048*	*+0.044*	*+0.054*	*+0.034*	*+0.182*	*0.000*	*0.000*
TMPA	8.377	7.766	7.546	7.281	3.852	-	2.037
$\Delta_{TMPA-Cu(I)}$	*+0.130*	*+0.013*	*-0.163*	*+0.067*	*+0.132*	-	*0.000*

V.A.2. Amyloid-β peptides

^{1}H NMR is a very useful spectroscopic method to probe the amino acid residues of peptide implicated in the coordination to Cu(I), and the binding of CO to the peptide-Cu complexes. Knowing the coordination sphere of Cu(I)Aβ(CO) adducts could help to understand their reactivity as Cu(I)Aβ complexes and toward O_2. TMPA presented previously is used as a reference for the study with Aβ peptides.

Peptides are very sensitive to pH changes and some of their proton chemical shifts appeared to be sensitive to the amount of CD_3CN between 5 and 15 %. Thus for the ^{1}H NMR experiments presented in the following, a special care was given to afford the same amount of CD_3CN in each NMR experiment to be able to compare them. The amount of CD_3CN was checked by looking at the absolute integral of the signal corresponding to HCD_2CN at 2.051 ppm.

V.A.2.a. $A\beta_{13-14}$

Figure V.A-2 presents the ^1H NMR of $A\beta_{13-14}$, $Cu(I)A\beta_{13-14}$ under Ar and under CO ($Cu(I)A\beta_{13-14}(CO)$) in CD_3CN/KPB pH 7.4 10/90 v/v. The chemical shifts of each proton are listed in Table V.A-2. The ^1H NMR spectrum of $A\beta_{13-14}$ shows two set of chemical shifts for aromatic protons, meaning that the two histidine residues are not equivalent. Every signal from the peptide is shifted through the coordination to Cu(I) center. The protons from the imidazole rings are deshielded, especially Hδ (by + 0.113 ppm if one considers that the two peaks moves similarly and + 0.097 ppm and + 0.129 ppm if they cross each other). Hε of the two histidine residues are not shifted by the same strength of +0.083 and +0.052 ppm (if one considers that they move in parallel). Those observations mirror the coordination of the two imidazole rings to Cu(I), probably in a fast dynamic mode between the two positions Nδ and Nε from each ring, as Hε and Hδ are both strongly impacted. The Hα are upfield shifted by - 0.052 and - 0.081 ppm. The inequivalent Hβ protons are affected and deshielded but it is hard to conclude about them as they appeared as unresolved multiplets. Futhermore, it is proposed that the coordination of imidazole ring by Nδ have a high impact on Hε, while by Nε, similar shifts occur on Hε and Hδ.[6] The main coordination mode of $Cu(I)A\beta_{13-14}$ is proposed to be 2N linear between the two imidazole rings, one via the Nδ and the other by Nε as both Hε are not shifted by the same strength (Scheme V.A-1).

A full attribution of His13 and His14 signals is required. To better attribute the change induced by Cu(I) in $A\beta_{13-14}$ peaks, an intermediate spectrum recorded at a ratio Cu(I)/ligand 0.5/1 instead of 1/1.1 would help to quantitatively attribute impact of Cu(I) to either H_{13} or H_{14} peaks. The proposition of Cu(I) binding would thus be more accurate with respect to Hε or Hδ binding from His13 or His14.

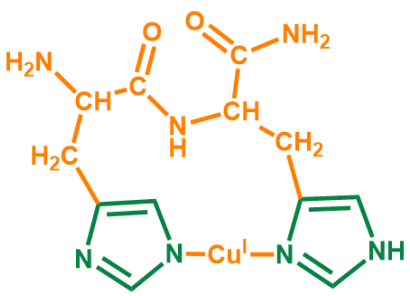

Scheme V.A-1: Binding mode proposition for $Cu(I)A\beta_{13-14}$.

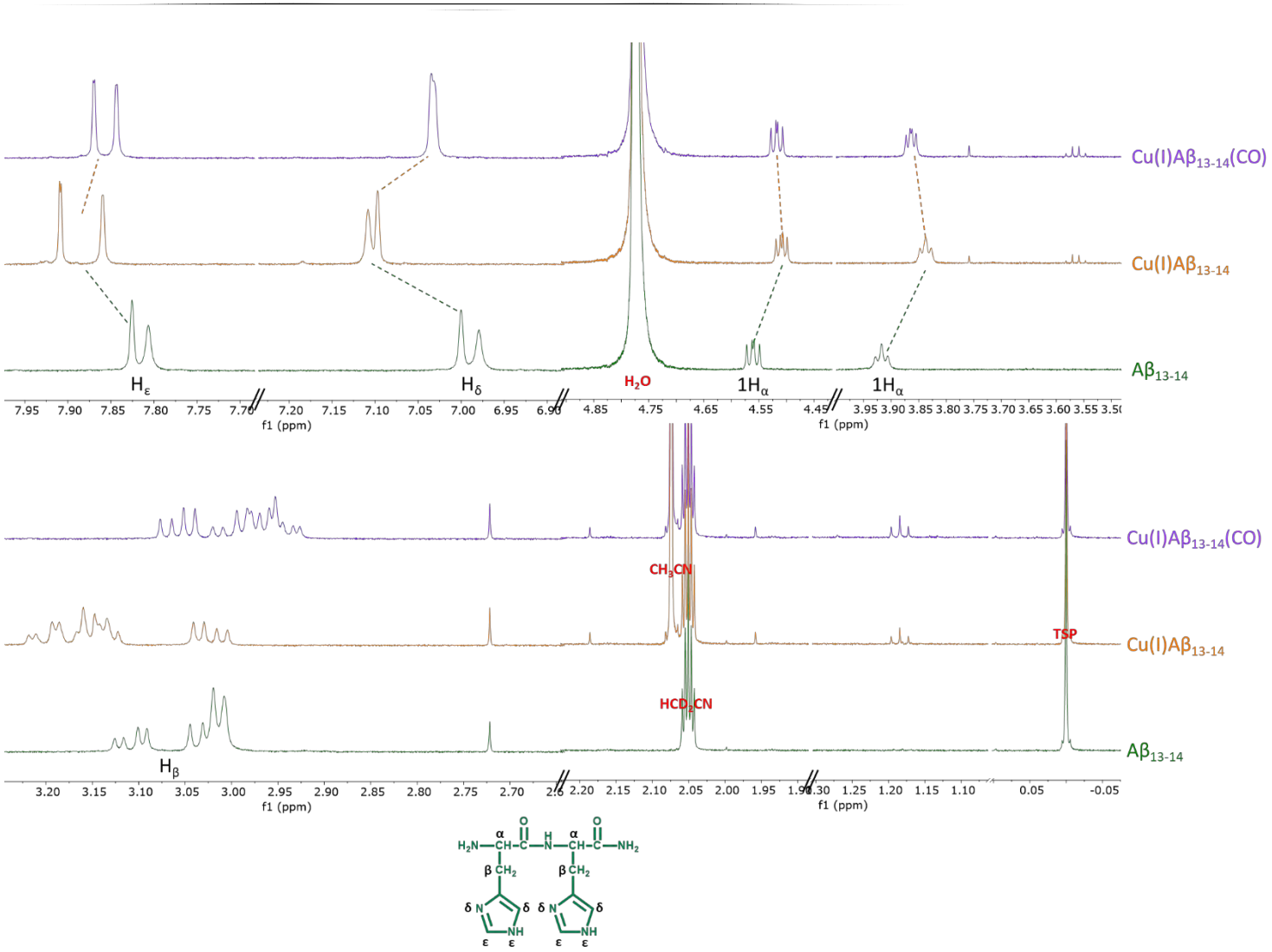

Figure V.A-2: ^{1}H NMR spectra of $A\beta_{13-14}$ (green) (Ar atmosphere), $Cu(I)A\beta_{13-14}$ (orange) (Ar atmosphere) and $Cu(I)A\beta_{13-14}(CO)$ (purple) (CO atmosphere) in CD_3CN/KPB pH 7.4 100 mM 10/90 v/v. The chemical shifts are indicated with dotted lines. Conditions: $[A\beta_{13-14}]$ = 2.2 mM; $[[Cu(CH_3CN)_4]BF_4]$ = 2 mM; [dithionite] = 3 mM; internal reference : TSP (0 ppm), (600 MHz).[Note: An impurity is present at 2.72 ppm coming from the synthesis of $A\beta_{13-14}$. As it remains at the same position in every experiment, its presence is considered innocent and negligible].

The CO atmosphere induces shifts of all the protons towards their initial position *i.e.* without Cu(I), to different extent (higher effect is seen for the aromatic protons). This behavior is attributed to coordination of CO and its properties that allow Cu(I) to give back electron density from its d orbitals to the π* of CO, thus reducing the effect of Cu(I) on the $A\beta_{13-14}$ peptide. As all protons are affected the same way, the coordination is postulated to remain the same as $Cu(I)A\beta_{13-14}$ with the addition of CO inducing a loss of linearity between the two histidine residues (Scheme V.A-2).

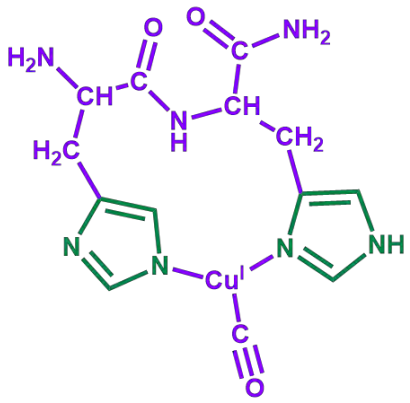

Scheme V.A-2: Binding mode proposition for $Cu(I)A\beta_{13-14}(CO)$.

Table V.A-2: Chemical shifts (δ) (in ppm) of ^1H NMR of $A\beta_{13-14}$, $Cu(I)A\beta_{13-14}$ and $Cu(I)A\beta_{13-14}(CO)$ in CD_3CN/KPB pH 7.4 100 mM 10/90 v/v, and Δδ from free $A\beta_{13-14}$ to $Cu(I)A\beta_{13-14}$ and to $Cu(I)A\beta_{13-14}(CO)$ (internal reference TSP = 0 ppm).

	Hε	**Hδ**	**Hβ**	**Hα**	**CH_3CN**	**HCD_2CN**
$Cu(I)A\beta_{13-14}(CO)$	7.870-7.844	7.035-7.032	between 3.082 and 2.919	4.518-3.864	2.074	2.051
$Cu(I)A\beta_{13-14}$	7.909-7.859	7.108-7.097	between 3.225 and 2.994	4.509-3.837	2.074	2.051
$\Delta_{Cu(I)-Cu(I)CO}$	*-0.027*	*-0.069*	-	*+ 0.009* *+ 0.027*	*0.000*	*0.000*
$A\beta_{13-14}$	7.826-7.807	7.000-6.979	between 3.135 and 2.992	4.561-3.918	-	2.051
$\Delta_{A\beta-Cu(I)}$	*+ 0.067*	*+ 0.113*	-	*-0.052* *-0.081*	-	*0.000*

V.A.2.b. $A\beta_{1-7}$

Figure V.A-3 shows the ^1H NMR spectra of $A\beta_{1-7}$, $Cu(I)A\beta_{1-7}$ and $Cu(I)A\beta_{1-7}(CO)$ in CD_3CN/KPB pH 7.4 10/90 v/v. The chemical shifts of the main protons affected by the coordination of Cu(I) and CO are listed in Table V.A-3. They corresponds to protons on Asp1, Ala2, Phe4, and His6.

The signals at 7.84 ppm and 7.05 ppm attributed to Hε and Hδ of the imidazole ring from His6 are deshielded by + 0.033 ppm and + 0.019 ppm with the coordination of Cu(I), respectively. They are the most downfield shifted protons, revealing the coordination of the His6. The protons of Asp1 Hα and Hβ are slightly upfield shifted -0.023 ppm and -0.008 ppm respectively. Asp1 Hα being more shifted than the Hβ could mirror the coordination of the N-terminal amine to Cu(I). It is hard to monitor the protons attributed to Asp7 as its Hα and Hβ are at the same chemical shift than Phe4 and His6 Hα and Asp1 Hβ. However, those signals area around 4.55 ppm and 2.65 ppm are changing with the coordination of Cu(I). The Hγ of Phe4 and Hβ of Ala2 are shielded and deshielded respectively, despite that they are non-coordinating amino-acid residues. Ala protons are known to be sensitive to their environment,[7] suggesting a close coordination to them, probably related to the $-NH_2$ terminal coordination. For Phe4, the Hγ shift could arise from a structural 3D reorganization of the peptide due to the coordination of Cu(I), as it was already observed with $A\beta_{1-16}$.[7] $Cu(I)A\beta_{1-7}$ was already studied by ^1H NMR and Cu(I) K-edge XANES.[7-8] The coordination sphere proposed for this complex involved the terminal NH_2 from the Asp1, a N atom of imidazole ring from His6 and a carboxylate function from Asp1 or Asp7.[7] In this work, the ^1H NMR results are in agreement with the proposed binding mode especially for the terminal NH_2 and the imidazole ring, however no clear conclusion is made for Asp1 or Asp7 carboxylate group involvement (Scheme V.A-3).

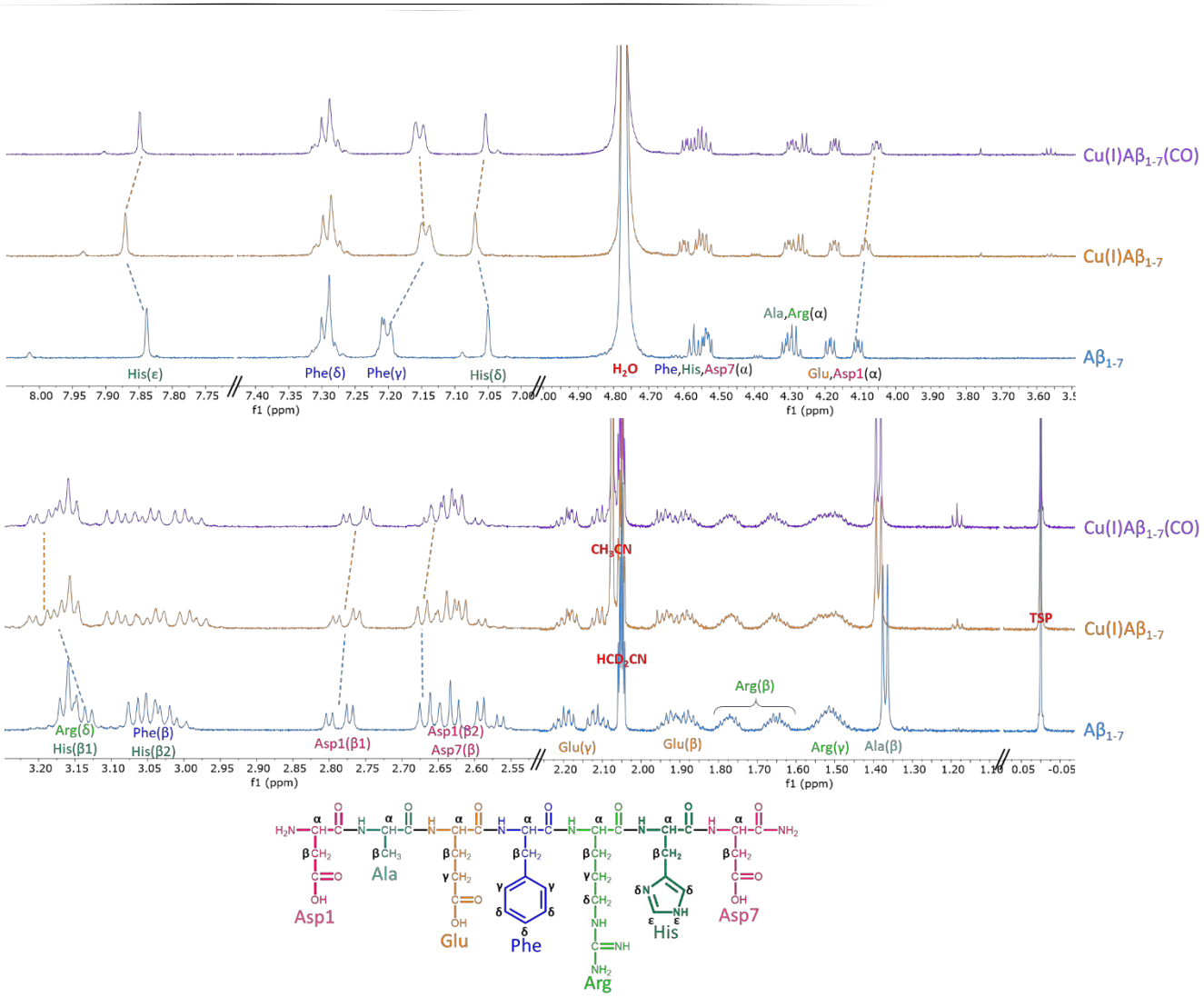

Figure V.A-3: : ^{1}H NMR spectra of $A\beta_{1-7}$ (blue) (Ar atmosphere), $Cu(I)A\beta_{1-7}$ (orange) (Ar atmosphere) and $Cu(I)A\beta_{1-7}(CO)$ (purple) (CO atmosphere) in CD_3CN/KPB pH 7.4 100 mM 10/90 v/v. The chemical shifts are indicated with dotted lines. Conditions: $[A\beta_{1-7}]$ = 2.2 mM; $[[Cu(CH_3CN)_4]BF_4]$ = 2 mM; [dithionite] = 3 mM; internal reference : TSP (0 ppm), (600 MHz).

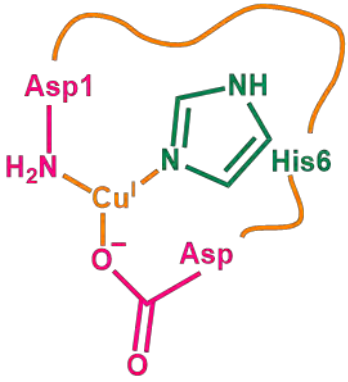

Scheme V.A-3: Binding mode proposition for Cu(I)Aβ1-7.

Overall, upon CO atmosphere, the chemical shifts of Cu(I)Aβ$_{1-7}$ are slightly affected suggesting the coordination of CO. The addition of CO affects mainly the protons of His6 and Asp1. Similarly than for Aβ$_{13-14}$ the Hε and Hδ are shifted back toward their initial position due to the π-acceptor feature of CO that lower the electronic density from Cu(I). However, Hα and Hβ from Asp1 are even more shielded with CO coordination, this behavior was observed for the protons (H5; H4; H2 and H1) of Cu(I)TMPA through the coordination of CO. Hβ from Ala2 remain at the same chemical shift, meaning that their chemical environment is unchanged. Hγ of Phe4 are slightly shifted back by + 0.009 ppm, which is indicative of small 3D structural change. Thus it is postulated that Aβ$_{1-7}$ coordination to Cu(I) remains the same when CO is coordinated as there is no drastic environment and 3D structural change (Scheme V.A-4).

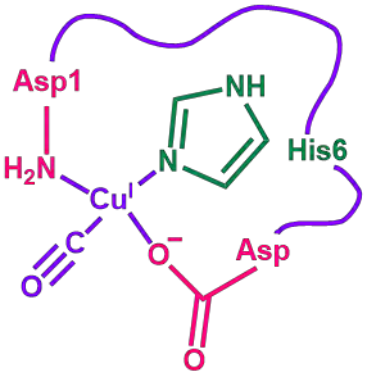

Scheme V.A-4: Binding mode proposition for Cu(I)Aβ1-7(CO).

Table V.A-3: Chemical shifts (δ) (in ppm) of ^{1}H NMR of $A\beta_{1-7}$, $Cu(I)A\beta_{1-7}$ and $Cu(I)A\beta_{1-7}(CO)$ in CD_3CN/KPB pH 7.4 100 mM 10/90 v/v and Δδ from free $A\beta_{1-7}$ to $Cu(I)A\beta_{1-7}$ and to $Cu(I)A\beta_{1-7}(CO)$ (only main protons from the residues affected are listed) (internal reference: TSP = 0 ppm).

	His(ε)	**Phe(γ)**	**His(δ)**	**Asp1(α)**	**Asp1(β1)**	**Ala(β)**	**CH_3CN**	**HCD_2CN**
$Cu(I)A\beta_{1-7}(CO)$	7.849	7.153	7.054	4.054	2.764	1.388	2.074	2.051
$Cu(I)A\beta_{1-7}$	7.871	7.144	7.069	4.084	2.779	1.388	2.074	2.051
$\Delta_{Cu(I)-Cu(I)CO}$	*-0.022*	*+0.009*	*-0.015*	*-0.030*	*-0.015*	*0.000*	*0.000*	*0.000*
$A\beta_{1-7}$	7.838	7.202	7.050	4.107	2.787	1.370	-	2.051
$\Delta_{A\beta-Cu(I)}$	*+0.033*	*-0.058*	*+0.019*	*-0.023*	*-0.008*	*+0.018*	-	*0.000*

V.A.2.c. $A\beta_{1-16}$

Figure V.A-4, displays the ^{1}H NMR spectra of $A\beta_{1-16}$, $Cu(I)A\beta_{1-16}$ and $Cu(I)A\beta_{1-16}(CO)$ in CD_3CN/KPB pH 7.4 10/90 v/v. The chemical shifts of the main protons affected by the coordination of Cu(I) and CO are listed in Table V.A-4. $A\beta_{1-16}$ was already studied by ^{1}H NMR and its coordination to Cu(I) as well.[6-7, 9-11] The main protons affected by the coordination to Cu(I) and CO are localized on His, Phe and Val residues.

The signals attributed to Hε and Hδ of the three His residues are all deshielded with Cu(I) coordination and became broader, either because of trace amount of Cu(II) or mirroring a dynamic exchange of the three His. The Phe4 and Val12 are non-coordinating residues but sensitive to the 3D structure of the peptide or chemical environment. The protons Hγ of Val12 are shielded due to the participation of His13 to the coordination to Cu(I). The protons Hδ and Hγ of Phe4 are upfield shifted probably because of the folding of the peptide when coordinated to Cu(I). Minor shifts located on other amino acid residues can be observed but are hard to interpret as different protons signal are overlapped. All those observations are in agreement with the literature for a coordination of $A\beta_{1-16}$ to Cu(I) between two of the three His residues in dynamic exchange (Scheme V.A-5).[6, 9, 12]

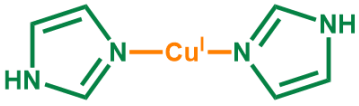

Scheme V.A-5: Binding mode proposition for $Cu(I)A\beta_{1-16}$ with a fast equilibrium between the three His couples.

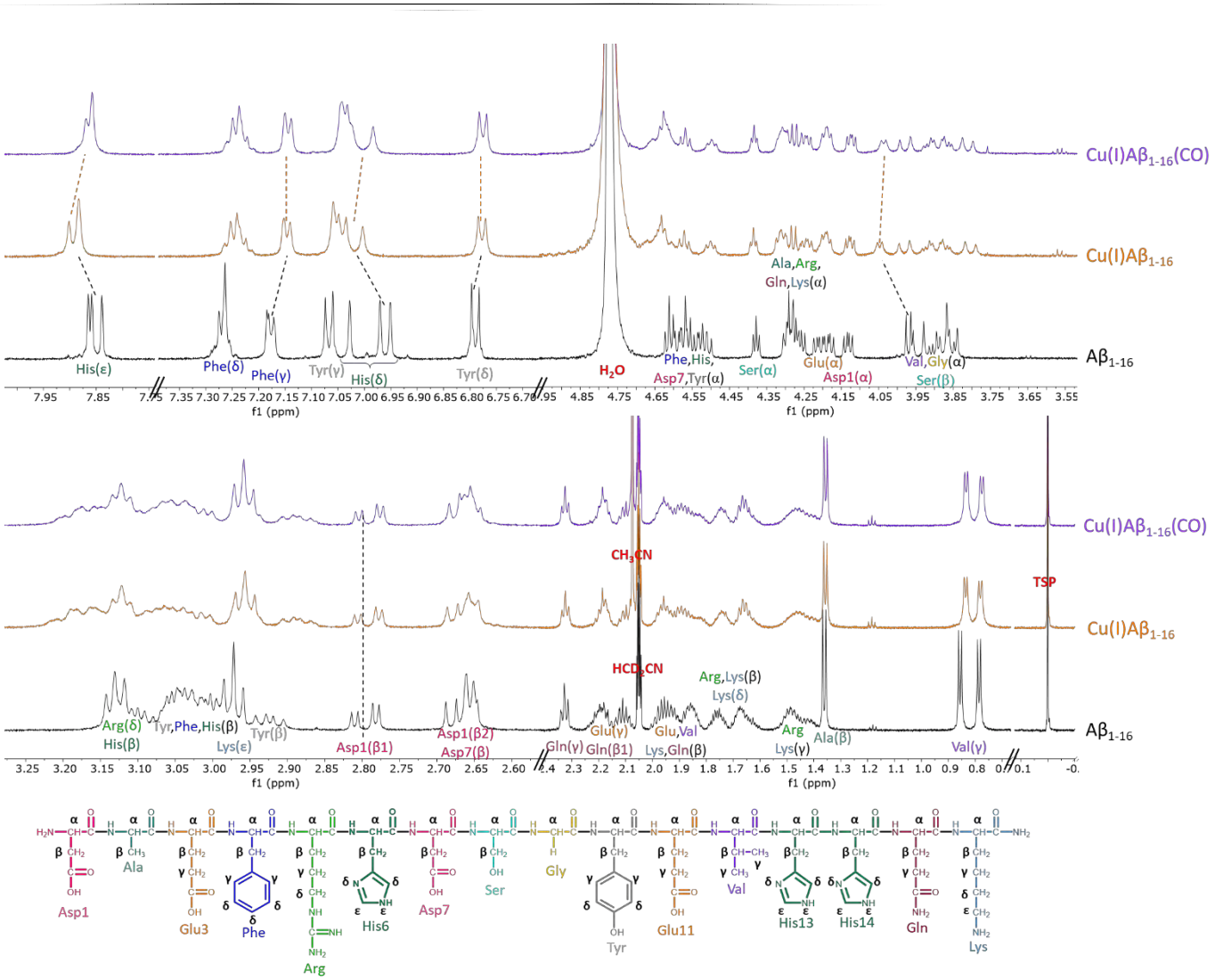

Figure V.A-4: ^{1}H NMR spectra of $A\beta_{1-16}$ (black) (Ar atmosphere), $Cu(I)A\beta_{1-16}$ (orange) (Ar atmosphere) and $Cu(I)A\beta_{1-16}(CO)$ (purple) (CO atmosphere) in CD_3CN/KPB pH 7.4 100 mM 10/90 v/v. The chemical shifts are indicated with dotted lines. Conditions: $[A\beta_{1-16}]$ = 2.2 mM; $[[Cu(CH_3CN)_4]BF_4]$ = 2 mM; [dithionite] = 3 mM; internal reference : TSP (0 ppm), (600 MHz).

The addition of CO, affects mainly protons from His residues by shifting them toward their free peptide position, as observed for His residues of $A\beta_{13-14}$ and $A\beta_{1-7}$. The other protons are not much affected revealing that the main organization of the peptide around the Cu(I) remains the same. Thus it is postulated that CO is coordinated to Cu(I) which induces the loss of linearity of the bis-His binding to Cu(I) similarly than for $Cu(I)A\beta_{13-14}(CO)$ (Scheme V.A-6).

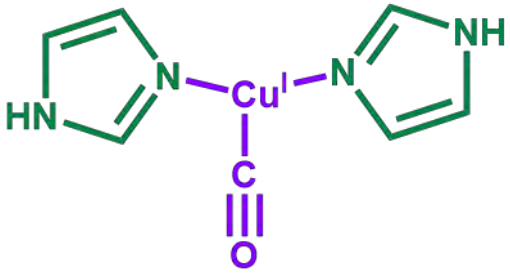

Scheme V.A-6: Binding mode proposition for $Cu(I)A\beta_{1-16}(CO)$ with a fast equilibrium between the three His couples.

Table V.A-4: Chemical shifts (δ) (in ppm) of ^1H NMR of $A\beta_{1-16}$, $Cu(I)A\beta_{1-16}$ and $Cu(I)A\beta_{1-16}(CO)$ in CD_3CN/KPB pH 7.4 100 mM 10/90 v/v and Δδ from free $A\beta_{1-16}$ to $Cu(I)A\beta_{1-16}$ and to $Cu(I)A\beta_{1-16}(CO)$ (only main protons from the residues affected are listed) (internal reference TSP = 0 ppm).

	His(ε)	**Phe(γ)**	**His(δ)**	**Val(α)**	**Val(β)**	**CH_3CN**	**HCD_2CN**
$Cu(I)A\beta_{1-16}(CO)$	7,869 7,858	7,144	7,027 6,984	4.037	0.834 0.776	2,074	2,051
$Cu(I)A\beta_{1-16}$	7,901 7,883	7,146	7,035 7,003	4.047	0.836 0.781	2,074	2,051
$\Delta_{Cu(I)-Cu(I)CO}$	*-0.028*	*-0.002*	*-0.013*	*-0.010*	*-0.004*	*0.000*	*0.000*
$A\beta_{1-16}$	7,865 7,858 7,839	7,177	7,028 6,970 6,951	3.969	0.856 0.786	-	2,051
$\Delta_{A\beta-Cu(I)}$	*+0.040*	*-0.031*	*+0.029*	*+0.078*	*-0.012*	-	*0.000*

For every peptides, the CH_3CN (coming from the source of Cu(I) salt) and HCD_2CN signals remain at the same position (2.07 ppm and 2.05 ppm) and no other signal that could be attributed to them is seen. Similarly to Cu(I)TMPA, no clear conclusion can be made about their coordination to Cu(I)Aβ model complexes. However, the electrochemical studies on Cu(II)Aβ in chapter IV, revealed that CH_3CN has an impact on Cu(I)Aβ state for each model.

The coordination of CO to Cu(I)Aβ complexes is confirmed by ^1H NMR studies. Similar behaviors are detected for chemical shifts of the protons located close to the coordination sites,

especially on His residues. The CO back-bonding properties applied to Cu(I) induces a chemical shift of His protons toward their free peptide position. However, the peptide is known to still be coordinated as the protons located on non-coordinating residues such as Phe or Ala are not much affected, meaning that the 3D structure and chemical environment is not much affected by the coordination of CO to Cu(I)Aβ complexes.

Comparison of the effects experienced by the three peptides upon addition of Cu(I) and further addition of CO revealed the specific behavior of $A\beta_{1-7}$ (containing only one His residues) compared to the other two two-His containing peptides. This is particularly obvious when comparing the impact on the protons of the first residues: weak impact in $A\beta_{1-16}$ and a strong one in $A\beta_{1-7.}$ The $A\beta_{13-14}$ seems to be an appropriate model of Cu(I) binding to the $A\beta_{1-16}$.

This seminal NMR study will have to be completed to gain more structural insights. Attribution of the protons resonances of $A\beta_{1-7}$ and $A\beta_{13-14}$ is foreseen, as well as study in ^{1}H-^{1}H 2D experiments to make possible to distinguish among protons in multiplet. Furthermore, Cu(I) addition will be performed progressively (by 0.25 equiv. per peptide for instance) to be able to track the impact on each signal (for close signals, it is not possible to decipher which goes where with 1D ^{1}H spectra at 0 and 1 equiv. only).

V.B. UV-Vis

V.B.1. TMPA

UV-Vis spectroscopy allows electronic transitions to be seen. Cu(I) ions have ten electrons in their d orbitals, thus no d-d transition can be observed so UV-Vis spectroscopy is not the best technique to follow their reactivity. However, when coordinated with ligands having empty low-energy π* orbitals such as aromatic, or carbonyl ligands, metal to ligand charge transfer (MLCT) band can be observed.[13] The appearance or disappearance of MLCT can probe the coordination of CO, but if no UV-Vis change is observed, no conclusion can be drawn.

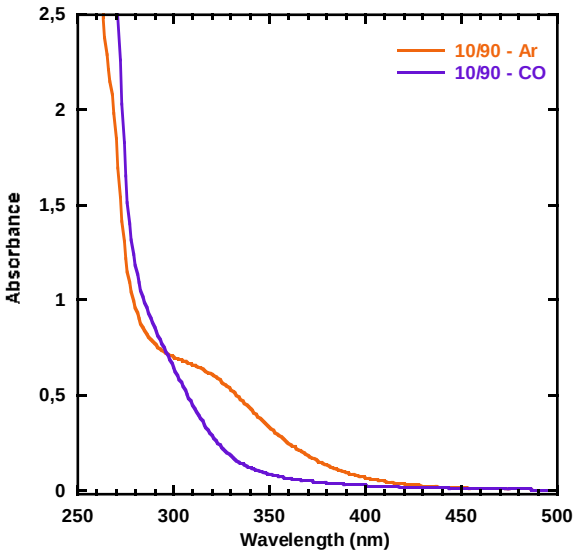

Figure V.B-1: UV-Vis spectra of Cu(I)TMPA under Ar (orange line) or CO atmosphere (purple line) in CH_3CN/HEPES 10/90 v/v. Conditions: [TMPA] = 0.22 mM; [Cu] = 0.2 mM; [HEPES pH 6.5] = 50 mM under Ar; [HEPES pH 7.4] = 100 mM under CO; ℓ = 1 cm; T = 25 °C.

Figure V.B-1 displays the UV-Vis spectra of Cu(I)TMPA under Ar or CO atmosphere in CH_3CN/HEPES 10/90 v/v. Cu(I)TMPA under Ar is characterized by a shoulder around 310 nm (ε = 3300 ± 170 $M^{-1}cm^{-1}$) attributed to MLCT from Cu(I) to TMPA. It is also observed in HEPES buffer at pH 7.0 and in organic solvents (THF, CH_3CN, EtCN) between 300 and 360 nm.[3, 14-15] Upon coordination of CO, this MLCT either disappeared or is blue-shifted and hidden behind the TMPA internal transition bands (Figure V.B-1). A similar observation was made in CH_3CN and in THF where the MLCT absorption decreases with the increasing amount of CO.[3]

V.B.2. Amyloid-β peptides

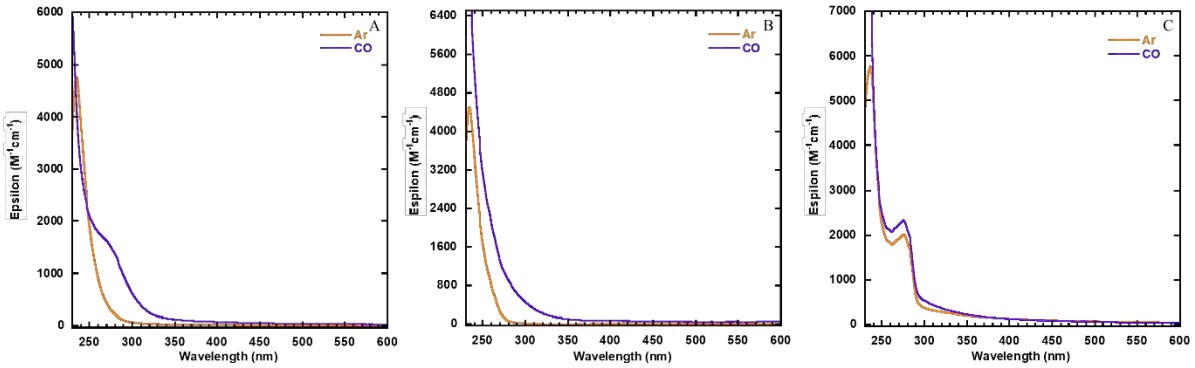

Figure V.B-2: UV-Vis spectra of Cu(I)Aβ (orange) and Cu(I)Aβ(CO) (purple) in CH_3CN/HEPES pH 7.4 100 mM 10/90; $Aβ_{13-14}$ (A), $Aβ_{1-7}$ (B) and $Aβ_{1-16}$ (C). Conditions: $[[Cu(CH_3CN)_4]BF_4]$ = 500 µM; [Aβ] = 550 µM; ℓ = 1 cm; T = 25 °C.

Figure V.B-2 displays the spectra of Cu(I)Aβ (orange lines) and Cu(I)Aβ(CO) (purple lines) for each Aβ model peptides ($Aβ_{13-14}$ (A); $Aβ_{1-7}$ (B) and $Aβ_{1-16}$ (C)) in CH_3CN/HEPES pH 7.4 100 mM 10/90 v/v.

The spectrum of Cu(I)$Aβ_{13-14}$ presents no characteristic transition band other than the internal band of the ligand. However, with the addition of CO a shoulder appeared at 263 nm ($\varepsilon = 1730 \pm 90$ $M^{-1}cm^{-1}$). It is attributed to a MLCT due to the coordination of CO to Cu(I).

As for Cu(I)$Aβ_{13-14}$, Cu(I)$Aβ_{1-7}$ did not present any characteristic band. The addition of CO induces an unresolved increase in the foot of the peptide absorption bands. From UV-Vis data, CO coordination to Cu(I)$Aβ_{1-7}$ could not be unambiguously observed.

The UV-Vis spectrum of Cu(I)$Aβ_{1-16}$ presents a band at 275 nm ($\varepsilon = 2010$ $M^{-1}cm^{-1}$) attributed to the absorbance of Tyr10 also seen for the peptide alone (*vide infra*), but no additional charge transfer band is observed. The addition of CO does not induce any significant UV-Vis change.

UV-Vis is not the best spectroscopic technique to monitor Cu(I) complexes in general. However, as CO possesses empty π* orbitals, it was hoped to observe its coordination *via* MLCT band from Cu(I). This was verified with TMPA and $Aβ_{13-14}$ with opposite behavior as the MLCT disappeared with CO coordination to Cu(I)TMPA (maybe because of strong blue shift) and appeared with Cu(I)$Aβ_{13-14}$. Those singular observations are directly link to Cu(I)

geometry and coordination mode, being different for Cu(I)TMPA(CO) and Cu(I)$A\beta_{13-14}$(CO). Unfortunately, no significant UV-Vis spectral change is observed with $A\beta_{1-7}$ and $A\beta_{1-16}$, either because the reaction failed (due to O_2 leak and oxidation of the Cu(I) complex) or because the amount of CO coordinated is too low, or the MLCT is hidden by internal ligand transitions. The experiments can be improved by working at higher concentration in Cu(I)L to better see the changes through the coordination of CO. Also the amount of CO can be increased by bubbling it directly in the UV-Vis cuvette. CH_3CN is a quite good coordinating ligand for Cu(I), thus it might be in competition with CO binding. Another organic co-solvent less coordinating, such as THF, could be used instead of CH_3CN.

V.C. Cyclic voltammetry

Cyclic voltammetry (CV) is an electrochemical technique to monitor the redox properties of a compound. CO by coordinating Cu(I) can modify redox properties of the complex.

V.C.1. TMPA

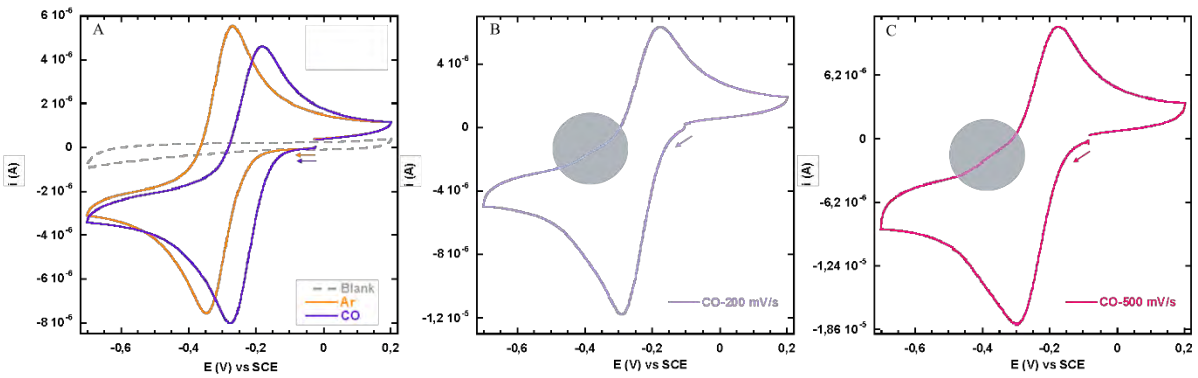

Figure V.C-1: Cyclic voltammograms (CVs) of Cu(II)TMPA(solvent) under Ar atmosphere (orange line), and CO atmosphere (purple, light purple and pink lines), and blank CV under Ar (grey dashed line) in CH_3CN/HEPES pH 7.4 100 mM 10/90 v/v. Conditions: [TMPA] = 0.75 mM; [$Cu(SO_4)$•$5H_2O$] = 0.5 mM; scan rate = 100 mV/s (A) or 200 mV/s (B, light purple) or 500 mV/s (C, pink); WE = Glassy carbon; Ref = SCE; CE = Pt wire. First scans are shown starting from the open circuit potential indicated by the arrows.

Figure V.C-1 displays the cyclic voltammograms of Cu-TMPA under Ar (orange line) and under CO atmosphere (purple and pink lines). Under Ar, Cu-TMPA in CH_3CN/HEPES pH 7.4 100 mM 10/90 has a $E_{1/2}$ = -0.31 V ($E_{1/2}$ = 0.37 V *vs* RHE) and a peak-to-peak separation of 0.08 V revealing a quasi-reversible one electron transfer process between

Cu(I)TMPA(solvent) and Cu(II)TMPA(solvent) (Figure V.C-1 (A) and Table V.C-1). The reversibility of the system is linked to fast electron transfer associated to weak reorganization energy between Cu(II) and Cu(I) redox states (Scheme V.C-1). Those values are consistent with literature data, with lower $E_{1/2}$ around 0.20 V *vs* RHE in aqueous buffered solution, and similar ΔE.[16-18] Indeed, as seen in chapter III, CH_3CN induces a shift of potential of Cu(II)TMPA toward more positive values.

Under CO atmosphere the $E_{1/2}$ is shifted by 0.08 V toward positive potentials mirroring the stabilization of the +I oxidation state by the coordination of CO while keeping the peak-to-peak separation almost constant (100mV). The origin of the slight decrease of reversibility observed (100 mV versus 80 mV in absence of CO) was questioned by varying the scan rate. Scanning at faster rate such as 200 mV/s (B, light purple line) and 500 mV/s (C, pink line) as shown in Figure V.C-1, revealed the apparition of a anodic peak at -0.36 V vs SCE (indicated by the blue circle) on the reverse scan. This could translate that the oxidation of Cu(I)TMPA(CO) goes through transient species (Scheme V.C-1). The shift of both anodic and cathodic waves to more positive potentials through the coordination of CO was already observed with dinuclear macrocyclic Cu complexes and a mononuclear Cu(I) complex with [difluoro-3,3'-(trimethylenedinitrilo)bis(2-butanone oximato)borate] ligand.[19-21] This shift toward positive potential values is attributed to Cu(I) stabilization by CO. On $Cu(I)(CH_3CN)_4$, it was shown that under CO, one CH_3CN is replaced by a carbonyl ligand. Its reversible redox behavior is accompanied by the loss of CO during oxidation and the formation of CO adduct during reduction by cyclic voltammetry coupled with IR studies.[22] Similar mechanism is expected in our case with an electrochemical-chemical-electrochemical mechanism type (Scheme V.C-1).

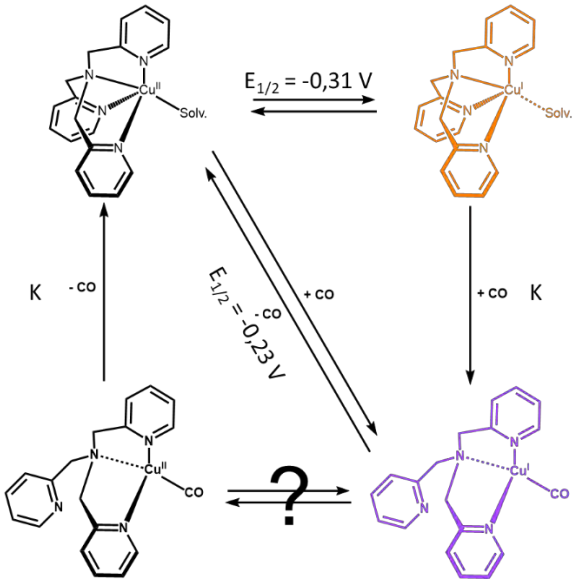

Scheme V.C-1: Electrochemical-chemical-electrochemical mechanisms for electron transfer process of Cu(II)TMPA under Ar and under CO atmosphere in CH_3CN/HEPES pH 7.4 10/90 v/v.

Table V.C-1: Cyclic voltammetry parameters for Cu(II)TMPA(solv.); Cu(II)Aβ$_{13-14}$; Cu(II)Aβ$_{1-7}$ and Cu(II)Aβ$_{1-16}$ in CH_3CN/HEPES pH 7.4 10/90 under Ar and CO atmospheres. Values given in V vs SCE.

	Atmosphere	E_{pc} (V)	E_{pa} (V)	ΔE (V)	$(E_{p,a} + E_{p,c})/2$ (V)
Cu-TMPA	Ar	-0.35	-0.27	0.08	-0.31
	CO	-0.28	-0.18	0.10	-0.23
Cu-Aβ$_{13-14}$	Ar	-0.59	-0.16	0.43	-0.38
	CO	-0.61	-0.11	0.50	-0.36
Cu-Aβ$_{1-7}$	Ar	-0.33	0.05	0.38	-0.14
	CO	-0.33	0.07	0.40	-0.13
Cu-Aβ$_{1-16}$	Ar	-0.53	0.23	0.76	-0.15
	CO	-0.53	0.23	0.76	-0.15

V.C.2. Amyloid-β peptides

Figure V.C-2 presents the cyclic voltammograms (CV) of Cu-Aβ$_{13-14}$, Cu-Aβ$_{1-7}$ and Cu-Aβ$_{1-16}$ in CH_3CN/HEPES pH 7.4 10/90 under Ar and CO atmospheres. The cyclic voltammogram of Cu(II)Aβ$_{1-16}$ was previously reported to be dependent on the concentration and the Cu:peptide ratio used, due to the amount of free Cu in solution.[23] For example a quasi-reversible shape was obtained at 0.2 mM of Cu(II)Aβ$_{1-16}$ complex concentration with a 1:1 Cu:Aβ ratio.[24] To overcome this issue, the Cu(II)Aβ complex concentration was 0.5 mM with a Cu:Aβ ratio of 1:5. Compared to the CV of Cu-TMPA under Ar, the Cu-Aβ complexes

displays non-reversible electron transfer process with peak-to-peak separation of 0.43 V; 0.38 V and 0.76 V respectively for Cu-Aβ$_{13-14}$, Cu-Aβ$_{1-7}$ and Cu-Aβ$_{1-16}$ (Table V.C-1). The irreversibility reveals slow electron transfer process and/or chemical-electrochemical associated processes (favored in our case).

The reduction of Cu(II)Aβ$_{13-14}$ occurs at -0.59 V vs. SCE and the anodic peak on the reverse scan at -0.16 V. The CV under argon of Cu-Aβ$_{13-14}$ is reminiscent of the one for a Cu(I)-bis-histidine complex in DMF, also irreversible,[25] and of other Cu(II) peptide complexes obtained with the motif H_2N-Xxx-His.[26] It corresponds to a Electrochemical-Chemical-Electrochemical-Chemical (ECEC) mechanism (chapter IV Scheme IV.B-3). The Cu(II) in the binding mode described in chapter IV (H_2N, N^-, Nim, $Nim_{second\ peptide}$) is first reduced (-0.59 V), then it reorganizes very rapidly to form the Cu(I) linearly bound by two His as described previously in this chapter. This latter species is oxidized at -0.16 V and the 2-His linearly bound Cu(II) evolved very rapidly to regenerate the starting Cu(II) species.

The cathodic and anodic potential values and peak-to-peak separations for Cu-Aβ$_{1-16}$, -0.53 V and 0.23 V and 0.76 V respectively are in agreement with the literature at pH 6.9 in piperazine-1,4-bis(2-ethanesulfonic acid) buffer of -0.43 V, 0.31 V and ΔE = 0.74 V.[9] A complete study by cyclic voltammetry of Cu-Aβ$_{1-16}$, elucidated the formation of the IBS mechanism (reminded in chapter IV, Scheme IV.B-1). Briefly, the Cu(II) resting state is in equilibrium with the Cu(II) in the IBS from which reduction occurs leading to Cu(I) in the IBS which further re-equilibrates with Cu(I) resting state (CEC mechanism).[23]

Cu-Aβ$_{1-7}$ has a similar profile than Cu-Aβ$_{1-16}$ and thus a similar mechanism is inferred. The peak-to-peak separation is weaker, the cathodic peak is broader than with the Aβ$_{1-16}$ peptide and this is the opposite for the anodic peak. This could mirror changes in the two equilibria (chapter IV Scheme IV.B-2).

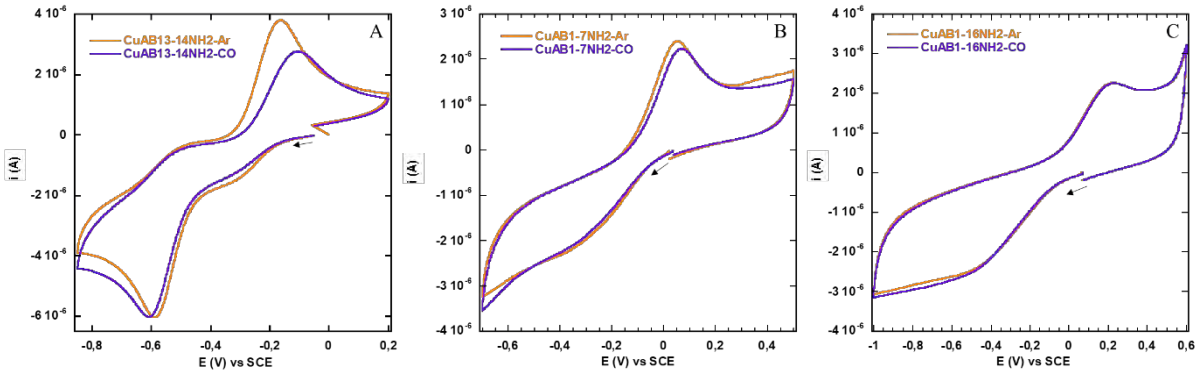

Figure V.C-2: Cyclic voltammogram (CV) of Cu-Aβ$_{13-14}$ (A); Cu-Aβ$_{1-7}$ (B) and Cu-Aβ$_{1-16}$ (C) under Ar (Orange) and under CO (purple) atmosphere in CH_3CN/HEPES pH 7.4 100 mM 10/90 v/v. Conditions: [Aβ] = 2.5 mM; [$Cu(SO_4)$•$5H_2O$] = 0.5 mM; scan rate = 100 mV/s; WE = Glassy carbon; Ref = SCE; CE = Pt wire. First scans are shown starting from the open circuit potential indicated by the arrows.

The cyclic voltammetry under CO atmosphere induces changes on the CV of Cu-Aβ$_{13-14}$ and Cu-Aβ$_{1-7}$ models and no change for Cu-Aβ$_{1-16}$ (Figure V.C-2, purple CV). For Cu-Aβ$_{13-14}$, a weak cathodic shift is observed on the reduction peak and a more significant anodic shift is observed on the oxidation peak. This mirrors the more difficult reoxidation of the electro generated bis-His-Cu(I) in presence of CO, in line with CO binding to the Cu(I) and stabilizing it. The electron transfer process remains the same ECEC mechanism as for Cu-Aβ$_{13-14}$ given in chapter IV with the coordination/decoordination of CO during the chemical rearrangement steps (Scheme V.C-2).

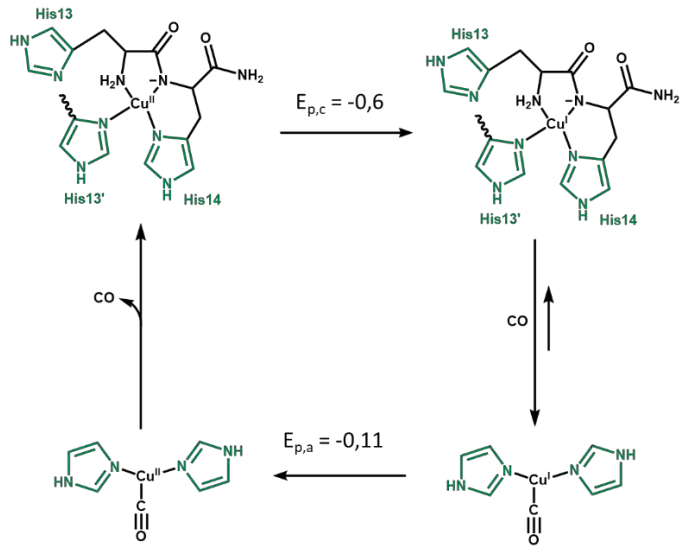

Scheme V.C-2: Electrochemical-chemical-electrochemical-chemical mechanisms for electron transfer process of Cu(II)Aβ$_{13-14}$ under CO atmosphere in CH_3CN/HEPES pH 7.4 10/90 v/v. His13' belongs to a second Aβ$_{13-14}$ peptide.

For Cu-Aβ$_{1-7}$, similar trends are observed but to a lesser extent. This could mirror that CO stabilize some of the Cu-Aβ$_{1-7}$ disfavoring the equilibrium with the IBS. The mechanism would remain the same as under argon but Cu(I)Aβ$_{1-7}$ will be in equilibrium with Cu(I)Aβ$_{1-7}$(CO) (Scheme V.C-3).

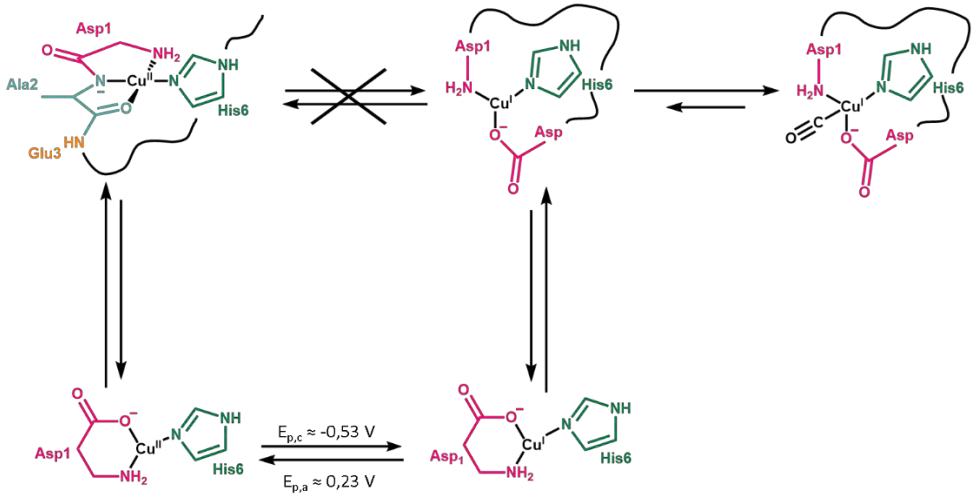

Scheme V.C-3: Chemical-electrochemical-chemical-chemical mechanisms for electron transfer process of Cu(II)Aβ$_{1-7}$ under CO atmosphere in CH$_3$CN/HEPES pH 7.4 10/90 v/v.

In case of Cu-Aβ$_{1-16}$, the absence of modification of the CV with CO addition indicated that binding of the CO to the Cu(I)Aβ$_{1-16}$ (observed by NMR) doesn't modify the equilibrium with the IBS.

Studies as function of the scan rates could afford more insights into the equilibria at play.

V.D. FT-IR

FT-IR is usually the spectroscopic method of choice to monitor the binding of CO to a compound. Indeed, the stretching frequency of CO triple bond is related to its bond strength that will be affected by its coordination to Cu(I). The position of the band can give information on the coordination of an ancillary ligand. Cu(I)TMPA is known to display two bands for CO stretching frequency. One around 2092 cm^{-1} (in CH_3CN) solution that was attributed to Cu(I)TMPA(CO) with a pyridyl-arm uncoordinated and the second one around 2077 cm^{-1} (in solid-state) corresponding to Cu(I)TMPA(CO) being coordinated by all the N-atoms from TMPA. The coordination sphere corresponding to υ_{CO} = 2092 cm^{-1} was elucidated thanks to another Cu(I)PY1(CO) complex (PY1 = tridentate ligand bis-(2-picolyl)amine, an analog of TMPA lacking a pyridyl-arm) displaying a CO band at the same frequency. The one at υ_{CO} = 2077 cm^{-1} was observed from solid-state Cu(I)TMPA(CO) prepared in Nujol mull and attributed according to the structure determined by X-ray spectroscopy.[3] Cu(I)TMPA(CO) is analyzed first in our aqueous conditions, *i.e.* CH_3CN/HEPES pH 7.4 10/90 v/v, to see how the υ_{CO} evolve. The Cu(I)Aβ(CO) models will be then studied in the same conditions and their CO bands compared with the one from Cu(I)TMPA(CO).

However, we have encountered several technical difficulties. HEPES buffer is very noisy between 2200 and 2000 cm^{-1} making the observation of IR band difficult. Gas bubbles were sometimes observed in the IR cell although the liquid was well introduced probably due to CO exhaust and CH_3CN evaporation, affecting the baseline of the spectrum. Oxygen leak is also fast happening during the loading of the solution into the cell, causing the oxidation of the Cu(I) complex and thus the loss of CO coordination.

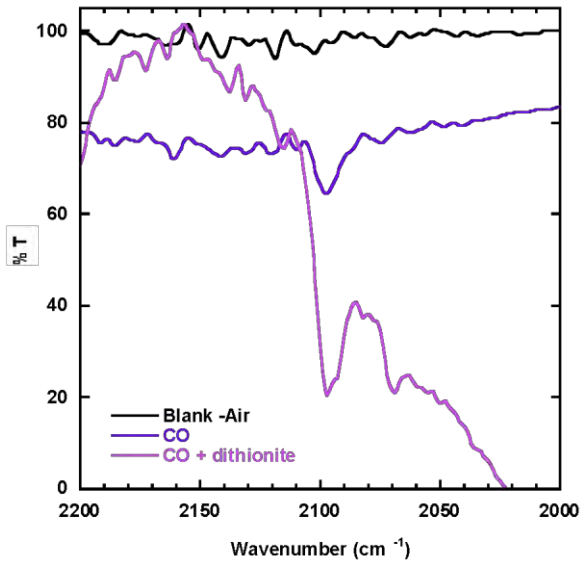

Figure V.D-1: FT-IR spectra of Cu(I)TMPA(CO) in CH_3CN/HEPES pH 7.4 100 mM 10/90 v/v (purple) and in presence of dithionite (light purple), and blank spectrum under air (black) centered on CO stretching band area. Conditions: [TMPA] = 2.2 mM; [$[Cu(CH_3CN)_4]BF_4$] = 2 mM; [dithionite] = excess.

Figure V.D-1 presents the IR spectra of Cu(I)TMPA(CO) with and without the presence of dithionite in CH_3CN/HEPES pH 7.4 10/90. On both spectra a band is seen at 2097 cm^{-1} corresponding to the CO stretching band assigned to Cu(I)TMPA(CO) with one pyridine arm uncoordinated as proposed in pure CH_3CN with a band at 2092 cm^{-1}.[3] The IR spectrum of Cu(I)TMPA(CO) in presence of dithionite also displays a second small band at 2070 cm^{-1} that could be attributed to CO stretching frequency when all the pyridine rings are coordinated to Cu(I) as observed in solid-state with a frequency at 2077 cm^{-1}.[3] The two CO stretching bands were also observed simultaneously at 2091 cm^{-1} and 2070 cm^{-1} in CH_3CN.[27] The baseline of the spectrum of Cu(I)TMPA(CO) in presence of dithionite is not flat due to the starting evaporation of the solvent in the IR cell.

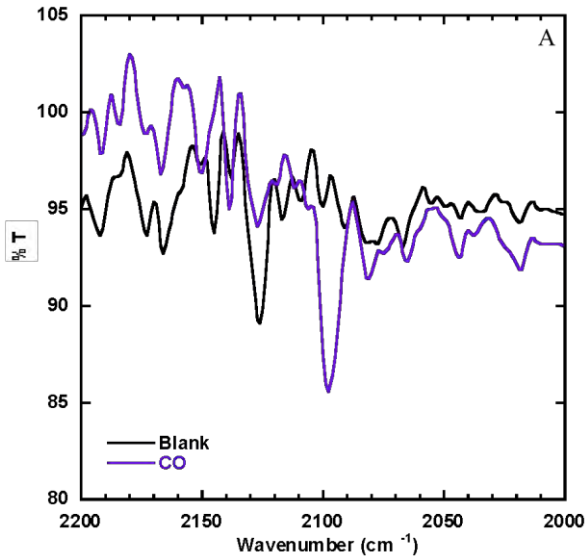

Figure V.D-2: FT-IR spectra of Cu(I)Aβ$_{13-14}$(CO) (purple) and blank spectrum under air in CH_3CN/HEPES pH7.4 100 mM 10/90 v/v. Conditions: [Aβ] = 2.2 mM; [[Cu(CH_3CN)$_4$]BF_4] = 2 mM.

Figure V.D-2 shows the IR spectra of Cu(I)Aβ$_{13-14}$(CO) in HEPES buffer pH 7.4 with 10 % of CH_3CN. The CO stretching is seen at 2098 cm^{-1}, very close to the υ_{CO} of Cu(I)TMPA(CO). This frequency is in the range of other bis-histidine Cu(I) complexes in organic solvents with υ_{CO} between 2110 and 2105 cm^{-1} [25] and 2092 cm^{-1}.[28] The CO frequencies for two coordinates Cu(I) complexes are usually higher around 2115-2120 cm^{-1}, and lower for three coordinates between 2060 cm^{-1} and 2090 cm^{-1}.[29]

For Cu(I)Aβ$_{1-7}$(CO) and Cu(I)Aβ$_{1-16}$(CO), no clear CO band could be detected although during the record of the spectra probable CO band were distinguished giving good hope to better see them in different conditions mentioned after.

No clear and strong conclusion can be made for the Cu(I)Aβ(CO) species based on FT-IR, as the probable CO stretching bands are not really getting out of the background noise. Further improvements could be made to strengthen the result: working in D_2O could help to reduce the background noise; increasing the concentration would increase the intensity of the band; using a tighter IR cell would prevent the evaporation and leakage.

V.E. Conclusion

The coordination of CO to Cu(I)TMPA is confirmed by each spectroscopic technique ^{1}H NMR, UV-Vis, FT-IR and cyclic voltammetry in biologically relevant media. It is proposed that Cu(I)TMPA has a coordination sphere including the 4 N atoms from TMPA and a molecule of solvent in the apical position, whereas Cu(I)TMPA(CO) is coordinated by the N_{alkyl} amine, two of the three pyridine rings and CO (Scheme V.E-1). Not many Cu(I)(CO) complexes in aqueous solvent are reported in literature.[30-32] Probing the coordination of CO to the Cu(I)Aβ peptides is much harder than for Cu(I)TMPA. The ^{1}H NMR is the main technique confirming the coordination of CO to the three model complexes and allow the proposition for binding mode. Cu(I)Aβ$_{13-14}$ and Cu(I)Aβ$_{1-16}$ would be coordinated in linear fashion between two histidine residues and CO will be added to form 3-coordinate compounds inducing a loss of the linearity in the binding mode (Scheme V.E-1). Cu(I)Aβ$_{1-7}$, on the other hand is a 3-coordinate Cu(I) complex and become a 4-coordinate with the binding of CO (Scheme V.E-1). UV-Vis, FT-IR and cyclic voltammetry studies are in agreement for the binding of CO to Cu(I)Aβ$_{13-14}$. However for the two other Cu(I) complexes, there is no proof of the coordination of CO.

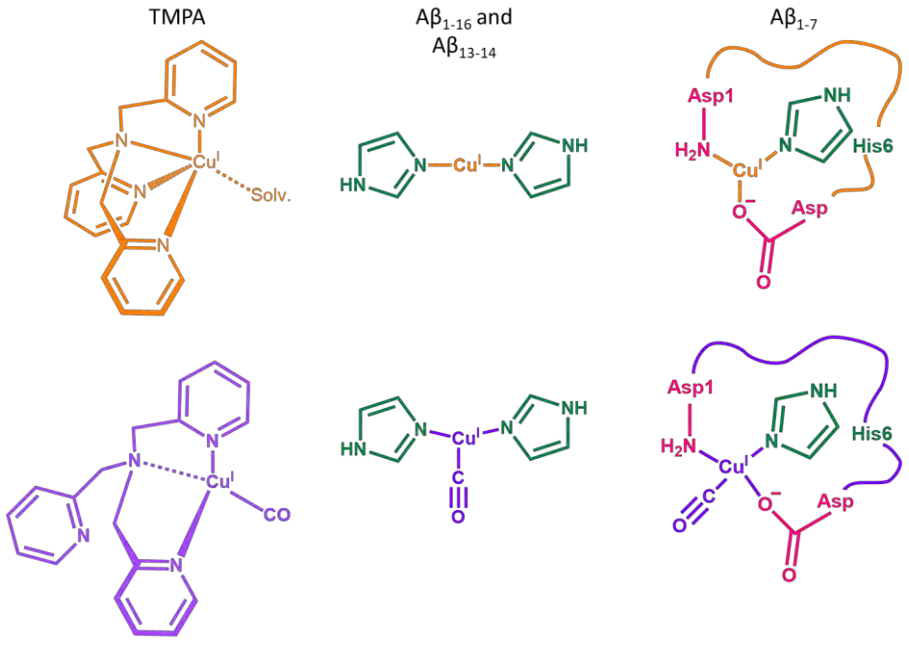

Scheme V.E-1: Binding mode proposition for Cu(I)Aβ$_{13-14}$ and Cu(I)Aβ$_{1-16}$ in linear fashion between two histidine residues(orange left); Cu(I)Aβ$_{13-14}$(CO) and Cu(I)Aβ$_{1-16}$(CO) in distorted T-shaped geometry (purple left); Cu(I)Aβ$_{1-7}$ with the N-terminal amine from Asp1, the imidazole ring from His6 and the carboxylate function from one Asp (orange right) and Cu(I)Aβ$_{1-7}$(CO) having the same coordination sphere with the addition CO (purple right).

Working with reduced Cu(I) complex in aqueous solution can be tricky as the trace amount of O_2 oxidized fast the complex to Cu(II) and no reactivity toward CO can be observed anymore. The cyclic voltammetry has the advantage to electrochemically reduced Cu(II) and it is easy enough to work under inert conditions, especially with argon which is a heavier gas (1.661 kg/m^3) than O_2 (1.205 kg/m^3). The electrochemical cell is not tight and working under CO (1.165 kg/m^3) atmosphere is harder as O_2 is heavier, and for safety reason the experiment is run under fume hood so the CO gas is evaporated away. For the other spectroscopic techniques, cells or tube equipped with septum cap can be used, but they don't fully prevent O_2 leakage. A dithionite reductant was used for ^{1}H NMR which is convenient as it also reduced O_2, however it is not convenient in UV-Vis as its absorption band (315 nm or 265 nm in case of ascorbate) matches the area of charge transfer of interest.

Hopefully, the experiments can be improved by increasing the concentration of Cu(I)L(CO) compounds under study to avoid the background noise effect (FT-IR) and reduced the impact of oxidation by trace amount of O_2. Preparing the Cu(I) solution in glovebox would also simplified the experiment and reduced the risk of O_2 contamination, or evaporation by the use of gas tight equipment (Young NMR tube) into which CO can be loaded without needle hole.

References

1. Eckenhoff, W. T.; Pintauer, T., Structural Comparison of Copper(I) and Copper(II) Complexes with Tris(2-pyridylmethyl)amine Ligand. *Inorganic Chemistry* **2010,** *49* (22), 10617-10626.

2. Wilson, N. Studies on the reactivity of copper complexes with NO and CO, and their applications in molecular imaging. Imperial College London, 2012.

3. Fry, H. C.; Lucas, H. R.; Narducci Sarjeant, A. A.; Karlin, K. D.; Meyer, G. J., Carbon Monoxide Coordination and Reversible Photodissociation in Copper(I) Pyridylalkylamine Compounds. *Inorganic Chemistry* **2008,** *47* (1), 241-256.

4. Zhang, C. X.; Kaderli, S.; Costas, M.; Kim, E.-i.; Neuhold, Y.-M.; Karlin, K. D.; Zuberbühler, A. D., Copper(I)−Dioxygen Reactivity of [(L)CuI]+ (L = Tris(2-pyridylmethyl)amine): Kinetic/Thermodynamic and Spectroscopic Studies Concerning the Formation of Cu−O2 and Cu2−O2 Adducts as a Function of Solvent Medium and 4-Pyridyl Ligand Substituent Variations. *Inorganic Chemistry* **2003,** *42* (6), 1807-1824.

5. Eckenhoff, W. T.; Garrity, S. T.; Pintauer, T., Highly Efficient Copper-Mediated Atom-Transfer Radical Addition (ATRA) in the Presence of Reducing Agent. *European Journal of Inorganic Chemistry* **2008,** *2008* (4), 563-571.

6. De Gregorio, G.; Biasotto, F.; Hecel, A.; Luczkowski, M.; Kozlowski, H.; Valensin, D., Structural analysis of copper(I) interaction with amyloid β peptide. *Journal of Inorganic Biochemistry* **2019,** *195*, 31-38.

7. Cheignon, C.; Jones, M.; Atrián-Blasco, E.; Kieffer, I.; Faller, P.; Collin, F.; Hureau, C., Identification of key structural features of the elusive Cu–Aβ complex that generates ROS in Alzheimer's disease. *Chemical Science* **2017,** *8* (7), 5107-5118.

8. Cheignon, C.; Faller, P.; Testemale, D.; Hureau, C.; Collin, F., Metal-catalyzed oxidation of Aβ and the resulting reorganization of Cu binding sites promote ROS production†. *Metallomics* **2016,** *8* (10), 1081-1089.

9. Hureau, C.; Balland, V.; Coppel, Y.; Solari, P. L.; Fonda, E.; Faller, P., Importance of dynamical processes in the coordination chemistry and redox conversion of copper amyloid-β complexes. *Journal of Biological Inorganic Chemistry* **2009,** *14* (7), 995-1000.

10. Alies, B.; Badei, B.; Faller, P.; Hureau, C., Reevaluation of Copper(I) Affinity for Amyloid-β Peptides by Competition with Ferrozine—An Unusual Copper(I) Indicator. *Chemistry – A European Journal* **2012,** *18* (4), 1161-1167.

11. Esmieu, C.; Ferrand, G.; Borghesani, V.; Hureau, C., Impact of N-Truncated Aβ Peptides on Cu- and Cu(Aβ)-Generated ROS: CuI Matters! *Chemistry – A European Journal* **2021,** *27* (5), 1777-1786.

12. Yako, N.; Young, T. R.; Cottam Jones, J. M.; Hutton, C. A.; Wedd, A. G.; Xiao, Z., Copper binding and redox chemistry of the Aβ16 peptide and its variants: insights into determinants of copper-dependent reactivity†. *Metallomics* **2017,** *9* (3), 278-291.

13. Förster, H., UV/vis spectroscopy. *Characterization I* **2004**, 337-426.

14. Wei, N.; Murthy, N. N.; Tyeklar, Z.; Karlin, K. D., Copper(I) Complexes with Pyridyl- and Imidazoyl-Containing Tripodal Tetradentate Ligands and Their Reactions with Dioxygen. *Inorganic Chemistry* **1994,** *33* (6), 1177-1183.

15. Asahi, M.; Yamazaki, S.-i.; Itoh, S.; Ioroi, T., Acid-base and redox equilibria of a tris(2-pyridylmethyl)amine copper complex; their effects on electrocatalytic oxygen reduction by the complex. *Electrochimica Acta* **2016,** *211*, 193-198.

16. Langerman, M.; Hetterscheid, D. G. H., Fast Oxygen Reduction Catalyzed by a Copper(II) Tris(2-pyridylmethyl)amine Complex through a Stepwise Mechanism. *Angewandte Chemie International Edition* **2019,** *58* (37), 12974-12978.

17. Nagao, H.; Komeda, N.; Mukaida, M.; Suzuki, M.; Tanaka, K., Structural and Electrochemical Comparison of Copper(II) Complexes with Tripodal Ligands. *Inorganic Chemistry* **1996,** *35* (23), 6809-6815.

18. Baek, H. K.; Holwerda, R. A., An Sulfur-Bonded Adduct of Cysteine with [tris (2-pyridylmethyl) amine] copper (II) Ion. *Inorganic Chemistry* **1983,** *22* (23), 3452-3456.

19. Gagne, R. R.; Allison, J. L.; Gall, R. S.; Koval, C. A., Models for copper-containing proteins: structure and properties of novel five-coordinate copper(I) complexes. *Journal of the American Chemical Society* **1977,** *99* (22), 7170-7178.

20. Gagne, R. R.; Koval, C. A.; Smith, T. J.; Cimolino, M. C., Binuclear complexes of macrocyclic ligands. Electrochemical and spectral properties of homobinuclear CuIICuII, CuIICuI, and CuICuI species including an estimated intramolecular electron transfer rate. *Journal of the American Chemical Society* **1979,** *101* (16), 4571-4580.

21. Nanda, K. K.; Addison, A. W.; Paterson, N.; Sinn, E.; Thompson, L. K.; Sakaguchi, U., Copper(II) and Nickel(II) Complexes of Dianionic and Tetraanionic Dinucleating Macrocycles. *Inorganic Chemistry* **1998,** *37* (5), 1028-1036.

22. Hernandez, R. M.; Aiken, L.; Baker, P. K.; Kalaji, M., Copper(I) carbonyl ([Cu(NCMe)4−n(CO)n][BF4]); in situ spectroscopic, electrochemical and spectroelectrochemical studies. *Journal of Electroanalytical Chemistry* **2002,** *520* (1), 53-63.

23. Balland, V.; Hureau, C.; Savéant, J.-M., Electrochemical and homogeneous electron transfers to the Alzheimer amyloid-β copper complex follow a preorganization mechanism. *Proceedings of the National Academy of Sciences* **2010,** *107* (40), 17113-17118.

24. Jiang, D.; Men, L.; Wang, J.; Zhang, Y.; Chickenyen, S.; Wang, Y.; Zhou, F., Redox Reactions of Copper Complexes Formed with Different β-Amyloid Peptides and Their Neuropathalogical Relevance. *Biochemistry* **2007,** *46* (32), 9270-9282.

25. Himes, R. A.; Park, G. Y.; Barry, A. N.; Blackburn, N. J.; Karlin, K. D., Synthesis and X-ray Absorption Spectroscopy Structural Studies of Cu(I) Complexes of HistidylHistidine

Peptides: The Predominance of Linear 2-Coordinate Geometry. *Journal of the American Chemical Society* **2007,** *129* (17), 5352-5353.

26. Hureau, C.; Eury, H.; Guillot, R.; Bijani, C.; Sayen, S.; Solari, P.-L.; Guillon, E.; Faller, P.; Dorlet, P., X-ray and Solution Structures of CuIIGHK and CuIIDAHK Complexes: Influence on Their Redox Properties. *Chemistry – A European Journal* **2011,** *17* (36), 10151-10160.

27. Hsu, S. C. N.; Chien, S. S. C.; Chen, H. H. Z.; Chiang, M. Y., Synthesis and Characterization of Copper(I) Complexes Containing Tri(2-Pyridylmethyl)Amine Ligand. *Journal of the Chinese Chemical Society* **2007,** *54* (3), 685-692.

28. Park, G. Y.; Lee, J. Y.; Himes, R. A.; Thomas, G. S.; Blackburn, N. J.; Karlin, K. D., Copper–Peptide Complex Structure and Reactivity When Found in Conserved His-Xaa-His Sequences. *Journal of the American Chemical Society* **2014,** *136* (36), 12532-12535.

29. Sorrell, T. N.; Jameson, D. L., Synthesis, structure, and reactivity of monomeric two-coordinate copper(I) complexes. *Journal of the American Chemical Society* **1983,** *105* (19), 6013-6018.

30. Rondelez, Y.; Bertho, G.; Reinaud, O., The First Water-Soluble Copper(I) Calix[6]arene Complex Presenting a Hydrophobic Ligand Binding Pocket: A Remarkable Model for Active Sites in Metalloenzymes. *Angewandte Chemie International Edition* **2002,** *41* (6), 1044-1046.

31. Hernández-R, R. M.; Kalaji, M., Electrochemical reactions of CO on polycrystalline copper electrodes. *Journal of Electroanalytical Chemistry* **1997,** *434* (1), 209-215.

32. Ogura, T., Complex formation of copper (I) perchlorate with ethylene or carbon monoxide in water and isolation of related complexes. *Inorganic Chemistry* **1976,** *15* (9), 2301-2303.

Chapter VI

Chapter VI. O_2 reactivity of Cu(I) complexes (with TMPA and Aβ peptides as ancillary ligands)

VI.A. Reactive oxygen species production

Ascorbate is a physiological reductant. Dioxygen has a triplet ground state and thus cannot react directly with ascorbate to generate reactive oxygen species (ROS), it requires a catalyst. Cu complexes can be good candidates in the catalysis of dioxygen reduction by cycling between their +I and +II oxidation states.[1] The ascorbate oxidation potential in aqueous solution at pH 7.1 is close to 0 V vs SCE.[2] Cu(II) complexes with an appropriate redox potential can be reduced by ascorbate to form the reduced Cu(I) complexes and this latter can react with O_2 to produce ROS. The consumption of ascorbate has been shown to be directly correlated to the ROS production by Cu-Aβ complexes.[3] Monoanionic ascorbate (Asc) displays a strong UV-Vis absorbance at 265 nm (with $\varepsilon = 14500\ M^{-1}cm^{-1}$). Thus, Asc consumption can be easily and directly followed by UV-Vis spectroscopy to give information on the ROS production. The ascorbate depletion is linked to the reduction of O_2 to H_2O_2 and further $HO^{\bullet}$ following two reactions depicted in Scheme VI.A-1.

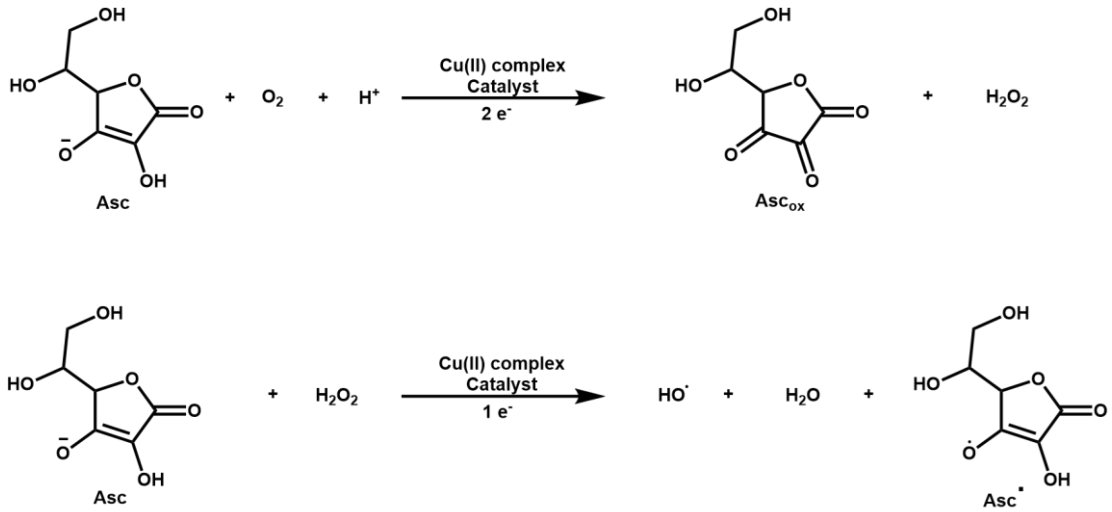

Scheme VI.A-1: Ascorbate oxidation by O_2 and H_2O_2 catalyzed by a Cu complex.

Different starting conditions for ROS production can be monitored, starting from (i) Cu(II) and triggered by addition of ascorbate, (ii) Cu(I) and triggered by addition of air, (iii) a mixture of Cu(II) and Cu(I) when the ligand under study is added during the Asc consumption

(Table VI.A-1). In the former case, two parameters are evaluated: the ability of the ligand to (i) bind Cu(II) and to (ii) form a Cu(II) species resistant to reduction by Asc. In the middle case, similarly the ability of the ligand to (i) bind Cu(I) and to (ii) form a Cu(I) species resistant to oxidation by dioxygen. In the latter case, the ability to form one stable species (either the Cu(I) or the Cu(II) complex) is sought. This is the one performed in our case. The ascorbate consumption was studied for Cu(I)/(II)TMPA and each Cu(I)/(II)Aβ model in HEPES pH 7.4 and in CH_3CN/HEPES pH 7.4 10/90 v/v to check for the influence of CH_3CN. The absorbance of ascorbate is followed by UV-vis and the maximum of absorbance (at 265 nm) is plotted as a function of time. The complexes are generated *in situ*, first the ascorbate is added into the UV-vis cuvette at 30 s, then the Cu(II)SO_4 at 180 s and finally the ligand at 240 s when Cu(I) and Cu(II) are coexisting (Figures VI-B-1; VI-C-1; VI-C-2; VI-C-3). A control of ascorbate consumption in HEPES and with 10 % CH_3CN (black and grey lines respectively) shows that ascorbate remains stable over time in both conditions. In HEPES pH 7.4, the addition of Cu(II)SO_4 salt to ascorbate (without any ligand) induces a fast consumption of ascorbate ($k = 2.80\ ms^{-1}$) in about 15 min (orange line). However, with 10 % of CH_3CN the decrease of the absorbance at 265 nm is slower ($k = 0.21\ ms^{-1}$) and only half of ascorbate has been consumed after 1 hour (yellow line). This behavior is in line with the fact that CH_3CN stabilizes Cu(I) in aqueous solution, as shown in the previous chapter IV (IV.B.1.).[4] CH_3CN, by stabilizing Cu(I) state shifts the redox potential of the Cu(II)/Cu(I) couple toward higher potentials farther from the reduction potential of O_2, thus disfavoring the oxidation of Cu(I) by O_2. For each Cu(I)L model there is a fast Asc consumption by free Cu before the addition of the ligand, in HEPES and slower in presence of 10 % CH_3CN, thus the concentration in Asc at the beginning of the consumption by Cu(I)L is different in both solvent systems, and is taken into account for the rate constant calculations (k in ms^{-1}).

Table VI.A-1: Different conditions for ROS production monitored by ascorbate consumption.

	Starting conditions	**Trigger**	**Evaluated parameters**
(i)	Cu(II)	addition of ascorbate	ability of ligand to bind Cu(II) and form a Cu(II) complex resistant to ascorbate reduction
(ii)	Cu(I)	addition of air	ability of ligand to bind Cu(I) and form a Cu(I) complex resistant to dioxygen oxidation
(iii)	Cu(II)/Cu(I) mixture	addition of ligand during the ascorbate consumption	ability to form a stable complex either Cu(II) or Cu(I)

VI.B. TMPA

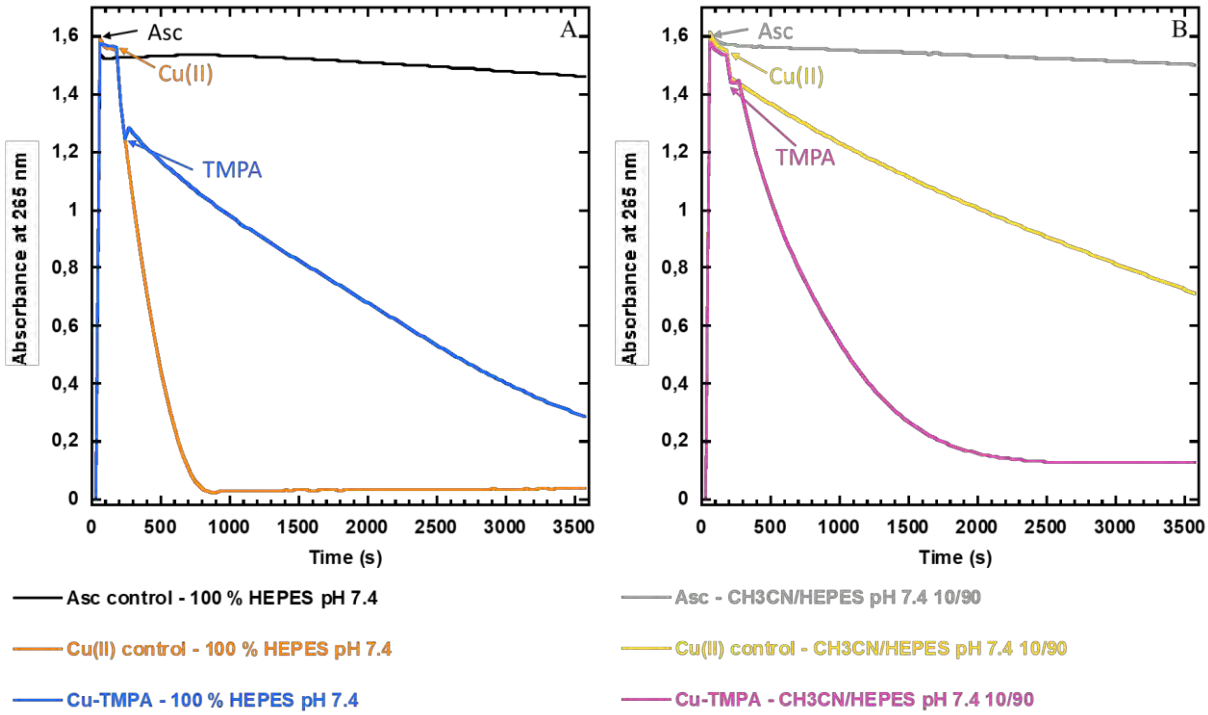

Figure VI.B-1: Ascorbate consumption by Cu(II)/Cu(I)TMPA (blue and pink lines), free Cu (orange and yellow lines) and control (black and grey lines) followed by UV-Vis (λ = 265 nm) as a function of reaction time (s) in CH_3CN/HEPES pH 7.4 100 mM 0/100 (A) and 10/90 (B) v/v. Conditions: [Asc] = 100 µM; [$Cu(SO_4)•5H_2O$] = 10 µM [TMPA] = 12 µM; ℓ = 1 cm; T = 25 °C.

Figure VI.B-1 shows the ascorbate consumption by Cu(I)/(II)TMPA in CH_3CN/HEPES pH 7.4 0/100 (panel A) and 10/90 (panel B). In HEPES pH 7.4 the rate of depletion of the band at 265 nm is moderate (k = 0.38 ms^{-1}), with about 20 % of the total amount of ascorbate remaining after one hour, meaning that either the reduction of Cu(II)TMPA to Cu(I)TMPA by ascorbate or the oxidation of Cu(I)TMPA by O_2 is slow, or both. However, Cu(I)TMPA is already known to catalyze the reduction of O_2 in aqueous solution by electrochemical studies,[5-7] thus the oxidation of Cu(I)TMPA to Cu(II)TMPA should be fast and the reduction is postulated to be the unfavorable step (Scheme VI.B-1). The addition of 10 % CH_3CN speed up the consumption of ascorbate (k = 1.23 ms^{-1}), being complete after about 45 min, compare to Cu-TMPA without CH_3CN (not complete after 1h) (Figure VI.C-4). As mentioned in previous chapter III (III.B.4.b), CH_3CN by stabilizing the Cu(I)TMPA state, shifts the redox potential of Cu(II)/Cu(I)TMPA toward more positive potentials compare to pure aqueous solution. The

reduction of Cu(II)TMPA to Cu(I)TMPA by ascorbate is thus favored and the rate of ROS production increased (Scheme VI.B-1).

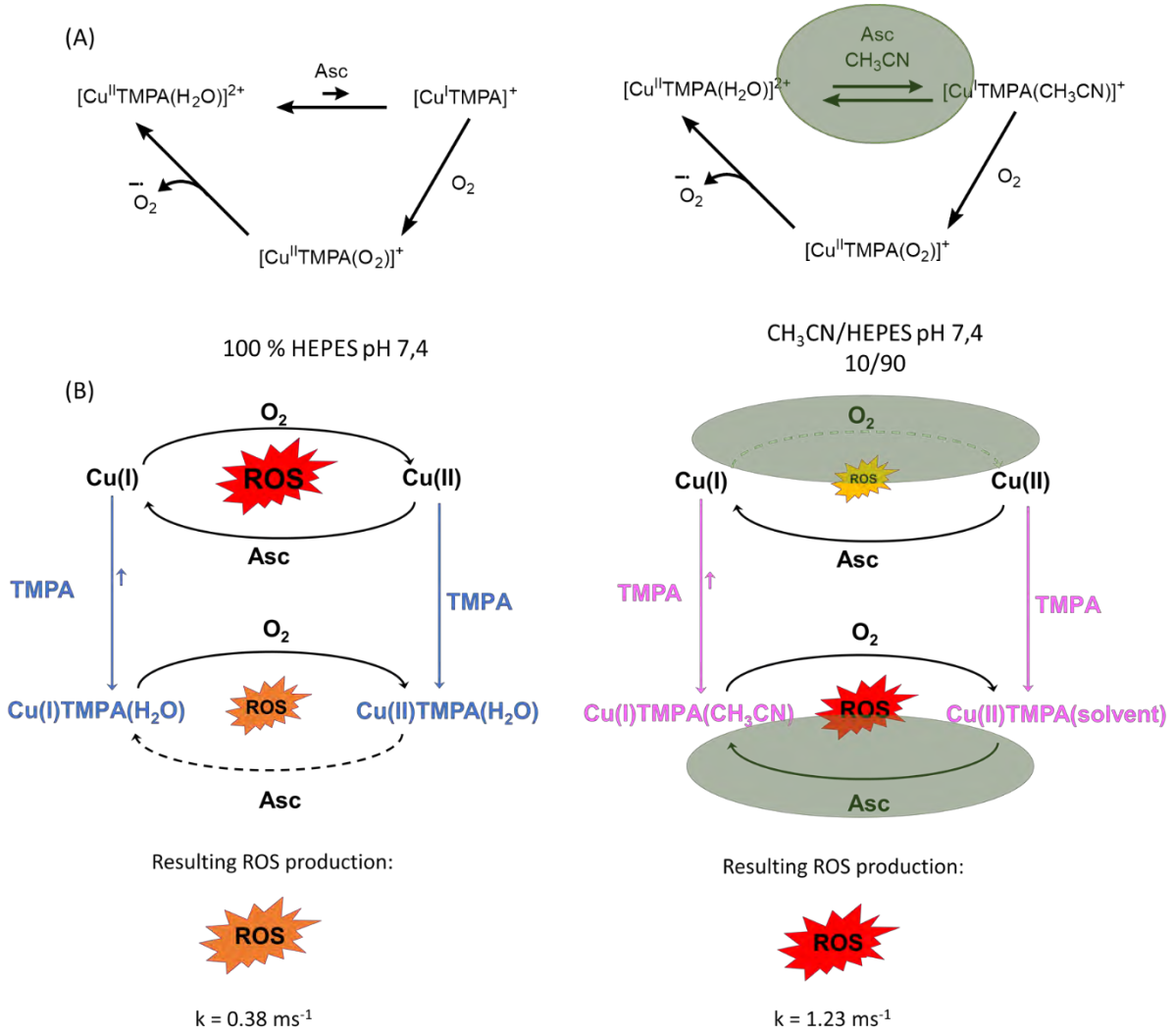

Scheme VI.B-1: Proposed mechanisms for ROS production by Cu-TMPA in HEPES pH 7.4 (left) and with 10 % CH_3CN (right) v/v. (A) The impact of CH_3CN on Cu-TMPA favors its reduction by ascorbate as indicated by the green circle. (B) Impact of CH_3CN on ROS production: decrease of ROS production by free Cu by disfavoring the oxidation of Cu(I) to Cu(II) and increase on Cu-TMPA by favoring the reduction of Cu-TMPA by ascorbate (indicated by the green circles). Both impacts are related to stabilization of Cu(I) states.

VI.C. Amyloid-β peptides

VI.C.1. $A\beta_{1-16}$

Figure VI.C-1 shows the kinetics of ascorbate consumption by Cu-$A\beta_{1-16}$ in HEPES pH 7.4 (panel A) and in CH_3CN/HEPES pH 7.4 10/90 (panel B). For this latter conditions two metal:peptide ratios were evaluated, Cu:Aβ of 1:1.2 (solid line) and 1:5 (dotted line). Without CH_3CN, the addition of 1.2 eq of $A\beta_{1-16}$ slows down the ascorbate degradation but it still remains fast ($k = 1.62\ ms^{-1}$) with a total depletion after 25 min in line with previously reported results (Figure VI.C-4).[3, 8] With 10 % of CH_3CN and the ratio Cu:Aβ of 1:1.2, the ascorbate is consumed slower ($k = 0.36\ ms^{-1}$) than in HEPES only. We tentatively explain the effect of CH_3CN in slowing down the ROS production by the stabilization of the highly reactive peptide-unbound Cu in line with the control experiments (peptide-unbound Cu in presence of CH_3CN produced less ROS than in HEPES only). It has been demonstrated that at peptide to Cu stoichiometry of 1.2 and in HEPES only, the contribution of unbound Cu to the ROS is not negligible,[3] 5 equivalent of peptides being necessary to neglect the peptide-unbound contribution.(Scheme VI.C-1).

The experiment in presence of five equivalents of $A\beta_{1-16}$ relative to Cu, compared to 1.2 equivalent in HEPES pH 7.4 only, shows a slower rate of ascorbate consumption ($k = 0.54\ ms^{-1}$ starting fom Cu(II))[3] due to the decrease of unbound Cu, for which the participation is neglected at this ratio. The same experiment with 10% CH_3CN shows slightly slower rate ($k = 0.49\ ms^{-1}$) than in HEPES with the same Cu:Aβ ratio, thus CH_3CN is only slightly implicated in the ROS production process by Cu-$A\beta_{1-16}$ without free Cu, probably by a slight stabilization of the Cu(I)IBS state. These observations are in line with the need in HEPES only to have more 5 equiv. of peptide to neglect the contribution of peptide-unbound Cu and with the formation of a more sluggish IBS in presence of CH_3CN.

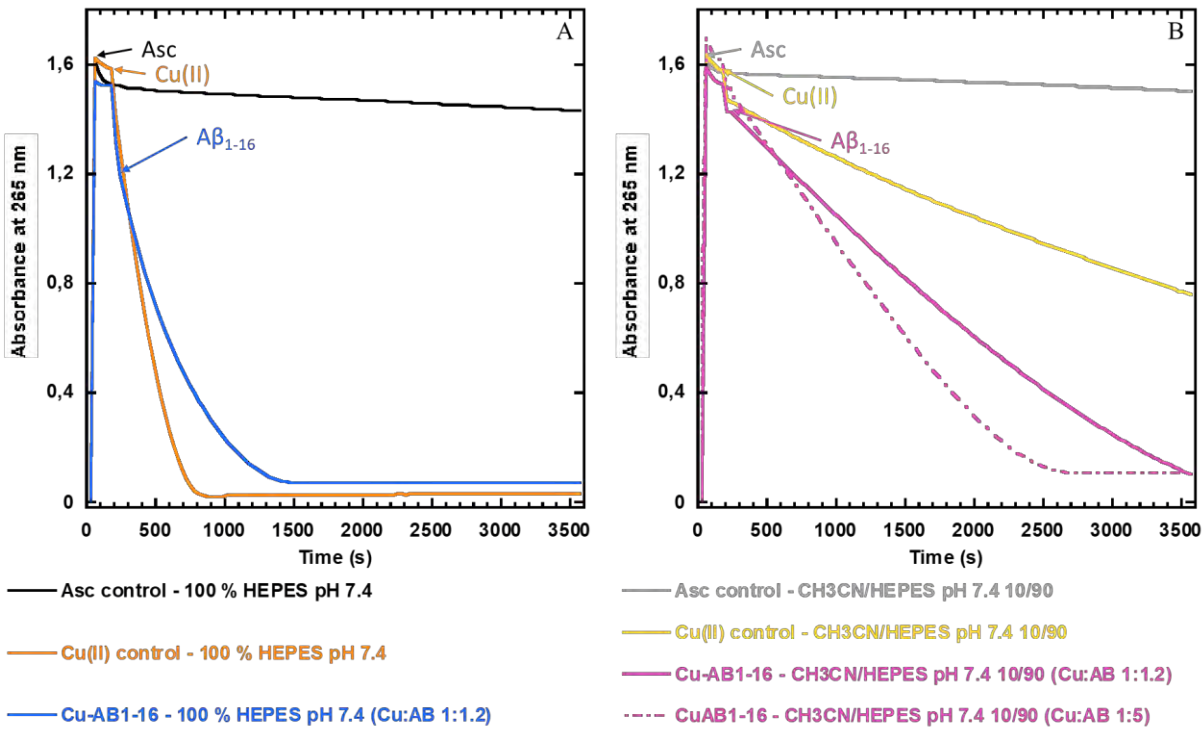

Figure VI.C-1: Ascorbate consumption by Cu(II)/Cu(I)Aβ$_{1-16}$ (blue and pink lines), free Cu (orange and yellow lines) and control (black and grey lines) followed by UV-Vis (λ = 265 nm) as a function of reaction time (s) in CH_3CN/HEPES pH 7.4 100 mM 0/100 (A) and 10/90 (B) v/v. Conditions: [Asc] = 100 µM; [Cu(SO$_4$)•5H$_2$O] = 10 µM; [Aβ$_{1-16}$] = 12 µM (solid lines) or 50 µM (dashdotted line); ℓ = 1 cm; T = 25 °C.

The mechanisms proposed for ROS production by Cu-Aβ$_{1-16}$ in HEPES pH 7.4 and with 10 % of CH_3CN are shown in Scheme VI.C-1. The ROS are produced from the in-between state (IBS) postulated to be the active species for O_2 reduction. Starting from the +2 oxidation state of IBS, it is reduced by ascorbate to its +1 form. The Cu(I)IBS is oxidized by O_2, to produce superoxide radical and Cu(II)IBS by electron transfer from Cu(I) to O_2 (Scheme VI.C-1, panels A left and B left). Only the first step of oxygen reduction is shown here, but the mechanism by which H_2O_2 and finally HO$^\bullet$ are produced is hypothesized to be the same.[9] In presence of CH_3CN, and with a Cu:Aβ ratio of 1:1.2, the Cu(I) unbound is stabilized by CH_3CN as previously observed (free Cu) (Scheme VI.C-1, panel B middle). With five equivalents of peptides, the contribution of Cu unbound is neglected, and CH_3CN is postulated to slightly stabilize Cu(I)IBS and lower its reactivity toward O_2 (Scheme VI.C-1, right).

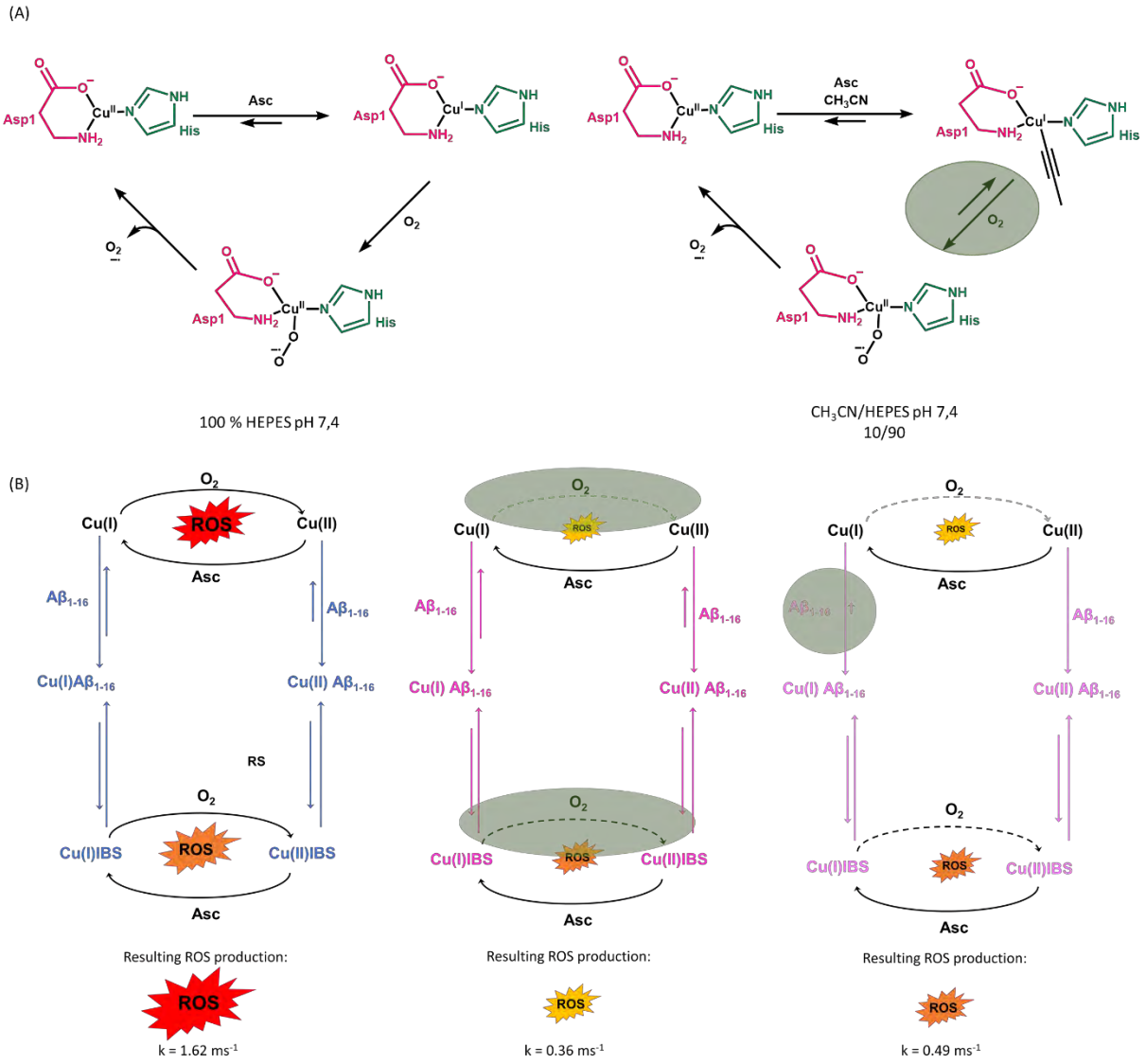

Scheme VI.C-1: Proposed mechanisms for ROS production by Cu-Aβ$_{1-16}$ from the IBS in CH$_3$CN/HEPES pH 7.4 0/100 (panel A and B left) and 10/90 Cu:Aβ 1:1.2 (panel B middle) and 10/90 Cu:Aβ 1:5 (panel A and B right). The changes through the addition of CH$_3$CN, and then 5 equivalents of Aβ$_{1-16}$ are indicated by green circles

VI.C.2. $A\beta_{1-7}$

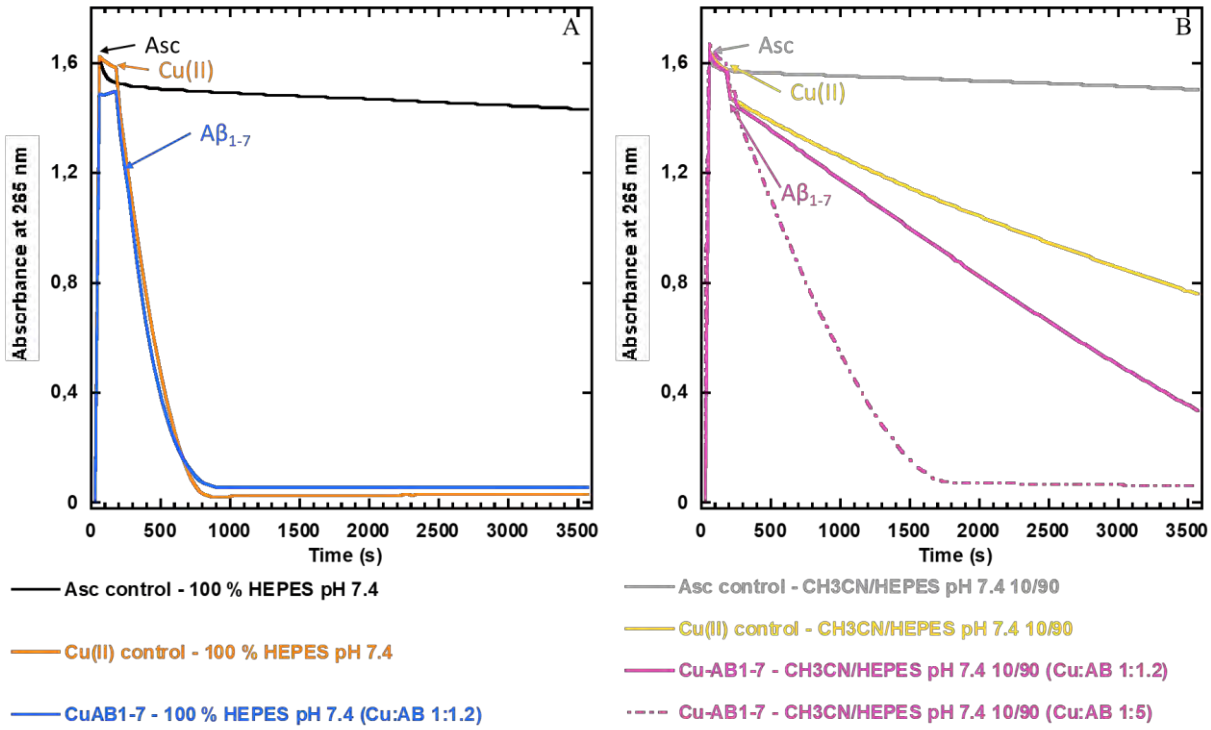

Figure VI.C-2: Ascorbate consumption by Cu(II)/Cu(I)Aβ$_{1-7}$ (blue and pink lines), free Cu (orange and yellow lines) and control (black and grey lines) followed by UV-Vis (λ = 265 nm) as a function of reaction time (s) in CH_3CN/HEPES pH 7.4 100 mM 0/100 (A) and 10/90 (B) v/v. Conditions: [Asc] = 100 µM; [Cu(SO_4)•5H_2O] = 10 µM; [Aβ$_{1-7}$] = 12 µM (solid lines) or 50 µM (dashdotted line); ℓ = 1 cm; T = 25 °C.

Figure VI.C-2 displays the results of ascorbate oxidation through the addition of Cu(II) and $A\beta_{1-7}$, in HEPES pH 7.4 (A) and in presence of 10 % CH_3CN (B). In HEPES pH 7.4, the rate of ascorbate consumption by Cu-$A\beta_{1-7}$ (k= 3.00 ms^{-1}) is equivalent to the one of free Cu (k = 2.80 ms^{-1}) (Figure VI.C-4), with a complete consumption after 15 min. Cu-$A\beta_{1-7}$ was already known to generate ROS faster than Cu-$A\beta_{1-16}$ by modification on the Cu(I) coordination site, since the geometry of its RS are closer to the IBS.[10-11] At a ratio of 1.2 ($A\beta_{1-7}$): 1 (Cu) the contribution of unbound Cu can be neglected, based on the evaluation of free Cu implication on ROS production by double His mutant H13AH14A-$A\beta_{1-16}$, postulated to have the same RS as Cu-$A\beta_{1-7}$.[3] The presence of 10 % CH_3CN on the ascorbate consumption by Cu:Aβ 1:1.2 induces a significant slowdown (k= 0.25 ms^{-1}) with only 80 % of Asc being consumed after 1h, reminiscent of the effect observed for Cu-$A\beta_{1-16}$. Here again, the addition of 5 equivalent of $A\beta_{1-7}$ relative to Cu, increases back the rate of ascorbate oxidation (k= 0.93 ms^{-1}) with a

complete disappearance after 30 min, but not as fast as without CH_3CN. However, this rate is slower than without CH_3CN with the same 5 (Aβ): 1 (Cu) ratio (k= 2.8 ms^{-1}).[3] From those observations, we deduced a shift of the equilibrium between Cu(I) unbound and Cu(I)Aβ_{1-7} toward free Cu by stabilization through CH_3CN binding. Indeed, the association constants of Aβ_{1-7} and CH_3CN binding to Cu(I) are comparable (for Cu(I)Aβ_{1-7}: $K_a < 0.02$ and for one CH_3CN molecule binding to Cu(I) in aqueous solution: $K_a = 0.04$)[3, 12] As for Cu-Aβ_{1-16}, CH_3CN is also postulated to slightly stabilize the IBS.

The proposed mechanisms for ROS generation by Cu-Aβ_{1-7} in HEPES and with 10 % of CH_3CN are shown in Scheme VI.C-2. They are based on coordination spheres of Cu-IBS. Both mechanisms are similar, starting by the reduction of Cu(II)IBS to Cu(I)IBS by ascorbate. The oxygen is then reduced by an electron transfer from Cu(I)IBS and Cu(II)IBS is regenerated. In presence of CH_3CN, there is a probable slight stabilization of Cu(I)IBS, lowering its reactivity toward O_2 (panel A, right). The ROS production is driven by Cu-Aβ_{1-7} only in HEPES (panel B, left), while in presence of CH_3CN the equilibrium between unbound Cu and Cu-Aβ_{1-7} is affected toward free Cu (panel B, middle) and to a lesser extent with five equivalents of Aβ_{1-7} (panel B, right).

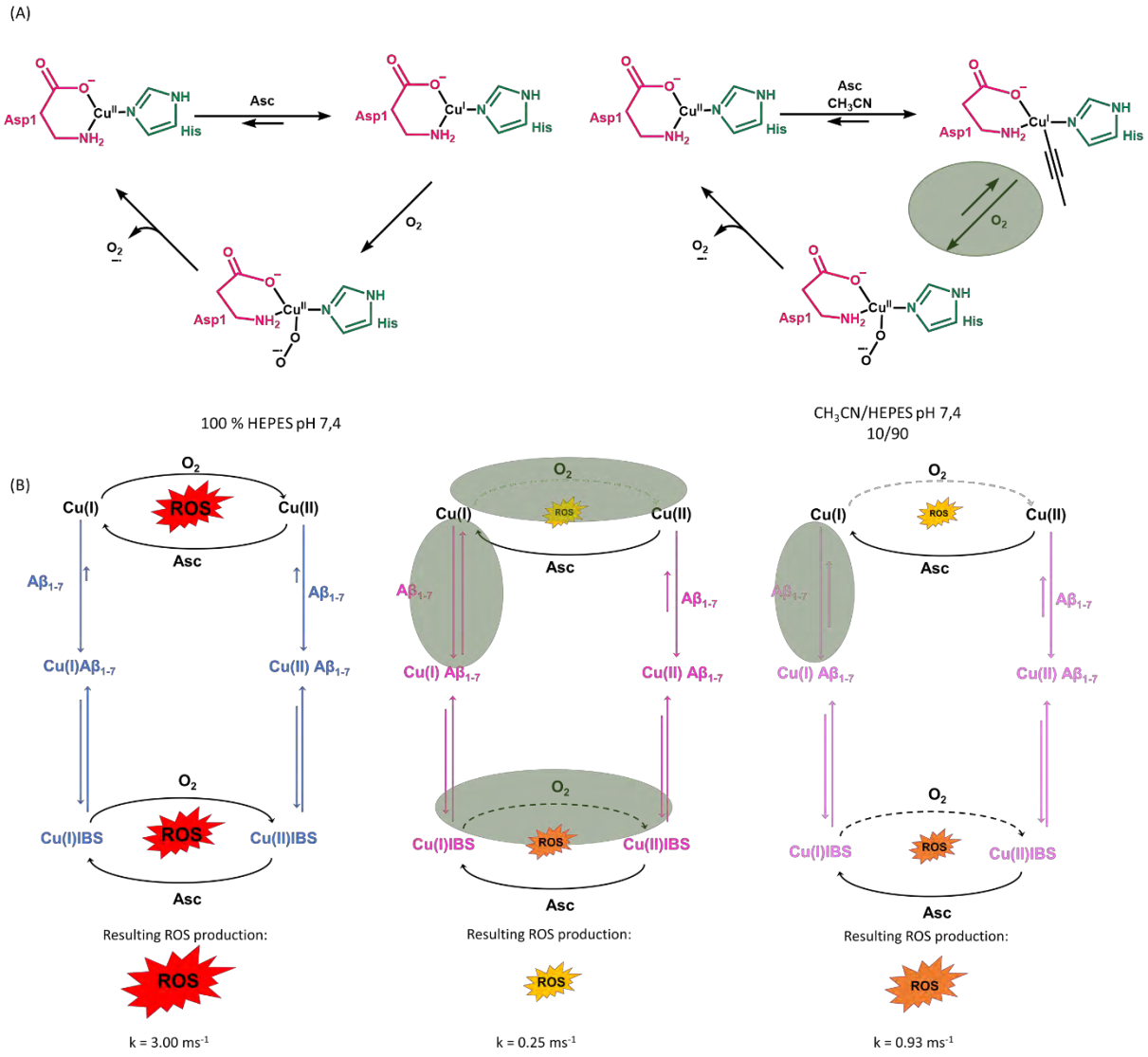

Scheme VI.C-2: Proposed mechanisms for ROS production by Cu-Aβ$_{1-7}$ from the IBS in CH$_3$CN/HEPES pH 7.4 0/100 (panel A and B left) and 10/90 Cu:Aβ 1:1.2 (panel B middle) and 10/90 Cu:Aβ 1:5 (panel A and B right). The changes through the addition of CH$_3$CN, and then 5 equivalents of Aβ$_{1-7}$ are indicated by green circles

VI.C.3. $A\beta_{13-14}$

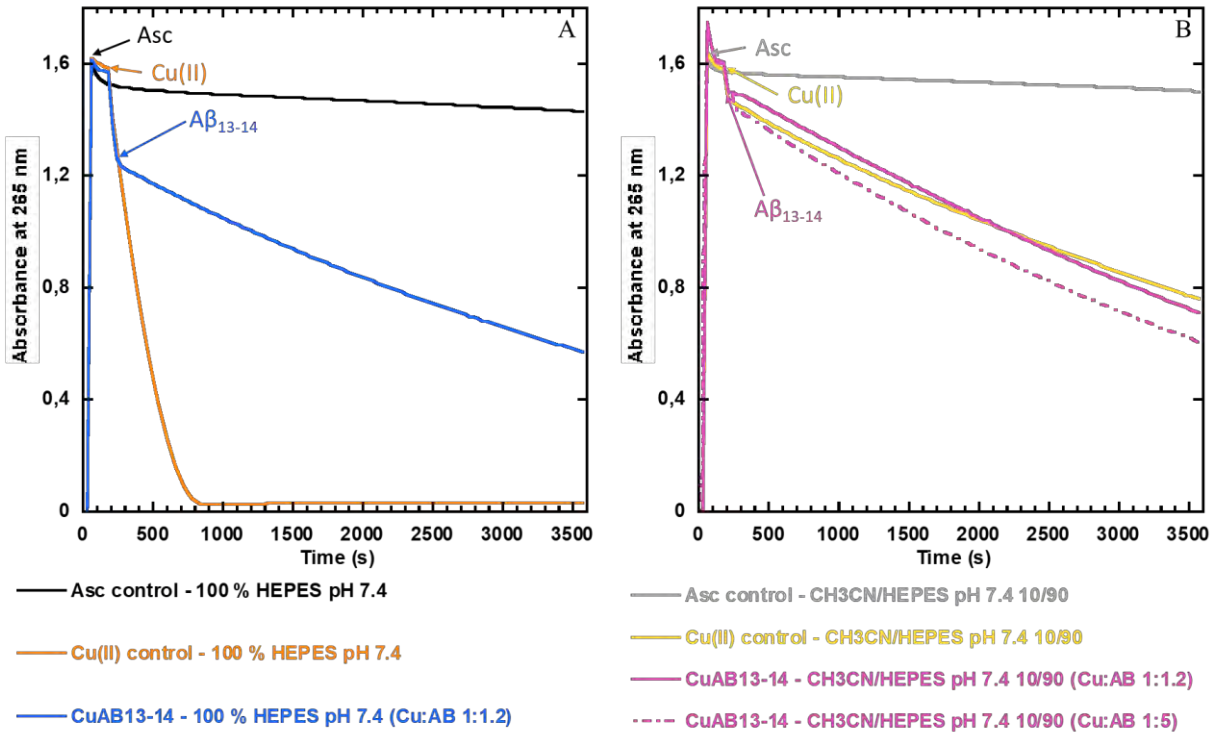

Figure VI.C-3: Ascorbate consumption by Cu(II)/Cu(I)$A\beta_{13-14}$ (blue and pink lines), free Cu (orange and yellow lines) and control (black and grey lines) followed by UV-Vis (λ = 265 nm) as a function of reaction time (s) in CH_3CN/HEPES pH 7.4 100 mM 0/100 (A) and 10/90 (B) v/v. Conditions: [Asc] = 100 µM; [$Cu(SO_4)$•$5H_2O$] = 10 µM; [$A\beta_{13-14}$] = 12 µM (solid lines) or 50 µM (dashdotted line); ℓ = 1 cm; T = 25 °C.

Figure VI.C-3 presents the kinetics of ascorbate oxidation by Cu-$A\beta_{13-14}$ in HEPES pH 7.4 (A) and with 10 % CH_3CN (B) at two ratios of Cu:Aβ 1:1.2 (solid pink line) and 1:5 (dash dotted pink line). In HEPES pH 7.4, after the addition of $A\beta_{13-14}$, the rate is drastically decreased ($k = 0.22\ ms^{-1}$) with 65 % of the total amount of ascorbate being consumed after 1h. This observation indicates that $A\beta_{13-14}$ is able to stabilize Cu(II) and/or Cu(I). The presence of 10 % CH_3CN on the same ratio of Cu:$A\beta_{13-14}$ 1:1.2 decreases the Asc consumption (by about 0.04 ms^{-1} ($k = 0.18\ ms^{-1}$), in the error bar of the measurements). The addition of 5 equivalents of $A\beta_{13-14}$ instead of 1.2, in presence of CH_3CN has no meaningful impact ($k = 0.23\ ms^{-1}$) (Figure VI.C-4). These two facts indicate that (i) there is no peptide unbound Cu and (ii) CH_3CN doesn't intervene in the whole ROS process.

The ROS production mechanism by Cu-$A\beta_{13-14}$ is proposed in Scheme VI.C-3. The coordination spheres of Cu(II)$A\beta_{13-14}$, proposed to be dimeric, based on EPR observations

(chapter IV), are very different than Cu(I)Aβ$_{13-14}$ postulated to be linear between two imidazole rings from His residues based on ^{1}H NMR study (chapter V). The reduction of Cu(II)Aβ$_{13-14}$ by ascorbate is not favorable as shown by the low (-0.56 V vs. SCE) cathodic potential of Cu-Aβ$_{13-14}$ (chapter IV) regardless the presence of CH_3CN. Hence once bound by the Aβ$_{13-14}$ peptide, Cu(II) will be in redox-inert state and almost unable to reach a putative IBS that would be redox active species.

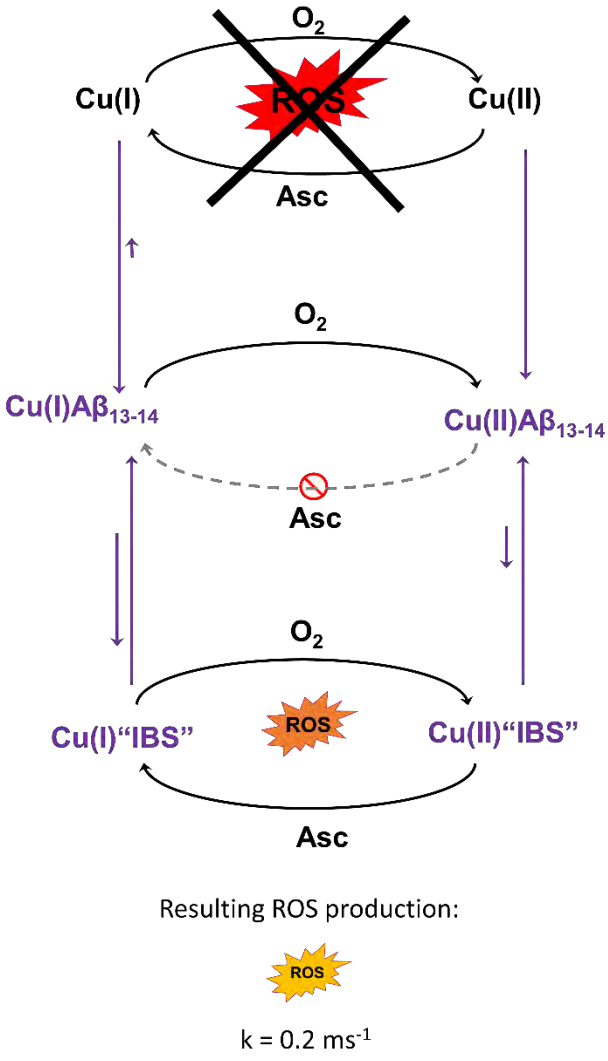

Scheme VI.C-3: Proposed mechanisms for ROS production by Cu-Aβ$_{13-14}$ postulated to remain the same regardless of the presence of CH_3CN and the Cu:Aβ ratio.

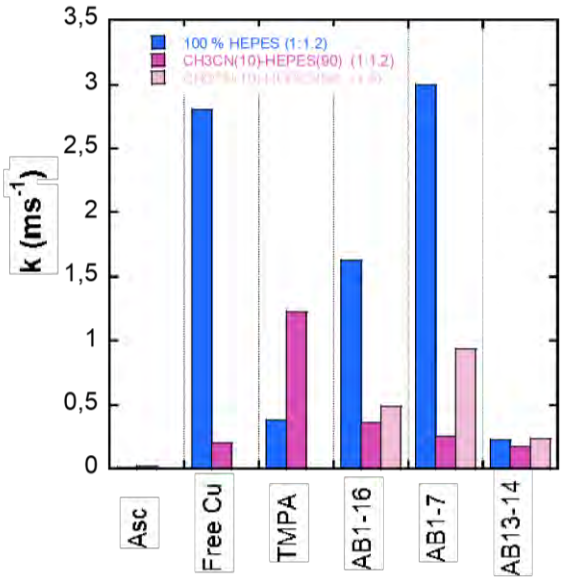

Figure VI.C-4: Rate constant of the ascorbate consumption of each experiment calculated at the beginning of the kinetics, during the first 4 min after the addition of TMPA or Aβ.

The straightforward Asc consumption assays makes it possible to evaluate the ability of Cu(I) complexes to reduce dioxygen, but results obtained also depend on their capacity to be reduced by Asc. Here, the study of ascorbate consumption by mixture of Cu(I)L and Cu(II)L complexes (L = TMPA; $A\beta_{1-16}$; $A\beta_{1-7}$ and $A\beta_{13-14}$) revealed different trends and mechanisms of ROS formation. In HEPES pH 7.4, the order of the faster to the slower ROS producer is free Cu = Cu-$A\beta_{1-7}$ > Cu-$A\beta_{1-16}$ >Cu-TMPA> Cu-$A\beta_{13-14}$ (Figure VI.C-4, blue bars). The presence of CH_3CN slows down the rate of ascorbate consumption of free Cu, Cu-$A\beta_{1-16}$ and Cu-$A\beta_{1-7}$. The opposite is seen with Cu-TMPA, for which CH_3CN speeds up the ascorbate oxidation rate, and no significant change is observed with Cu-$A\beta_{13-14}$. In case of fast consumption, encountered with Cu-$A\beta_{1-16}$ and Cu-$A\beta_{1-7}$ both reduction and oxidation are fast, and the presence of CH_3CN is stabilizing the Cu(I) state for both free and coordinated Cu lowering their reactivity in the IBS. Furthermore, the association constant of Cu-$A\beta_{1-7}$ is much lower than for Cu-$A\beta_{1-16}$, the equilibrium between bound Cu and unbound Cu is shifted toward the latter. In case of slow consumption of ascorbate, as for Cu-$A\beta_{13-14}$, the reduction by Asc is unfavorable and thus slow. In case of moderate ascorbate consumption, for Cu-TMPA, the oxidation is already known to happen fast, thus the rate limiting step would be the reduction. As already known for Cu-Aβ complexes, the rate of oxidation of ascorbate is a contribution of free Cu and Cu bound to peptide due to the moderate affinity of Aβ peptide for Cu.[3] This is well illustrated with the presence of 10 % of CH_3CN known to stabilize Cu(I), on Cu:Aβ ratio of 1:1.2 that induce a

decrease of the consumption speed, which is speed up back with five equivalents of Aβ by reducing the amount of peptide unbound Cu.

Among the 4 complexes studied, there are three trends that could be identified:

- The IBS mechanism observed for both Cu-Aβ_{1-16} and Cu-Aβ_{1-7}. The latter complex is more efficient in producing ROS, in line with the closest geometry of its RS to the postulated IBS.
- Cu-TMPA has a ROS production limited by its low cathodic potential. There is *a priori* no path through an IBS, because the geometry of the Cu(II) and Cu(I) in the RS are already very close.
- Cu-Aβ_{13-14} has a ROS production limited by its low cathodic potential. If the redox process goes through an IBS, then the contribution is limited by a weak equilibrium towards the formation of the IBS from the Cu(II) RS.

VI.D. Cyclic voltammetry

VI.D.1. TMPA

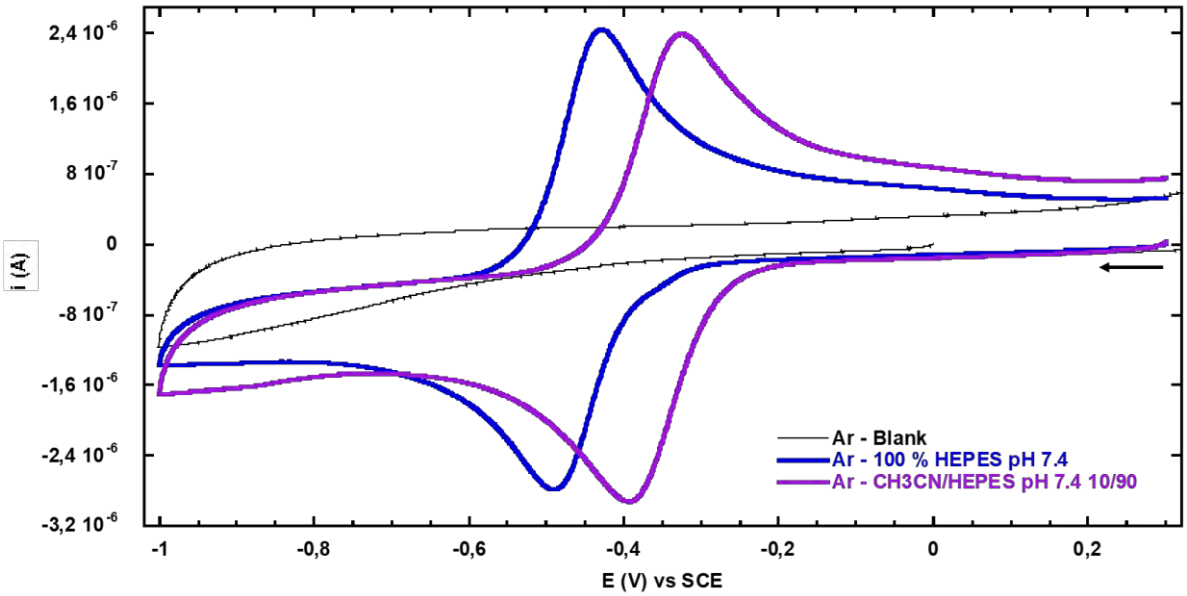

Figure VI.D-1: Cyclic voltammogram of Cu(II)TMPA under Ar in CH_3CN/HEPES pH 7.4 100 mM 0/100 (blue line) and 10/90 (purple line) v/v and blank (black thin line). Conditions: [TMPA] = 0.75 mM; [$Cu(OTf)_2$] = 0.5 mM; scan rate = 100 mV/s; WE = Glassy carbon; Ref = SCE; CE = Pt wire. First scans are shown starting from 0.3 V indicated by the arrow.

The cyclic voltammograms (CV) of Cu(II)TMPA in CH_3CN/HEPES pH 7.4 0/100 and 10/90 under Ar are shown in Figure VI.D-1. In both systems of solvent, Cu(II)TMPA complex shows reversible one electron transfer process. From HEPES pH 7.4, the addition of 10 % CH_3CN induces a shift of $E_{1/2}$ of 10 mV from -0.46 V to -0.36 V. The reversibility remains the same with a peak-to-peak separation of 0.06 V. The shift of potential toward more positive potential values in presence of CH_3CN is consistent with the observation of potential shift observed from aqueous solution to pure acetonitrile solution in chapter III. This shift of potential, is also in agreement with the increasing rate of ascorbate consumption by Cu-TMPA in presence of 10 % CH_3CN, related to a more favorable reduction of Cu(II)TMPA by ascorbate.

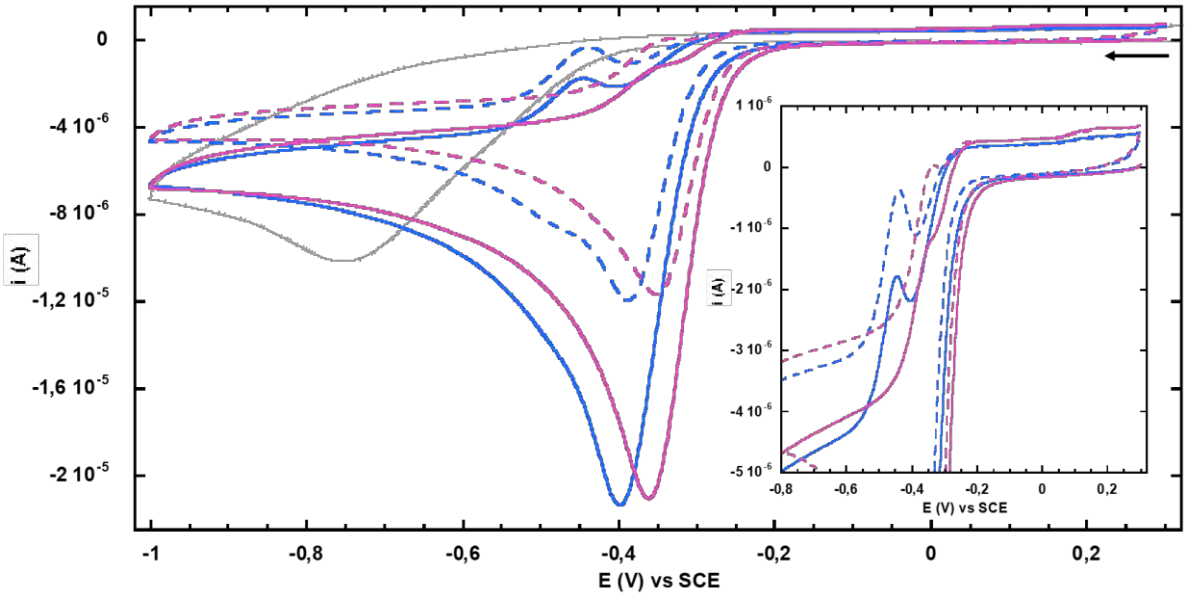

Figure VI.D-2: Cyclic voltammogram of Cu(II)TMPA under air in CH_3CN/HEPES pH 7.4 100 mM 0/100 (blue lines) and 10/90 (pink lines) v/v (first scan (solid lines) and second scan (dashed lines)) and blank under air (grey thin line). Inset: zoom on oxidation waves. Conditions: [TMPA] = 0.75 mM; [Cu(OTf)$_2$] = 0.5 mM; scan rate = 100 mV/s; WE = Glassy carbon; Ref = SCE; CE = Pt wire. Scans starting from 0.3 V indicated by the arrow.

Under air, in both systems of solvent, Cu(II)TMPA catalyzes the reduction of oxygen as mirrored by the high intensity reduction peak at -0.40 V in HEPES pH 7.4 and at -0.36 V with 10 % CH_3CN (Figure VI.D-2). All the oxygen is reduced in the diffusion layer as no peak is observed at the initial potential of O_2 reduction at -0.75 V as seen on the blank CV in HEPES pH 7.4. The amount of oxygen is the limiting reagent in the catalysis of its reduction, as seen on the second scans with a less intense reduction peak and the reappearance of the reduction wave of the Cu(II)TMPA to Cu(I)TMPA in HEPES pH 7.4 at -0.49 V (Figure VI.D-2). This indicates that the diffusion of dioxygen to the surface is slow compared to its consumption rate and thus that the O_2 level is not fully restored under our recording condition (100mV.s^{-1} and 2.6 V of potential sweep). The O_2 concentration limitation is well illustrated in Figure VI.D-3, where the catalytic peak of O_2 reduction increases with the increasing amount of O_2 while the reduction wave of Cu(II) to Cu(I)TMPA decreases as well as the Cu(I) to Cu(II)TMPA oxidation wave at -0.43 V. Even when bubbling pure O_2, no catalytic plateau was observed, but the peak associated with the reduction of O_2 has largely increased in intensity and the oxidation of Cu(I) to Cu(II)TMPA has almost disappeared (Figure VI.D-3 inset). The catalytic activity of Cu(II)TMPA for O_2 reduction was already studied in aqueous solution,[5-6] with the elucidation of a

mechanism. O_2 reduction occurs through a stepwise mechanism, starting with the O_2 binding to Cu(I) that would be the active species and the rate determining step. Cu(II)TMPA($O_2^{\bullet-}$) intermediate would formed and a proton coupled electron transfer would lead to the formation of Cu(II)TMPA(OOH) species. The presence of proton from the aqueous medium would lead to the generation of H_2O_2. Hydrogen peroxide would be further reduced to H_2O through a second catalytic cycle involving Cu(I)TMPA as the active species again (Scheme VI.D-1).[7]

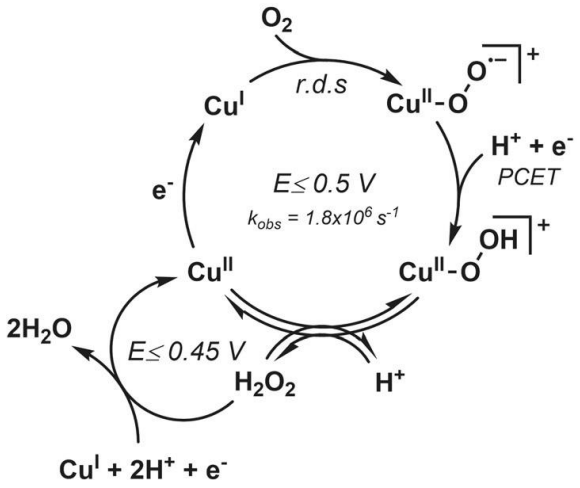

Scheme VI.D-1: Proposed stepwise mechanism for the electrocatalytic O_2 reduction by Cu-TMPA in neutral aqueous solution. For clarity, the TMPA ligand is not depicted. (PCET = proton-coupled electron transfer)[7]

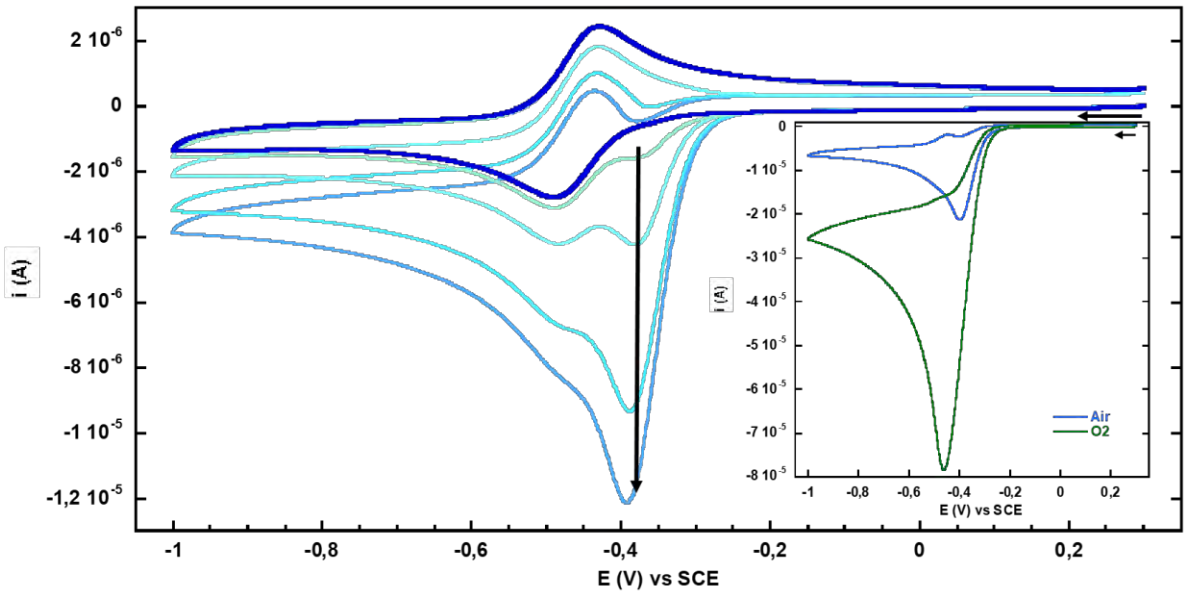

Figure VI.D-3: Cyclic voltammogram (CV) of Cu(II)TMPA under increasing amount of air (blue lines) and O_2 (inset green line) in HEPES pH 7.4 100 mM. Conditions: [TMPA] = 0.75 mM; [Cu(OTf)$_2$] = 0.5 mM; scan rate = 100 mV/s; WE = Glassy carbon; Ref = SCE; CE = Pt wire. First scans are shown, starting from 0.3 V indicated by the arrow.

Figure VI.D-4 shows the CV of Cu(II)TMPA under O_2 in HEPES pH 7.4 and with 10 % of CH_3CN at different scan rates. Even at the lower scan rate (20mV.s^{-1}), the process is limited by O_2 diffusion to the electrode. With the increasing scan rate, the catalytic reduction peak shifted toward lower potentials. The reduction peak is less intense with 10 % of CH_3CN than in HEPES only. On reverse scan, two oxidation waves are observed around 0.10 V and 0.16 V in HEPES pH 7.4 whereas only one is observed around 0.2 V in CH_3CN/HEPES pH 7.4 10/90. Those waves could correspond to the oxidation of intermediates formed during the catalysis. With 10 % of CH_3CN, the oxidation wave is broader and more intense than the two oxidation waves in HEPES probably due to their coalescence. The exact attribution of these anodic peaks was not searched, yet of interest.

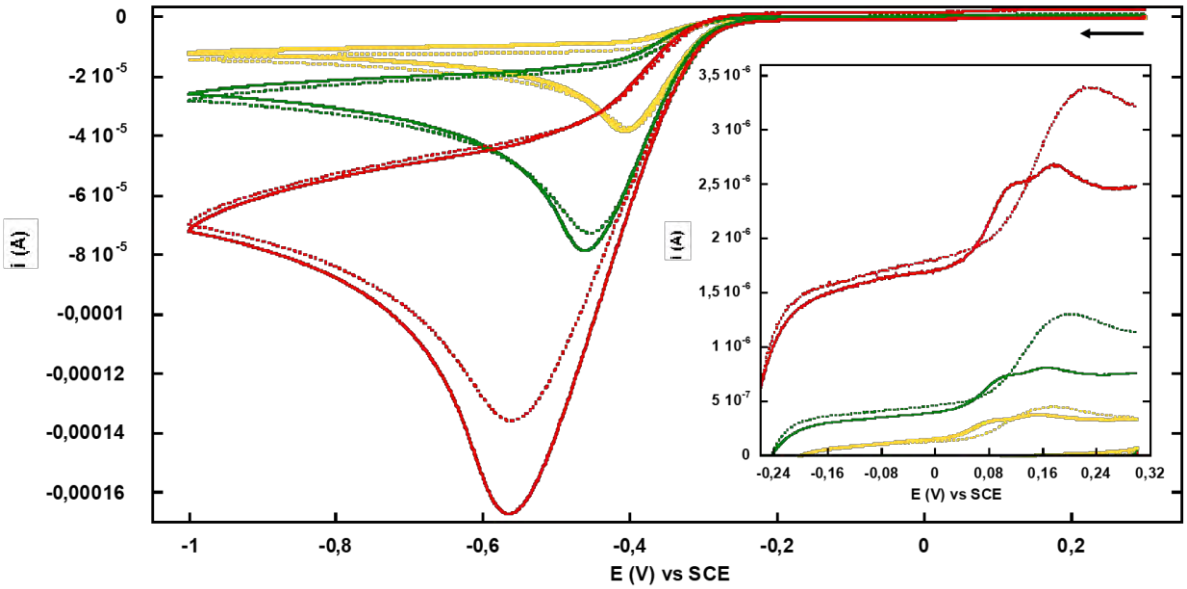

Figure VI.D-4: Cyclic voltammogram (CV) of Cu(II)TMPA under O_2 at different scan rates: 20 mV/s (yellow), 100 mV/s (green) and 500 mV/s (red) in CH_3CN/HEPES pH 7.4 100 mM 0/100 (solid lines) and 10/90 (dotted lines) v/v. Inset: zoom on oxidation waves. Conditions: [TMPA] = 0.75 mM; [Cu(OTf)$_2$] = 0.5 mM; WE = Glassy carbon; Ref = SCE; CE = Pt wire. First scan are shown, starting from 0.3 V indicated by the arrow.

VI.D.2. Aβ peptides

Cyclic voltammetry performed under air with the peptide-unbound Cu and Cu(II)Aβ model complexes in HEPES pH 7.4 and with 10 % of CH_3CN can help to understand their reactivity with ascorbate and O_2 reported in the previous part.

VI.D.2.a. Free copper

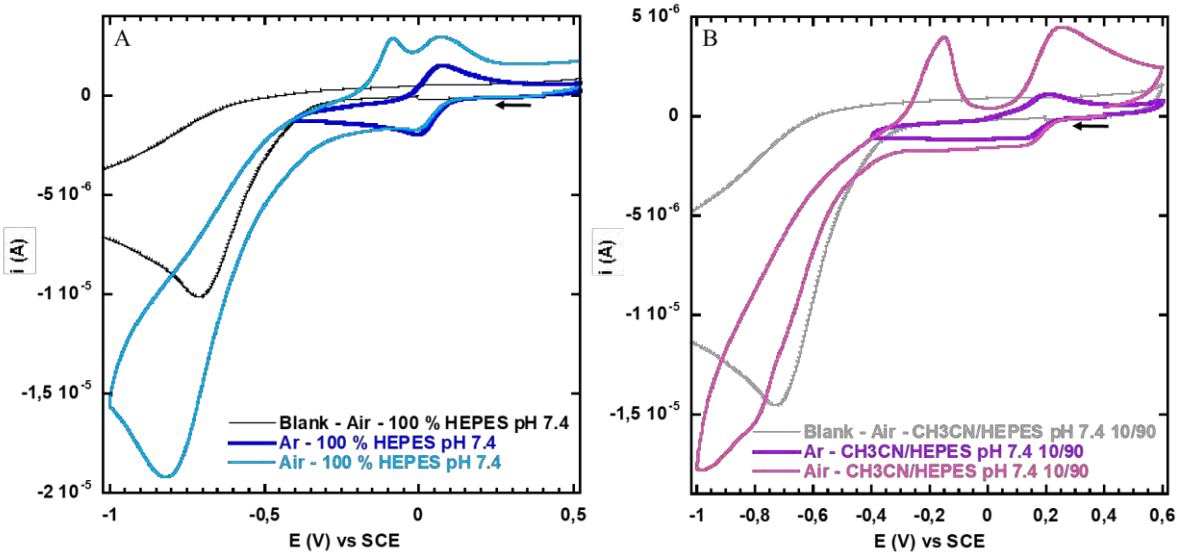

Figure VI.D-5: Cyclic voltammograms of free Cu under Ar (bold lines) and air in CH_3CN/HEPES pH 7.4 100 mM 0/100 (blue lines (A)) and 10/90 (purple and pink lines (B)) v/v and blank (thin lines). Conditions: $[Cu(SO_4)•5H_2O]$ = 0.5 mM; scan rate = 100 mV/s; WE = Glassy carbon; Ref = SCE; CE = Pt wire. First scans are shown starting at 0.4 V indicated by the arrow.

The cyclic voltammogram of peptide-unbound Cu under Ar and air in HEPES pH 7.4 (panel A) and with 10 % CH_3CN (panel B) are shown in Figure VI.D-5. In HEPES, in presence of O_2, an intense broad irreversible reduction peak is observed at -0.82 V. This peak is more intense than the reduction peak of O_2 in the blank spectrum (black thin line) and at a more negative potential. This reduction occurs after the reduction potential of Cu(II) to Cu(I) at -0.01 V indicating that the electrogenerated Cu(I) is reacting with O_2, but that the catalysis is weak. On the reverse scan, two oxidations peaks are observed, the sharp one at -0.08 V may correspond to the oxidation of the reduced Cu(I) to Cu(0) adsorbed at the electrode surface. The other one at 0.07 V correspond to the oxidation of Cu(I) to Cu(II) with the same potential than under Ar. With the addition of 10 % CH_3CN and O_2, the O_2 reduction peak is shifted toward lower potentials and is divided in two peaks one around -0.8 V (at the same potential value than

the one in HEPES only) and the second one at -1.0 V. When scanning backward, the oxidation peak attributed to Cu(0)/Cu(I) is also seen (at -0.15 V). The second oxidation wave at 0.26 V is attributed to the oxidation of Cu(I) to Cu(II) and is slightly shifted toward higher potential compare to the one under argon at 0.21 V. The fast ROS production by free Cu monitored previously is related to its redox potential Cu(II)/Cu(I) with $E_{1/2}$ = 0.03 V favorable for ascorbate reduction and dioxygen reduction. The slower ascorbate consumption in presence of CH_3CN is explained by the stabilization of Cu(I) through CH_3CN coordination illustrated by the redox potential shift toward higher potential values ($E_{1/2}$ = 0.17 V).

VI.D.2.b. $A\beta_{1-16}$

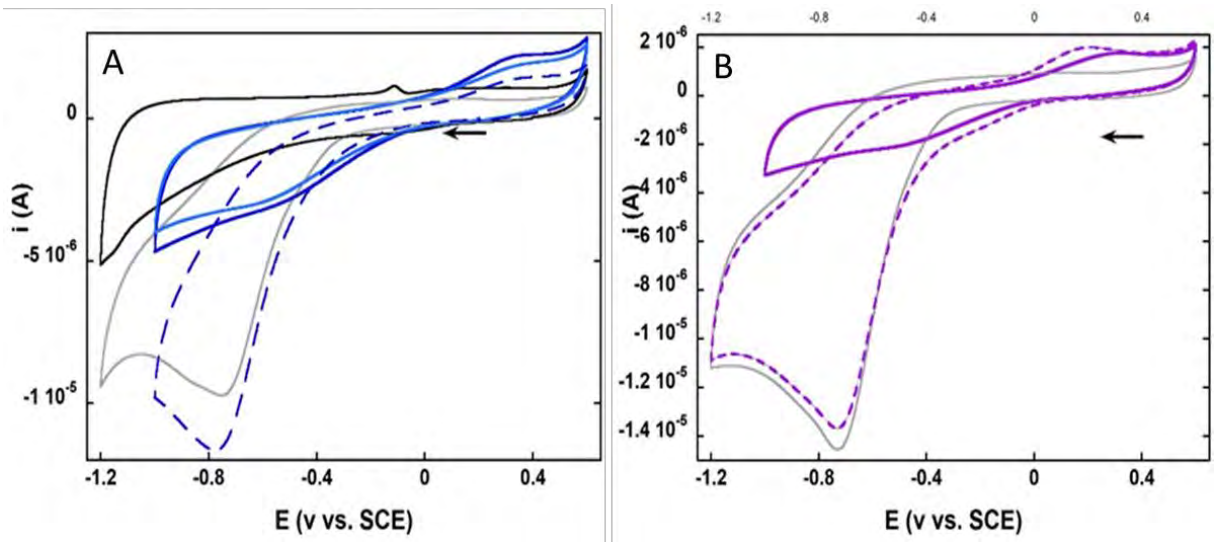

Figure VI.D-6: Cyclic voltammograms of Cu-$A\beta_{1-16}$ under Ar (solid lines) and air (dashed lines) in CH_3CN/HEPES pH 7.4 100 mM 0/100 (blue lines (A)) and 10/90 (purple lines (B)) v/v and blank (black and grey solid lines). Conditions: [$A\beta_{1-16}$] = 0.55 mM; [$Cu(SO_4)•5H_2O$] = 0.5 mM; scan rate = 100 mV/s; WE = Glassy carbon; Ref = SCE; CE = Pt wire. First scans are shown starting at 0.2 V indicated by the arrow.

Figure VI.D-6 presents the cyclic voltammograms of Cu(II)$A\beta_{1-16}$ under Ar and air in HEPES pH 7.4 (panel A) and with 10 % CH_3CN (panel B). Under Ar, the CV of Cu-$A\beta_{1-16}$ is strongly dependent on the polisginh of the electrode (compared the two blue lines in Figure VI.D-6, left). Under air, the reduction peaks seen at -0.78 V in HEPES with Cu-$A\beta_{1-16}$ is slightly shifted toward lower potentials and more intense compare to the one from the blank CV (grey line) at -0.75 V mirroring small reactivity between O_2 and Cu-$A\beta_{1-16}$. The oxidation peak at 0.34 V attributed to the oxidation of Cu(I) to Cu(II)$A\beta_{1-16}$ is the same than under argon but slightly less intense due to the Cu(I)$A\beta_{1-16}$ amount already oxidized by O_2 in the diffusion layer.

The reactivity of Cu-Aβ$_{1-16}$ with O_2 appeared very low probably because it involves too small fraction of reactive species to be significantly observable in those conditions. Lowering the scan rate and increasing the concentration of O_2 and complexes could ease the observation of the reactivity. In presence of 10 % CH_3CN the intense reduction peak attributed to O_2 reduction remains the same than in the blank CV, and the reduction peak of Cu(II)Aβ$_{1-16}$ to Cu(I)Aβ$_{1-16}$ is still observed at the foot of the wave. The oxidation peak at 0.21 V attributed to Cu(I)/Cu(II)Aβ$_{1-16}$ oxidation is shifted toward lower potential and has an higher intensity compared to the ones in HEPES / air and HEPES/CH_3CN /Ar. This suggests that CH_3CN prevents the oxidation of Cu(I)Aβ$_{1-16}$ to Cu(II)Aβ$_{1-16}$ in the diffusion layer, in line with the previously described ROS results. It thus is postulated that (i) CH_3CN coordination to the Cu(I)IBS is precluding its oxidation by O_2 or (ii) CH_3CN coordination to Cu(I)Aβ$_{1-16}$ RS is preventing the IBS formation.

VI.D.2.c. Aβ$_{1-7}$

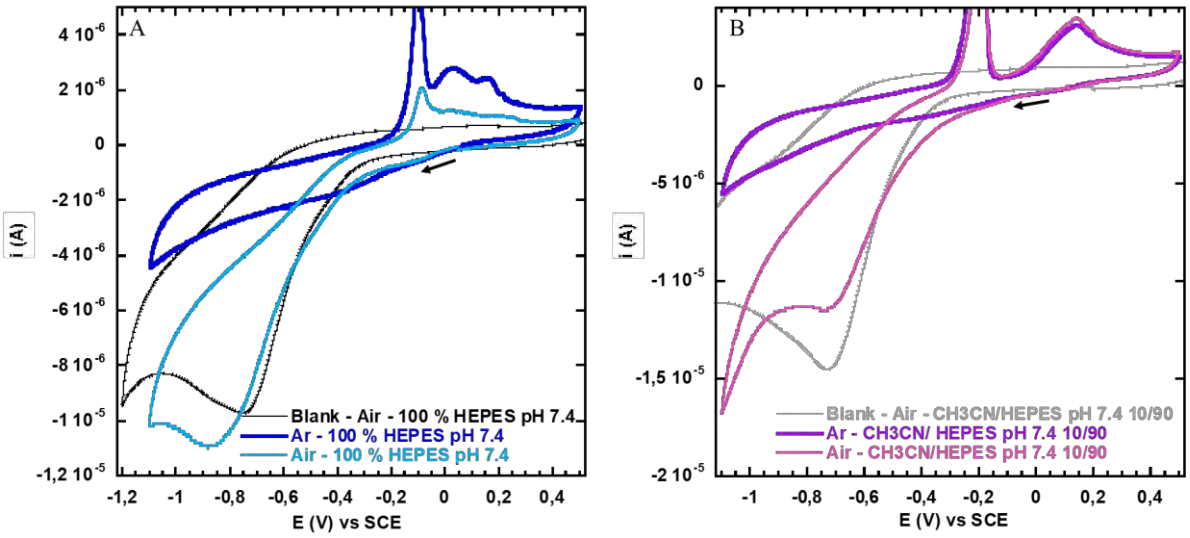

Figure VI.D-7: Cyclic voltammograms of Cu-Aβ$_{1-7}$ under Ar (bold lines) and air in CH_3CN/HEPES pH 7.4 100 mM 0/100 (blue lines (A)) and 10/90 (purple and pink (B)) v/v and blank (thin lines). Conditions: [Aβ$_{1-7}$] = 0.55 mM; [Cu(SO$_4$)•5H$_2$O] = 0.5 mM; scan rate = 100 mV/s; WE = Glassy carbon; Ref = SCE; CE = Pt wire. First scans are shown starting from the open circuit potential indicated by the arrow.

The cyclic voltammogram of Cu(II)Aβ$_{1-7}$ in HEPES pH 7.4 under air presents a reduction peak at -0.88 V slightly after the the one from the blank attributed to O_2 reduction (Figure VI.D-7). With 10 % of CH_3CN, both reduction peaks are at the same potential (-0.73 V), and slightly shifted toward more positive potentials compared to the one in HEPES. On the

reverse scan, the oxidation peak has almost disappeared in HEPES meaning that Cu(I)Aβ$_{1-7}$ is already oxidized to Cu(II)Aβ$_{1-7}$ by O_2. With 10 % of CH_3CN, the oxidation peak remains the same under Ar and under air meaning that Cu(I)Aβ$_{1-7}$ was not oxidized by O_2 in line with CH_3CN preventing oxidation of Cu(I)Aβ$_{1-7}$ to Cu(II)Aβ$_{1-7}$, as previously described in the sister case of Cu(I)Aβ$_{1-16}$.

VI.D.2.d. Aβ$_{13-14}$

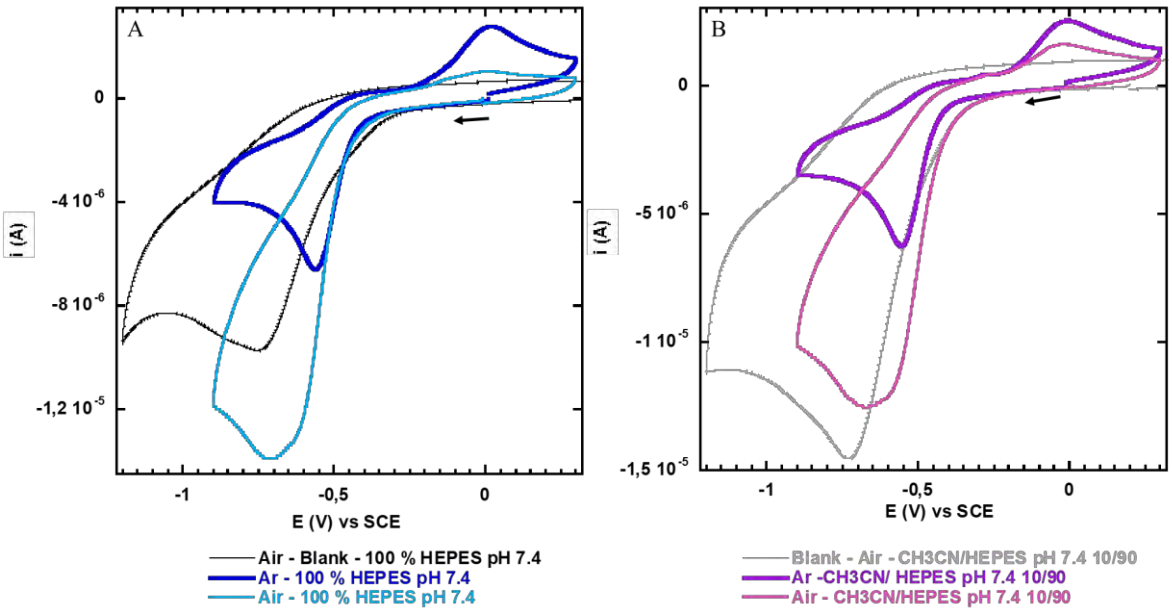

Figure VI.D-8: Cyclic voltammograms of Cu-Aβ$_{13-14}$ under Ar (bold lines) and air in CH_3CN/HEPES pH 7.4 100 mM 0/100 (blue lines (A)) and 10/90 (purple and pink lines) v/v and blank under air (thin lines). Conditions: [Aβ$_{13-14}$] = 0.55 mM; [Cu(SO$_4$)•5H$_2$O] = 0.5 mM; scan rate = 100 mV/s; WE = Glassy carbon; Ref = SCE; CE = Pt wire. First scans are shown starting from the open circuit potential indicated by the arrow.

Figure VI.D-8 shows the CVs of Cu(II)Aβ$_{13-14}$ in CH_3CN/HEPES pH 7.4 0/100 and 10/90 under Ar and air. An intense broad irreversible reduction peak is observed at -0.71 V, slightly before the O_2 reduction peak observed in the blank CV at -0.75 V but that also contains the reduction peak of Cu(II)Aβ$_{13-14}$ to Cu(I)Aβ$_{13-14}$. This peak could mirrors the reduction of O_2 by Cu(I)Aβ$_{13-14}$, but the process is not catalytic. The width of the peak is indicating that diverse O_2 reduction processes are ongoing, including by the electro- and chemically generated 2-His linearly bound Cu(I)Aβ$_{13-14}$. On the reverse scan, the oxidation of Cu(I)Aβ$_{13-14}$ to Cu(II)Aβ$_{13-14}$ is still observed but less intense than under argon. This is in line with a fast oxidation of the Cu(I)Aβ$_{13-14}$ species by O_2 decreasing the level of species to be electrochemically oxidized in

the diffusion layer. The presence of CH_3CN slightly shifts the reduction peak to more positive potential values in line with a possible faster reactivity towards O_2 due to higher level of solubilized O_2. Similar effect was detected for the other two peptide complexes. On the reverse scan, the re-oxidation peak is weaker with CH_3CN present. Once again, CH_3CN prevents the reoxidation of the Cu(I)Aβ_{13-14}.

The peptide complexes and free Cu were not showing great reactivity toward O_2 by cyclic voltammetry. In the previous chapter V, when the reactivity of the Cu-Aβ model complexes was studied toward CO by cyclic voltammetry, only Cu-Aβ_{13-14} cyclic voltammogram was really affected by the binding of CO. Cu-Aβ_{1-7} was also slightly impacted, but no change occurred for Cu-Aβ_{1-16}. In this case when studying the reactivity of Cu-Aβ model toward O_2 by cyclic voltammetry, Cu-Aβ_{13-14} is also the one showing the most reactivity compared to Cu-Aβ_{1-16} and Cu-Aβ_{1-7}.

Concluding remarks. Chemical ROS production versus redox properties and dioxygen activation by electrogenerated Cu(I) species.

To draw correlation between the two experiments previously described, it is first necessary to remind the difference in the processes they probe.

(1) In ROS experiments, both the reduction by ascorbate and oxidation by O_2 are probed, while in electrochemistry, only the reductive half-reaction is under focus.
(2) In ROS experiments, the reductive and oxidative strengths are set by the concentration of oxidant and reductant in solution (100 µM of Ascorbate at the beginning of the reaction and about 200 µM of O_2) while in electrochemistry these strengths depends on the applied potential.
(3) In ROS experiments, the level of O_2 is maintained by stirring of the mixture while in electrochemistry, because cyclic voltammetry requires to be performed in diffusion mode, the level of O_2 evolves during the experiment.

Hence, in line with (1), if Cu(II)-complexes reduction occurs at a too low potential for its reduction by ascorbate, it will be unable to produce ROS although it could activate dioxygen. This is the case of Cu-Aβ_{13-14}. Along the same line, Cu-TMPA highly

activates O_2 but produces moderate ROS since its reduction potential is quite low in aqueous solution.

For the two peptide complexes producing high level of ROS, it was expected that they are also competent in O_2 activation but this is not the case. This suggests that the step to enter in the Cu(I)IBS state responsible for ROS formation is eased by ascorbate reduction versus electrochemical reduction. This could either be due to a better reduction by inner-sphere reduction (compared to outer-sphere reduction by electrochemistry) and/or that binding of ascorbate to the peptide complex help the formation of the IBS (Scheme VI.D-2).

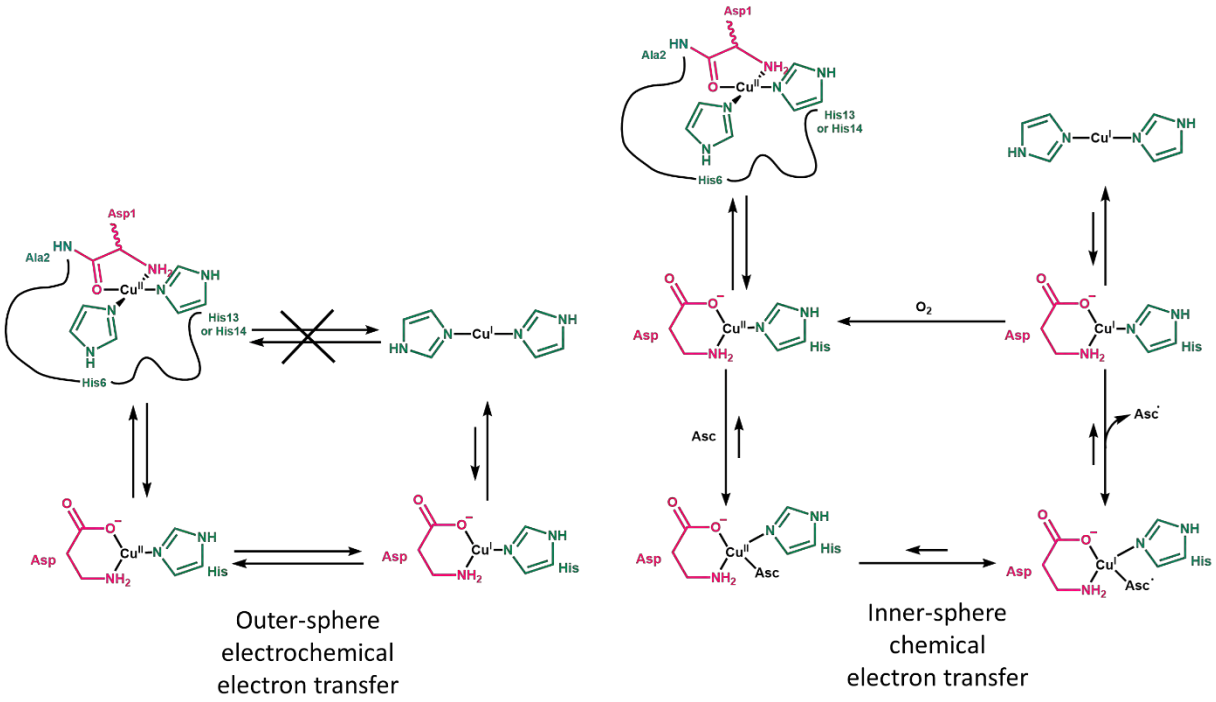

Scheme VI.D-2: Outer-sphere mechanism electron transfer by electrochemistry (left) and inner-sphere mechanism electron transfer through binding of Asc that could favor the formation of IBS (right)

VI.E. Conclusion

This chapter presented complementary studies on Cu(I)L reactivity toward O_2 by UV-Vis ROS production experiments and cyclic voltammetry studies. The ascorbate consumption that mirrors the production of ROS by Cu-L complexes is linked to the redox behavior of the complexes studied by cyclic voltammetry. Indeed, ROS production by Cu complexes involved two steps: (i) the reduction of Cu(II)L to Cu(I)L by ascorbate, and (ii) the oxidation of Cu(I)L to Cu(II)L through the reduction of O_2 into $O_2^{\bullet-}$.

Cu(I/II)Aβ_{1-16} and Cu(I/II)Aβ_{1-7} were shown to fast consume ascorbate. Cu(I/II)Aβ_{13-14}, on the other hand was shown to almost stop the ROS production. Cu(I/II)TMPA induces moderate oxidation of ascorbate. For the two Cu(I/II)L complexes less competent in ROS production, *i.e.* Cu-TMPA in aqueous solution and Cu-Aβ_{13-14}, their cyclic voltammetry studies revealed low reduction potential, making their reduction by ascorbate unfavorable. Cu(II)TMPA is already known to catalytically reduce O_2 into H_2O following a stepwise mechanism in which O_2 binding was shown to be the rate determining step.[7] The complex Cu-Aβ_{13-14}, although not showing catalytic behavior is reacting with O_2 as seen by cyclic voltammetry. For the two other complexes, producing high level of ROS, the redox behavior of Cu-Aβ_{1-16} was already study and shown to go through an in-between state (IBS) having a coordination in the mid-way between the Cu(II)Aβ_{1-16} and Cu(I)Aβ_{1-16} coordination spheres.[13] Cu-Aβ_{1-7} is postulated to behave similarly to Cu-Aβ_{1-16} by going through an IBS form that would be the active species but faster than Cu-Aβ_{1-16}. This means that Cu-Aβ_{1-7} would favor the formation of the IBS by having RS geometries closer to the one of the IBS.

In the conditions chosen to study CO reactivity, in HEPES buffer at pH 7.4 with 10 % of CH_3CN, the fast ROS production is decreased by the stabilization of Cu(I) state unbound and bound to Aβ_{1-16} and Aβ_{1-7} as also probed by cyclic voltammetry. For Cu-TMPA which displays a reversible redox behavior, the ascorbate consumption is increased by CH_3CN due to the shift of the overall redox process toward more positive potential values. Regarding O_2 reactivity, CH_3CN has no influence on Cu-Aβ_{13-14} although destabilizing Cu(I) RS by the loss of linearity under inert conditions.

Finally, all peptides complexes were shown to react with O_2 either by ascorbate consumption experiments or by cyclic voltammetry studies. The ROS production to monitor the reactivity of a complex toward O_2 can be limited by the ascorbate oxidation potential non-appropriate for all complexes (Cu(II)TMPA in aqueous solution and Cu(II)Aβ_{13-14}). On the other side, cyclic voltammetry through outer-sphere electron transfer mechanism might restrict the formation of IBS compare to inner-sphere electron transfer through Asc binding. Deeper electrochemical studies with lower scan rate and higher concentration of oxygen by bubbling O_2 instead of air could give more information. Also studies starting from Cu(I) and in presence of ascorbate in cyclic voltammetry to probe the second (oxidative) half-reaction are foreseen. Ascorbate consumption studies starting with Cu(I)L or Cu(II)L (not a mixture of both as done here) would also be useful to supplement this study, as well as the use of other physiological reductants.

References

1. Du, C.; Gao, X.; Chen, W., Recent developments in copper-based, non-noble metal electrocatalysts for the oxygen reduction reaction. *Chinese Journal of Catalysis* **2016,** *37* (7), 1049-1061.

2. Conte-Daban, A.; Boff, B.; Candido Matias, A.; Aparicio, C. N. M.; Gateau, C.; Lebrun, C.; Cerchiaro, G.; Kieffer, I.; Sayen, S.; Guillon, E.; Delangle, P.; Hureau, C., A Trishistidine Pseudopeptide with Ability to Remove Both CuI and CuII from the Amyloid-β Peptide and to Stop the Associated ROS Formation. *Chemistry – A European Journal* **2017,** *23* (67), 17078-17088.

3. Atrián-Blasco, E.; del Barrio, M.; Faller, P.; Hureau, C., Ascorbate Oxidation by Cu(Amyloid-β) Complexes: Determination of the Intrinsic Rate as a Function of Alterations in the Peptide Sequence Revealing Key Residues for Reactive Oxygen Species Production. *Analytical Chemistry* **2018,** *90* (9), 5909-5915.

4. Johnson, D. K.; Stevenson, M. J.; Almadidy, Z. A.; Jenkins, S. E.; Wilcox, D. E.; Grossoehme, N. E., Stabilization of Cu(i) for binding and calorimetric measurements in aqueous solution. *Dalton Transactions* **2015,** *44* (37), 16494-16505.

5. Asahi, M.; Yamazaki, S.-i.; Itoh, S.; Ioroi, T., Acid-base and redox equilibria of a tris(2-pyridylmethyl)amine copper complex; their effects on electrocatalytic oxygen reduction by the complex. *Electrochimica Acta* **2016,** *211*, 193-198.

6. Asahi, M.; Yamazaki, S.-i.; Itoh, S.; Ioroi, T., Electrochemical reduction of dioxygen by copper complexes with pyridylalkylamine ligands dissolved in aqueous buffer solution: the relationship between activity and redox potential. *Dalton Transactions* **2014,** *43* (28), 10705-10709.

7. Langerman, M.; Hetterscheid, D. G. H., Fast Oxygen Reduction Catalyzed by a Copper(II) Tris(2-pyridylmethyl)amine Complex through a Stepwise Mechanism. *Angewandte Chemie International Edition* **2019,** *58* (37), 12974-12978.

8. Esmieu, C.; Ferrand, G.; Borghesani, V.; Hureau, C., Impact of N-Truncated Aβ Peptides on Cu- and Cu(Aβ)-Generated ROS: CuI Matters! *Chemistry – A European Journal* **2021,** *27* (5), 1777-1786.

9. Reybier, K.; Ayala, S.; Alies, B.; Rodrigues, J. V.; Bustos Rodriguez, S.; La Penna, G.; Collin, F.; Gomes, C. M.; Hureau, C.; Faller, P., Free Superoxide is an Intermediate in the Production of H2O2 by Copper(I)-Aβ Peptide and O2. *Angewandte Chemie International Edition* **2016,** *55* (3), 1085-1089.

10. Cheignon, C.; Jones, M.; Atrián-Blasco, E.; Kieffer, I.; Faller, P.; Collin, F.; Hureau, C., Identification of key structural features of the elusive Cu–Aβ complex that generates ROS in Alzheimer's disease. *Chemical Science* **2017,** *8* (7), 5107-5118.

11. Cheignon, C.; Faller, P.; Testemale, D.; Hureau, C.; Collin, F., Metal-catalyzed oxidation of Aβ and the resulting reorganization of Cu binding sites promote ROS production†. *Metallomics* **2016,** *8* (10), 1081-1089.

12. Kamau, P.; Jordan, R. B., Complex Formation Constants for the Aqueous Copper(I)−Acetonitrile System by a Simple General Method. *Inorganic Chemistry* **2001,** *40* (16), 3879-3883.

13. Balland, V.; Hureau, C.; Savéant, J.-M., Electrochemical and homogeneous electron transfers to the Alzheimer amyloid-β copper complex follow a preorganization mechanism. *Proceedings of the National Academy of Sciences* **2010,** *107* (40), 17113-17118.

General conclusion

General conclusion

In the context of Alzheimer's disease (AD), and especially the catalysis of reactive oxygen species (ROS) production by Aβ-bound copper ions, the reactivity of Cu(I)Aβ model complexes toward carbon monoxide (CO) and oxygen (O_2) has been aimed in this PhD's. The well-known Cu-TMPA (TMPA = Tris(2-MethylPyridyl)Amine) complex was systematically used as a reference complex and to establish the reaction conditions. To reach this objective, a stepwise study has been undertaken, during which Cu(II)TMPA and Cu(II)Aβ model complexes were characterized as well as CO-adducts of Cu(I)TMPA and Cu(I)-Aβ. Last, dioxygen activation/reactivity investigations with TMPA and peptide complexes were performed.

A thorough study was completed on Cu(II)TMPA in different solvent conditions and in presence of various inorganic anions. Most of the Cu(II)TMPA complexes was shown to be in trigonal bipyramid (TBP) geometry taking a variety, by nature and size, of ligands in its labile apical position. The fifth ligand under study were (i) anions [SO_3^{2-} (sulfite) and $S_2O_3^{2-}$ (thiosulfate) both coordinated *via* S atom; SO_4^{2-} (sulfate), ClO_4^- (perchlorate), NO_3^- (nitrate) and HO^- (hydroxide) coordinated through O atom] and (ii) solvent molecules [CH_3CN coordinated by N atom or H_2O coordinated via O atom]. A trinuclear $(Cu(II)TMPA)_3(CO_3)$ was also isolated as a crystallization by-product in the solid-state. Those Cu(II) complexes formed were characterized in solid state by X-ray crystallography and in solution by UV-Vis and EPR spectroscopies. The preferred distorted TBP geometry adopted by Cu(II)TMPA remains regardless of the 5th ligand both in solid-state and solution, except for the solid-state structure of $Cu(II)TMPA(S_2O_3)$ for which the interaction of an O atom with the Cu(II) center distorted the geometry toward square based octahedron.

The coordination spheres of the Cu(II)Aβ models complexes were elucidated by UV-Vis and EPR characterizations, all displaying square planar geometry. $Cu(II)A\beta_{1-16}$ and $Cu(II)A\beta_{1-7}$ have 3N1O coordination modes in agreement with their previous characterizations regardless the C-terminal protection by amidation. $Cu(II)A\beta_{13-14}$ is postulated to be a 2:2 dimeric species, where each Cu(II) center has a 4N coordination mode provided by a 3N scaffold from the peptide ancillary set of ligands and completed by a 1N from the His of a

second peptide. The conditions established to study the reactivity of Cu(I)L (L= TMPA and Aβ models) complexes require 10 % of CH_3CN as a co-solvent to aqueous buffered solution to increase the carbon monoxide solubility. The impact of such amount of co-solvent on Cu(II)Aβ complexes was evaluated by UV-Vis and EPR and was shown to not participate to their coordination sphere. However, the study of the redox properties of Cu(II)Aβ model complexes by cyclic voltammetry revealed that CH_3CN, as expected, is not fully inert with respect to the stability of Cu(I)Aβ state. For the complexes postulated to have a linear coordination mode such as Cu(I)Aβ_{1-16} and Cu(I)Aβ_{13-14}, CH_3CN destabilizes them by inducing the loss of the linearity, but stabilizes the Cu(I)Aβ_{1-7} complex postulated to have a 2N1O coordination set by formation of a 3N1O tetrahedral complex.

The study of reactivity of Cu(I)L complexes started by elucidating their coordination spheres by ^{1}H NMR. Cu(I)TMPA was proposed to be 5 coordinated with the 4N from TMPA being bound and having a solvent molecule in the fifth labile position. Cu(I)Aβ_{13-14} and Cu(I)Aβ_{1-16} are proposed to have linear coordination between two imidazole rings from the His residues. Cu(I)Aβ_{1-7} is proposed to have 2N1O coordination set including the N terminal amine, the N atom from imidazole ring of His6 and O atom from carboxylate of one Asp residue (either Asp1 or Asp7). The CO binding to those complexes was monitored by ^{1}H NMR, UV-Vis, FT-IR spectroscopies and by cyclic voltammetry. CO was shown to bind to each complex by ^{1}H NMR. CO coordination was also detected for Cu(I)TMPA and Cu(I)Aβ_{13-14} by FT-IR, UV-Vis and cyclic voltammetry. Eventually, the reactivity of Cu-L toward dioxygen was monitored through ascorbate consumption experiments followed by UV-Vis spectroscopy known to mirror the ROS production, and by cyclic voltammetry studies under aerobic conditions. All the complexes were shown to react with dioxygen. Cu-TMPA was the only one showing catalytic reduction of O_2 by electrochemistry, however it was not the fastest ascorbate consumer due to its low reduction potential (too low to be reduced by ascorbate). In contrast, Cu-Aβ_{1-16} and Cu-Aβ_{1-7} consume ascorbate rapidly (*i.e.* have a high ROS production rate) but their cyclic voltammograms were not much impacted by the presence of O_2. Cu-Aβ_{13-14} was the slowest ascorbate consumer almost stopping ROS production. However its cyclic voltammetry showed some reactivity toward O_2. Its non-efficient ROS production is thus attributed to its low reduction potential.

The results of my thesis give additional knowledge on Cu-TMPA complex, especially through studies in aqueous solution with direct application (sulfite detection in food sample broached in the annex chapter). The reactivity studies toward CO and O_2 by the Cu(I)Aβ model complexes strengthen the hypothesis of the elusive active species having a geometry "in-between" (IBS) the two resting states (+II and +I) of Cu-Aβ.

In the context of AD, similar study using other Aβ mutants could give more insight into the IBS. Photolysis of coordinated CO to Cu-Aβ complexes and competition with O_2 binding studies could give information on the rate of reactivity, and thus on the active state. The dioxygen activation is implicated in many other biological processes and not always well understood. This thesis work could further be useful to study the dioxygen activation by other bio-complex models in aqueous medium.

Annex chapter

Journal of Inorganic Biochemistry 225 (2021) 111601

Contents lists available at ScienceDirect

Journal of Inorganic Biochemistry

journal homepage: www.elsevier.com/locate/jinorgbio

Solid-state and solution characterizations of [(TMPA)Cu(II)(SO_3)] and [(TMPA)Cu(II)(S_2O_3)] complexes: Application to sulfite and thiosulfate fast detection

Léonie Berthonnaud [a,b], Charlène Esmieu [a], Sonia Mallet-Ladeira [a], Christelle Hureau [a,*]

[a] LCC-CNRS, Université de Toulouse, CNRS, Toulouse, France
[b] Division of Materials Science, Nara Institute of Science and Technology, 8916-5 Takayama, Ikoma, Nara, Japan

ARTICLE INFO

Keywords:
Copper(II)
TMPA
Sulfite
Thiosulfate
EPR
UV–Vis

ABSTRACT

Sulfite (SO_3^{2-}) and thiosulfate ($S_2O_3^{2-}$) ions are used as food preservative and antichlor agent respectively. To detect low levels of such anions we used Cu(II) complex of the Tris-Methyl Pyridine Amine (TMPA) ligand, denoted L. Formation of [LCu(SO_3)] (1) and [LCu(S_2O_3)] (2) in solution were monitored using UV–Vis, EPR and cyclic voltammetry, while the solid-state X-ray structures of both complexes were solved. In addition, we also evaluated the pH range in which the complexes are stable, and the anions binding affinity values for the [LCu(solvent)]$^{2+}$ (3) parent complex. As a matter of illustration, we determined the sulfite content in a commercial crystal sugar.

1. Introduction

Copper is an essential element in biology [1], being present in many key enzymes, such as in Cytochrome C oxidase (CcO) that provides the four-electron-four-proton-reduction of dioxygen to water leading to the formation of a proton gradient across the cellular membrane and ultimately to the biosynthesis of ATP [2]. In CcO, the hetero-binuclear catalytic center is provided by a heme and a copper-bound to three N-ligands from side-chains of Histidine (His) residues, while the dioxygen substrate bridges the two metallic centers [3]. Many bioinspired models of CcO have been developed in the last 30 years [3,4]. In several of them, the copper first coordination sphere was mimicked using 4 N-containing tripodal ligands. Among them the multi-functions ligand TMPA (Tris-Methyl Pyridine Amine, also reported as TPA and TPMA) [5] is the one of the most, if not the most studied ligand. In addition to its potential in CcO modelling, Cu(TMPA) and its derivatives have been used for the investigations of dioxygen activation using mononuclear model (for recent examples, see for instance refs. [6–11]). This was the motivation for the use of this ligand in our research that aims at evaluating dioxygen activation by Cu-peptide complexes [12,13]. In this context Cu(TMPA) complex would have served as a widely–recognized reference for dioxygen activation. In the course of our experiments, we evidenced that the Cu(TMPA) complex can also be a very interesting probe for the detection of sulfite and thiosulfate ions and this is what we will mainly describe in the present report.

Sulfite (E221) ion is a well-known food and beverages additive, used as preservative agent to counteract food evolution and browning [14,15]. Thiosulfate (E539, also known as hyposulfite) ion is used to neutralize the effects of chlorine used for water treatment, bleaching in paper and textile industries and as highly specific medications [16]. A tuned balance is required since excess of sulfite has unwanted side-effects for health such as allergic reaction and asthma [17]; the daily consumption is thus limited (below 0.7 mg/kg of body weight) [18]. Hence, the need for probes to detect sulfite ions and to a lesser extent thiosulfate ions. Although they are already available techniques to detect sulfite and thiosulfate ions [19], it is interesting to complete them with easy-to-use probes and detection methods.

The full characterization of [LCu(SO_3)] (1) and [LCu(S_2O_3)] (2) in solid state by X-ray crystallography and in solution by various methods (UV–Vis, EPR and cyclic voltammetry) together with the speciation of the two complexes as a function of pH, and the evaluation of the affinity of SO_3^{2-} and $S_2O_3^{2-}$ for [LCu(solvent)]$^{2+}$ (3) are described in the present report. Then, the use of 3 to detect sulfite ions in crystal sugar is reported and briefly discussed with respect to other current methods, while a short description on how we serendipitously detected species 1 is also given.

* Corresponding author.
E-mail address: christelle.hureau@lcc-toulouse.fr (C. Hureau).

https://doi.org/10.1016/j.jinorgbio.2021.111601
Received 30 June 2021; Received in revised form 3 August 2021; Accepted 9 September 2021
Available online 22 September 2021

2. X-ray crystallographic studies of [LCu(SO_3)] (1), [LCu(S_2O_3)] (2)

An ORTEP representation of the structures of [LCu(SO_3)] (1) and [LCu(S_2O_3)] (2) is given in Fig. 1 and crystallographic details of the structures are given in Table S1. Selected bond distances and angles are listed in Tables 1, S2 and S3, where they are compared with those of $[LCu(H_2O)]^{2+}$ [20–24], $[LCu(AcN)]^{2+}$ (AcN = acetonitrile) [25–27] (Table 1), and [L_TCu(S_2O_3)] [28] where L_T is a ligand from the tren (tris (2-methylaminoethyl)amine)) family, namely tren, Me_3tren and Bz_3tren (Tables S2 and S3). The empirical Addison parameter τ is a very useful tool to compare geometries of penta-coordinated structures. It is defined by τ = (difference between the 2 largest L-M-L angles)/60. When τ = 1 the complex geometry is trigonal bipyramidal (TBP) and when τ = 0 it is square pyramidal (SQ) [29].

1 has a nearly perfect TBP geometry (τ = 1) as have the two parent complexes $[LCu(H_2O)]^{2+}$, $[LCu(AcN)]^{2+}$ with τ = 0.94 and τ = 0.84, respectively. The equatorial angles are similar and close to 120°. The angle S(1)-Cu-N(2) is close to linearity with 178.9°. All the Cu—N bond distances are comparable (2.07 Å - 2.09 Å) except the Cu-S(1) bond distance that is longer (2.25 Å) in line with binding to bulky sulfur atom, while the O and N atoms of $[LCu(H_2O)]^{2+}$ and $[LCu(AcN)]^{2+}$ respectively are much closer (1.95 Å and 1.98 Å). The angles N(2)-Cu-N_{eq} are less than 90°, the Cu(II) center is thus out of the equatorial plane toward the sulfite ion. Similar trends were also observed for $[LCu(H_2O)]^{2+}$ and $[LCu(AcN)]^{2+}$ (Table 1) and thus is not linked to the nature of the exogenous ligand. To the best of our knowledge, there is no X-ray structure of a Cu(II)-sulfite complex reported so far.

2 has an intermediate structure because of the O(1) atom from the thiosulfate ion that is not bound to the Cu(II) center (Cu-O(1) distance equals 2.70 Å), but occupies the sixth position of an octahedron. Hence, this interaction induces a high distortion in the classical TBP toward square pyramidal (SP) geometry with τ = 0.11, also characterized by an elongation of the Cu-N(3) bond distance (2.20 Å) in trans to the O(1) atom. Such SP geometry has only been reported once for one of the two inequivalent complexes characterized in the X-ray structures of [(Me_3tren)Cu(S_2O_3)]. Otherwise, the geometry around [(tren)Cu(S_2O_3)]$^{2+}$, [(Bz_3tren)Cu(S_2O_3)]$^{2+}$ and [(Me_3tren)Cu(RS_2O_2)]$^{2+}$ (R = Me, Ph and MePh) [30] are TBP. Such an unusual coordination might be due to crystal packing. The N(3)-Cu(II) bond thus represents the axial direction, with the equatorial plane defined by the other three N and S (1) atoms. Indeed, the angles S(1)-Cu-N(2) and N(1)-Cu-N(4) are approaching linearity with 168.1 Å and 161.6 Å, respectively. The Cu-S (1) bond distance of 2.29 Å is in the same range as the one in 1 and the [L_TCu(S_2O_3)] parent complexes.

Table 1
Selected distances (Å) and angles (°) for 1 and 2. The longest distances are shown in bold.

	1	2	$[LCu(H_2O)]^{2+}$ [a]	$[LCu(AcN)]^{2+}$ [a]
Cu-N(1)	2.071 (7)	2.029(1)	2.071(1)	2.042(5)
Cu-N(2)	2.087 (7)	2.0618(9)	2.006(1)	2.021(4)
Cu-N(3)	2.078 (7)	2.2025 (9)	2.059(1)	2.082(4)
Cu-N(4)	2.086 (7)	2.0417(9)	2.061(1)	2.025(5)
Cu-S(1)/O_w/N_{AcN}	2.253 (2)	2.2878 (4)	1.952(1)	1.976(5)
Cu-O(1)	–	2.695(1)	–	–
S(1)/O_w/N_{AcN}-Cu-N (2)	178.9 (2)	168.09(3)	176.54(5)	177.7(2)
N(1)-Cu-N(3)	118.5 (3)	93.95(4)	117.66(5)	113.9(2)
N(1)-Cu-N(4)	116.1 (3)	161.62(4)	117.04(5)	127.2(2)
N(3)-Cu-N(4)	117.2 (3)	92.80(4)	119.9(5)	114.1(2)
O(1)-Cu-N3	–	173.72(3)	–	–

[a] To ease comparison, the N atoms in $[LCu(H_2O)]^{2+}$ and $[LCu(AcN)]^{2+}$ have been labelled according to the present convention (N(2) for amine nitrogen atom and N(1), N(3) and N(4) for pyridine nitrogen atoms).

3. Solution characterizations of SO_3^{2-} and $S_2O_3^{2-}$ interactions with $[LCu(solvent)]^{2+}$

3.1. UV–Vis and EPR characterizations

The UV–Visible and EPR spectra of *in situ* generated complexes 1, 2 and the reference $[LCu(solvent)]^{2+}$ (3) are reported in Fig. 2 panel A and B, respectively. In the d-d region of the UV–Vis spectra and in EPR, the three species have different fingerprints, mirroring a different environment around the Cu(II) center. 1–3 have UV–Vis transition bands characteristic of a TBP geometry with an intense peak in the near-infrared region at 750 nm (ε = 390 $M^{-1}cm^{-1}$), 935 nm (ε = 180 M^{-1} cm^{-1}) and 870 nm (ε = 230 M^{-1} cm^{-1}), respectively, and a higher energy band at 573 nm (ε = 490 M^{-1} cm^{-1}) for 1, 700 nm (ε = 100 M^{-1} cm^{-1}) for 2 and an ill-defined shoulder near 680 nm in case of 3 (Table 2). A ligand to Cu(II) charge transfer (LMCT) band is observed for 1 at 430 nm (ε = 8600 ± 200 M^{-1} cm^{-1}) and 2 at 401 nm (ε = 6000 ± 200 M^{-1} cm^{-1}), reminiscent of those observed for the parent complexes [L_TCu(S_2O_3)] [28].

In EPR, the spectra are characteristic of TBP Cu(II) complexes exhibiting a reverse axial pattern ($g_\perp > g_{||}$) indicating a d_{z2} ground state [31]. This is a quite unusual feature for Cu(II) species that more often lie into elongated octahedral, square planar or square-based pyramid geometries, with $g_\perp > g_{//}$ [1]. However, it is a fingerprint of Cu(II)

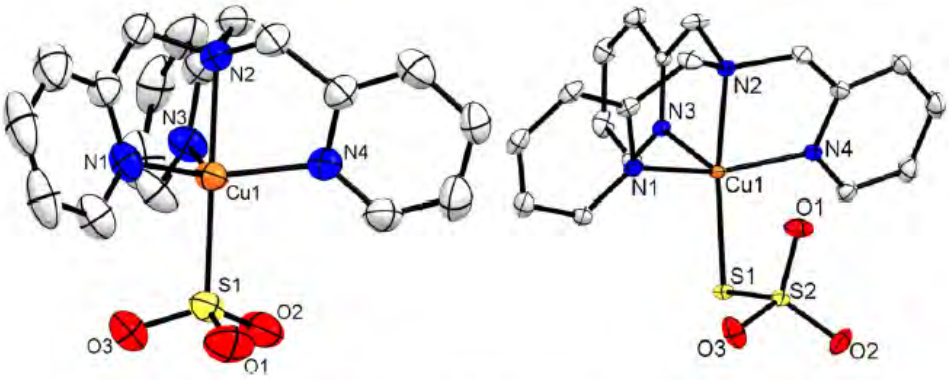

Fig. 1. X-ray structures of LCu(SO_3) (1), LCu(S_2O_3) (2) drawn with 50% of ellipsoid.

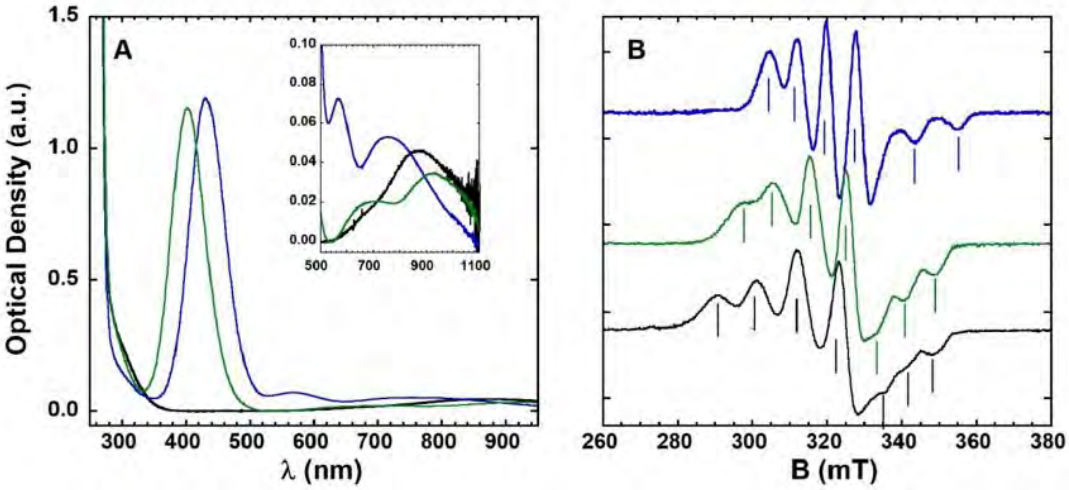

Fig. 2. UV–Vis (panel A) and 9-GHz EPR (panel B) of complexes 1 (blue line), 2 (green line) and 3 (black line). Complexes were generated *in situ*. Panel A: [Cu] = 0.2 mM; [L] = 0.22 mM; $[SO_3^{2-}] = [S_2O_3^{2-}] = 1$ mM; AcN/HEPES (pH 6.5) 100 mM (50/50 *v*/v). $\ell = 1$ cm; $T = 25$ °C. Panel B: $[^{65}Cu] = 500$ μM; [L] = 550 μM; $[SO_3^{2-}] = [S_2O_3^{2-}] = 2.5$ mM in AcN/HEPES (pH 6.5) 100 mM (50/50 *v*/v). $T = 120$ K, microwave power: 5 mW. (For interpretation of the references to colour in this figure legend, the reader is referred to the web version of this article.)

Table 2
Physico-chemical parameters of complexes 1–3 in AcN/HEPES (pH 6.5) 100 mM (50/50 *v*/v).

complex	λ_{max1} (nm)	ε^a (M^{-1} cm^{-1})	λ_{max2} (nm)	ε^a (M^{-1} cm^{-1})	pKa_1	pKa_2	^{app}Ka (10^3 M^{-1})	$g_\perp{}^c$ ($A_\perp$, 10^4 cm^{-1})	$g_{//}{}^c$ ($A_{//}$, 10^4 cm^{-1})	$E_{1/2}$ (V. vs SCE)	ΔE^p (mV)
1	430	8600 ± 200	573	490 ± 20	6.0 ± 0.1	9.5 ± 0.1	2.5 ± 0.5	2.14 (76)	2.00 (104)	−0.25	100
			750	390 ± 20							
2	401	6000 ± 200	700	100 ± 20	1.6 ± 0.1	9.0 ± 0.1	40 ± 10	2.17 (101)	2.00 (69)	−0.27	90
			935	180 ± 20							
3			680	80 ± 20				2.21 (110)	2.00 (60)	−0.21	120
			870	230 ± 20							
1[b]	418	8200 ± 400	665	80 ± 20			7 ± 1				
			870	260 ± 20							

[a] The ε values of the LMCT and d-d bands were deduced from the fits of the titration curves (See Section 7).
[b] Values in aqueous buffer (HEPES 100 mM, pH 6.5).
[c] EPR parameters were deduced from the position of the second and third hyperfine lines in the perpendicular plan and along the parallel direction (except for 2, where the third and four hyperfine parallel lines were used). g values were calculated from the average of the field position of the second and third hyperfine lines, while the hyperfine values correspond to the field differences between these two lines. ^{65}Cu isotope was used.

complexes of 4 N-tripodal ligands [32–36]. Although a slight rhombicity can be anticipated (*i.e.* the situation doesn't exactly correspond to $g_\perp = g_x = g_y$), especially in case of 2 and 3, we will consider the three EPR signatures as axial. Similar patterns have been reported for LCu(II)-based complexes in various solvents and solvent mixtures [20,37–39], and for LCu(II)-oxygen intermediate adducts [7,40–43]. The hyperfine couplings can be detected in both perpendicular and parallel directions. We have directly measured them on the spectra (Fig. 2B and parameters listed in Table 2). For 1 and 2 the signatures are narrower than in 3, in line with closer $g_\perp$ and $g_{//}$ values. For 1, the $A_{//}$ is smaller than $A_\perp$ while this is the opposite in case of 2 and 3. For 2 and 3, the hyperfine lines are broader and less well-defined, mirroring the presence of several species in solution and/or anisotropically strained spectra. Such features are not observed in 1, in line with a well-defined TBP structure of 1 in solution.

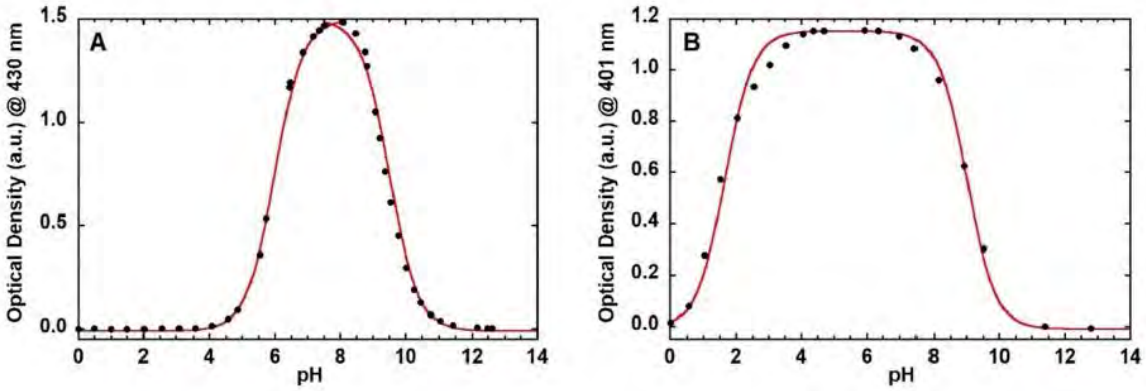

Fig. 3. pH titration of complexes 1 (panel A) and 2 (panel B) measured on the LMCT (plain circles) together with fit (plain red lines). $[LCu(solvent)]^{2+} = 0.2$ mM, $[SO_3^{2-}] = [S_2O_3^{2-}] = 1$ mM, AcN/HEPES (pH 6.5) 100 mM (50/50 *v*/v); $\ell = 1$ cm; $T = 25$ °C.

3.2. pH stability domains

The pH[#] domain where complexes 1 and 2 predominate were determined using pH-titration monitored by UV–Vis following the LMCT band. The results are given in Fig. 3. From the fits of the curves, the two pKa values corresponding to evolution of the complexes in acidic or basic media were determined (reported in Table 2). The first pKa value of 1 and 2 (6.0 and 1.6) is directly linked to the protonation constants of SO_3^{2-} and $S_2O_3^{2-}$ (pKa values of 7.0 and 1.7, respectively). The slightly lower pKa value obtained for 1 versus SO_3^{2-} indicates a stabilization of the SO_3^{2-} protonation state by binding to the Cu(II) ion. The second pKa values of 1 and 2, which are very close for both dianions, may witness a similar competition between SO_3^{2-} or $S_2O_3^{2-}$ and HO^- for Cu(II) binding.

[#] For a matter of simplicity, pH is here used abusively as the experiment is in a mixture of AcN/HEPES (pH 6.5) 100 mM (50/50 *v*/v).

3.3. Binding constants of SO_3^{2-} and $S_2O_3^{2-}$ to [LCu (solvent)]$^{2+}$

The affinity of SO_3^{2-} and $S_2O_3^{2-}$ for 3 were determined by UV–Vis titration on the LMCT and d-d bands. Experiments at two concentrations were performed to (i) probe both transitions and (ii) to cover as much as possible the affinity range. They were performed in triplicate and both titrations on LMCT and d-d transitions were fitted (Fig. 4). The apparent binding affinity values (^{app}Ka) obtained are given in Table 2. Two main observations can be made: at pH 6.5 the affinity of $S_2O_3^{2-}$ is about 10 times higher than that of SO_3^{2-} for [LCu (solvent)]$^{2+}$ and is close to the one reported in case of [(L_T)Cu(H_2O)]$^{2+}$ as the receiving complexes [28].

3.4. Cyclic voltammetry studies

The binding of SO_3^{2-} and $S_2O_3^{2-}$ was also probed by cyclic voltammetry (CV). Fig. 5 shows the CV of complex 3 and upon addition of 1–5 equiv. of SO_3^{2-} and $S_2O_3^{2-}$. Complex 3 shows a reversible wave at $E_{1/2} = -0.21$ V vs. SCE ($\Delta E^p = 120$ mV) corresponding to the Cu(II)/Cu (I) redox couple. This value lies in the range [−0.4 to 0 V] (vs. SCE) reported for [LCu(H_2O)]$^{2+}$ and [LCu(AcN)]$^{2+}$ in refs. [8, 21, 44–47], and mirrors the importance of solvation effects on redox potential values as well as the higher stabilization of [LCu^I(AcN)]$^+$ in AcN and of [LCu^{II}(H_2O)]$^{2+}$ in water medium. Upon addition of SO_3^{2-} and $S_2O_3^{2-}$ the redox potential is shifted toward more cathodic (negative) values in line with the substitution of a neutral solvent ligand by an anionic ligand in the Cu(II) complexes coordination sphere. The shift equals 40 mV for SO_3^{2-} and 60 mV for $S_2O_3^{2-}$ indicating a stronger stabilization by $S_2O_3^{2-}$ in agreement with the higher affinity determined previously and/or the higher negatively charged binding sulfur atom.

4. Determination of the sulfite concentration in sugar

As an application of the above described complexes characterizations, we determined the sulfite concentration in crystal sugar using the method of standard additions, by following the appearance of the LMCT band at 418 nm (see Table 2, Fig. S1). The results are shown in Fig. 6. The quantity of SO_3^{2-} in sugar was evaluated as 1.2 mg/kg of sugar (corresponding to a detection in the μM range). This indicates that this method although very simple and straightforward compares well with other methodologies developed for evaluation of SO_3^{2-} [19], including colorimetric ones [48–54]. SO_3^{2-} content in sugar was previously detected with other methods, which have, as the current method, a threshold level in the μM range as well [55–58].

5. Formation of 1 by reduction of 3 with dithionite

Sulfite binding to 3 was first observed upon addition of dithionite ($S_2O_4^{2-}$) to 3 whereas we aimed at forming in-situ the [LCu^I(solvent)]$^+$ species in order to evaluate its reactivity toward dioxygen. The UV–Vis (especially the LMCT band) and EPR signatures that appeared were highly reminiscent of those of superoxide/hydroperoxide [LCu(II)]$^{2+}$ adducts [7,11,40–43] but were further attributed to formation of 1 by comparison with direct addition of SO_3^{2-} to 3. 1 originates from the reduction of dithionite in the medium as described in Scheme 1. The mechanism is based on the kinetic evolution of dithionite, and complexes 3 and 1 (Fig. 7) and on refs. [59–62] about the various condition-dependent pathways of dithionite evolution. Briefly, dithionite ($S_2O_4^{2-}$) reacts with dioxygen to form sulfite (SO_3^{2-}), including in the stock solution of dithionite (reaction 1, Scheme 1). In addition to this, likely minor way of producing sulfite ions, the reduction of 3 (or 1) in the UV–Vis cuvette by dithionite leads to sulfite as a second product (reaction 2). In presence of 3 and sulfite, there is formation of 1, which can be further reduced by dithionite (reaction 3) until dithionite is fully consumed. Hence, the first increase in the UV–Vis band at 430 nm (Table 2) corresponds to the formation of 1 along with reaction 1 (complex 3 to which is added dithionite from the stock solution, thus containing sulfite). Then and as long as there is still dithionite, 1 is formed but continuously reduced (no increase in the sulfite to Cu(II) LMCT band) in line with the respective redox potential of 1 (Table 2). Finally, once the concentration in dithionite is not enough to reduce 1, 1 starts to accumulate. It is thus worth noting that dithionite in chemical or biological experiments has to be carefully handled to avoid formation of undesired by-products including Cu(II) complexes [63,64].

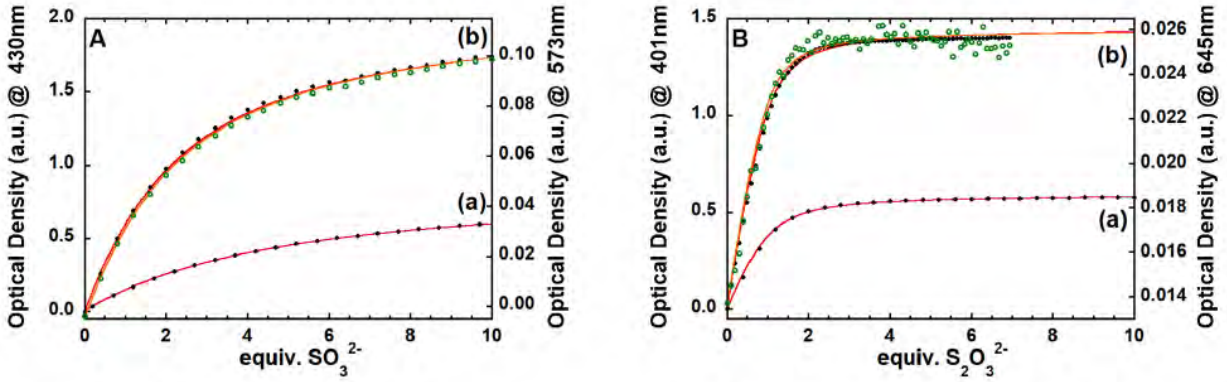

Fig. 4. SO_3^{2-} (panel A) and $S_2O_3^{2-}$ (panel B) titrations into [LCu(solvent)]$^{2+}$. Variations of the absorbance measured on the LMCT (black plain circles) or d-d bands (green open circles), at 0.1 mM (a) and 0.25 mM (b) concentration in [LCu(solvent)]$^{2+}$, and corresponding fits (red lines: LMCT bands, orange line: d-d bands). AcN/HEPES (pH 6.5) 100 mM (50/50 *v*/v); $\ell = 1$ cm; $T = 25$ °C. (For interpretation of the references to colour in this figure legend, the reader is referred to the web version of this article.)

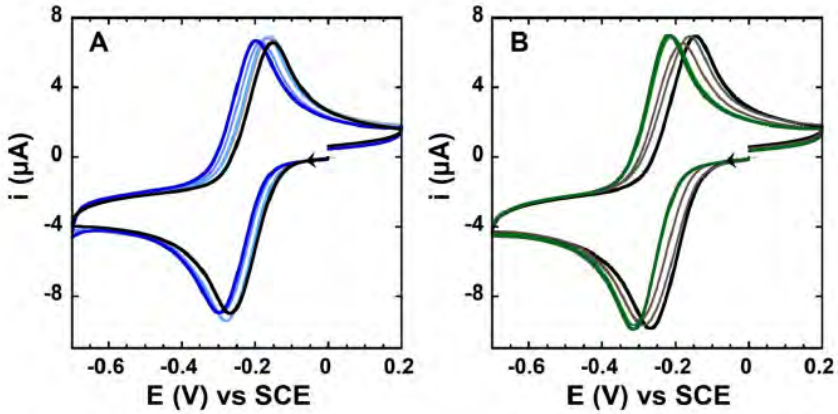

Fig. 5. Cyclic voltamograms of $[LCu(solvent]^{2+}$ in presence of 0 (black line) to 5 equiv. of SO_3^{2-} (panel A, blue line) and $S_2O_3^{2-}$ (panel B, green line). AcN/HEPES (pH 6.5) 100 mM (50/50 *v*/v), scan rate = 100 mV.s^{-1}, working electrode = vitrous carbon, counter electrode: Pt, reference: SCE. (For interpretation of the references to colour in this figure legend, the reader is referred to the web version of this article.)

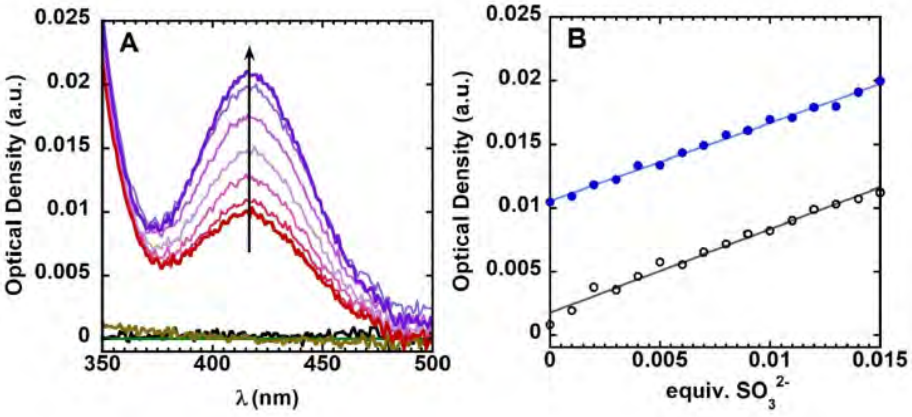

Fig. 6. UV–Vis determination of SO_3^{2-} level in sugar determined by the method of standard additions. (A) LMCT band of complex 1 *in situ* generated due to the presence of sugar (red bold line) and then as a function of controlled addition of SO_3^{2-} (up to 0.015 equiv. versus $[LCu(H_2O)]^{2+}$, purple bold line). $[LCu(H_2O)]^{2+}$ = 0.25 mM, [sugar] = 0.4 g.mL^{-1}. (B) Titration curve and its linear fit (y = 0.0105 + 0.61 x, R = 0.997, blue dots and line) together with the same titration curve without sugar (black open dots and grey line). Value of the intercept with the y-axis and slope releases the level of SO_3^{2-} in sugar. (For interpretation of the references to colour in this figure legend, the reader is referred to the web version of this article.)

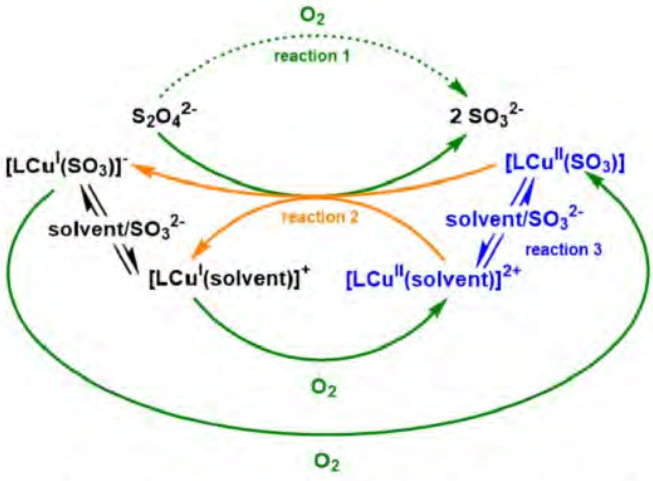

Scheme 1. Proposed mechanism for the formation of complex 1 from the aerobic reduction of 3 by dithionite.

6. Concluding remarks

In the present short report, we described the synthesis and full spectroscopic and analytic characterizations of two Cu(II) complexes obtained with the well-known TMPA (L) ligand, where the fifth coordination site is occupied either by a sulfite (SO_3^{2-}) or thiosulfate ($S_2O_3^{2-}$) ion. The in-situ formation of the $[LCu(SO_3)]$ complex was further used to evaluate the sulfite content in crystal sugar, in order to illustrate one possible application of the basic study shown here. It is here worth noting that in addition to be very easy to set up (commercial ligand, UV–Vis detection method, ratiometric), the threshold level of detection of the present method compares well with previous probes reported in the literature, including those relying on more indirect paths. Besides, because the UV–Vis depends on the nature of the adduct (here $[LCu(SO_3)]$ or $[LCu(S_2O_3)]$), the method is also specific for the detection of a given exogenous ligand.

The formation of $[LCu(SO_3)]$ was discovered by chance in the course of an experiment based on the aerobic reduction of $[(L)Cu(solvent)]^{2+}$ by dithionite, illustrating the complexity and hazard to use such reductant in Cu(II) chemistry. In the present case, however, it leads to the full analyses of the $[LCu(SO_3)]$ and parent $[LCu(S_2O_3)]$ complexes, including by X-ray crystallography.

7. Experimental section

7.1. Chemicals

$CuSO_4 \bullet 5(H_2O)$, sodium thiosulfate anhydrous, sodium dithionite, sodium hydroxide and HEPES buffer were purchased from Sigma (purity ≥98%). Tris(2-pyridylmethyl)amine was purchased from TCI (purity ≥98%). Sulfuric acid was bought from Fluka (purity 95.0–97.0%). Sodium sulfite was purchased from Fluorochem. Every reagents was used without further purification. Acetonitrile (AcN) was purchased from Carlo Erba (HPLC isocratic grade).

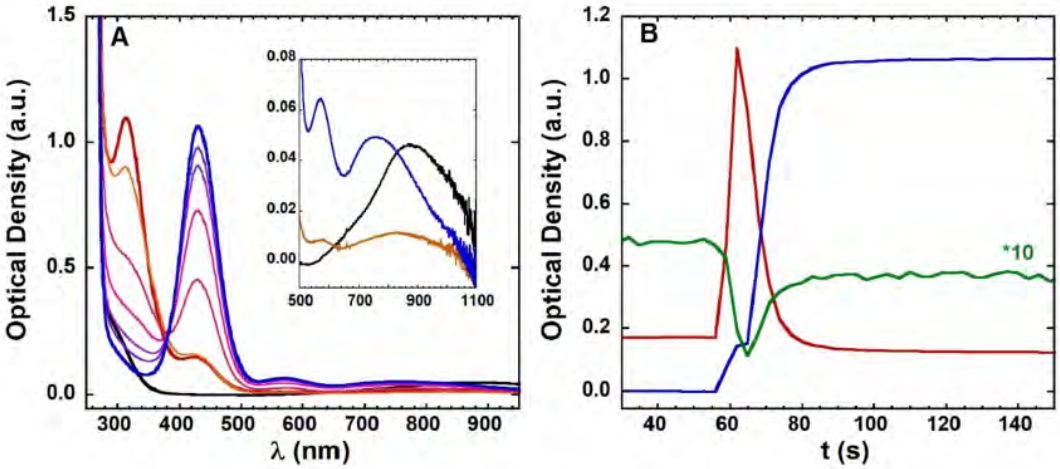

Fig. 7. *In situ* formation of 1 by reduction of 3 with dithionite. Panel A: selection of key spectra (black: 3, red: just after addition of dithionite and then orange to light blue: every 3 s after addition of dithionite and blue: after completion of reaction), inset: d-d bands; panel B: kinetic monitoring at key wavelengths (315 nm in red, 430 nm in blue and 870 nm in green, intensity *10 to ease comparison with other kinetic traces). Dithionite was added at $t = 56$ s. (For interpretation of the references to colour in this figure legend, the reader is referred to the web version of this article.)

Every aqueous solutions were prepared in ultrapure water with a resistivity of 18.2 MΩ·cm.

HEPES buffer: A 500 mM stock solution of HEPES buffer is prepared by dissolution of 5.98 g of HEPES in 50 mL H_2O. The pH is adjusted by addition of a stock solution of NaOH (5 M) drop by drop under stirring until pH 6.5 is reached.

Cu(II)SO_4: A 100 mM stock solution of Cu(II)SO_4 is prepared by dissolution of 1.25 g of Cu(II)SO_4•$5H_2O$ in 50 mL H_2O. Cu^{II} concentration was measured by UV–visible absorption (the absorbance was measured at 800 and 450 nm, the difference A800 − A450 was used with $\varepsilon = 12\ M^{-1}\ cm^{-1}$ to determine the concentration). The solution was diluted down to 25 mM in Cu^{II} to form the final stock solution used further in experiments.

For EPR experiments, a ^{65}Cu(NO_3) stock solution was obtained from the nitric acid attack of a ^{65}Cu foil (Eurisotop).

TMPA ligand (L): A 10 mM stock solution of Tris(2-pyridylmethyl) amine (TMPA) is prepared by dissolution of 14.5 mg of TMPA in 50 mL H_2O. The exact concentration is determined by UV–vis titration using stock solution of Cu(II)SO_4 and monitoring the absorbance at 890 nm corrected with the absorbance at 480 nm, see Fig. S2).

Sodium sulfite (Na_2SO_3), sodium thiosulfate ($Na_2S_2O_3$) and sodium dithionite ($Na_2S_2O_4$) solutions are freshly prepared at the desired concentration by dissolution in H_2O just before use.

7.2. Crystallographic samples and data

Formation of crystals of 1 and 2. A 100 mM solution of 1 was prepared by mixing TMPA (1.1 eq; 32 mg) with Cu(II)SO_4•$5H_2O$ (1 eq; 25 mg) in 1 mL AcN/HEPES (pH 6.5) 500 mM (50/50 *v*/v) (turquoise solution), then Na_2SO_3 (7 eq, 88 mg) was added (dark brown solution). The solution is sonicated and filtered. Dark green crystals suitable for X-ray crystallography were obtained by slow diffusion of diethylether into the filtrate at room temperature in the dark. A 100 mM solution of 2 was prepared, by mixing TMPA (1.1 eq; 32 mg) with Cu(II)SO_4•$5H_2O$ (1 eq; 25 mg) in 1 mL AcN/HEPES (pH 6.5) 500 mM (50/50 *v*/v) (turquoise solution), then $Na_2S_2O_3$ (5 eq, 79 mg) was added (dark green solution). The solution is sonicated. Blue-greenish crystals suitable for characterization were obtain by slow diffusion of diethylether at room temperature in the dark.

Crystallographic data were collected at 273(2) K (1) or 110(2)K (2), on a Bruker-AXS Kappa APEX II diffractometer equipped with a 30 W air-cooled microfocus source, using MoK_α radiation ($\lambda = 0.71073$ Å). Phi- and omega-scans were used. Space groups were determined on the basis of systematic absences and intensity statistics. Empirical absorption correction was employed [1].The structures were solved using an intrinsic phasing method (SHELXT) [2], and refined using the least-squares method on F^2 [3].All non-H atoms were refined with anisotropic displacement parameters. The hydrogen atoms on carbon atoms were refined isotropically at calculated positions using the riding model. All hydrogen atoms of water molecules of 2 were located in the difference Fourier maps and refined freely.

CCDC-2068976 (1), CCDC-2068975 (2), contain the supplementary crystallographic data for this paper. These data can be obtained free of charge from The Cambridge Crystallographic Data Centre via www.ccdc.cam.a-c.uk/data_request/cif.

7.3. UV–Visible spectroscopy

The UV–vis were recorded on a Hewlett Packard Agilent 8453 or 8454 spectrophotometer at 25 °C under a 800 rpm stirring.

- pH titration of 1 and 2. The pH of a 0.2 mM solution 1 (resp. 2) *in situ* generated by mixing $[LCu(solvent)]^{2+} = 0.2$ mM and $[SO_3^{2-}] = 1$ mM or $[S_2O_3^{2-}] = 1$ mM in AcN/HEPES (pH 6.5) 100 mM (50/50 *v*/v) is varied by addition of H_2SO_4 or NaOH from stock solutions and monitored using a pH micro-electrode directly put in the UV–Vis cuvette. A UV–vis spectrum is recorded for each pH value and the absorbance at 430 nm (resp. 401 nm) monitored.
- Sulfite and thiosulfate titrations to 3: To a 0.25 mM solution of 3 in AcN/HEPES (pH 6.5) 100 mM (50/50 *v*/v), 1 µL of a freshly prepared 50 mM solution of Na_2SO_3 (0.1 eq, 25 µM) or Na_2SO_3 (0.1 eq, 25 µM) is added every 90 s by a automatic fluid dispenser and titration machine (Dostal Dosy) under stirring in an initial volume of 2 mL. A UV–Vis spectrum is recorded after each addition and further analyzed.

The titration curves were analyzed using a in-house procedure written in Kaleidagraph software.

Change in the absorbance at xyz nm (xyz stands for the maximum absorbance of the LMCT and d-d bands in 1 and 2) was reproduced according to the following procedure.

Absorbance was calculated as a function SO_3^{2} or $S_2O_3^{2-}$ equivalent numbers according to:

$$Abs = \left[([\mathbf{3}] - [\alpha]C_O)\bullet\varepsilon^{3}_{xyz\ nm} + [\alpha]C_O\bullet\varepsilon^{1}_{xyz\ nm}\right]1 \text{ or}$$
$$Abs = \left[([\mathbf{3}] - [\alpha]C_O)\bullet\varepsilon^{3}_{xyz\ nm} + [\alpha]C_O\bullet\varepsilon^{2}_{xyz\ nm}\right]1.$$

where α stands for the progression of the following reaction: $\underline{3} + SO_3^{2-} \rightarrow \underline{1}$ or $\underline{3} + S_2O_3^{2-} \rightarrow \underline{2}$ where the affinity constant was adjusted to obtain the best reproduction of the experimental data.

Fits of the LMCT and d-d bands were performed simultaneously to increase constraints of the affinity value.

Titration of sulfite in sugar: 1 g of crystal sugar was dissolved by addition of 1 mL of a 100 mM HEPES buffer solution at pH 6.5 affording a sugar stock solution of 2.5 mL. 25 mg of Na_2SO_3 was dissolved in 2 mL H_2O and diluted again just before use to afford a solution at 0.5 mM. A 3 mL UV–vis cuvette is loaded with 1924 µL of the crystal sugar stock solution. 60 µL of a 10 mM TMPA stock solution and 20 µL of a 25 mM Cu(II)SO_4 stock solution are added affording a total concentration of 0.25 mM Cu(II)TMPA. 1 µL of a freshly prepared 0.5 mM solution of Na_2SO_3 (0.001 eq, 0.25 µM) is added every 60 s by a automatic fluid dispenser and titration machine (Dostal Dosy) under stirring. A UV–vis spectrum is recorded prior to each addition. The absorbance at 418 nm is monitored.

The absorption band at 418 nm of the $\underline{1}$ with sugar as source of SO_3^{2-} corresponds to 0.015 equivalent of Na_2SO_3, corresponding to a concentration of 3.75 µM in the UV-cuvette.

$$[Na_2SO_3]_{stock\ solution} = \frac{[Na_2SO_3]_{UVcuvette} * V_{UVcuvette}}{V_{sucre}}$$

$$[Na_2SO_3]_{stock\ solution} = \frac{3.75*10^{-6}*2*10^{-3}}{1924*10^{-6}}$$

$$[Na_2SO_3]_{stock\ solution} = 3.90\ \mu M$$

$$m_{Na_2SO_3 stock\ solution} = [Na_2SO_3]_{stock\ solution} * V_{stock\ solution} * MW_{Na_2SO_3}$$

$$m_{Na_2SO_3 stock\ solution} = 3.90*10^{-6}*2.5*10^{-3}*126.04$$

$$m_{Na_2SO_3 stock\ solution} = 1.23 * 10^{-6} g \text{ per } 1 \text{ g of sugar}$$

$$m_{Na_2SO_3 sugar} = 1.23\ mg/kg$$

7.4. EPR spectroscopy

Electron Paramagnetic Resonance (EPR) data were recorded using an Elexsys E 500 Bruker spectrometer, operating at a microwave frequency of approximately 9.5 GHz. Spectra were recorded using a microwave power of 5 mW across a sweep width of 200 mT (centered at 320 mT) with modulation amplitude of 0.5 mT. Experiments were carried out at 120 K using a liquid nitrogen cryostat.

Sample preparation for EPR experiments: the TMPA ligand was dissolved in water to have a final concentration at about 10 mM. The solution was diluted down to 0.55 mM in a mixture of AcN/HEPES (pH 6.5) 100 mM (50/50 *v*/v) and 0.9 equivalent of $^{65}Cu(II)NO_3$ was added from stock solution. Depending to the EPR sample desired, 5 equivalents of Na_2SO_3, or $Na_2S_2O_3$ were added. 200 µL of the solution was transferred to an EPR tube and frozen until used.

7.5. Cyclic voltammetry

Cyclic voltammetry was performed in a standard three-electrode cell by using an Autolab potentiostat (PGSTAT302N, Autolab) interfaced to a PC computed and piloted with GPES software (version 4.9). A saturated calomel electrode, isolated from the solution by a glass frit, and a platinum wire were used as reference and counter electrodes, respectively. Working electrode was a glassy carbon electrode (3 mm diameter) polished by a 1 µm and 0.3 µm alumina slurry (2 min each) on a cloth polishing pad and washed with water under sonication (1 min). CVs were recorded under argon pressure passing through a bubbler containing AcN at room temperature. The cyclic voltammograms were recorded at a scan rate of 100 mV/s, with a step potential of 1 mV.

A 0.5 mM solution of $\underline{3}$ were *in situ* generated by mixing TMPA (1.5 eq; 0.75 mM) with Cu(II)SO_4•$5H_2O$ (1 eq; 0.5 mM,) in 6 mL AcN/HEPES (pH 6.5) 100 mM (50/50 *v*/v), then 1–5 equivalents of Na_2SO_3 or $Na_2S_2O_3$ were added from 200 mM stock solution freshly prepared in H_2O.

7.6. Elemental analysis of **2**

A 100 mM solution of $\underline{2}$ was prepared in a mixture of AcN/HEPES (pH 6.5) 100 mM (50/50 *v*/v), by mixing TMPA (1.1 eq; 110 mM, 16 mg) with Cu(II)SO_4•$5H_2O$ (1 eq; 100 mM, 12.5 mg) (turquoise solution), then $Na_2S_2O_3$ (5 eq, 500 mM, 39.5 mg) is added (dark green solution). The solution is sonicated. A shiny dark blue-greenish powder is obtained by precipitation in diethylether and filtered. The powder is freeze-dried to afford 11.4 mg of $\underline{2}$ suitable for elemental analysis. Theoretical values for $\underline{2}$, 0.12 $Na_2S_2O_3$: C (44.3); H (3.7) and N (11.5); experimental values: C (44.3); H (3.4) and N (11.5).

Author statement

LB performed the studies and participated to the writing of the publication. CE supervised the research. SML resolved the X-ray structures and wrote the crystallographic part. CH supervised the research and wrote the publication.

Declaration of Competing Interest

The authors have no conflict of interest to declare.

Acknowledgments

L.B. thanks the University Paul Sabatier (UPS) for a PhD Fellowship allocated to the NAIST-UPS doctoral double degree program.

Appendix A. Supplementary data

Supplementary data to this article can be found online at https://doi.org/10.1016/j.jinorgbio.2021.111601.

References

[1] E.I. Solomon, D.E. Heppner, E.M. Johnston, J.W. Ginsbach, J. Cirera, M. Qayyum, M.T. Kieber-Emmons, C.H. Kjaergaard, R.G. Hadt, L. Tian, Copper active sites in biology, Chem. Rev. 114 (7) (2014) 3659–3853.
[2] M. Wikström, V. Sharma, Proton pumping by cytochrome c oxidase – a 40 year anniversary, Biochim. Biophys. Acta BBA – Bioenerg. 1859 (9) (2018) 692–698.
[3] G.J. Reed, Q.N. Lam, E.N. Mirts, Y. Lu, Molecular understanding of heteronuclear active sites in heme–copper oxidases, nitric oxide reductases, and sulfite reductases through biomimetic modelling, Chem. Soc. Rev. 50 (4) (2021) 2486–2539.
[4] S.M. Adam, G.B. Wijeratne, P.J. Rogler, D.E. Diaz, D.A. Quist, J.J. Liu, K.D. Karlin, Synthetic Fe/Cu complexes: toward understanding heme-copper oxidase structure and function, Chem. Rev. 118 (22) (2018) 10840–11022.
[5] C. Bravin, E. Badetti, G. Licini, C. Zonta, Tris(2-pyridylmethyl)amines as emerging scaffold in supramolecular chemistry, Coord. Chem. Rev. 427 (2021) 213558.
[6] N.W.G. Smits, B. van Dijk, I. de Bruin, S.L.T. Groeneveld, M.A. Siegler, D.G. H. Hetterscheid, Influence of ligand denticity and flexibility on the molecular copper mediated oxygen reduction reaction, Inorg. Chem. 59 (22) (2020) 16398–16409.
[7] D.E. Diaz, D.A. Quist, A.E. Herzog, A.W. Schaefer, I. Kipouros, M. Bhadra, E. I. Solomon, K.D. Karlin, Impact of intramolecular hydrogen bonding on the reactivity of cupric superoxide complexes with O–H and C–H substrates, Angew. Chem. Int. Ed. 58 (49) (2019) 17572–17576.
[8] M. Langerman, D.G.H. Hetterscheid, Fast oxygen reduction catalyzed by a copper (II) Tris(2-pyridylmethyl)amine complex through a stepwise mechanism, Angew. Chem. Int. Ed. 58 (37) (2019) 12974–12978.
[9] D.A. Quist, M.A. Ehudin, K.D. Karlin, Unprecedented direct cupric-superoxo conversion to a bis-μ-oxo dicopper(III) complex and resulting oxidative activity, Inorg. Chim. Acta 485 (2019) 155–161.
[10] F. Mehlich, A.E. Roberts, M. Kerscher, P. Comba, G.A. Lawrance, C. Würtele, J. Becker, S. Schindler, Synthesis and characterization of copper complexes with a series of tripodal amine ligands, Inorg. Chim. Acta 486 (2019) 742–749.

[11] M. Bhadra, J.Y.C. Lee, R.E. Cowley, S. Kim, M.A. Siegler, E.I. Solomon, K.D. Karlin, Intramolecular hydrogen bonding enhances stability and reactivity of mononuclear cupric superoxide complexes, J. Am. Chem. Soc. 140 (29) (2018) 9042–9045.
[12] C. Cheignon, M. Jones, E. Atrián-Blasco, I. Kieffer, P. Faller, F. Collin, C. Hureau, Identification of key structural features of the elusive Cu–Aβ complex that generates ROS in Alzheimer's disease, Chem. Sci. 8 (7) (2017) 5107–5118.
[13] E. Atrian-Blasco, M. Del Barrio, P. Faller, C. Hureau, Ascorbate oxidation by Cu (amyloid-β) complexes: determination of the intrinsic rate as a function of alterations in the peptide sequence revealing key residues for reactive oxygen species production, Anal. Chem. 90 (9) (2018) 5909–5915.
[14] R. Franco, G. Navarro, E. Martínez-Pinilla, Antioxidants versus food antioxidant additives and food preservatives, Antioxidants 8 (11) (2019) 542.
[15] E. Kontaxakis, E. Trantas, F. Ververidis, Resveratrol: a fair race towards replacing sulfites in wines, Molecules 25 (10) (2020) 2378.
[16] P.L. McGeer, E.G. McGeer, M. Lee, Medical uses of sodium thiosulfate, J. Neurol. Neuromed. 1 (3) (2016) 28–30.
[17] I.J. Skypala, M. Williams, L. Reeves, R. Meyer, C. Venter, Sensitivity to food additives, vaso-active amines and salicylates: a review of the evidence, Clin. Transl. Allergy 5 (1) (2015) 34.
[18] Summary of Evaluations Performed by the Joint FAO/WHO Expert Committee on Food Additives. Sulfur Dioxide, Food and Agriculture Organization/World Health Organization, Rome, Italy and Geneva, Switzerland, 2007.
[19] C.S. Pundir, R. Rawal, Determination of sulfite with emphasis on biosensing methods: a review, Anal. Bioanal. Chem. 405 (10) (2013) 3049–3062.
[20] A.G. Porras Gutiérrez, J. Zeitouny, A. Gomila, B. Douziech, N. Cosquer, F. Conan, O. Reinaud, P. Hapiot, Y. Le Mest, C. Lagrost, N. Le Poul, Insights into water coordination associated with the CuII/CuI electron transfer at a biomimetic Cu Centre, Dalton Trans. 43 (17) (2014) 6436–6445.
[21] H. Nagao, N. Komeda, M. Mukaida, M. Suzuki, K. Tanaka, Structural and electrochemical comparison of copper(II) complexes with tripodal ligands, Inorg. Chem. 35 (23) (1996) 6809–6815.
[22] H. Guo, C. Gong, X. Zeng, H. Xu, Q. Zeng, J. Zhang, Z. Zhong, J. Xie, Isopolymolybdate-based inorganic–organic hybrid compounds constructed by multidentate N-donor ligands: syntheses, structures and properties, Dalton Trans. 48 (17) (2019) 5541–5550.
[23] I.J. Bazley, E.A. Erie, G.M. Feiereisel, C.J. LeWarne, J.M. Peterson, K.L. Sandquist, K.D. Oshin, M. Zeller, X-ray crystallography analysis of complexes synthesized with Tris(2-pyridylmethyl)amine: a laboratory experiment for undergraduate students integrating interdisciplinary concepts and techniques, J. Chem. Educ. 95 (5) (2018) 876–881.
[24] S.S. Massoud, F.R. Louka, M.A. Gazzaz, M.M. Henary, R.C. Fischer, F.A. Mautner, Polynuclear copper(II) complexes bridged by polycarboxylates of aromatic and N-heterocyclic compounds, Polyhedron 111 (2016) 45–52.
[25] B.S. Lim, R.H. Holm, Molecular heme–cyanide–copper bridged assemblies: linkage isomerism, trends in νCN values, and relation to the Heme-a3/CuB site in cyanide-inhibited Heme–copper oxidases, Inorg. Chem. 37 (19) (1998) 4898–4908.
[26] A.L. Ward, L. Elbaz, J.B. Kerr, J. Arnold, Nonprecious metal catalysts for fuel cell applications: electrochemical dioxygen activation by a series of first row transition metal Tris(2-pyridylmethyl)amine complexes, Inorg. Chem. 51 (8) (2012) 4694–4706.
[27] T. Fujii, A. Naito, S. Yamaguchi, A. Wada, Y. Funahashi, K. Jitsukawa, S. Nagatomo, T. Kitagawa, H. Masuda, Construction of a square-planar hydroperoxo-copper(ii) complex inducing a higher catalytic reactivity, Chem. Commun. 21 (2003) 2700–2701.
[28] A.J. Fischmann, A.C. Warden, J. Black, L. Spiccia, Synthesis, characterization, and structures of copper(II)–thiosulfate complexes incorporating tripodal tetraamine ligands, Inorg. Chem. 43 (21) (2004) 6568–6578.
[29] A.W. Addison, T.N. Rao, J. Reedijk, J. van Rijn, G.C. Verschoor, Synthesis, structure, and spectroscopic properties of copper(II) compounds containing nitrogen–sulphur donor ligands; the crystal and molecular structure of aqua[1,7-bis(N-methylbenzimidazol-2'-yl)-2,6-dithiaheptane]copper(II) perchlorate, J. Chem. Soc. Dalton Trans. (7) (1984) 1349–1356.
[30] A.J. Fischmann, C.M. Forsyth, L. Spiccia, Stabilization of copper(II) Thiosulfonate coordination complexes through cooperative hydrogen bonding interactions, Inorg. Chem. 47 (22) (2008) 10565–10574.
[31] E. Garribba, G. Micera, The determination of the geometry of Cu(II) complexes: an EPR spectroscopy experiment, J. Chem. Educ. 83 (8) (2006) 1229.
[32] G. Kokoszka, K.D. Karlin, F. Padula, J. Baranowski, C. Goldstein, EPR of copper(II) complexes with tripodal ligands: dynamical properties, Inorg. Chem. 23 (25) (1984) 4378–4380.
[33] M.Q. Ehsan, O. Yasunori, Y. Seigo, I. Masamoto, EPR and ENDOR study of trigonal bipyramidal copper complexes with a nitrogen donor tripodal ligand, Bull. Chem. Soc. Jpn. 69 (8) (1996) 2201–2209.
[34] M. Duggan, N. Ray, B. Hathaway, G. Tomlinson, P. Brint, K. Pelin, Crystal structure and electronic properties of ammine[tris(2-aminoethyl)amine]copper(II) diperchlorate and potassium penta-amminecopper(II) tris(hexafluorophosphate), J. Chem. Soc. Dalton Trans. (8) (1980) 1342–1348.
[35] S. Paria, Y. Morimoto, T. Ohta, S. Okabe, H. Sugimoto, T. Ogura, S. Itoh, Copper(I)–dioxygen reactivity in the isolated cavity of a nanoscale molecular architecture, Eur. J. Inorg. Chem. 2018 (19) (2018) 1976–1983.
[36] C. Suspène, S. Brandès, R. Guilard, Reversible coordination of dioxygen by tripodal tetraamine copper complexes incorporated in a porous silica framework, Chem. Eur. J. 16 (21) (2010) 6352–6364.
[37] G. Izzet, X. Zeng, H. Akdas, J. Marrot, O. Reinaud, Drastic effects of the second coordination sphere on neutral vs. anionic guest binding to a biomimetic Cu(ii) center embedded in a calix[6]aza-cryptand, Chem. Commun. 8 (2007) 810–812.
[38] N. Le Poul, B. Douziech, J. Zeitouny, G. Thiabaud, H. Colas, F. Conan, N. Cosquer, I. Jabin, C. Lagrost, P. Hapiot, O. Reinaud, Y. Le Mest, Mimicking the protein access channel to a metal center: effect of a funnel complex on dissociative versus associative copper redox chemistry, J. Am. Chem. Soc. 131 (49) (2009) 17800–17807.
[39] G. Thiabaud, A. Brugnara, M. Carboni, N. Le Poul, B. Colasson, Y. Le Mest, O. Reinaud, Synthesis and studies of a water-soluble and air-stable CuI/CuII open-shell funnel complex, Org. Lett. 14 (10) (2012) 2500–2503.
[40] S. Kim, C. Saracini, M.A. Siegler, N. Drichko, K.D. Karlin, Coordination chemistry and reactivity of a cupric Hydroperoxide species featuring a proximal H-bonding substituent, Inorg. Chem. 51 (23) (2012) 12603–12605.
[41] Y.J. Choi, K.-B. Cho, M. Kubo, T. Ogura, K.D. Karlin, J. Cho, W. Nam, Spectroscopic and computational characterization of CuII–OOR (R = H or cumyl) complexes bearing a Me6-tren ligand, Dalton Trans. 40 (10) (2011) 2234–2241.
[42] D. Maiti, D.-H. Lee, K. Gaoutchenova, C. Würtele, M.C. Holthausen, A.A. Narducci Sarjeant, J. Sundermeyer, S. Schindler, K.D. Karlin, Reactions of a copper(II) superoxo complex Lead to C-H and O-H substrate oxygenation: modeling copper-monooxygenase C-H hydroxylation, Angew. Chem. Int. Ed. 47 (1) (2008) 82–85.
[43] T. Fujii, S. Yamaguchi, Y. Funahashi, T. Ozawa, T. Tosha, T. Kitagawa, H. Masuda, Mononuclear copper(ii)-hydroperoxo complex derived from reaction of copper(i) complex with dioxygen as a model of DβM and PHM, Chem. Commun. 42 (2006) 4428–4430.
[44] M. Asahi, S.-i. Yamazaki, S. Itoh, T. Ioroi, Electrochemical reduction of dioxygen by copper complexes with pyridylalkylamine ligands dissolved in aqueous buffer solution: the relationship between activity and redox potential, Dalton Trans. 43 (28) (2014) 10705–10709.
[45] W.T. Eckenhoff, S.T. Garrity, T. Pintauer, Highly efficient copper-mediated atom-transfer radical addition (ATRA) in the presence of reducing agent, Eur. J. Inorg. Chem. 2008 (4) (2008) 563–571.
[46] C.X. Zhang, S. Kaderli, M. Costas, E.-i. Kim, Y.-M. Neuhold, K.D. Karlin, A. D. Zuberbühler, Copper(I)–dioxygen reactivity of [(L)CuI]+ (L = Tris(2-pyridylmethyl)amine): kinetic/thermodynamic and spectroscopic studies concerning the formation of Cu– O2 and Cu2– O2 adducts as a function of solvent medium and 4-Pyridyl ligand substituent variations, Inorg. Chem. 42 (6) (2003) 1807–1824.
[47] C.-L. Chuang, O. dos Santos, X. Xu, J.W. Canary, Synthesis and cyclic voltammetry studies of copper complexes of bromo- and alkoxyphenyl-substituted derivatives of Tris(2-pyridylmethyl)amine: influence of cation–alkoxy interactions on copper redox potentials, Inorg. Chem. 36 (9) (1997) 1967–1972.
[48] Y. Ma, X. Fu, W. He, X. Gao, A label free colorimetric assay for detection of sulfite root based on Cu2+, IOP Conf. Ser. Mater. Sci. Eng. 729 (2020), 012090.
[49] M. Chi, Y. Zhu, L. Jing, C. Wang, X. Lu, Fabrication of oxidase-like polyaniline-MnO2 hybrid nanowires and their sensitive colorimetric detection of sulfite and ascorbic acid, Talanta 191 (2019) 171–179.
[50] K. Xiang, S. Chang, J. Feng, C. Li, W. Ming, Z. Liu, Y. Liu, B. Tian, J. Zhang, A colorimetric and ratiometric fluorescence probe for rapid detection of SO2 derivatives bisulfite and sulfite, Dyes Pigments 134 (2016) 190–197.
[51] W. Qin, L. Su, C. Yang, Y. Ma, H. Zhang, X. Chen, Colorimetric detection of sulfite in foods by a TMB–O2–Co3O4 nanoparticles detection system, J. Agric. Food Chem. 62 (25) (2014) 5827–5834.
[52] J. Zhang, X. Xu, X. Yang, Role of Tris on the colorimetric recognition of anions with melamine-modified gold nanoparticle probe and the visual detection of sulfite and hypochlorite, Analyst 137 (15) (2012) 3437–3440.
[53] J. Xu, K. Liu, D. Di, S. Shao, Y. Guo, A selective colorimetric chemosensor for detecting SO32- in neutral aqueous solution, Inorg. Chem. Commun. 10 (6) (2007) 681–684.
[54] K. Venkatachalam, G. Asaithambi, D. Rajasekaran, V. Periasamy, A novel ratiometric fluorescent probe for "naked-eye" detection of sulfite ion: applications in detection of biological SO32− ions in food and live cells, Spectrochim. Acta A Mol. Biomol. Spectrosc. 228 (2020) 117788.
[55] X. Jiang, J. Xu, Y. Zhang, H. Wang, L. Zeng, Y. Zhang, A colorimetric and ratiometric fluorescent probe for the rapid and sensitive detection of sulfite in sugar, Anal. Methods 8 (7) (2016) 1572–1576.
[56] H. Feng, J. Liu, A. Qaitoon, Q. Meng, Y. Sultanbawa, Z. Zhang, Z.P. Xu, R. Zhang, Responsive small-molecule luminescence probes for sulfite/bisulfite detection in food samples, TrAC Trends Anal. Chem. 136 (2021) 116199.
[57] R.-F. Zeng, J.-S. Lan, T. Wu, L. Liu, Y. Liu, R.J.Y. Ho, Y. Ding, T. Zhang, A novel mitochondria-targetted near-infrared fluorescent probe for selective and colorimetric detection of sulfite and its application in vitro and vivo, Food Chem. 318 (2020) 126358.
[58] G. Zhang, R. Ji, X. Kong, F. Ning, A. Liu, J. Cui, Y. Ge, A FRET based ratiometric fluorescent probe for detection of sulfite in food, RSC Adv. 9 (2) (2019) 1147–1150.
[59] J.F. Read, J. John, J. MacPherson, C. Schaubel, A. Theriault, The kinetics and mechanism of the oxidation of inorganic oxysulfur compounds by potassium ferrate: Part I. Sulfite, thiosulfate and dithionite ions, Inorg. Chim. Acta 315 (1) (2001) 96–106.
[60] D.K. Singh, R.N. Sharma, R.D. Srivastava, Kinetics of oxidation of sodium dithionite by flow thermal method, AICHE J. 24 (2) (1978) 232–237.
[61] M. Wayman, W.J. Lem, Decomposition of aqueous dithionite. Part II. A reaction mechanism for the decomposition of aqueous sodium dithionite, Can. J. Chem. 48 (5) (1970) 782–787.

[62] L. Burlamacchi, G. Guarini, E. Tiezzi, Mechanism of decomposition of sodium dithionite in aqueous solution, Trans. Faraday Soc. 65 (1969) 496–502.
[63] C.M.R. Abreu, L. Fu, S. Carmali, A.C. Serra, K. Matyjaszewski, J.F.J. Coelho, Aqueous SARA ATRP using inorganic sulfites, Polym. Chem. 8 (2) (2017) 375–387.
[64] N.J. Blackburn, R.W. Strange, R.T. Carr, S.J. Benkovic, X-ray absorption studies of the copper-dependent phenylalanine hydroxylase from Chromobacterium violaceum. Comparison of the copper coordination in oxidized and dithionite-reduced enzymes, Biochemistry 31 (23) (1992) 5298–5303.

Experimental part

Experimental part

All chemicals and solvents are from Sigma-Aldrich, Acros Organics and Tokyo Chemical Industry. They were used without purification. The aqueous solutions were prepared in ultrapure water (resistance: 18.2 MΩ.cm). The peptides were either bought from Genecust or synthesized. Oxygen-sensitive products were handled under an argon atmosphere with a schlenk line.

Stock solutions

Cu(II) stock solutions were prepared from a $CuSO_4 \bullet 5H_2O$, $Cu(OTf)_2$ and $Cu(ClO_4)_2 \bullet 5H_2O$ salts dissolved in ultrapure water or dry acetonitrile (only $Cu(OTf)_2$) to achieve 20 mM concentration.

Cu(I) solution were prepared from a $Cu(CH_3CN)_4BF_4$ salt dissolved in acetonitrile at a concentration around 50 mM. The solution remain stable when preserved in the freezer. The exact concentration was determined by UV-Vis and adding excess sodium bicinchoninic acid (BCA, 2-(4-carboxyquinolin-2-yl)quinoline-4-carboxylic acid) and measuring the absorbance of $Cu(BCA)_2^{3-}$ with an extinction coefficient of 7700 $M^{-1}cm^{-1}$ at 562 nm. When notified, the Cu(I) was generated *in situ* by the reduction of Cu(II) with ascorbate for the ROS experiments.

HEPES buffer (sodium salt of 2-[4-(2-hydroxyethyl)piperazin-1-yl]ethanesulfonic acid) was prepared by dissolution in ultrapure water at an initial concentration of 500 mM and pH was adjusted to 7.4 with the addition of NaOH aqueous solution.

Phosphate buffer was prepared by mixing two stock solutions prepared by dissolution of K_2HPO_4 and KH_2PO_4 salt in in ultrapure water (or D_2O for NMR experiments) at 500 mM, until reaching the desired pH (pH 7 and 7.4).

Sodium ascorbate was prepared by dissolution at 5 mM in H_2O and freshly used.

The ligand stock solution were prepared by dissolution of TMPA or peptide powder in ultrapure water (or dry acetonitrile for TMPA) to reach a concentration around 15 mM.

Titration of peptides, TMPA ligand and copper salts

Many experiments throughout this manuscript are performed from stock solutions of Aβ model peptides, TMPA, and Cu(II) or Cu(I) with precise concentration determined by UV-vis titrations.

Cu(II) and Cu(I) Dosage

The exact concentration of the Cu(II) stock solutions from a $CuSO_4•5H_2O$, $Cu(OTf)_2$ and $Cu(ClO_4)_2•5H_2O$ salts, that can be hygroscopic such as $Cu(II)(OTf)_2$, were determined. In ultrapure water, the concentration of the Cu(II) stock solutions is determined using the absorbance at 800 nm (with a baseline correction at 450 nm) with ε_{800} = 12 $M^{-1}cm^{-1}$.[1] In other solvent, the dosage of Cu(II) is based on the mass weighed and the molecular weight of the salt used.

The exact concentration of Cu(I) stock solutions was determined by UV-Vis and adding excess sodium bicinchoninic acid (BCA, 2-(4-carboxyquinolin-2-yl)quinoline-4-carboxylic acid) and measuring the absorbance of $Cu(BCA)_2^{3-}$ with an extinction coefficient of 7700 $M^{-1}cm^{-1}$ at 562 nm. When notified, the Cu(I) was generated *in situ* by the reduction of Cu(II) with ascorbate for the ROS experiments.

Peptides and TMPA

The peptide are synthesized or commercially available usually in powder, however the amount of sodium trifluoroacetate co-precipitating with the peptide is batch dependent (it can reach up to 30%). Thus, determining the concentration of a peptide solution by its weight is not enough accurate. Hence, each Aβ model peptide stock solution is titrated prior to use.

The concentration of peptides containing a tyrosine residue is determined at pH ~2 by its absorption considered as free tyrosine with ε_{276}-ε_{296} = 1410 $M^{-1}cm^{-1}$.[1] The procedure is the same for peptides with a phenylalanine residue using ε_{258}-ε_{280} = 193 $M^{-1}cm^{-1}$ considered as free phenylalanine.[1] Other peptides are quantified by progressive addition of a Cu(II) solution of a known concentration following the absorbance of the d-d transition band of the Cu(II)-peptide complex in aqueous buffered solution around 0.2 mM.

As an illustration, Figure 1 shows the dosage of Aβ13-14 by adding 0.1 equivalent of a Cu(II)SO_4 solution in HEPES buffer at pH 7.4 until no more increase of the d-d band corresponding to the Cu(peptide) complex and until turbidimetry due to unbound Cu(II) precipitation are observed. The concentration is calculated from the equivalence obtained by the intersection of the two straight lines, from the absorbance of the d-d transition band measured at 600 nm (and corrected from the baseline at 400 nm) of the Cu(II)Aβ13-14 complex.

TMPA solution is dosed by the same method, following the d-d transition band of Cu(II)TMPA complex in aqueous solution (870 nm).

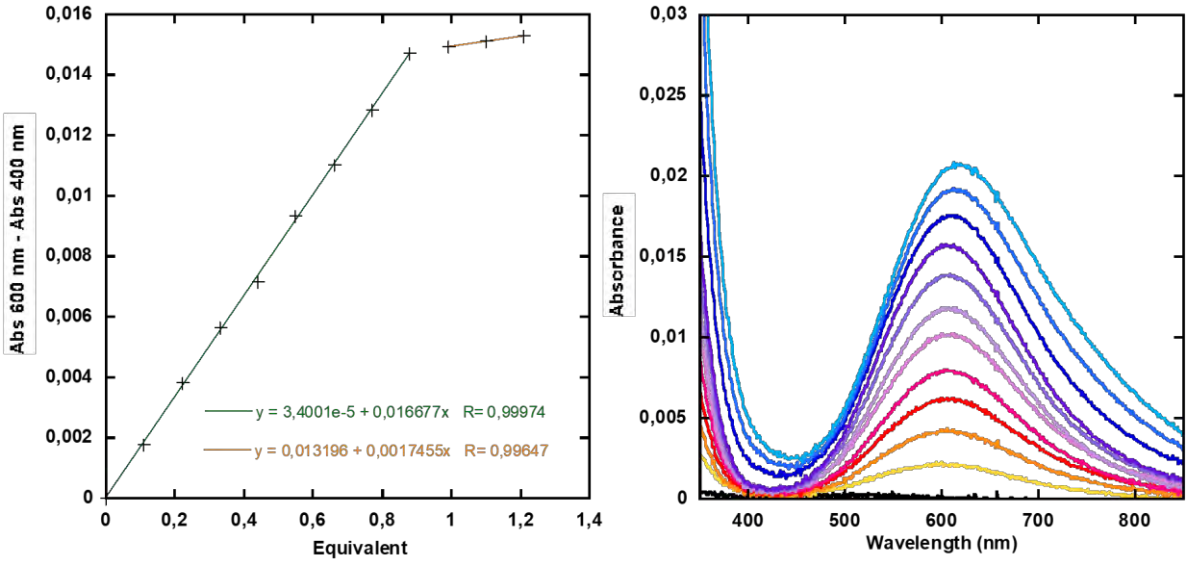

Figure 1: Dosage of Aβ13-14 by Cu(II)SO_4 in HEPES buffer (100 mM) pH 7.4 at 25 °C; l = 1 cm.

Classical experimental conditions

All the UV-vis solutions were prepared directly in a quartz UV-vis cuvette of 2 mL and path length of 1 cm from stock solutions of the required compounds. The concentrations were 100 mM in HEPES buffer, 0.2 mM in copper salts and 0.22 mM in TMPA for CuTMPA complexes, and 0.5 mM in $CuSO_4.5H_2O$ for 0.55 mM in peptides for Cu(peptides) complexes, unless otherwise mentioned. Prior to each measurement, a blank spectrum is recorded with the solvents used under inert or ambient atmosphere according to the experiment.

Crystal structure:

Cu(II)TMPA(SO_3):

A 100 mM solution of Cu(II)TMPA(SO_3) was prepared by mixing TMPA (1.1 eq; 32 mg) with Cu(II)SO_4•5H_2O (1 eq; 25 mg) in 1 mL CH_3CN/HEPES (pH 6.5) 500 mM (50/50 *v*/v) (turquoise solution), then Na_2SO_3 (7 eq, 88 mg) was added (dark brown solution). The solution is sonicated and filtered. Dark green crystals suitable for X-ray crystallography were obtained by slow diffusion of diethylether into the filtrate at room temperature in the dark.

Cu(II)TMPA(S_2O_3):

A 100 mM solution of Cu(II)TMPA(S_2O_3) was prepared, by mixing TMPA (1.1 eq; 32 mg) with Cu(II)SO_4•5H_2O (1 eq; 25 mg) in 1 mL CH_3CN/HEPES (pH 6.5) 500 mM (50/50 *v*/v) (turquoise solution), then $Na_2S_2O_3$ (5 eq, 79 mg) was added (dark green solution). The solution is sonicated. Blue-greenish crystals suitable for characterization were obtain by slow diffusion of diethylether at room temperature in the dark.

Cu(II)TMPA(SO_4):

A 0.2 mM solution of Cu(II)TMPA(SO_4) was prepared, by slowly mixing under vigorous agitation stocks solutions of TMPA (1.1 eq; 0.22 mM) with Cu(II)SO_4•5H_2O (aqueous solution) (1 eq; 0.2 mM) and diluted by slow addition of CH_3CN to afford 50 mL final solution. Crystals were obtained from this solution preserved in the freezer.

Cu(II)TMPA(ClO_4):

A 100 mM solution of Cu(II)TMPA was prepared by mixing TMPA (1.1 eq; 32 mg) with Cu(II)$(ClO_4)_2$•6H_2O (1 eq; 37 mg) in 1 mL CH_3CN (blue solution), then Na_2SO_3. Blue crystals suitable for X-ray crystallography were obtained by slow diffusion of diethylether into the solution at room temperature in the dark.

Cu(II)TMPA(NO_3):

A 100 mM solution of Cu(II)TMPA(NO_3) was prepared by mixing TMPA (1.1 eq; 32 mg) with Cu(II)NO_3•2.5H_2O (1 eq; 24 mg) in 1 mL THF. The solution is sonicated. Crystals suitable for

X-ray crystallography were obtained by slow diffusion of diethylether into the solution at room temperature in the dark.

Cu(II)TMPA(H_2O):

A 100 mM solution of Cu(II)TMPA(H_2O) was prepared by mixing TMPA (1.1 eq; 32 mg) with Cu(II)$(OTf)_2$ (1 eq; 37 mg) in 1 mL wet THF. The solution is sonicated. Crystals suitable for X-ray crystallography were obtained by slow diffusion of diethylether into the solution at room temperature in the dark.

Cu(II)TMPA(CH_3CN):

A 100 mM solution of Cu(II)TMPA(CH_3CN) was prepared by mixing TMPA (1.1 eq; 32 mg) with Cu(II)$(OTf)_2$ (1 eq; 37 mg) in 1 mL CH_3CN. The solution is sonicated. Crystals suitable for X-ray crystallography were obtained by slow diffusion of diethylether into the solution at room temperature in the dark.

(Cu(II)TMPA)$_3(CO_3)$:

A 100 mM solution of Cu(II)TMPA was prepared by mixing TMPA (1.1 eq; 32 mg) with Cu(II)SO_4•$5H_2O$ (1 eq; 25 mg) in 1 mL H_2O/dioxane. The pH was adjusted around 12 with addition of NaOH solution, and KPF_6 (2eq) were added. The solution is sonicated. Crystals suitable for X-ray crystallography were obtained by slow evaporation of the solvent.

All the crystal data, data collection, and structure refinement are presented in Tables 1 and 2.

Preparation of CuL(CO)

CuL(CO) complexes were prepared in a schlenk flask under CO atmosphere: 1 equivalent of [Cu(I)$(CH_3CN)_4$]BF_4 (0.1 M in acetonitrile) is added to a solution of 1.1 equivalent of TMPA in the desired mixture of solvent to afford 2 mM solution. The IR spectrum is recorded directly from the reaction mixture injected in the IR liquid cell flushed with CO gas. The UV-vis is recorded upon dilution to 0.2 mM or 0.5 mM (peptides) in a sealed UV-vis cuvette containing a mixture of the desired solvents under CO atmosphere. The NMR are prepared the same way but in deuterated solvent directly in the NMR tube closed with a septum cap.

Ascorbate consumption assay

Ascorbate consumption was monitored by UV-Vis spectrophotometry. The decrease of the absorption band at λ_{max} = 265 nm of the Asc (ε = 14 500 $M^{-1}.cm^{-1}$, corrected at 800 nm) was plotted as a function of time. The samples were prepared from stock solutions of peptides and Cu(II) diluted down to 12 and 10 µM respectively in HEPES (100 mM, pH 7.4) in a 1 cm path length quartz cuvette. Final volume was adjusted with ultrapure water to 2 mL.

Electron Paramagnetic Resonance

Electron Paramagnetic Resonance (EPR) data were recorded using an Elexsys E 500 Bruker spectrometer, operating at a microwave frequency of approximately 9.4 GHz. Spectra were recorded using a microwave power of 5 mW across a sweep width of 200 mT (centered at 320 mT) with modulation amplitude of 0.5 mT. Experiments were carried out at 120 K using a liquid nitrogen cryostat.

EPR samples were prepared from stock solutions of peptides or TMPA diluted down, in the appropriated mixture of solvent, to 0.2 mM or 0.5 mM and 0.9 eq. of Cu(II) was added. When necessary, pH was adjusted with H_2SO_4 and NaOH solutions. Samples were frozen in quartz tube with 10 % glycerol as a cryoprotectant (when less than 50 % of organic co-solvent) and with $TBAPF_6$ or KPF_6 salts when mentioned to reach a concentration of 100 mM.

UV-Vis Spectroscopy

The UV-Vis were recorded on a Hewlett Packard Agilent 8453 or 8454 spectrometers at 25 °C under stirring at 800 rpm.

Experiments were performed in a 2 mL and a 1 cm path length quartz cuvette. For sample sensitive to dioxygen (Cu(I) complexes) a sealed UV-vis cuvette was used. The stock solutions of peptides, TMPA and Cu were diluted down to the desired concentration in the appropriate mixture of solvents.

Nuclear Magnetic Resonance

^{1}H NMR spectra were recorded on a Bruker Avance NEO 600 spectrometer equipped with a 5 mm broadband inverse triple resonance probe ^{1}H BB (^{31}P-$1^{03}Rh$)/^{31}P with Z field gradients. The chemical shifts in 1H-NMR are reported in ppm relative to tetramethylsilane (TMS, δ = 0.00 ppm). The temperature was set at 298K.

^{1}H spectra were recorded using the following parameters: spectral width, 12 ppm; 90° nutation angle duration, 6.7µs; recycling delay, 32-s (2-s acquisition time and 30-s relaxation delay). The spectra were 2x zero-filled and subject to an exponential prior for Fourier transformation.

Water-suppression was achieved by *excitation sculpting* method with a « zgesgp » sequence (Bruker).

The tubes were prepared from stock solutions with a known concentration of peptides or TMPA in D_2O, $[Cu(I)(CH_3CN)4]BF_4$ salt in CD_3CN under argon, dithionite in D_2O freshly prepared (for the peptides) under argon, and phosphate buffer (KPB) in D_2O. The final concentration in the tube were 2 mM in Cu(I), 2.2 mM in peptide or TMPA or peptide, 100 mM in KPB in aqueous phase, with 1.5 equivalent of dithionite, 10 % of CD_3CN, and the addition of an internal reference TSP-d4 (3-(Trimethylsilyl)propionic-2,2,3,3-d4 acid sodium salt) when stated. NMR peaks of peptides are particularly sensitive to pH variations. The amount of CD_3CN can induce a slight change of real pH and thus chemical shifts of the peaks. Consequently, a special attention was provided to monitor the amount of CD_3CN in each tube of a same peptide under different conditions of a series of experiments to secure that the changes in the NMR spectrum are not due to pH variations. This is determined by the absolute integrations of the HCD_2CN and TSP peaks. The experiments under CO atmospheres were performed by bubbling CO gas directly in the NMR tube equipped with a septum cap.

Infra-red spectroscopy

The IR spectra were recorded on Perkin Elmer FT-IR Frontier and Perkin Elmer Spectrum Two FT-IR spectrometers.

All the IR spectra were obtained from liquid samples loaded into a thin-film IR cell between two CaF_2 windows separated by a spacer. The samples were prepared from stock solutions in a vial under CO atmosphere. Except when mentioned the concentration was 2 mM in $[Cu(I)(CH_3CN)_4]BF_4$ dissolved in CH_3CN, 2.2 mM in TMPA or peptide, and 100 mM in HEPES at pH 7.4 in aqueous phase. The experiments were performed with 10 % of CH_3CN to increase the CO solubility. Prior to each measurement, a background spectrum was recorded with the solvents used under air.

Cyclic voltammetry

Electrochemistry measurements were performed either under argon, air, O_2 or CO atmosphere by bubbling the appropriate gas, at room temperature. Dry acetonitrile was used when the experiment is in acetonitrile only. Cyclic voltammetry were performed with a classical three-electrode configuration:

A glassy carbon electrode (3 mm diameter) as working electrode, a platinum wire as counter electrode and a saturated calomel electrode (SCE) in case of aqueous solution, or a $Ag/Ag(NO_3)$ electrode in case of organic solvent as reference electrode. The reference electrode with a Vycor sinter was directly immersed in the electrochemical solution. The experiments were performed using an Autolab-potentiostat (PGSTAT302N, Autolab) piloted from a computer with GPES software (version 4.9).

The carbon electrode was polished on an MD-Nap polishing cloth with 1 µm and 0.3 µm alumina slurry (at least 2 min) and rinsed with water between each measurement. The supporting electrolyte was a $TBAPF_6$ salt (tetrabutylammonium hexafluorophosphate) at 100 mM for organic solution, and a HEPES or KPB buffer at 100 mM for aqueous solutions. The samples were prepared from stock solutions of peptides or TMPA and Cu(II) down to the desired concentration.

$A\beta_{13\text{-}14}NH_2$ synthesis

$A\beta_{13\text{-}14}NH_2$ was synthesised according to the Scheme 1.

In a 20 mL syringe for peptide synthesis, 1 g of MBHA Rink Amide Fmoc-protected resin was deprotected using 5 mL of 20 % piperidine in DMF (3x10 min). Deprotected Fmoc was titrated using UV-visible spectroscopy to determine the loading of the resin (0,3 mmol/g). Histidine was coupled to the resin using Fmoc-His(Trt)-OH (4 eq), HBTU (3,9 eq), HOBt (4 eq) and DIPEA (10 eq), in 5 mL of DMF (1 h), and Fmoc-deprotected using 20 % piperidine in DMF (3x10 min). This step was realized twice. The cleavage from the resin was achieved using 20 mL of TFA:TIPS:H_2O (95:2.5:2.5) solution (3 h). The resin was rinsed with TFA and the filtrates were collected and concentrated under vacuum. The product was precipitated by addition of ca. 30 mL of cold diethyl ether, collected by centrifugation and dried over vacuum. The product was purified by ChromatoFlash on an INTERCHIM PURIFLASH BIO 100 C18-T (pore size 200 Å, particle size 15 µm, 25 g) using a gradient of solvents A (H_2O with 0.1 % TFA) and B (MeOH with 0.1 % TFA). Fractions containing the product were collected and lyophilized to yield a white solid (56 mg, 29 %).

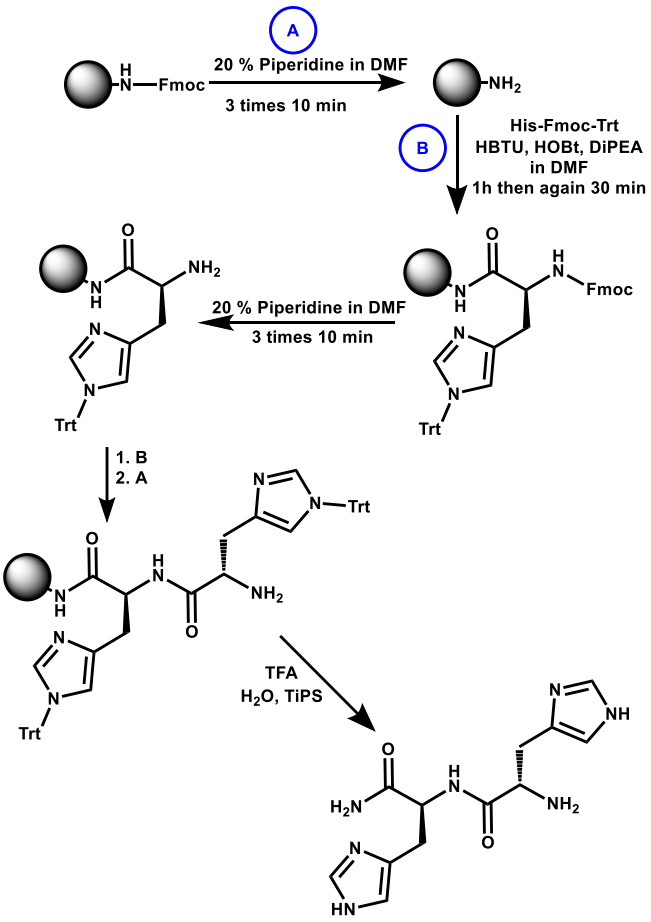

Scheme 1: Aβ13-14 synthesis pathway on Rink Amide MBHA resin.

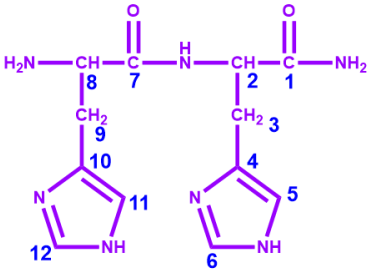

^{1}H NMR (400 MHz, D_2O) δ 8.70 (s, 1H)$_{12}$, 8.65 (s, 1H)$_{6}$, 7.42 (s, 1H)$_{11}$, 7.35 (s, 1H)$_{5}$, 4.74 – 4.70 (m, 1H)$_{2}$, 4.36 – 4.28 (m, 1H)$_{8}$, 3.48 – 3.33 (m, 2H)$_{9}$, 3.29 – 3.15 (m, 2H)$_{3}$. **^{13}C NMR (101 MHz, D_2O)** δ 173.20$_{1}$, 167.84$_{7}$, 134.41$_{12}$, 133.65$_{6}$, 127.78$_{4}$, 125.58$_{10}$, 118.49$_{11}$, 117.29$_{5}$, 52.41$_{3}$, 51.88$_{9}$, 26.44$_{8}$, 26.04$_{2}$. **MS** (ESI) $[M+H]^+$ *m/z* = 292,15.

The ^{1}H NMR and ^{13}C NMR spectra of the resulting Aβ$_{13-14}$NH$_2$ presented in Figure 2 and Figure 3, are well integrated and correspond well (12 peak for ^{13}C NMR). However there is a small peak at 2.74 ppm integrating for 0.2 that is not assigned in the ^{1}H NMR. In the 2D NMR

(Figures 4, 5, and 6) this peak doesn't seem to be part of the molecule, but it is an impurity. The mass analysis (Figure 7), also shows a single peak corresponding to $A\beta_{13\text{-}14}NH_2$.

Annex

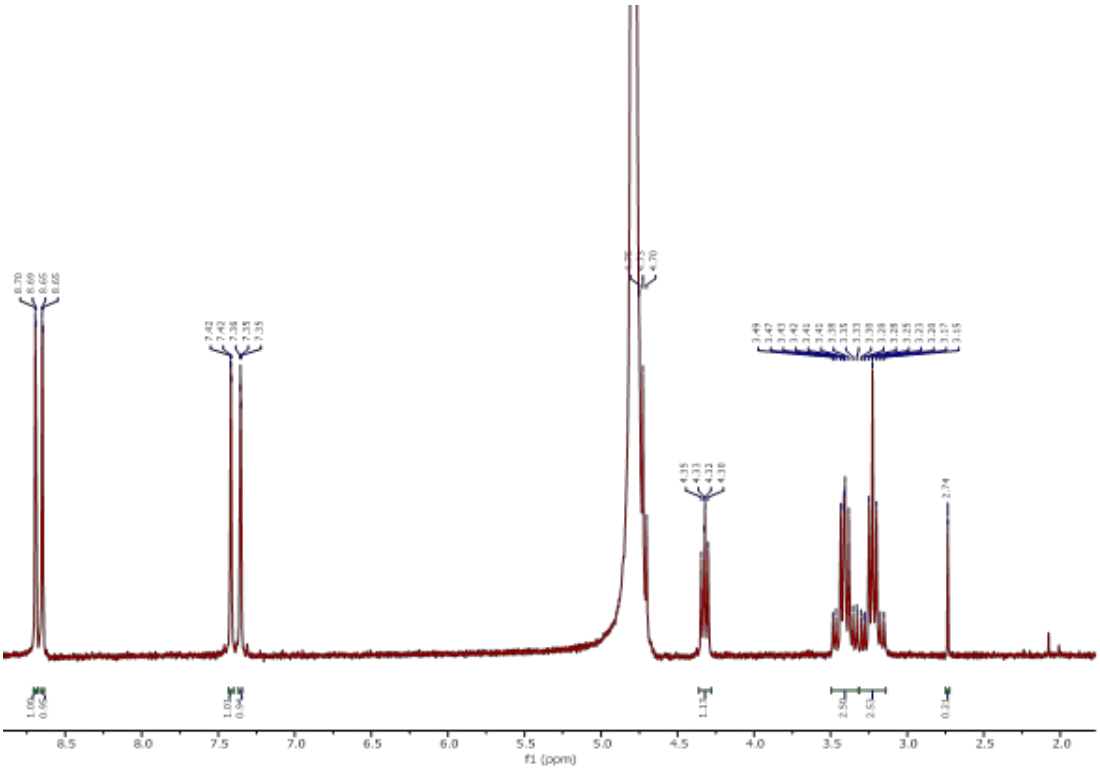

Figure 2: ^1H NMR of $A\beta_{13\text{-}14}$ in D_2O (400 MHz).

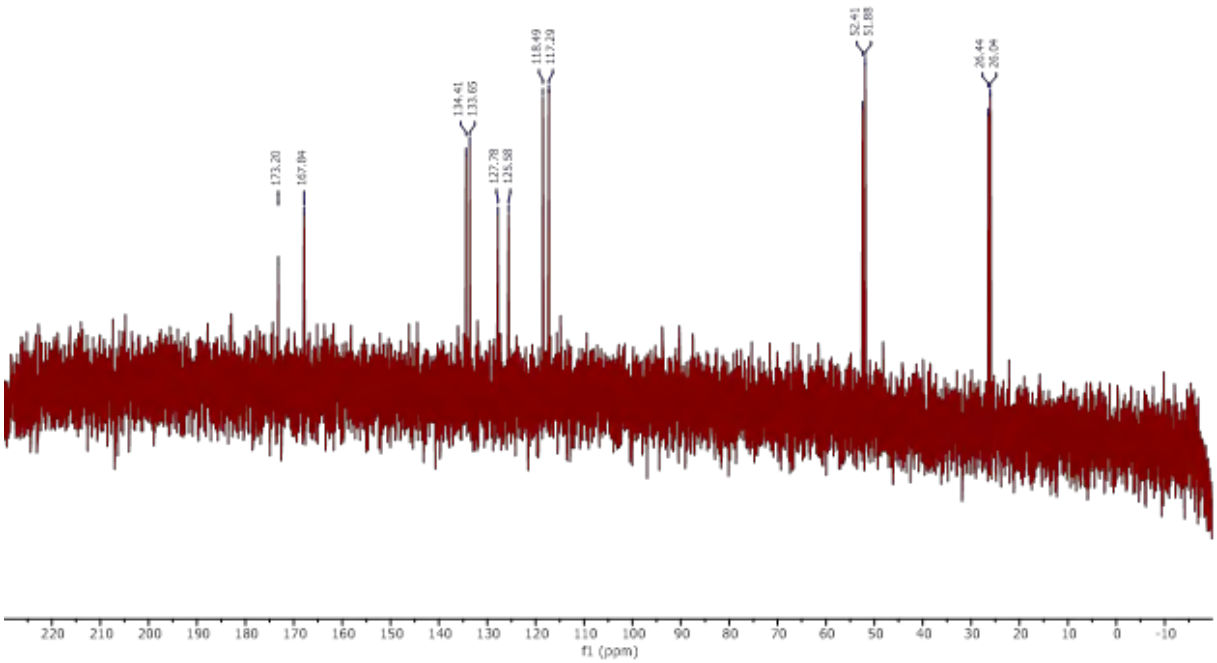

Figure 3: ^{13}C NMR of $A\beta_{13-14}$ in D_2O (400 MHz).

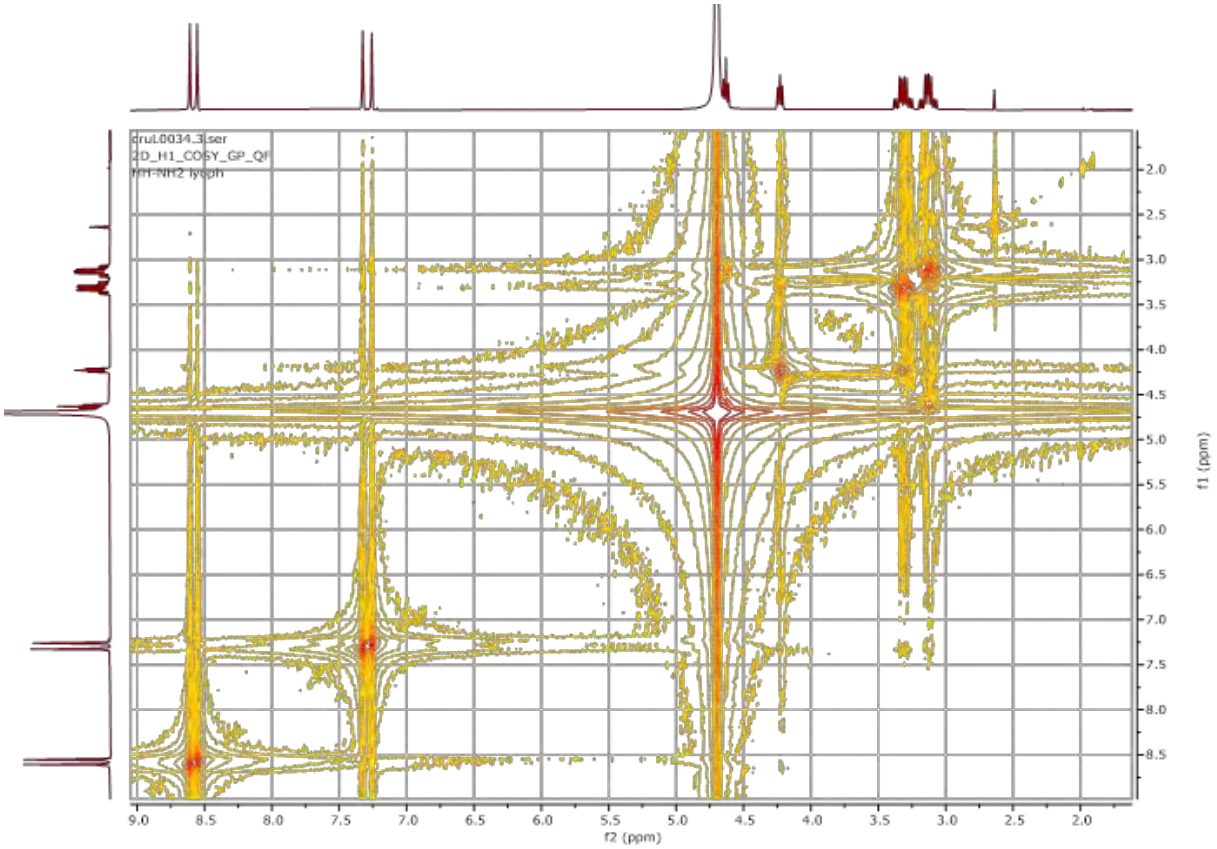

Figure 4: 2D NMR COSY of $A\beta_{13-14}$ in D_2O (400 MHz).

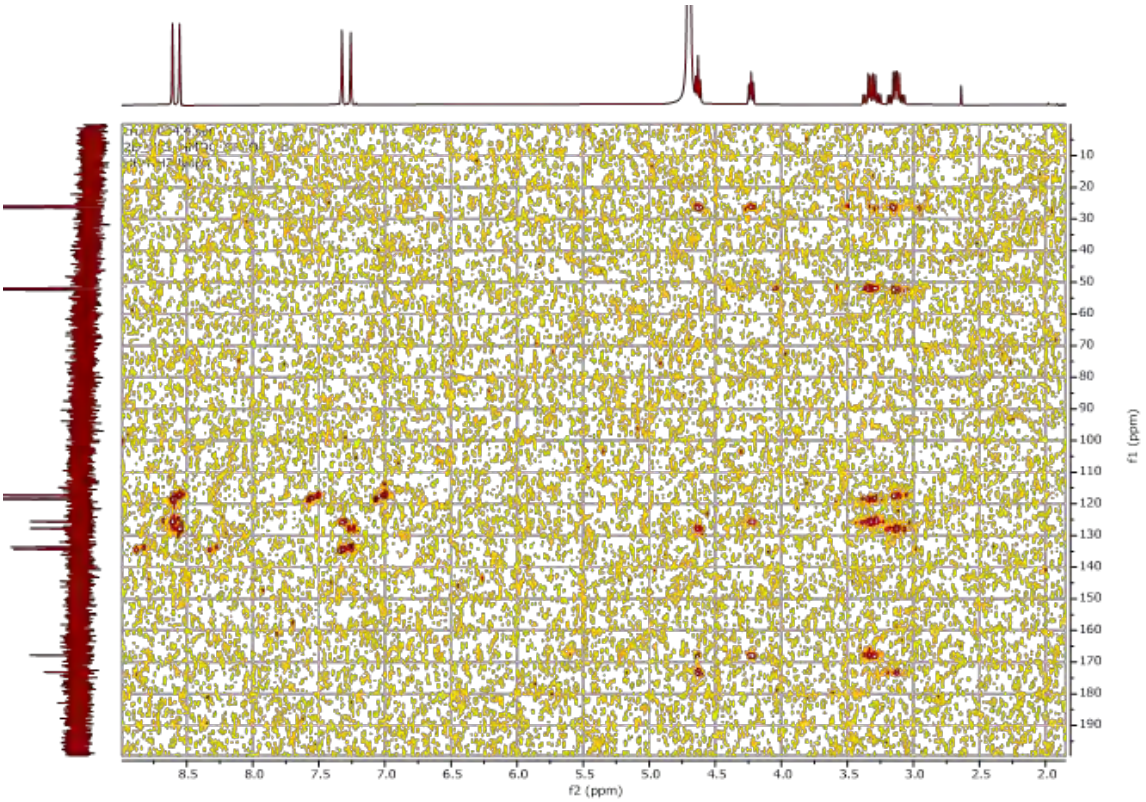

Figure 5: 2D NMR HMQC of $A\beta_{13-14}$ in D_2O (400 MHz).

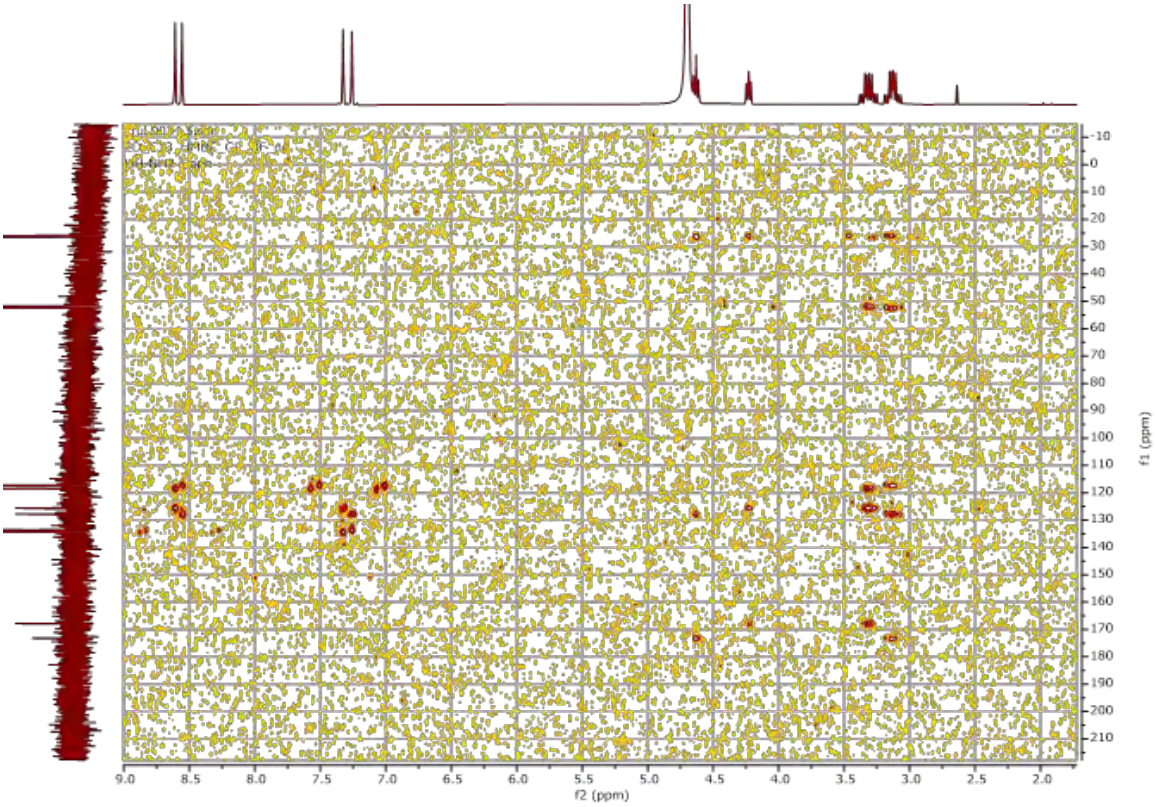

Figure 6: 2D NMR HMBC of $A\beta_{13-14}$ in D_2O (400 MHz).

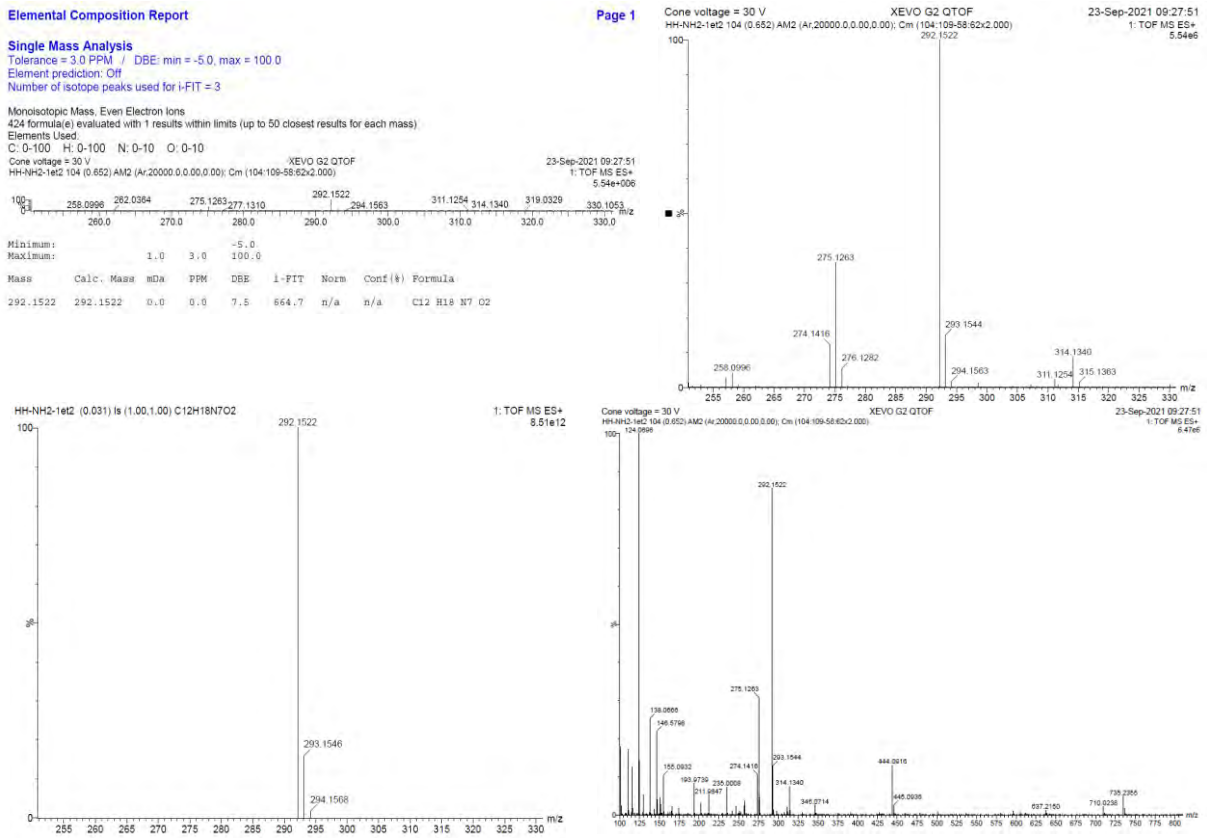

Figure 7: Mass spectrometry of Aβ$_{13-14}$

Table 1: Crystal data, data collection, and structure refinement for [CuTMPA(SO$_3$)]; [CuTMPA(S$_2$O$_3$)]; [CuTMPA(SO$_4$)] and [CuTMPA(NO$_3$)]$^+$.

ID	[CuTMPA(SO$_3$)]	[CuTMPA(S$_2$O$_3$)], 2H$_2$O	[CuTMPA(SO$_4$)], 4H$_2$O	[CuTMPA(NO$_3$)]$^+$
formula	C$_{18}$H$_{18}$CuN$_4$O$_3$S	C$_{18}$H$_{18}$CuN$_4$O$_3$S$_2$, 2(H$_2$O)	C$_{18}$H$_{18}$CuN$_4$O$_4$S, 4(H$_2$O)	C$_{18}$H$_{18}$CuN$_5$O$_3$
M_r	433.97	502.07	522.04	415.92
crystal system	orthorhombic	monoclinic	trigonal	monoclinic
space group	*P*cca	*C* 2/c	*P* 32	P 21/c
a (Å)	17.086(4)	13.1003(12)	13.02170(10)	14.64480(10)
b (Å)	14.960(3)	12.1622(11)	13.02170(10)	8.96550(10)
c (Å)	17.372(4)	25.323(2)	11.21240(10)	14.85530(10)

α (°)	90	90	90	90
β (°)	90	90.589(3)	90	92.9710(10)
γ (°)	90	90	120	90
V (Å^3)	4440.4(17)	4034.5(6)	1646.51(3)	1947.85(3)
Z	8	8	3	4
ρ_{calc} (g cm^{-3})	1.298	1.653	1.579	1.418
μ (mm^{-1})	1.100	1.33	2.769	1.823
F(000)	1784	2072	813	856
crystal size (mm^3)	0.20 x 0.16 x 0.04	0.20 x 0.08 x 0.08	0.20 x 0.18 x 0.12	0.20 x 0.18 x 0.04
T/K	273(2)	110(2)	100(2)	100(2)
measd reflns	67459	88088	30545	36333
Unique reflns (Rint)	4025 (0.0739)	7397 (0.0466)	30545 (?)	4181 (0.0450)
Data/restraints/parameters	4025/0/244	7397/0/287	30545/1/322	4181/0/244
GOF on F^2	1.062	1.111	1.026	1.104
R_1[a] [I>2σ(I)]	0.0927	0.0244	0.0212	0.0410
wR_2[b] [all data]	0.2797	0.0624	0.0577	0.0965

[a] $R_1 = \Sigma||F_o| - |F_c||/ \Sigma |F_o|$. [b] $wR_2 = [\Sigma[w(F_o^2 - F_c^2)^2] / \Sigma [w(F_o^2)^2]]^{1/2}$.

Table 2: Crystal data, data collection, and structure refinement for $[CuTMPA(H_2O)]^{2+}$; $[CuTMPA(CH_3CN)]^{2+}$ .and $[\{CuTMPA\}_3(CO_3)]^{4+}$.

ID	$[CuTMPA(H_2O)]^{2+}$, $2CF_3SO_3$	$[CuTMPA(CH_3CN)]^{2+}$, $2CF_3SO_3$, CH_3CN	$[CuTMPA(SO_3)]$	$[\{CuTMPA\}_3(CO_3)]^{4+}$, $4PF_6$, $C_4H_8O_2$
formula	$C_{18}H_{20}CuN_4O$, $2(CF_3O_3S)$	$C_{20}H_{21}CuN_5$, $2(CF_3O_3S)$, C_2H_3N	$C_{18}H_{18}CuN_4O_3S$	$C_{55}H_{54}Cu_3N_{12}O_3$, $4(F_6P)$, $C_4H_8O_2$
M_r	670.07	734.16	433.97	1789.74
crystal system	orthorhombic	trigonal	orthorhombic	monoclinic
space group	Pbca	P3c1	*P*cca	P21/c
a (Å)	14.89330(10)	12.5122(11)	17.086(4)	23.19290(10)
b (Å)	15.15850(10)	12.5122(11)	14.960(3)	11.757

c (Å)	23.18930(10)	33.359(3)	17.372(4)	25.42270(10)
α (°)	90	90	90	90
β (°)	90	90	90	94.34
γ (°)	90	120	90	90
V (Å^3)	5235.22(5)	4522.8(9)	4440.4(17)	6912.36(4)
Z	8	6	8	4
ρ_{calc} (g cm^{-3})	1.700	1.617	1.298	1.720
μ (mm^{-1})	3.519	0.949	1.100	3.057
F(000)	2712	2238	1784	3612
crystal size (mm^3)	? x ? x ?	0.200 x 0.200 x 0.200	0.20 x 0.16 x 0.04	0.20 x 0.18 x 0.14
T/K	100(2)	110(2)	273(2)	100(2)
measd reflns	98923	196443	67459	141255
Unique reflns (Rint)	5673 (0.0335)	15496 (0.0727)	4025 (0.0739)	14996 (0.0539)
Data/restraints/parameters	5673/0/369	15496/560/557	4025/0/244	14996/600/1093
GOF on F^2	1.060	1.083	1.062	1.041
R_1[a] [I>2σ(I)]	0.0299	0.0422	0.0927	0.0429
wR_2[b] [all data]	0.0789	0.1099	0.2797	0.1084

[a] $R_1 = \Sigma||F_o| - |F_c||/ \Sigma |F_o|$. [b] $wR_2 = [\Sigma[w(F_o^2 - F_c^2)^2] / \Sigma [w(F_o^2)^2]]^{1/2}$.

References

1. Atrián-Blasco, E.; del Barrio, M.; Faller, P.; Hureau, C., Ascorbate Oxidation by Cu(Amyloid-β) Complexes: Determination of the Intrinsic Rate as a Function of Alterations in the Peptide Sequence Revealing Key Residues for Reactive Oxygen Species Production. *Analytical Chemistry* **2018,** *90* (9), 5909-5915.

Résumé français

Résumé français

A. Contexte général

1. La maladie d'Alzheimer

La maladie d'Alzheimer (MA) est une maladie neurodégénérative qui touche plus de 30 millions de personnes dans le monde. Elle atteint principalement les personnes âgées. La MA a été décrite pour la première fois en 1906 par Alois Alzheimer, un neurologue et psychiatre allemand. Les symptômes sont la perte de mémoire et des déficiences cognitives qui s'intensifient au cours de la maladie. Les fonctions physiques et vitales sont peu à peu touchées jusqu'à ce que le patient soit alité et meurt. Le diagnostic est donné grâce à :

- des tests cognitifs ;
- une IRM qui permet de déceler une atrophie du cerveau ;
- une ponction lombaire qui confirme la maladie révélant des taux anormalement élevés de deux marqueurs biologiques de la MA, le peptide amyloïde-β et la protéine Tau hyper-phosphorylée.

Il n'existe pas de traitement contre la maladie, seulement des médicaments pour lutter contre les symptômes qui sont souvent peu efficaces et peuvent provoquer des effets secondaires. Les mécanismes à l'origine de la MA sont encore mal compris.

D'un point de vue histopathologique, on retrouve comme marqueur biologique de la MA la formation de plaques séniles. Ces dernières sont composées principalement du peptide amyloïde-β (Aβ) et de bio-métaux tels que le cuivre (Cu). Aβ est un peptide flexible composé de 40 à 43 acides aminés (Figure 1). Avec le cuivre ils peuvent former un complexe (Cu-Aβ) capable de s'agréger sous forme d'oligomères pouvant se réorganiser en fibres qui composent les plaques séniles.

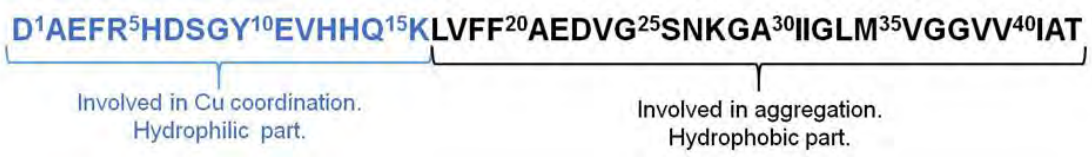

Figure 1 : Séquence peptidique du peptide Aβ.

2. La coordination du peptide amyloïde β avec le cuivre

Le complexe Cu-Aβ est retrouvé sous deux états d'oxydation, +II et + I. A pH physiologique (environ pH 7,4) deux espèces sont à l'équilibre pour Cu(II)Aβ avec une géométrie plan carré et un pKa de 7,8 présentées Figure 2. Le composé I correspond à l'espèce majoritaire à pH 7,4 pour lequel le Cu(II) est coordiné par :

- l'amine terminale $–NH_2$;
- un atome d'oxygène de la liaison amide entre Asp1 et Ala2 ;
- deux atomes d'azote des cycles imidazoles des His6 et His13 ou His14.

Le composé II, favorisé à plus haut pH est coordiné par :

- l'amine terminale de l'Asp1 ;
- l'atome d'azote déprotoné de la liaison amide entre Asp1 et Ala2 ;
- l'oxygène de la liaison amide entre Ala2 et Glu3 ;
- un atome d'azote d'un cycle imidazole parmi les 3 résidus histidine His6, His13 ou His14.

Pour les deux espèces, un ligand aqua ou carboxylate peut se retrouver en position apicale. La constante d'affinité entre Aβ et Cu(II) est de l'ordre de 10^9 à 10^{10} M^{-1}. La coordination du complexe Cu(I)Aβ est dynamique et linéaire entre deux imidazoles parmi les trois résidus histidine His6, His13 et His14 à l'équilibre (Figure 2). La constante d'affinité est de l'ordre de 10^7 à 10^{10} M^{-1}.

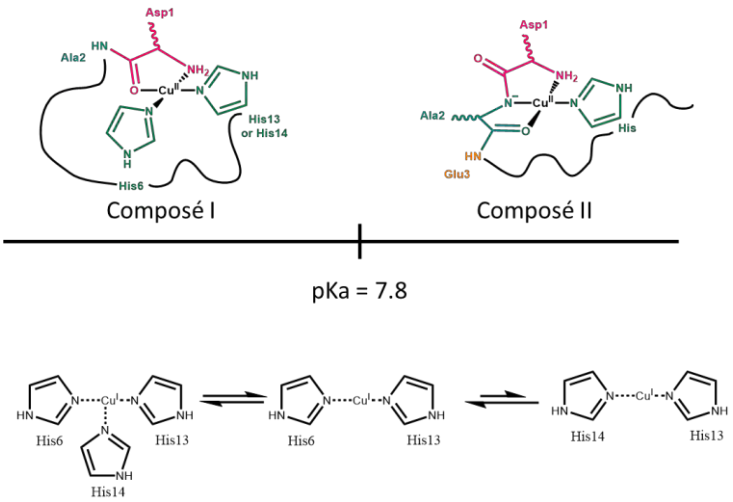

Figure 2 : Coordination des complexes Cu(II)Aβ et Cu(I)Aβ à pH physiologique.

3. La production d'espèces réactives de l'oxygène

Le complexe Cu-Aβ a la faculté de catalyser la production d'Espèces Réactives de l'Oxygène (ERO) en cyclant entre ses degrés d'oxydation +I et +II en présence de dioxygène et d'un réducteur physiologique tel que l'ascorbate (Figure 3). Les ERO sont des espèces hautement réactives causant la destruction des molécules environnantes. Normalement la génération de ces espèces fait partie de processus biologiques contrôlés. Cependant, il arrive que des facteurs internes ou externes induisent une surproduction d'ERO et/ou un dysfonctionnement dans le traitement de ces espèces. Le mécanisme d'activation du dioxygène par le complexe Cu-Aβ n'est pas connu. Il est toutefois suggéré que pendant son cycle redox, le complexe Cu-Aβ passe par un état intermédiaire qui serait l'espèce catalytique.

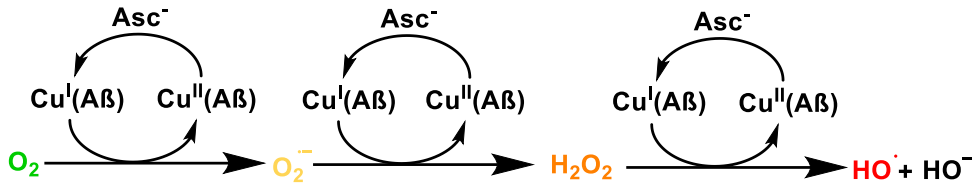

Figure 3 : Schéma de la catalyse des espèces réactives de l'oxygène par le complexe Cu-Aβ en présence d'ascorbate.

4. La théorie de l'« in-between state »

Des études en électrochimie ont montré que le transfert d'électron entre les états stationnaires (ES) Cu(II)Aβ et Cu(I)Aβ ne pouvait pas être direct du fait de leur grande différence de géométrie qui nécessiterait une haute énergie de réarrangement. Des analyses fines en voltammétrie cyclique démontrent que le transfert d'électron se fait par la pré-organisation du complexe Cu-Aβ à travers un mécanisme Chimie-Electrochimie-Chimie (Figure 4). Le complexe Cu-Aβ pré-organisé est à l'équilibre avec les deux ES et a une géométrie intermédiaire pour permettre une énergie de réorganisation minimale pendant le transfert électronique. Cet état est appelé « in-between state » (IBS). Il est atteint grâce à la flexibilité du peptide Aβ, et représenterait 0,1 % des espèces en solution. D'autres études impliquant des réactions chimiques en présence de substrats tels que l'ascorbate et O_2, ont appuyé l'existence de cet IBS. Une potentielle sphère de coordination a été proposée pour cet état: Aβ serait coordiné au Cu par l'amine terminale, l'acide carboxylate de l'Asp1 et un atome d'azote du cycle imidazole d'un des trois résidus histidine (Figure 4).

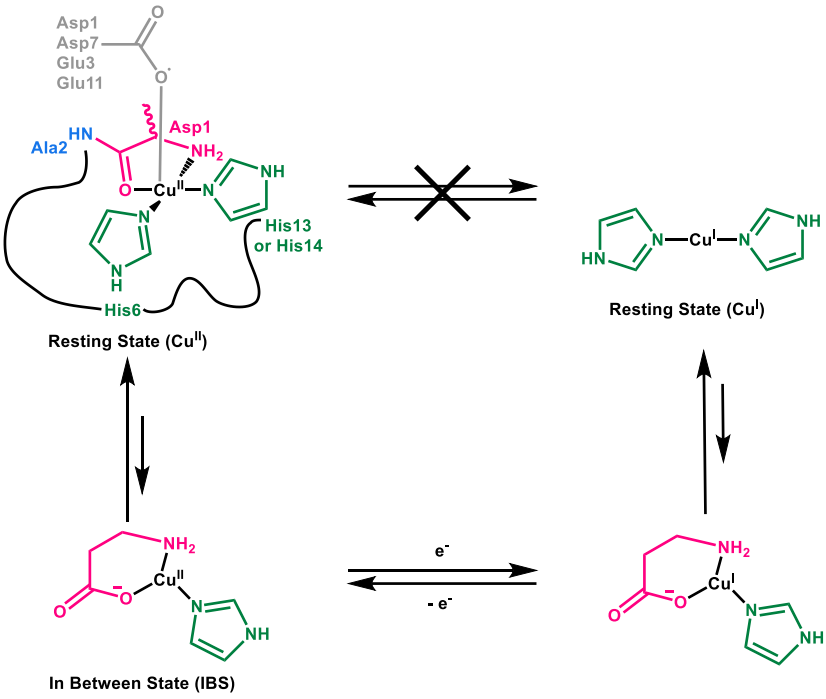

Figure 4 : Mécanisme Chimie-Electrochimie-Chimie proposé par voltammétrie cyclique.

En chimie, le mécanisme d'activation du dioxygène implique la présence d'un substrat, l'ascorbate qui réduit le Cu(II)IBS en Cu(I)IBS. Ce dernier peut former une liaison avec O_2. Après un transfert d'électron du centre Cu(I) à l'oxygène, il sera transformé en radical superoxyde ($O_2^{\bullet -}$) qui peut lui-même retourner dans le cycle réactionnel pour former H_2O_2 et $HO^{\bullet}$ (Figure 5).

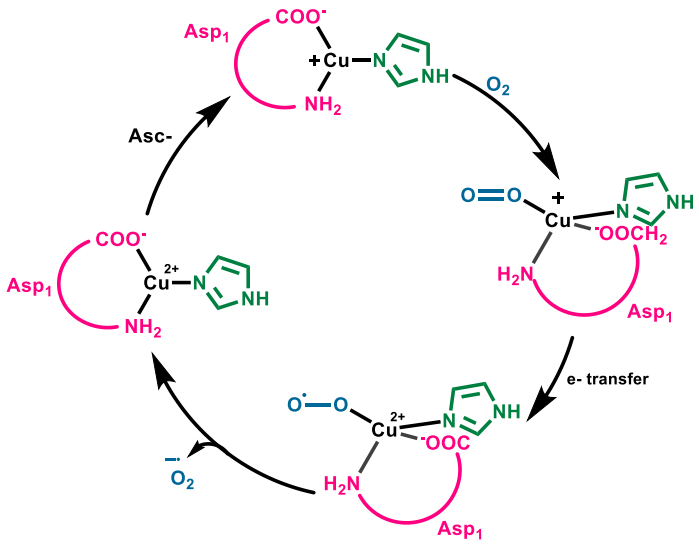

Figure 5 : Mécanisme proposé pour l'activation du dioxygène par le complexe Cu-Aβ via l'IBS.

B. Objectifs et défis de la thèse

L'objectif principal de la thèse et d'identifier un intermédiaire réactionnel de l'IBS au cours du cycle d'activation d'O_2, dans le but de confirmer la sphère de coordination de l'IBS et de sonder le mécanisme à l'origine de la catalyse des ERO. La nature de l'IBS soulève différents défis, en effet son caractère élusif et peu peuplé ne permet pas de l'observer par les techniques de spectroscopies. Pour être pertinente, l'étude de l'IBS doit se faire en milieu biologique, c'est-à-dire en solvant aqueux tamponné à pH physiologique (environ pH 7,4). La sphère de coordination dynamique du complexe Cu-Aβ due à la grande flexibilité du peptide Aβ doit être également considérée, et nécessite l'utilisation de modèles plus contraints. L'utilisation de solvant aqueux ne permet pas de diminuer significativement la température du milieu réactionnel afin de ralentir la réactivité, pour cela, l'une des stratégies pour maitriser l'instabilité de l'IBS est d'utiliser le monoxyde de carbone (CO) comme substitut non redox actif du dioxygène. CO devrait se lier à Cu(I)Aβ, le stabiliser par une liaison Cu(I)-CO forte (due à la rétro-donation du Cu(I) vers les orbitales π vides du CO) et ainsi permettre son accumulation et la détection de l'adduit Cu(I)Aβ(CO). Le nouvel objectif est donc d'identifier un intermédiaire clé Cu(I)Aβ(CO) au cours du cycle catalytique Cu(I)/Cu(II)Aβ (Figure 6).

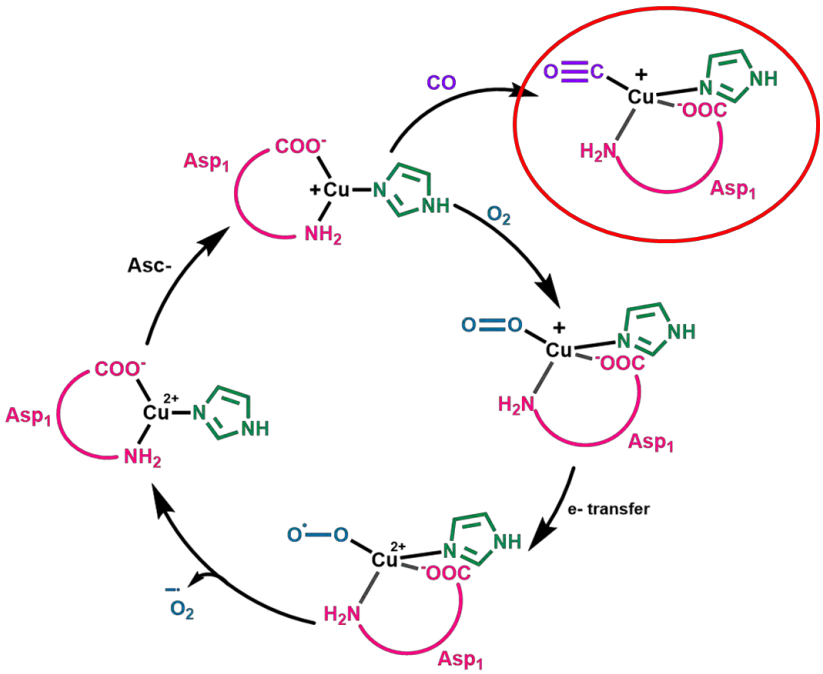

Figure 6 : Proposition d'un adduit Cu(I)Aβ(CO) au cours du cycle catalytique de la réduction d'O_2 par Cu-Aβ IBS.

Pour être analysable par spectroscopies RMN (Résonance Magnétique Nucléaire) et IR (Infrarouge), l'adduit doit être concentré autour de 2 mM. Cependant, la concentration de CO dans l'eau est autour de 1 mM, il serait donc le réactif limitant. La solubilité du CO dans l'acétonitrile (CH_3CN) est 100 fois plus élevée que dans l'eau (autour de 100 mM), ainsi pour augmenter la quantité de CO dans le milieu réactionnel et tirer la réaction Cu(I)Aβ + CO ⇄ Cu(I)Aβ(CO) vers la formation de l'adduit, 10 % de CH_3CN seront utilisés. Cette quantité de CH_3CN ne devrait pas impacter significativement le comportement de Cu-Aβ. Cependant cela devra être confirmé expérimentalement.

La flexibilité du peptide Aβ, permet aux complexes Cu(I)Aβ ou Cu(II)Aβ d'adopter différents modes de coordination à l'équilibre. Cette caractéristique complique la détection et l'identification de l'IBS par les différentes techniques de spectroscopie. La flexibilité du peptide peut être diminuée en réduisant la longueur du peptide et le nombre de sites de coordination disponibles. Différents modèles tronqués du peptide $A\beta_{1-16}$ ont été choisis afin de stabiliser et favoriser différents modes de coordination spécifiques : $A\beta_{1-16}$ (considéré comme le meilleur modèle de coordination du peptide Aβ), $A\beta_{13-14}$ (pour modéliser Cu(I)Aβ ES), et $A\beta_{1-7}$ (pour favoriser l'IBS). Chaque peptide est protégé en position C-terminale par une amidation pour empêcher la coordination du $-COO^-$ peu pertinente.

L'utilisation et l'étude de la coordination du monoxyde de carbone nécessite la mise en place d'un protocole expérimental s'appuyant sur des références solides. Le ligand TMPA (Tris(2-MethylPyridine)Amine) sous forme complexé avec Cu, dont la réactivité envers CO ou O_2 a été fortement étudiée en solvants organiques, sera utilisé comme référence. Il présente l'avantage d'être soluble en solvants organiques et aqueux.

Dans un premier temps, l'étude du complexe Cu-TMPA a été adaptée d'un milieu organique à un milieu aqueux. Dans un second temps, l'impact de 10 % de CH_3CN a été analysé pour les complexes modèles Cu-Aβ. Enfin, la réactivité des complexes Cu(I)Aβ envers CO et O_2 dans les conditions établies a été étudiée, avec le complexe Cu(I)TMPA comme référence systématique. Toutes les études ont été menées grâce à différentes techniques de spectroscopies telles que l'UV-Vis (UV-Visible), l'IR, la RMN, la RPE (Résonance Paramagnétique Electronique), ainsi que par électrochimie avec la voltammétrie cyclique.

C. La diversité du 5ème ligand du complexe Cu(II)TMPA

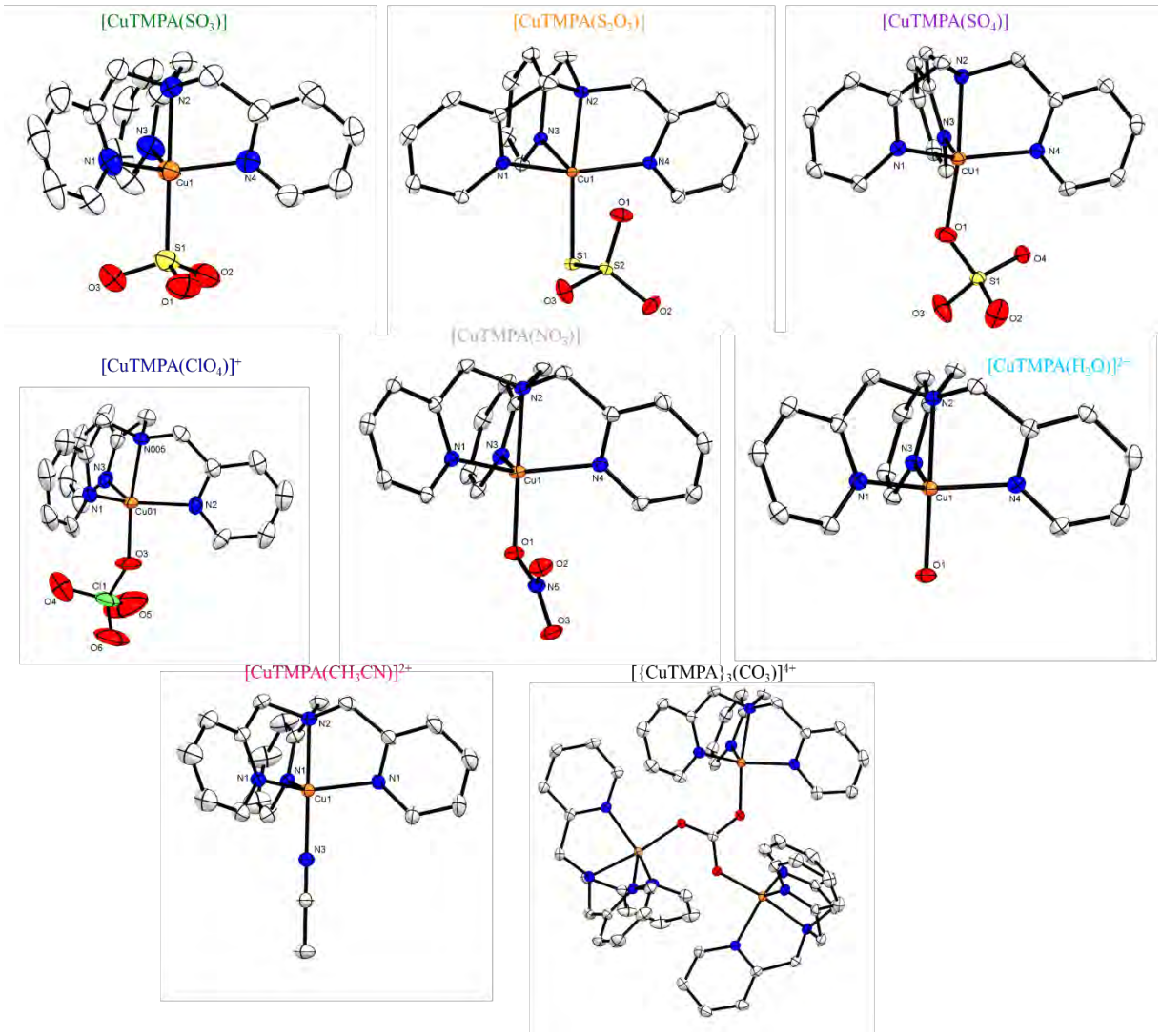

Figure 7: Structures RX des complexes [CuTMPA(SO_3)]; [CuTMPA(S_2O_3)]; [CuTMPA(SO_4)]; [CuTMPA(ClO_4)]$^+$; [CuTMPA(NO_3)]$^+$; [CuTMPA(H_2O)]$^{2+}$; [CuTMPA(CH_3CN)]$^{2+}$ et [{CuTMPA}$_3$(CO_3)]$^{4+}$ représentés avec 50 % d'ellipsoïde.

Au cours de l'étude du complexe Cu(II)TMPA en milieu organique et aqueux, différents cristaux ont été obtenus et caractérisés par diffraction des Rayons-X. Les structures de ces complexes sont présentées en Figure 7. Le complexe Cu(II)TMPA principal peut prendre une diversité de ligands exogènes par leurs natures et leurs tailles en position apicale. En effet, on retrouve des ligands anioniques coordinés par un atome de soufre (SO_3^{2-} et $S_2O_3^{2-}$) ou par un atome d'oxygène (SO_4^{2-}, ClO_4^- et NO_3^-) et des ligands neutres tels que H_2O coordiné par l'oxygène et CH_3CN coordiné par l'azote. La flexibilité du ligand TMPA, permet même de

former un complexe trinucléaire avec un carbonate pour ligand central. Ces cristaux ont été obtenus en utilisant différents sels de Cu(II) et mélanges de solvant.

Les complexes Cu(II)TMPA ont également été étudiés en solution par analyses UV-Vis, RPE et par voltammétrie cyclique quand cela était possible. Les complexes sont caractérisés par une géométrie trigonale bipyramidale sous forme solide et en solution. Seul le complexe [CuTMPA(S_2O_3)] présente une géométrie pyramide à base carrée à l'état solide due à une interaction faible d'un atome d'oxygène avec le centre Cu(II), et une géométrie trigonale bipyramide en solution. Dans nos conditions d'étude, c'est-à-dire en milieu tamponné avec de l'HEPES à pH 7,4 et 10 % de CH_3CN, le 5ème ligand est une molécule d'eau.

D. Etude des complexes modèles Cu-Aβ en solution aqueuse tamponnée avec 10 % d'acétonitrile.

1. Sphères de coordination des modèles Cu(II)Aβ

Les sphères de coordination des complexes de Cu(II) avec les trois modèles peptidiques $A\beta_{1-16}$, $A\beta_{1-7}$ et $A\beta_{13-14}$ ont été élucidées en solution dans l'HEPES à pH 7,4 et avec 10 % d'acétonitrile.

Les signatures UV-Vis et RPE des trois complexes Cu(II)Aβ dans chacune des conditions sont présentées en Figure 8. Les spectres UV-Vis et RPE des trois complexes sont attribués à une géométrie plane carrée. Pour chaque espèce, les spectres sont très similaires avec et sans la présence de 10 % de CH_3CN qui ne participe donc pas aux sphères de coordination des modèles Cu(II). Les sphères de coordination des complexes Cu(II)$A\beta_{1-16}$ et Cu(II)$A\beta_{1-7}$ à pH physiologique sont déjà connues dans la littérature avec des peptides non protégés par l'amidation en position C-terminale. Les signatures UV-Vis et RPE obtenues dans cette étude sont en accord avec celles de la littérature pour ces deux complexes. Le complexe Cu(II)$A\beta_{1-16}$ est caractérisé par la cohabitation de deux composés à l'équilibre avec un pKa de 7,8. Ils ont les mêmes sphères de coordination que les deux composé de Cu(II)Aβ présentés précédemment au paragraphe A-2. Le spectre RPE du complexe Cu(II)$A\beta_{1-7}$ est similaire à celui de composé II (lignes pointillées, Figure 8). La sphère de coordination de Cu(II)$A\beta_{1-7}$ est donc la même que

celle du composé II, présentée précédemment sans échange entre les résidus His, puisque seul l'His6 est présente (Figure 9, milieu).

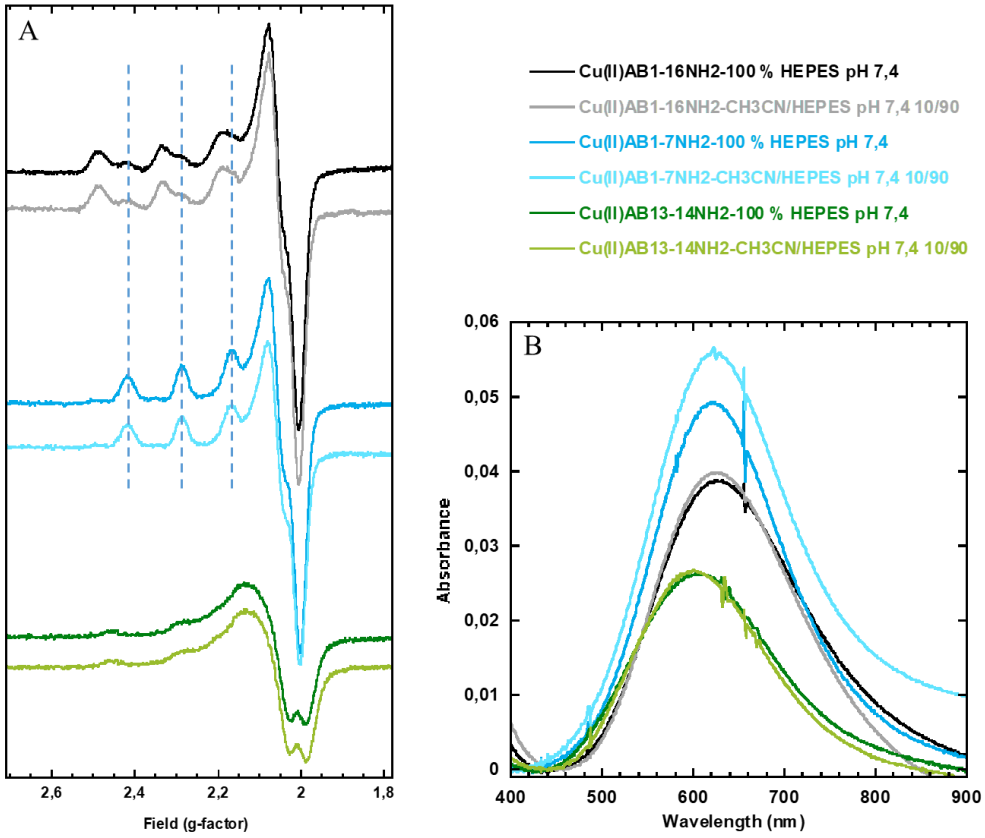

Figure 8 : Spectres RPE (A) et UV-Vis (B) des complexes Cu(II)Aβ$_{1-16}$ (noir) ; Cu(II)Aβ$_{1-7}$ (bleu) et Cu(II)Aβ$_{13-14}$ (vert) dans l'HEPES à pH 7,4 (lignes foncées) et avec 10 % de CH_3CN (lignes claires). Les lignes verticales en pointillés sur les spectres RPE montrent la position des transitions hyperfines correspondant au composé II. Conditions RPE : [Aβ] = 0,55 mM ; [^{65}Cu] = 0.5 mM ; 10 % glycerol ; T = 120 K ; microwave power : 5 mW. Conditions UV-Vis : [Aβ] = 0.55 mM; [$Cu(SO_4)•5H_2O$] = 0.5 mM; ℓ = 1 cm; T = 25 °C.

Le complexe Cu(II)Aβ$_{13-14}$ n'a pas été étudié auparavant, l'élucidation de sa sphère de coordination a donc nécessité une analyse approfondie. Les signatures RPE et UV-Vis de ce complexe sont différentes de celles des deux complexes précédents Cu(II)Aβ$_{1-16}$ et Cu(II)Aβ$_{1-7}$. En effet, le signal RPE est moins intense et les raies hyperfines sont plus larges. En UV-Vis la bande de transition d-d est à une plus petite longueur d'onde et moins intense. Il a été proposé que l'écrasement du signal RPE soit dû à une interaction dipôle-dipôle entre deux centres Cu(II) liés par Aβ$_{13-14}$ jouant le rôle de ligand pontant. Cette hypothèse est corroborée par l'addition d'imidazole qui empêche la formation du dimère et présente un spectre RPE ayant les mêmes positions de raies hyperfines que le spectres RPE de Cu(II)Aβ$_{13-14}$ sans imidazole. La structure

superhyperfine est également visible et laisse apparaitre neuf lignes dans la région $g_{\perp}$ qui traduisent une coordination 4N. Il est donc proposé que le mode de coordination de Cu(II) avec $A\beta_{13-14}$ soit sous forme de dimère (Figure 9, droite) où les centres métalliques ont une géométrie plane carrée composée de :

- l'amine N-terminale
- la liaison amide déprotonnée entre les deux résidus His
- deux atomes N de cycles imidazole l'un provenant d'un résidu His14 d'un premier peptide $A\beta_{13-14}$, et l'autre d'un résidu His13 d'un deuxième peptide $A\beta_{13-14}$'.

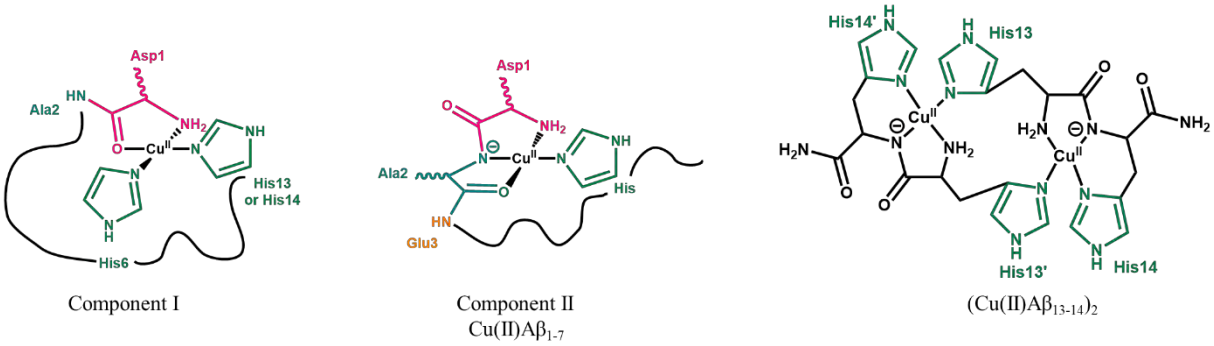

Figure 9: Représentation des sphères de coordination de Cu(II) à $A\beta_{1-16}$ en composé I et II (gauche et milieu), à $A\beta_{1-7}$ en composé II (milieu) et à $A\beta_{13-14}$ en tant que dimère (droite).

2. Etudes des modèles Cu(II)/Cu(I) et impact de 10 % de CH_3CN par voltammétrie cyclique

Tous les complexes modèles, Cu-TMPA compris, ont été caractérisés par voltammétrie cyclique dans l'HEPES à pH 7,4 et avec 10 % de CH_3CN. Les résultats sont présentés en Figure 10.

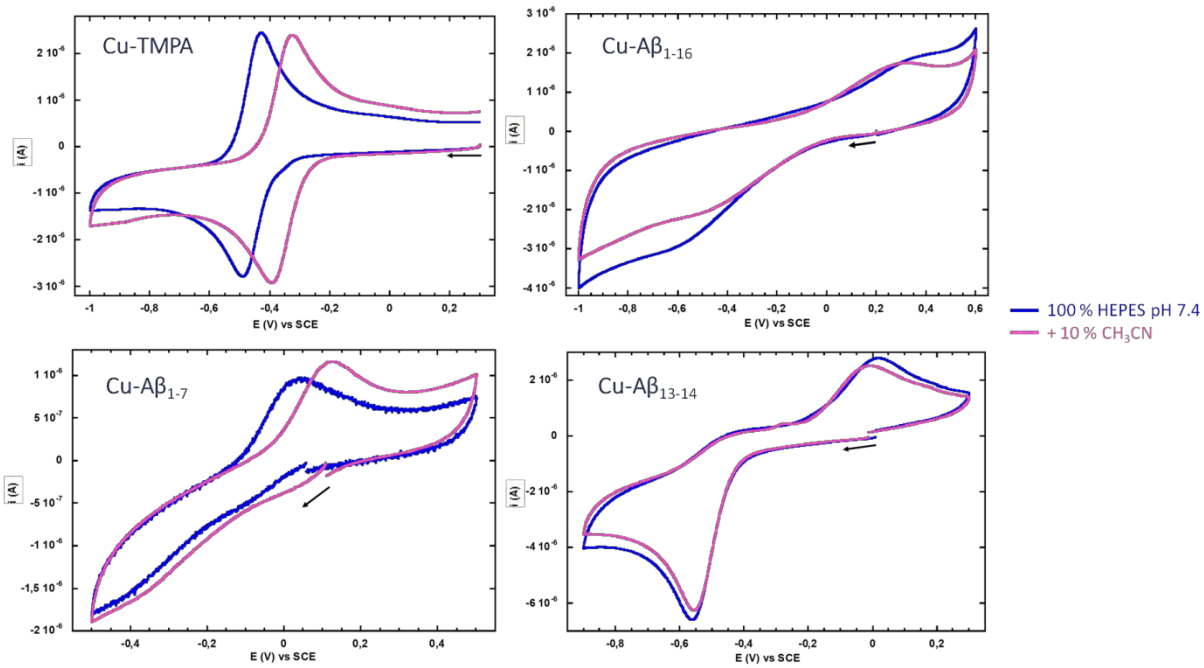

Figure 10 : Voltammogrammes cycliques des complexes Cu-TMPA ; Cu-Aβ1-16 ; Cu-Aβ1-7 et Cu-Aβ13-14 dans l'HEPES à pH 7,4 (bleu) et avec 10 % de CH_3CN (rose). Conditions : [ligand] = 0.55 mM ; [Cu(II)] = 0.5 mM ; vitesse de balayage : 100 mV/s ; Electrode de Travail : Carbone vitreux ; Référence : SCE ; Contre Electrode : Fil de platine. Les premiers scans sont montrés, le départ est indiqué par la flèche.

Le complexe Cu-TMPA présente un voltammogramme réversible avec un $E_{1/2}$ de -0,46 V vs SCE dans l'HEPES. Avec l'ajout de 10 % de CH_3CN, le voltammogramme reste réversible mais la vague redox est déplacée vers des potentiels plus positifs avec un $E_{1/2}$ de -0,36 V vs SCE. Ce déplacement montre une meilleure stabilisation de Cu(I)TMPA en présence de CH_3CN, et de Cu(II)TMPA en solvant aqueux. Les analyses UV-Vis et RPE ont montré qu'avec 10 % de CH_3CN dans l'HEPES à pH 7,4 c'est une molécule de H_2O qui est coordinée à Cu(II)TMPA en position labile. Le déplacement de potentiel peut donc s'expliquer (i) par le fait que H_2O reste coordiné au Cu(I), mais que le potentiel est sensible à la polarité du solvant

ou, (ii) par un remplacement de H_2O par CH_3CN à l'état d'oxydation +1 et donc un déplacement du $E_{1/2}$ qui suit un mécanisme ECEC (Electrochimie-Chimie-Electrochimie-Chimie).

Les complexes modèles Cu-Aβ présentent tous des voltammogrammes irréversibles dans l'HEPES à pH 7,4. Pour les complexes Cu-$A\beta_{1-16}$ et Cu-$A\beta_{1-7}$, le transfert électronique se fait par un état de transition appelé « in-between state » présenté précédemment. Dans le cas du complexe Cu-$A\beta_{1-16}$, la présence de 10 % de CH_3CN réduit l'irréversibilité. Cependant, pour le complexe Cu-$A\beta_{1-7}$ l'état Cu(I) est stabilisé probablement par la coordination de CH_3CN au Cu(I) qui permet le passage d'une géométrie trigonale à une géométrie tétraédrique plus stable. Les voltammogrammes du complexe Cu-$A\beta_{13-14}$, avec et sans la présence de 10 % de CH_3CN, présentent le même pic en réduction, ce qui est en accord avec la non participation de CH_3CN à la sphère de coordination de Cu(II)$A\beta_{13-14}$. En revanche, le pic d'oxydation est déplacé vers des plus bas potentiels. Ce déplacement traduit une déstabilisation de Cu(I)$A\beta_{13-14}$ en présence de CH_3CN, qui pourrait provenir de la coordination de CH_3CN à Cu(I) et donc induire la perte de la linéarité pour une géométrie trigonale moins stable.

Finalement, la présence de 10 % de CH_3CN dans l'HEPES à pH 7,4, n'a pas d'impact sur les sphères de coordination des modèles Cu(II)TMPA et Cu(II)Aβ. En revanche, elle induit des changements sur les propriétés redox des complexes avec un effet sur les états d'oxydation Cu(I) et l'IBS.

E. La réactivité des complexes Cu(I)L envers CO

Le monoxyde de carbone (CO) est un ligand diamagnétique approprié pour le Cu(I) avec des orbitales favorables pour former une forte liaison σ et accepter la retro-donation dans ses orbitales π (Figure 11).

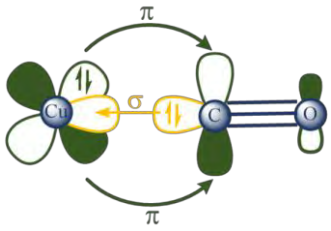

Figure 11 : Schéma de la liaison Cu-CO montrant les propriétés σ-donneur et π-accepteur de CO.

La réactivité envers CO de chaque complexe Cu(I)TMPA et Cu(I)Aβ a été étudiée en solution aqueuse tamponnée à pH 7,4 contenant 10 % de CH_3CN par RMN, électrochimie, UV-Vis et IR. Les deux premières techniques ont donné les résultats les plus probants. Par les propriétés π-accepteur, la coordination de CO devrait réduire la densité électronique sur Cu(I) et ainsi réduire l'effet du Cu(I) sur les protons proches des sites de coordination du ligand. Cet effet se traduit par un déplacement des signaux en RMN ^1H. Le spectre RMN ^1H de chaque ligand est comparé avec ceux de la forme complexée Cu(I) et de l'adduit Cu(I)-CO.

Les spectres RMN ^1H du TMPA, de Cu(I)TMPA et Cu(I)TMPA(CO) sont présentés Figure 12 et montrent seulement un ensemble de cinq pics qui traduit l'équivalence des trois motifs methyl-pyridine. L'ajout de Cu(I) sur le TMPA induit un déblindage des signaux, à l'exception du signal correspondant à H3 qui est blindé. Par comparaison avec d'autres spectres RMN ^1H de complexes Cu(I)TMPA de la littérature étudiés en solvants organiques, il est proposé que dans nos conditions Cu(I)TMPA soit pentacoordiné par les quatre amines du TMPA et une molécule de solvant (H_2O ou CH_3CN indéterminée) occupant la cinquième position.

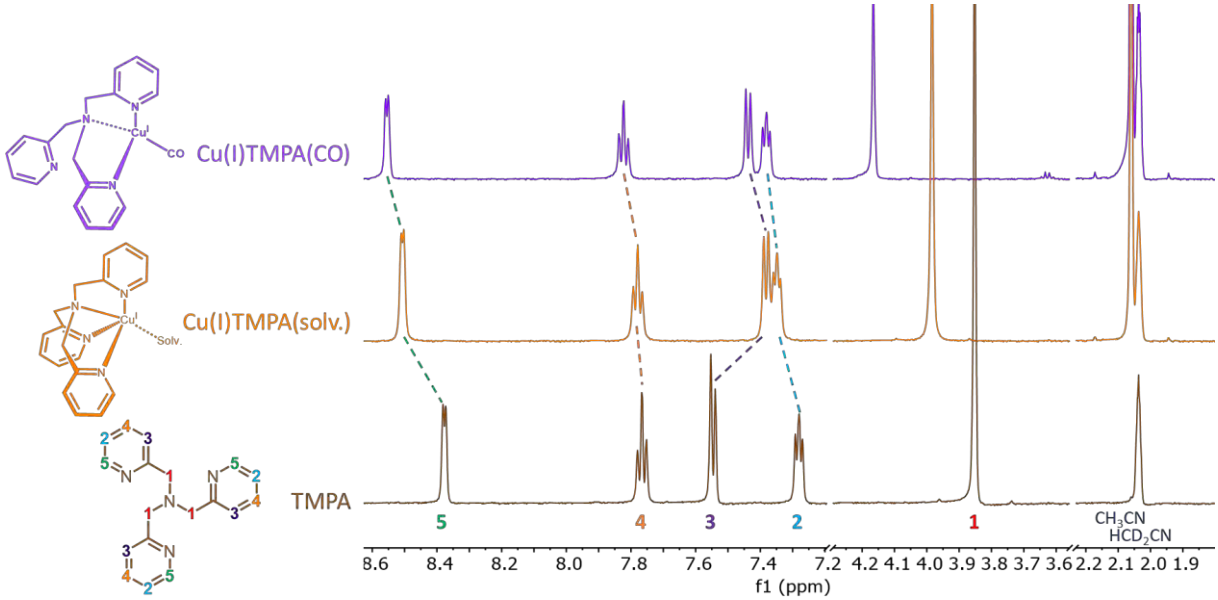

Figure 12 : Spectres RMN ^1H du TMPA (marron), Cu(I)TMPA(solvant) (orange) et Cu(I)TMPA(CO) (violet) dans CD_3CN/KPB pD 7,4 100 mM (13/87 v/v) sous atmosphères ambiante, d'Ar ou de CO respectivement. Les déplacements chimiques sont indiqués par des lignes en pointillés. Condition : [TMPA] = 2.2 mM ; [$[Cu(CH_3CN)_4]BF_4$] = 2 mM ; référence interne HCD_2CN à 2,037 ppm.

Sous atmosphère de CO, chaque signal est déblindé par rapport à ceux de Cu(I)TMPA. L'effet électronique induit par le Cu(I) sur les protons proches des sites de coordination de TMPA est renforcé, sauf pour le signal du proton H3 qui revient à une position plus proche de celle du ligand seul. Ces observations peuvent traduire la décoordination d'un bras pyridyle et le remplacement du ligand solvant par CO lors de la formation de l'adduit Cu(I)CO. Ce mode de coordination a déjà été proposé dans la littérature, basé sur des analyses IR de complexes Cu(I)TMPA(CO). Les signaux fins et équivalents des bras pyridyles suggèrent un échange rapide entre eux.

Dans l'étude des complexes peptidiques, la RMN ^{1}H est très utile pour identifier les acides aminés impliqués dans la coordination au Cu(I). La Figure 13 présente les spectres RMN ^{1}H des peptides modèles seuls ($A\beta_{1-16}$, $A\beta_{1-7}$ et $A\beta_{13-14}$), des complexes Cu(I)Aβ et Cu(I)Aβ(CO). Ils sont centrés sur la zone des protons aromatiques. Les résidus His sont particulièrement impliqués dans la coordination des Aβ au Cu(I), c'est pourquoi les protons qui leur sont attribués sont également ceux qui subissent le plus de déplacements chimiques.

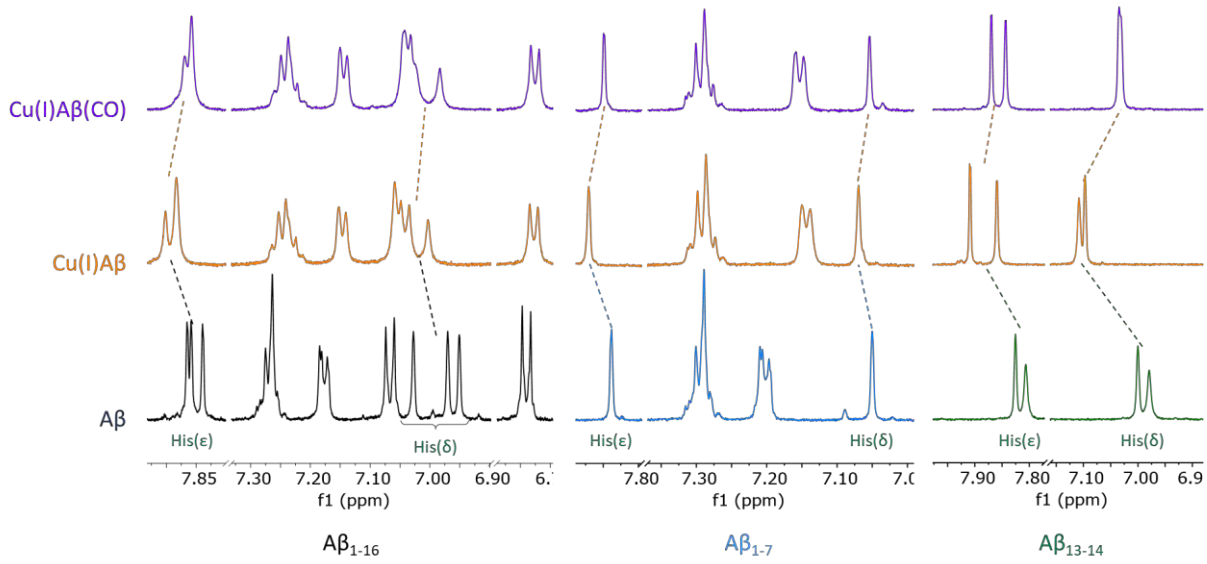

Figure 13 : Spectres RMN ^{1}H des peptides modèles $A\beta_{1-16}$ (noir), $A\beta_{1-7}$ (bleu) et $A\beta_{13-14}$ (vert),de leur coordination avec Cu(I) (orange) et sous forme d'adduit Cu(I)Aβ(CO) (violet) dans CD_3CN/KPB pH 7,4 100 mM (10/90 v/v) sous atmosphères d'Ar ou de CO. Seules les parties des spectres attribuées aux protons aromatiques sont montrées et les déplacements chimiques sont indiqués par des lignes en pointillés. Condition : [Aβ] = 2.2 mM ; $[[Cu(CH_3CN)_4]BF_4]$ = 2 mM ; référence interne TSP à 0 ppm.

Pour chaque peptide, la coordination du Cu(I) induit un déblindage des signaux des protons des cycles imidazole des résidus His. Le complexe Cu(I)Aβ$_{1-16}$ a un mode de coordination linéaire entre deux résidus His parmi les trois dans un équilibre dynamique (Figure 14). La même sphère de coordination est proposée pour Cu(I)Aβ$_{13-14}$. Le complexe Cu(I)Aβ$_{1-7}$ a une géométrie trigonale impliquant la coordination de l'amine terminale NH_2, d'un atome d'azote du cycle imidazole de l'His6 et de la fonction carboxylate entre Asp1 et Asp7. La coordination du CO induit un blindage des signaux des protons aromatiques des His vers leur position initiale en peptide libre. Comme attendu, le CO réduit l'effet électronique de Cu(I) sur les protons proches des sites de coordination. La liaison Cu(I)-CO est donc confirmée. Les modes de coordination des adduits Cu(I)CO proposés restent les mêmes que ceux des parents Cu(I)Aβ avec un ligand CO en plus. Cu(I)Aβ$_{1-16}$(CO) et Cu(I)Aβ$_{13-14}$(CO) adoptent une géométrie trigonale et Cu(I)Aβ$_{1-7}$(CO) une géométrie tétraédrique (Figure 14).

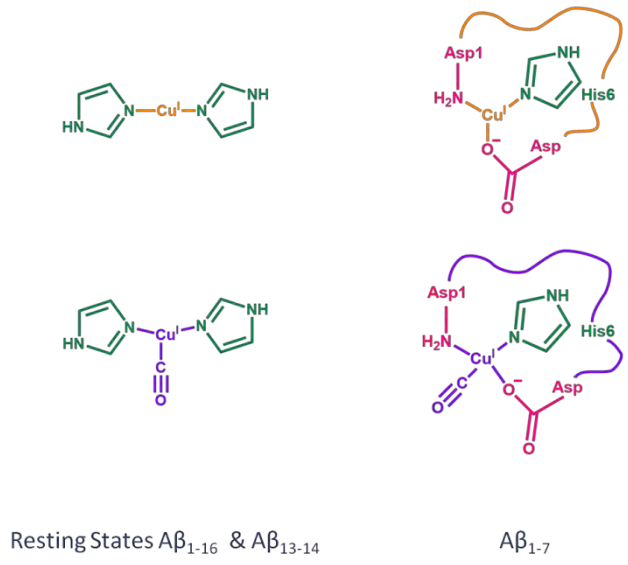

Figure 14 : Schémas des modes de coordination des complexes Cu(I)Aβ$_{1-16}$, Cu(I)Aβ$_{13-14}$, Cu(I)Aβ$_{1-7}$ et des adduits Cu(I)CO correspondants.

Pour les complexes Cu(I)TMPA et Cu(I)Aβ$_{13-14}$, la coordination de CO est confirmée par électrochimie avec une liaison forte au Cu(I). En revanche, pour les complexes Cu(I)Aβ$_{1-7}$ et Cu(I)Aβ$_{1-16}$ pour lesquels la voltammétrie cyclique permet de sonder l'IBS, la coordination de CO à l'IBS n'est pas confirmée ou alors avec une force de liaison plus faible.

CO est capable de se coordiner à chaque modèle Cu(I) étudié et une sphère de coordination a été proposée basée sur les études RMN ^{1}H et les données de la littérature.

F. La réactivité des complexes Cu(I)L envers O_2

La réactivité envers O_2 des complexes Cu(I)TMPA et des modèles Cu(I)Aβ a été étudiée de deux manières différentes dans l'HEPES à pH 7,4 et avec 10 % de CH_3CN. L'une consiste à suivre la consommation de l'ascorbate par UV-Vis au cours du temps à 265 nm. L'ascorbate est un réducteur naturellement présent dans le corps. Il participe à la catalyse de la réduction du dioxygène en ERO. La cinétique de sa consommation implique la présence de deux substrats, l'ascorbate et O_2 ; donc le suivi de deux réactions : (i) la réduction de Cu(II)L par l'ascorbate et (ii) l'oxydation de Cu(I)L par O_2. Ces deux réactions suggèrent un transfert électronique par un mécanisme de sphère interne. L'autre manière s'intéresse aux propriétés redox des complexes en présence d'O_2 et suit la réactivité par voltammétrie cyclique. Elle implique la présence d'un seul substrat, l'oxygène, donc une seule réaction chimique de réduction d'O_2. La réduction de Cu(II)Aβ est électrochimique, le transfert électronique se fait donc par sphère externe.

Le complexe Cu(I)TMPA est déjà connu pour catalyser la réduction d'O_2 en milieu aqueux tamponné à pH physiologique, ce qui concorde avec les résultats obtenus par voltammétrie cyclique avec et sans les 10 % de CH_3CN. Cependant, l'étude de consommation de l'ascorbate par Cu(II/I)TMPA révèle une vitesse de consommation du réducteur lente expliquée par une mauvaise fenêtre de potentiel. Le complexe Cu-$Aβ_{13-14}$ se comporte de manière similaire à Cu-TMPA, avec toutefois une réactivité moins forte pour la réduction d'O_2 en voltammétrie cyclique (pas d'apparition de pic catalytique). L'étape limitante est donc la réduction par l'ascorbate.

La consommation de l'ascorbate se fait très rapidement pour les complexes Cu(II/I)$Aβ_{1-16}$ et Cu(II/I)$Aβ_{1-7}$, ce qui traduit que les deux réactions suivies se font rapidement. Cependant, aucun pic catalytique n'est observé en voltammétrie cyclique. Dans ces cas, l'étape limitante serait la réduction d'O_2 (Figure 15).

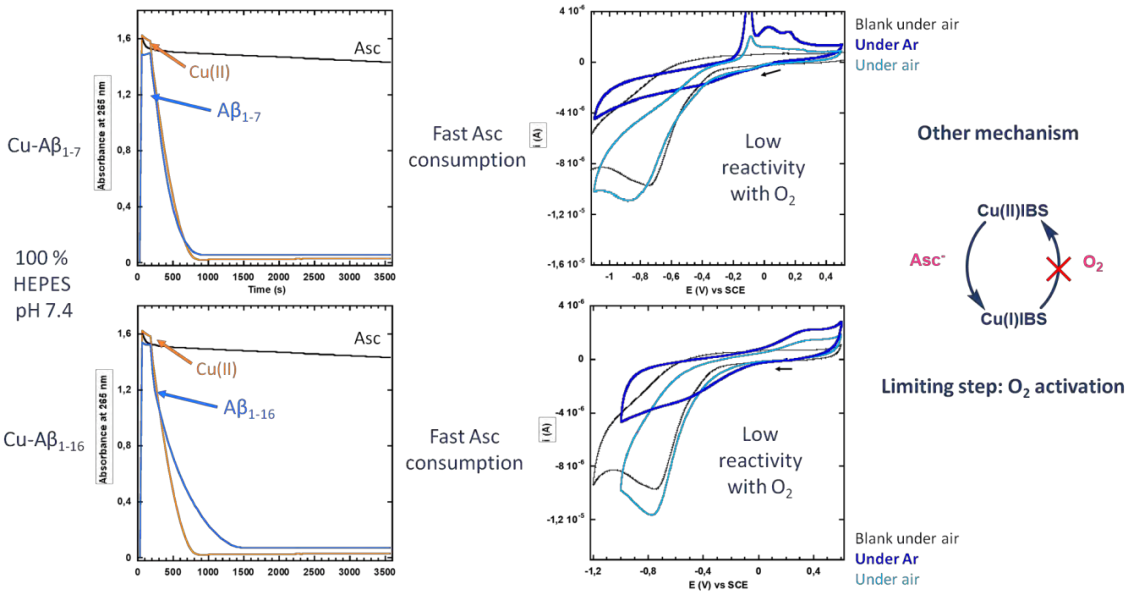

Figure 15 : (Gauche) consommation de l'ascorbate en fonction du temps par les complexes Cu(II/I)Aβ1-16 (haut) et Cu(II/I)Aβ1-7 (bas) dans l'HEPES à pH 7,4. (Droite) Voltammétrie cyclique des complexes Cu-Aβ1-16 et Cu-Aβ1-7 sous air dans l'HEPES à pH 7,4.

La principale différence entre les deux techniques d'étude est la présence d'ascorbate. Il serait indispensable pour la réduction d'O_2 par les complexes Cu-Aβ1-7 et Cu-Aβ1-16 connus pour réagir par l'intermédiaire de l'IBS. Il est proposé que l'ascorbate réduit Cu(II)IBS par un transfert électronique en sphère interne et que sa coordination au Cu(I)IBS permet une pré-organisation du complexe, indispensable à sa réactivité avec O_2. Cette dernière n'est pas observée en électrochimie due à l'absence de substrat (Figure 16).

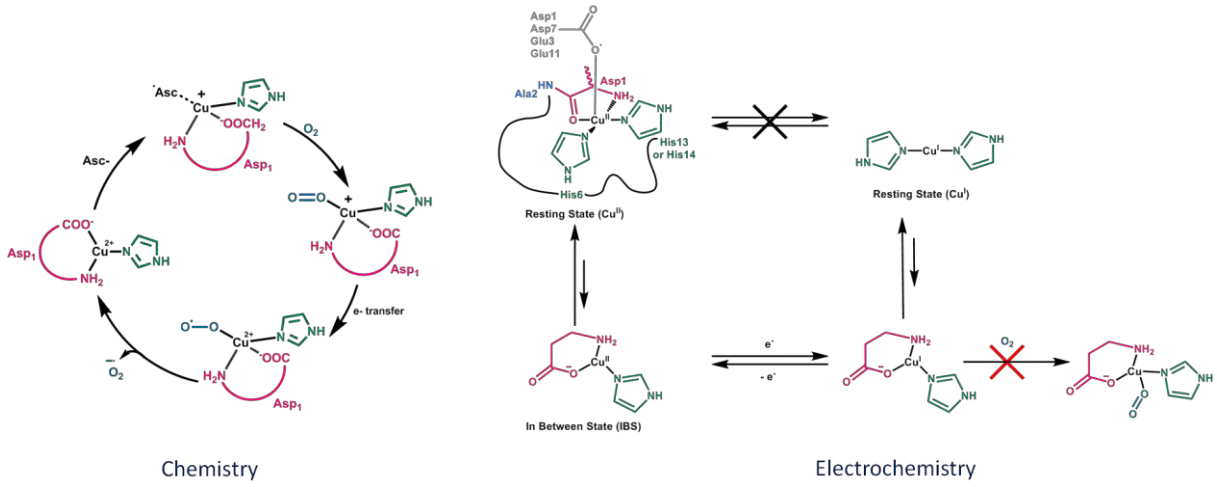

Figure 16 : (Gauche) Schéma de la pré-organisation du Cu(I)IBS dans le cycle catalytique de réduction d'O_2 en présence d'ascorbate. (Droite) Schéma carré du mécanisme Chimie-Electrochimie-Chimie de Cu-Aβ sous air, pour lequel la catalyse de réduction d'O_2 n'est pas observée.

G. Conclusion et perspectives

Dans le contexte de la maladie d'Alzheimer et plus particulièrement de la catalyse de la production d'ERO par le complexe Cu-Aβ, trois complexes modèles Cu-Aβ_{1-16}, Cu-Aβ_{1-7} et Cu-Aβ_{13-14} ont été caractérisés. La réactivité de ces complexes a été étudiée envers O_2 et CO (utilisé comme substitut d'O_2), en comparant systématiquement avec celle du complexe Cu-TMPA bien connu. L'objectif était de sonder le mécanisme de réactivité de l'IBS, supposé être l'espèce active, dans le cycle catalytique de la réduction d'O_2.

Une analyse approfondie du complexe Cu(II)TMPA en milieu aqueux tamponné et dans des mélanges de solvants a permis d'isoler et de caractériser de nouveaux complexes. Ils peuvent prendre une variété de ligands en position apicale. La géométrie trigonale bipyramidale est conservée pour la plus part des complexes à l'état solide et en solution.

Les conditions d'étude, en solution aqueuse tamponnée à pH physiologique avec 10 % de CH_3CN ont été choisies afin d'être pertinentes avec un contexte biologique, mais également pour augmenter la concentration de CO en solution et tirer la réaction Cu(I)L + CO ⇄ Cu(I)L(CO) vers la formation de l'adduit.

Les modes de coordination des quatre complexes Cu(II)L ont été élucidés dans nos conditions et ne sont pas impactés par la présence de 10 % de CH_3CN. Les études en voltammétrie cyclique montrent toutefois l'impact de CH_3CN sur l'IBS et sur les états Cu(I)L.

L'étude de la réactivité des complexes Cu(I)L envers CO a révélé qu'il est possible de former l'adduit Cu(I)TMPA(CO) en milieu principalement aqueux tamponné. La forte liaison Cu(I)CO a été confirmée par toutes les techniques de spectroscopie et d'analyses utilisées (UV-Vis, RMN ^{1}H, IR, et voltammétrie cyclique) pour Cu(I)TMPA(CO). En revanche, la coordination de CO aux complexes modèles Cu(I)Aβ_{1-16} et Cu(I)Aβ_{1-7} n'est observée que par RMN ^{1}H et par voltammétrie cyclique pour Cu(I)Aβ_{13-14}. L'utilisation d'une boîte à gants permettrait de travailler dans de meilleures conditions inertes et sous pression de CO, et ainsi s'affranchir de la présence de CH_3CN en tant que co-solvant. Des études RMN ^{1}H à différentes fréquences, températures et stœchiométries Cu/Aβ permettrait une meilleure attribution des signaux.

La production d'ERO par les complexes Cu-L a été indirectement étudiée par le suivi de l'oxydation de l'ascorbate en UV-Vis. Elle a également été suivie directement en voltammétrie cyclique, sous air et sans présence de réducteur. Ces études ont révélé que l'ascorbate semble essentiel à la pré-organisation de l'IBS pour lui permettre de réagir avec O_2. Cette hypothèse pourrait être vérifiée par des études en voltammétrie cyclique en présence d'ascorbate ou d'un substitut, mais aussi par un suivi cinétique en UV-Vis en présence d'un réducteur non-coordinant.

Le travail de cette thèse pourrait être appliqué à d'autres études de mécanisme d'activation du dioxygène par différents bio-complexes modèles en milieux aqueux.

Annexes

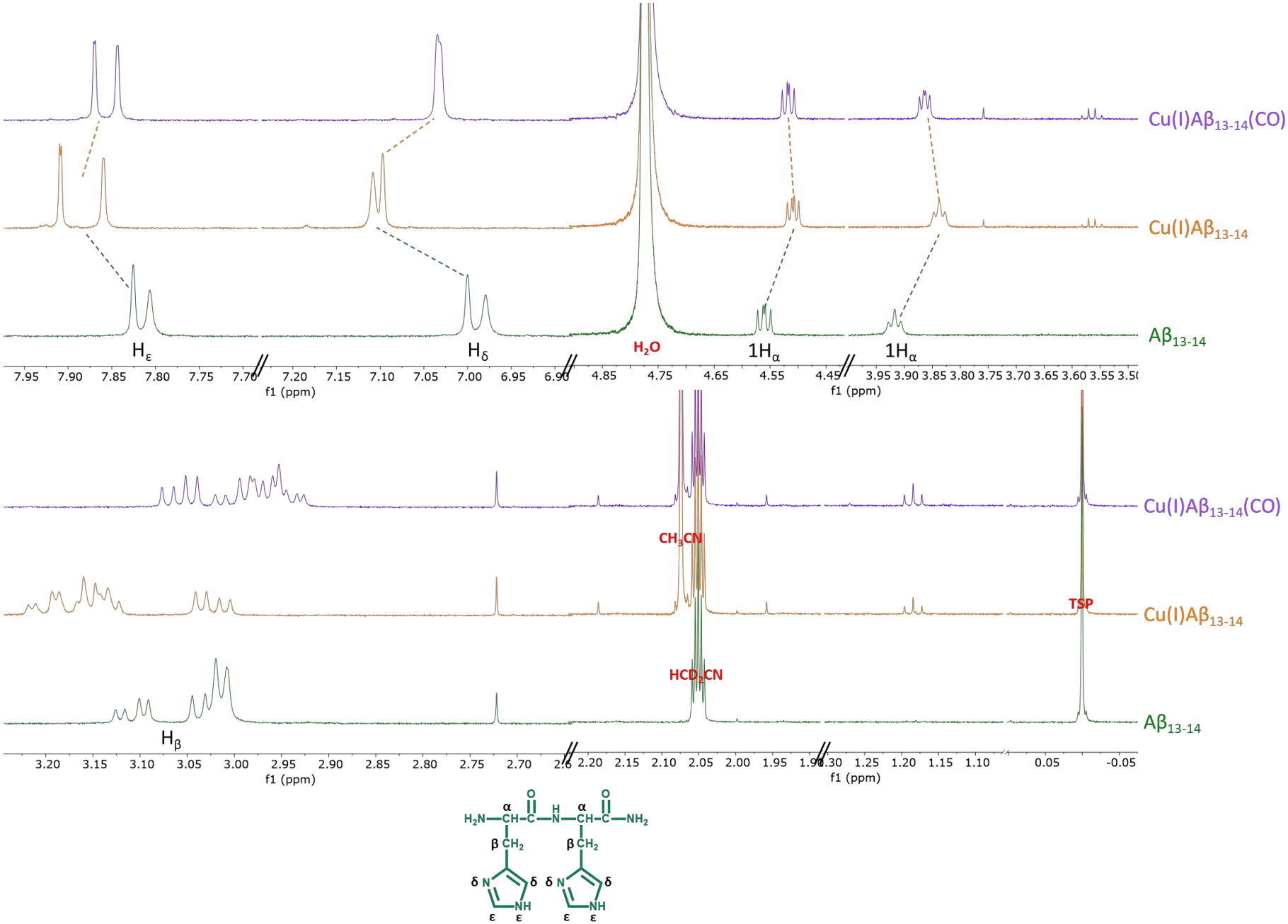

Figure V.A-2: ^{1}H NMR spectra of $A\beta_{13\text{-}14}$ (green) (Ar atmosphere), $Cu(I)A\beta_{13\text{-}14}$ (orange) (Ar atmosphere) and $Cu(I)A\beta_{13\text{-}14}(CO)$ (purple) (CO atmosphere) in CD_3CN/KPB pH 7.4 100 mM 10/90 v/v. The chemical shifts are indicated with dotted lines.

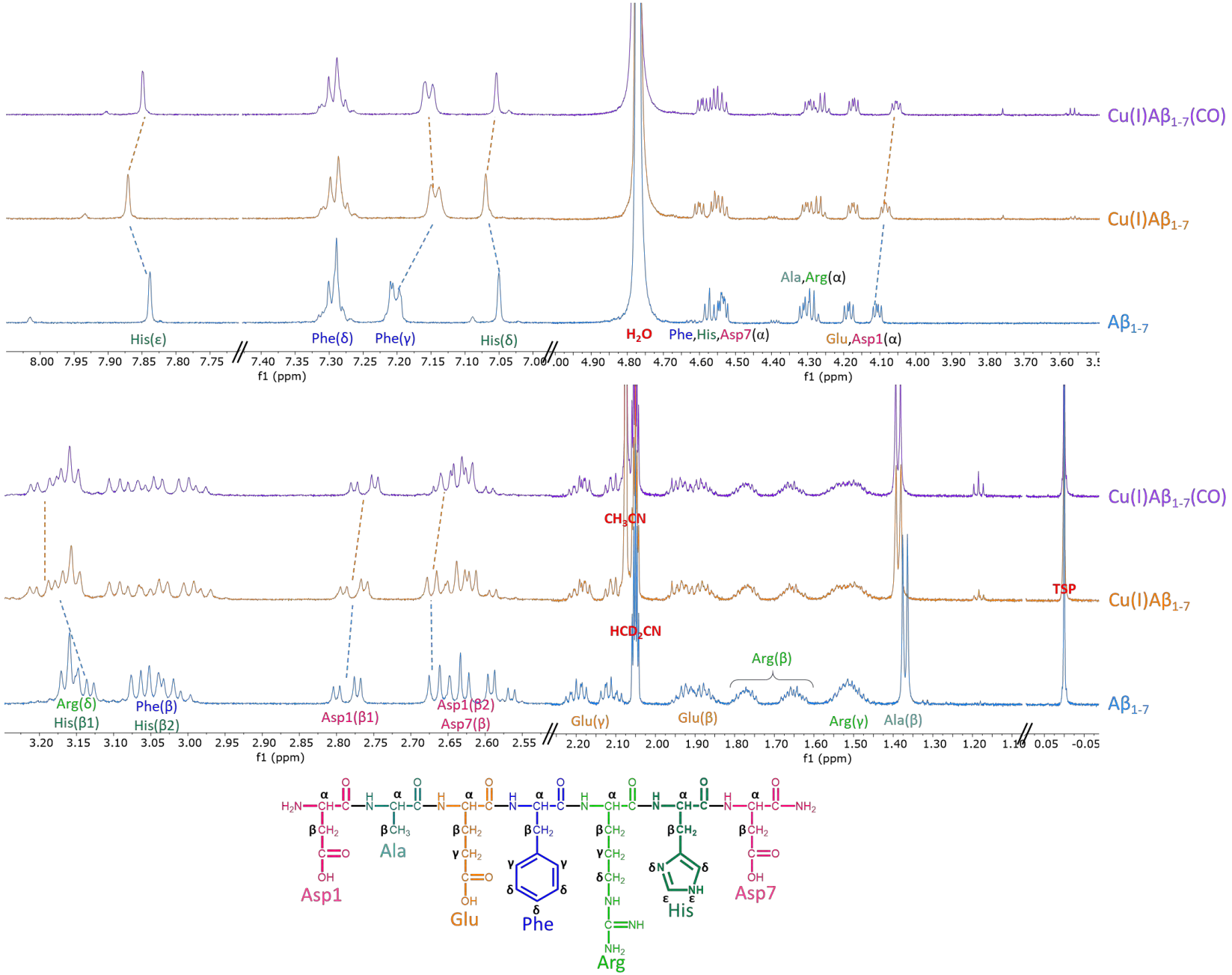

Figure V.A-3: ^{1}H NMR spectra of Aβ$_{1-7}$ (blue) (Ar atmosphere), Cu(I)Aβ$_{1-7}$ (orange) (Ar atmosphere) and Cu(I)Aβ$_{1-7}$(CO) (purple) (CO atmosphere) in CD_3CN/KPB pH 7.4 100 mM 10/90 v/v. The chemical shifts are indicated with dotted lines.

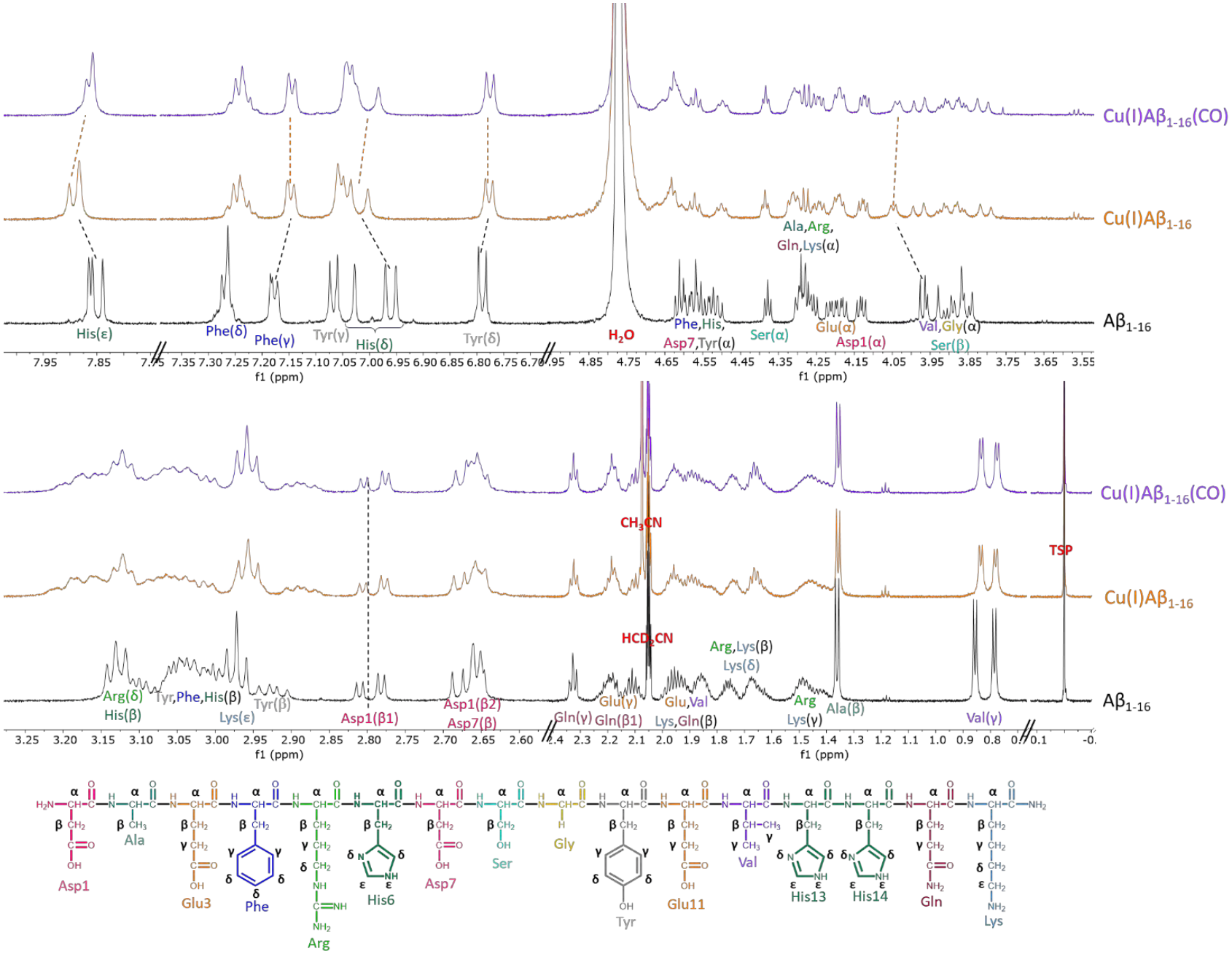

Figure V.A-4: ^{1}H NMR spectra of $A\beta_{1\text{-}16}$ (black) (Ar atmosphere), $Cu(I)A\beta_{1\text{-}16}$ (orange) (Ar atmosphere) and $Cu(I)A\beta_{1\text{-}16}(CO)$ (purple) (CO atmosphere) in CD_3CN/KPB pH 7.4 100 mM 10/90 v/v. The chemical shifts are indicated with dotted lines.

Abstract

Dementia is affecting about 50 million persons worldwide with Alzheimer's Disease (AD) being the most spread one. AD is a neurodegenerative disorder affecting the elderly. High oxidative damages of the brain associated with an abnormally high extracellular level of amyloid-β peptide (Aβ) leading to its aggregation in senile plaques are typical features of AD. Bio-metal ions such as copper (Cu) are found in high amount in amyloid plaques. Cu was shown to bind Aβ and the resulting complex has the ability to catalyze reactive oxygen species (ROS) production in presence of dioxygen (O_2) and a reductant such as ascorbate by cycling between the +I and +II oxidation states. However, the exact catalytic mechanism remains misunderstood. The two coordination spheres of Cu-Aβ (in +I and +II oxidation states) are strongly different, precluding direct electron transfer process. Electrochemical studies revealed that the redox cycling goes through an "in-between-state" (IBS) that would be the redox active species and be in equilibrium with the two spectroscopically characterized resting states. The elusive feature of the IBS makes it highly challenging to identify and study. The objective of my thesis was to gain new insights into the IBS reactivity with O_2. To overcome its elusive character, carbon monoxide (CO) was used as a redox inactive surrogate of O_2 to accumulate CO-bound Cu(I)Aβ intermediates.

The well-known tripodal Cu-TMPA (TMPA = tris(2-pyridylmethyl)amine) complex has been used as a reference compound with respect of CO and O_2 binding and reactivity. Then truncated Aβ peptides were chosen to identify the minimal binding site of Cu in the IBS in presence of CO and O_2. The study of Cu(II)TMPA complexes in solid-state by X-ray crystallography and in solution by UV-vis and EPR spectroscopies, and cyclic voltammetry, revealed the diversity of ligands occupying the fifth Cu(II) position while the distorted trigonal bipyramid geometry is kept. In aqueous solution Cu(II)TMPA has an aqua ligand in fifth position, which remains bound with 10 % of CH_3CN as co-solvent.

The conditions needed to further study the reactivity of Cu(I)L (L= TMPA or Aβ models) toward CO are in HEPES buffer, pH 7.4 with 10 % CH_3CN to increase CO solubility. Hence it was checked that 10 % CH_3CN doesn't participate in Cu(II)Aβ models coordination spheres by UV-vis and EPR studies.

Then reactivity of Cu(I)L toward CO was studied by ^{1}H NMR, UV-vis, cyclic voltammetry and FT-IR. CO was shown to bind Cu(I)TMPA by all spectroscopic or electrochemical techniques. For Cu(I)Aβ models, CO was shown to bind Cu(I) complexes by ^{1}H NMR and cyclic voltammetry. However the other techniques give less clear-cut signatures of CO binding probably due to the higher flexibility of the peptide ligand inducing a diversity of Cu coordination sites.

Finally, the reactivity of Cu(I)L toward O_2 was investigated by cyclic voltammetry and their ability to produce ROS was measured by ascorbate consumption experiments. Two out of the three Cu-Aβ complexes were fast consuming ascorbate in HEPES pH 7.4. The last one was shown to partially stop the ROS production while Cu-TMPA has a moderate rate of ascorbate consumption. In contrast, the electro-catalysis of O_2 reduction was only clearly observed for Cu-TMPA. Together with the structural insights gained into the Cu(II) species and the Cu(I)-CO adducts, this points out to ligand-dependent mechanism of O_2 reduction. The "IBS state" mechanism is observed for the peptides only but its contribution (and thus the level of ROS produced) depends strongly on the sequence of the peptide.

Résumé

Les démences touchent environ 50 millions de personnes dans le monde et la maladie d'Alzheimer (MA) en est la forme la plus répandue. La MA est une maladie neurodégénérative qui touche les personnes âgées. Elle est caractérisée par des lésions cérébrales liées à un fort stress oxydant, associé à une concentration extracellulaire anormalement élevée en peptide amyloïde-β (Aβ) conduisant à son agrégation en plaques séniles. Les bio-métaux tels que les ions cuivre (Cu) sont présents en grande quantité dans les plaques amyloïdes. Il a été démontré que le Cu se lie à Aβ formant un complexe capable de catalyser la production d'espèces réactives de l'oxygène (ERO) en présence de O_2 et d'un réducteur tel que l'ascorbate, en effectuant des cycles entre les états d'oxydation +I et +II. Cependant, le mécanisme catalytique exact reste incompris. Les deux sphères de coordination de Cu-Aβ (dans les états d'oxydation +I et +II) sont très différentes, empêchant le transfert direct d'électrons. Des études électrochimiques ont révélé que le cycle redox passe par un "in-between state" (IBS) qui serait l'espèce active et en équilibre avec les états stables des ions Cu(I) et Cu(II) caractérisés par spectroscopie. Le caractère transitoire de l'IBS le rend difficile à détecter et à étudier. L'objectif de ma thèse était d'acquérir de nouvelles connaissances sur la réactivité de l'IBS avec le dioxygène. Pour cela, le monoxyde de carbone (CO) a été utilisé comme substitut redox inactif de O_2 afin d'accumuler les intermédiaires CO-Cu(I)Aβ.

Le complexe Cu-TMPA (TMPA = tris(2-pyridylméthyl)amine), qui a été largement étudié, a été utilisé comme composé de référence pour sa réactivité et son mode de coordination avec CO et O_2. Ensuite, des peptides Aβ modèles ont été choisis pour identifier le site de coordination minimal de Cu dans l'IBS en présence de CO et O_2. L'étude des complexes Cu(II)TMPA à l'état solide et en solution par cristallographie aux rayons X, spectroscopies UV-vis et RPE, et par voltammétrie cyclique, a révélé la coordination d'une diversité de cinquième ligand, avec une géométrie de type bipyramide trigonale distordue conservée. En solution aqueuse, Cu(II)TMPA possède un ligand aqua en cinquième position, qui se maintient avec 10 % de CH_3CN.

La réactivité de Cu(I)L (L= TMPA ou modèles Aβ) pour CO a été étudiée en milieu tamponné à pH 7.4 avec 10 % de CH_3CN pour augmenter la solubilité du CO dans le milieu. Il a donc été vérifié par des études UV-vis et RPE, que CH_3CN à un taux de 10 %, ne participe pas à la sphère de coordination des modèles Cu(II)Aβ.

La réactivité des complexes Cu(I)L en présence de CO a été étudiée par RMN ^1H, UV-vis, voltammétrie cyclique et FT-IR. La coordination du CO au Cu(I)TMPA a été observée par chaque technique de spectroscopie et électrochimique. Pour les modèles Cu(I)Aβ, la liaison du CO est surtout mise en évidence par des études RMN ^1H et de voltammétrie cyclique. Les autres techniques spectroscopiques ne montraient pas de signatures convaincantes, ce qui est probablement dû à la flexibilité des peptides Aβ et donc à la diversité de modes de coordination des complexes Cu-Aβ.

Enfin, la réactivité des Cu(I)L envers O_2 a été étudiée par voltammétrie cyclique et leur capacité à produire des ERO a été mesurée par des expériences de consommation d'ascorbate. Deux des trois complexes Cu-Aβ ont consommé rapidement l'ascorbate dans HEPES pH 7.4. Le dernier a partiellement arrêté la production d'ERO tandis que Cu-TMPA a une vitesse modérée de consommation d'ascorbate. En revanche, l'électro-catalyse de la réduction de l'O_2 n'a été clairement observée que pour Cu-TMPA. En se basant sur les connaissances structurelles acquises sur les espèces de Cu(II) et les adduits LCu(I)-CO, on peut en déduire que le mécanisme de réduction de l'O_2 dépend du ligand. Le mécanisme de "l'état IBS" est observé uniquement avec les peptides, mais sa contribution (et donc le niveau d'ERO produit) dépend fortement de la séquence du peptide.